The influence of convection on tidal flows

Craig Davidson Duguid

The University of Leeds

EPSRC Centre for Doctoral Training in Fluid Dynamics

School of Mathematics

Submitted in accordance with the requirements
for the degree of *Doctor of Philosophy*

31st December 2020

Intellectual property and publication statement

The candidate confirms that the work submitted is his own, except where work which has formed part of jointly authored publications has been included. The contribution of the candidate and the other authors to this work has been explicitly indicated below. The candidate confirms that appropriate credit has been given within the thesis where reference has been made to the work of others.

Ch. 1, 2, 3, 4, 5, 7 and 8 contain material from the jointly authored publication (Duguid et al., 2020a):
Duguid C. D., Barker A. J., Jones C. A., (2020),
"Tidal flows with convection: frequency-dependence of the effective viscosity and evidence for anti-dissipation", Monthly Notices of the Royal Astronomical Society, 491, 923.

Ch. 1, 2, 6, 7 and 8 contain material from the jointly authored publication (Duguid et al., 2020b):
Duguid C. D., Barker A. J., Jones C. A., (2020),
"Convective turbulent viscosity acting on equilibrium tidal flows: new frequency scaling of the effective viscosity", Monthly Notices of the Royal Astronomical Society, 497, 3400.

Both papers were primarily authored by C. D. Duguid who was responsible for all simulations, analysis and writing. Contributions of all other authors were through advisory and editorial roles. The numerical code, Snoopy, was supplied by A. J. Barker. The MESA simulations and analysis in Ch. 7 and the latter paper was performed by A. J. Barker (Barker, 2020).

Vidal J., Duguid C. D., Barker A. J., (2020),
"Anomalous $1/f$ frequency spectrum of thermal convection", Physical Review Fluids, in review.

C. D. Duguid provided data from the shear-less simulations in Ch. 6 for this paper as well as editorial advice (Vidal et al., 2020).

Acknowledgements

First and foremost I would like to thank the reader of this thesis or the associated papers. The greatest pleasure from research comes from knowing it has been useful or interesting to someone else.

I would also like to thank my supervisor team who were better than I could have asked for. Adrian Barker has been infinitely patient and generous with his time as well as exceptionally knowledgeable. Chris Jones for being an archive of fluids knowledge and guidance. Sven van Loo for various academic related discussions. If not for my MSc supervisor Frank Hermann I would never have had the confidence to pursue a PhD and career in science so he too deserves my thanks.

I would also like to thank the examiners, Stéphane Mathis and Rainer Hollerbach, for an engaging discussion about my work. A further thanks to Rainer for spotting typographical errors!

This work would not have been possible without EPSRC funding the CDT in Fluid Dynamics at the University of Leeds. I am very grateful to the CDT management team for giving me the opportunity to pursue a PhD at the University of Leeds. Also for the exceptional support and structure of the CDT programme which I strongly believe is a system that should be greatly expanded upon to allow greater diversity of individuals into science.

A huge thanks to the ARC super computer. Without you I could not have got so much data! Rest in pieces ARC1/MHD nodes.

It has been a great experience to work alongside the variety of PhD students. Tom Sykes for helping me navigate Leeds University, Fryderyk Wilczyǹski for being a font of useful knowledge, Khaled Hamood Al-Ghaithi for fun philosophical(?) discussions, Colin Hardy for being constantly attending the same conferences/workshops making travel easier, Hannah Kreczak for being my Newcastle buddy, and everyone else who I have not forgotten.

Technically, I should also thank my parents as without them I would not even be here, they have also been very supportive throughout!

It seems common to have a quote, so...

"By fire be purged!" - Ragnaros the Firelord

Abstract

Tidal interactions are important in driving spin and orbital evolution in various astrophysical systems such as hot Jupiters, close binary stars, planetary satellites, and more. However, the fluid dynamical mechanisms responsible for tidal dissipation in giant planets and stars remain poorly understood. One key mechanism is the interaction between tidal flows and turbulent convection which is thought to act as an eddy viscosity (ν_E) dampening the large-scale tidal flow. The efficiency of this mechanism has long been debated, particularly in the regime of fast tides, when the tidal frequency (ω) exceeds the turnover frequency of the dominant convective eddies (ω_c). The pioneering work of Zahn (1966) proposed that $\nu_E \sim \omega^{-1}$ while Goldreich & Nicholson (1977) found $\nu_E \sim \omega^{-2}$.

Using hydrodynamical simulations we investigate the dissipation of the large-scale (non-wavelike) equilibrium tide as a result of its interaction with convection. Our approach is to conduct a wide parameter survey (over a number of parameters) in order to study the interaction between an oscillatory background shear flow, which represents a large-scale tidal flow, and the convecting fluid inside a small patch of a star or planet. We simulate Rayleigh-Bénard convection in this Cartesian model and explore how the effective viscosity depends on the tidal (shear) frequency in both laminar and turbulent regimes. We also provide a complementary asymptotic analysis which is an extension of the work of Ogilvie & Lesur (2012) which supports our findings in the laminar cases.

We will present the results from our simulations to determine the effective viscosity, and its dependence on the tidal frequency in both laminar and weakly turbulent regimes. The main results are: a new scaling law for the frequency dependence of the effective viscosity which has not previously been observed in simulations or predicted by theory and occurs for shear frequencies smaller than those in the fast tides regime; the possibility of anti-dissipation (which could result in inverse-tides); and a strong agreement with the frequency dependence of Goldreich & Nicholson (1977) (despite disagreement with the fundamental mechanism).

These results have important implications for tidal dissipation in convection zones of stars and planets which we will discuss. The results of this work indicate that the classical tidal theory of the equilibrium tide in stars and giant planets should be revisited.

Contents

Chapter 1

Astrophysical tides

Contents

1.1 The astrophysical importance of tides

Tidal interactions between astrophysical objects, such as stars, planets and moons, are important in driving the spin and orbital evolution of these systems. All such objects, which find themselves in sufficiently close proximity, are subject to tides, which are due to the variation in the gravitational potential across a body. Tidal theory can be applied to binary stars, planets orbiting a parent star, or moons orbiting a planet. In all these cases, tides can change the period and eccentricity of the orbit and affect the spin and orbital angular momentum vectors of the objects in the system. These changes usually occur very slowly, but over the very long times that these astronomical objects last, they can play a significant role. With such a diversity of applications, there is a growing interest in improving tidal theory. We begin by highlighting a few areas where tidal interactions, and in particular the work presented in this thesis, are of particular importance.

1.1.1 Earth

The study of tidal theory as it pertains to the Earth has a rich history (see aside 1.1) which we cover only briefly. One aspect we will discuss is the dissipation of tidal energy. As we will see in § 1.2 and § 1.3 the dissipation of tidal energy plays an important role in the spin-orbit evolution of the Earth-Moon system. The consequences of this have been detected and observed in length of day (LOD) (Williams, 2000; Stevenson, 2015) variations as well as the outward Lunar migration (which has consequences for the Lunar history and formation Ćuk et al. 2016) . However, understanding the mechanisms of dissipation in the Earth's tides has been an extremely difficult subject. One reason for this is the bathymetry of the oceans plays an important role in the resulting tidal flows, as evidenced by the differences between the tidal range at the Bay of Fundy (13 meters) and Venice (1 meter). Another complexity is the vast zoo of oceanic tidal dissipation sources (see Fig. 1.1).

Although in this work we do not explore the dissipation of tidal energy in terrestrial planets, this highlights the common theme in the understanding of the consequences of tidal interactions. That is, a thorough understanding of tidal dissipation is essential in understanding and predicting the consequence of tidal interactions.

Aside 1.1: A brief historical perspective of tidal theory

Much like the ebb and flow of the tides, progress in our understanding of Earth tides, from antiquity to modern day, has also had a somewhat periodic nature where progress has typically occurred in bursts. The earliest evidence for at least a practical understanding of the tides dates back to 2500-1500 BC in the form of a tidal dock at Kathiawar[a] (Cartwright, 2001). However, the complex nature of Earth tides had many great thinkers confused and proposing creative yet incorrect theories[b]. Some notable examples are: William Gilbert (1544-1603), who proposed the tides were of a magnetic nature (he was responsible for the discovery of the Earth's magnetic field); Galileo Galilei (1564-1642), who proposed the tides were a direct result of accelerations due to orbital motion of the Earth around the Sun (largely he used this as evidence for the Copernican model of the solar system); Johannes Kepler (1571-1630), who actually made the correct prediction (based on documented observations), that some attractive force between the Earth and Moon was responsible, although it met with fierce resistance from Galileo; and René Descartes (1596-1650), who introduced a quite creative Theory of Vortices which was regarded as the correct answer for many decades (despite not only completely ignoring Kepler's laws but also making no reference to any previous tidal theory!).

It was Newton's pioneering work in *Philosophiæ Naturalis Principia Mathematica* that provided the correct description for the cause of the tides, which came as a consequence of his Universal Law of Gravitation (which Kepler was close to). However, Newton's ideas were not accepted over the Theory of Vortices until 1740 with the help of giants such as Daniel Bernoulli, Leonhard Euler, Colin Maclaurin, and others. Newton, perhaps, gets an unfair amount of credit for his work on tidal theory (Newton's main contribution to tidal theory was the Universal Law of Gravitation) as it is the work of Pierre-Simon Laplace in 1776 which has become the real foundation of modern tidal theory. The brilliance of Laplace comes in the form of a set of linear partial differential equations to describe the response of a body to the tidal force.

An in depth review of tidal history can be found in Cartwright (2000).

---

[a] There is evidence, of a controversial nature, for humanity's understanding of the relationship between the tides and the lunar cycle that dates back to at least 2000 BC through ancient megaliths in western Europe.

[b] One such novel idea was that the tides were caused by the breathing in and out of a sea god/-monster.

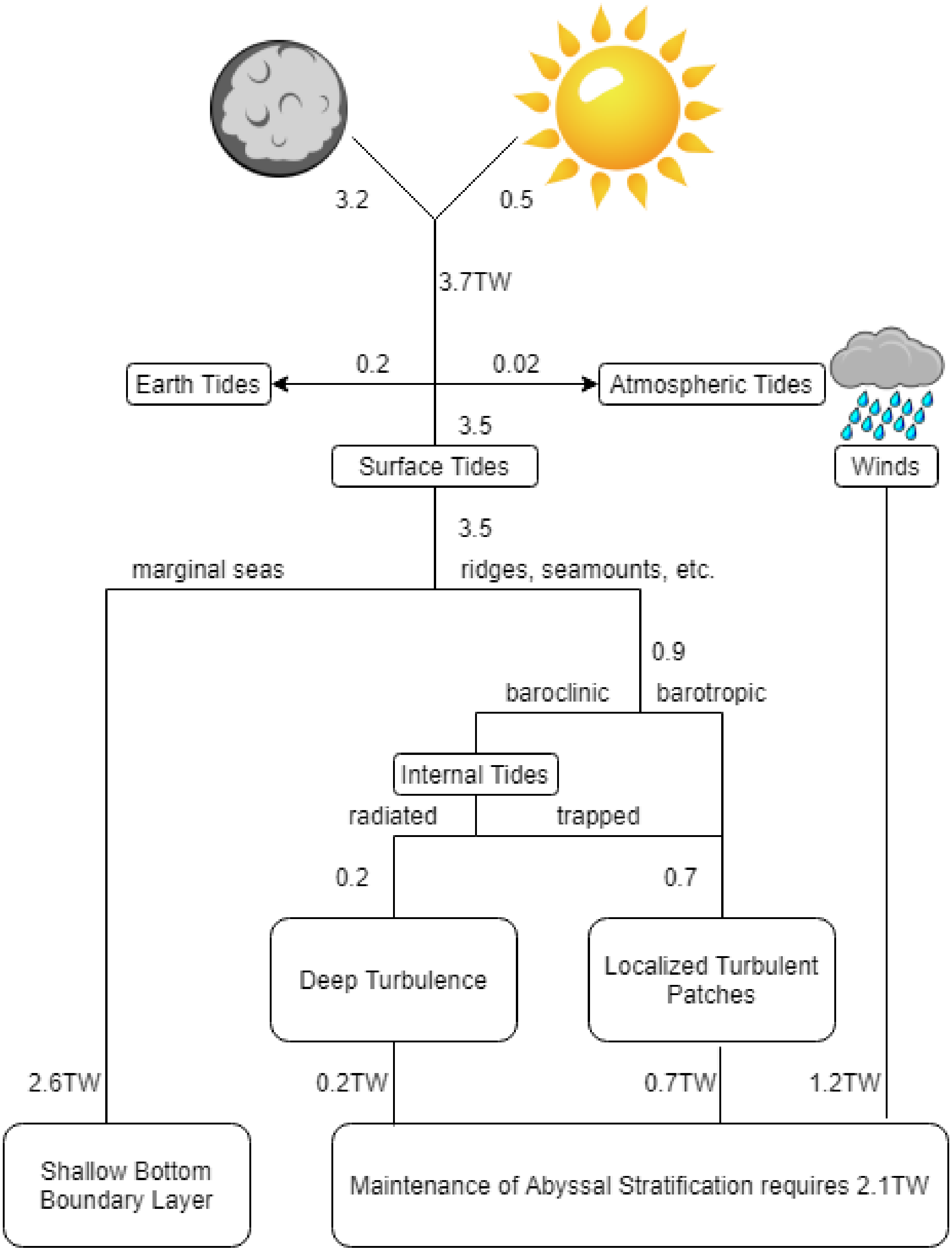

Figure 1.1: This schematic shows where tidal energy from the Sun and Moon is dissipated in the Earth. The quantities are measured in terawatts. This highlights the complexity of terrestrial tidal dissipation. Recreation from Munk & Wunsch (1998) (figure 4).

1.1.2 Hot Jupiters

In 1992 the first confirmed planets around another star were observed by Wolszczan & Frail (1992). These planets were discovered orbiting a neutron star, which were not previously thought to host planets, and gave us the first surprise in the new field of exoplanetary science. The next confirmed planet, 51 Peg b, was not until 1995, but this was of great importance due to it being found around a main sequence star (Mayor & Queloz, 1995). The significance of this stems from the fact that approximately 90% (Arnett, 1996) of stars fall into this category. Furthermore, 51 Peg falls into the same spectral class of star as the Sun, G-type, bringing this exoplanet closer to home. However this is where any familiarity ends.

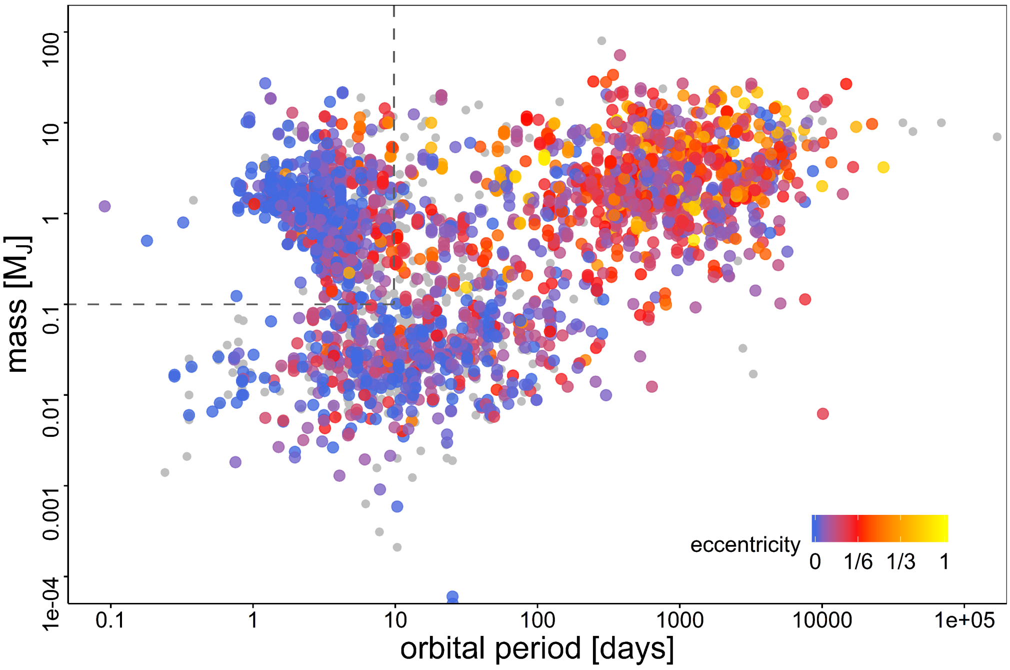

Figure 1.2: Mass-period diagram of all exoplanets from the NASA-Exoplanet Archive as of August 2020 (includes all planets contained within the 'planetary systems update' of the database). Each planet is coloured by its eccentricity where it is known or by grey where it is not. Planets without a known mass or orbital period are not displayed. The dashed lines indicate the lower mass and outer period boundary of HJs.

51 Peg b (Fakhouri, 1995) has roughly half the mass ($0.46\mathrm{M_J}$) of Jupiter but while Jupiter has an orbital period of 11.9 years, that of 51 Peg b is only a meagre 4.2 days. Naively, we expect giant planets to form further from their host stars than the observed 0.052AU of 51 Peg b, partly due to there being more solid material[1] in the proto-planetary disc at larger AU.

This may not have been so alarming if such planets were an exceptional rarity, however even by 2000 there were 28 confirmed planets discovered around main sequence stars (for a brief review of detection methods see aside 8.1) of which 7 of them fell into the classification of what is now termed the HJ class due to being in the mass regime of a gas giant but orbiting very close to their host star. We now have in excess of 4200 confirmed exoplanet discoveries as of August 2020 of which more than 300 fall into the HJ category, highlighting the surprising normality of such objects. HJ's are a subset of planets which are loosely defined as giant planets with orbital periods < 10 days[2] which is equivalent to a semi-major axis of $\lesssim 0.1$AU (Gaudi et al., 2005). This loose definition contains another poorly defined term of *giant planet*. Giant planets have a minimum mass, as defined by Clanton & Gaudi (2014), of $0.1\mathrm{M_J}$ which is based on compositional arguments. The maximum mass of a giant planet is

---

[1] Solid material, in the form of rocks and ices, are required for the classical core accretion pathway for planet formation. See Perryman (2018) for a complete review of planetary formation.

[2] Further subsets of HJ's are the *very hot Jupiters* and *ultra-short-period hot Jupiters* with < 3 day and $\lesssim 1$ day orbits respectively, however, in this thesis we will simply use the inclusive term HJ.

not yet well defined which stems from our incomplete understanding of brown dwarfs, however, one can conservatively exclude brown dwarfs from this category and regard the upper limit[3] as approximately $13\mathrm{M_J}$. Although the aforementioned figures make HJ's sound commonplace they are in fact reasonably rare. Occurrence rates vary depending on author and on the criteria used but around 1% of main sequence FGK stars are believed to host a HJ (Wang et al., 2015).

Aside 1.2: Planetary Detection

Without the many creative ways that observers have developed in order to detect exoplanets, using both ground and space based missions, we would never have uncovered the vast diversity of planetary systems. Figure 1.3, taken from Perryman (2018), highlights the various techniques that are now routinely used, as well as some of the mass limitations of each, and prospects for the future. Given how essential detection methods are to exoplanetary research, it is worth briefly discussing the main detection methods (for a more thorough review see Perryman 2018).

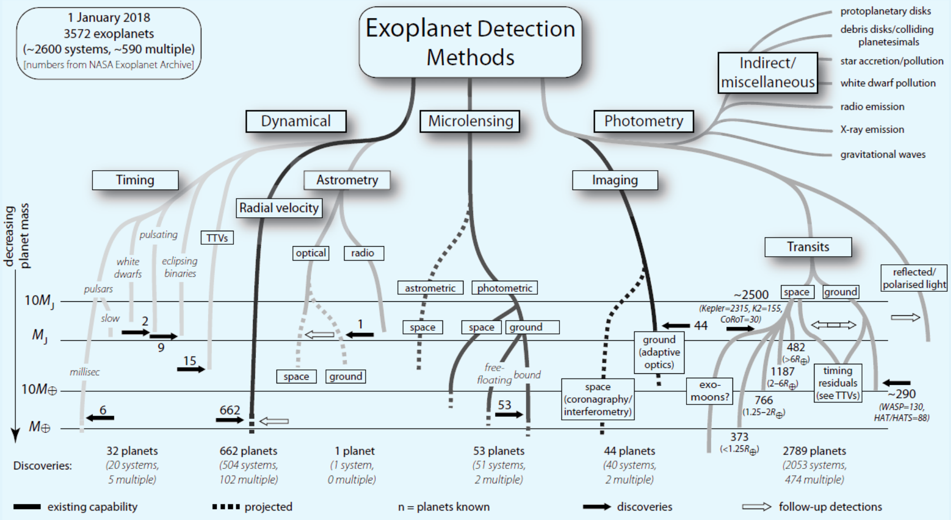

Figure 1.3: "*Exoplanet detection methods. The lower limits of the lines indicate masses within reach of present measurements (solid lines), and those that might be expected within the next few years (dashed). The (logarithmic) mass scale is shown at left. Miscellaneous signatures to the upper right are less well quantified in mass terms. Solid arrows show relevant discoveries. Open arrows indicate measurements of previously-detected systems. Numbers are from the NASA Exoplanet Archive, 2018 January 1.*". Figure and caption taken from Perryman (2018).

Radial Velocity: This detection method has been the second most successful technique used to detect exoplanets and is commonly used by the famous Keck facility and the highly successful HARPS observatory (Mayor, M. et al., 2003). In some regards it is also the pioneering method as it was used in the discovery of 51 Peg b.

When a star hosts a planet it will orbit the common centre of mass (barycentre), although this will be close to the centre of mass of the star itself due to the dominance of the star's mass. Providing the planet is not orbiting in the plane of the sky of the observer, the star will have some component of its orbital velocity directed towards the

---

[3] See Perryman (2018) for an extensive discussion on the classifications of planets.

observer. It is this velocity to/from the observer which can be detected and is the main component of the radial velocity method. Despite this velocity being very small, this method has been extremely successful and can even detect multi-planet systems (multis).

One major limitation of this technique is that it cannot directly estimate the planet's mass. The radial velocity technique measures the *mass function* of the system which can be obtained through Keplers third law as $\mathcal{M} = M_p^3 \sin^3 i/(M_\star + M_p)^2$, however, if we wish to evaluate the planet's mass M_p (where the stellar mass can be estimated, for example from its spectral type and luminosity class) then we must also know the angle of inclination with respect to the sky plane, $\sin i$, which cannot be obtained from the radial velocity method.

Astrometry: While radial velocity concerns itself with the motion of the star along the line of the observer, astrometry concerns itself with the motions parallel to the observer (in the plane of the sky). In essence the star is observed and its position in the plane of the sky is monitored for any slight change. Only one such planet at time of writing has been confirmed (DENIS-P J082303.1-491201 b, Sahlmann et al. 2013), although it is expected that GAIA will discover thousands of planets with this method.

Timing (pulsar/variable star): Some stellar objects have stable periodic behaviour which have their timings altered by the existence of a planet. The best example of this is the pulsar timing used in the discovery of the first exoplanets by Wolszczan & Frail (1992). Pulsars are a class of neutron star with powerful magnetic fields and a spin axis misaligned with the plane of the sky. This configuration results in periodic radio emission from their magnetic dipole axis to be directed at the observer. In the absence of a planet the periodicity is remarkably stable[a], this makes any slight variation from a planet easy to detect (although it remains difficult to confirm the discrepancy is from a planet and not some other source).

Similar techniques can be used for pulsating white dwarfs, rapidly pulsating subdwarfs and some eclipsing binaries.

Gravitational microlensing: Under general relativity matter acts to distort space-time causing light to take the shortest path in time (typically a curved path in space) rather than the most direct route in space (a straight line in space). If a suitably massive object lies between the observer and their desired target, then the light can bend around the massive object, which acts like a lens, amplifying the view of the observer's target object.

The major advantage of this technique is that, due to its magnifying effect, exoplanets can be discovered at much larger distances than is possible by other techniques. However, it has some quite major limitations. One limitation is that these systems are usually more difficult to characterise due to their distances from Earth. Another important limitation is the requirement for a massive enough object to happen to be in the correct position and for it to remain there for long enough for a detection to be possible.

Transits: This has been the most successful method of planetary detection, largely due to the impressive output of the Kepler space telescope. In essence this technique works by monitoring the change in light intensity from the host star as the planet passes in front of (and hence dimming) and behind of (this also causes a dimming due to the absence of the planet as a light source) the host star. Despite the dip in light intensity typically being $\leq 1\%$, this method can also be used to explore the composition of a planet's atmosphere/surface using spectroscopy and photometry which look at the changes in absorption lines[b] as the planet transits.

Direct imaging: All previously mentioned methods involve looking at the host star. In this method the host star is in fact masked out so as to bring the planet into view through either the reflection of its host star's light or its own thermal emission. Although this sounds simple, the flux from the star is significantly larger than that of the planet[c], however, despite this quite serious complication this method has been successful in discovering exoplanets, most famously Beta Pictoris b (fig 1.4).

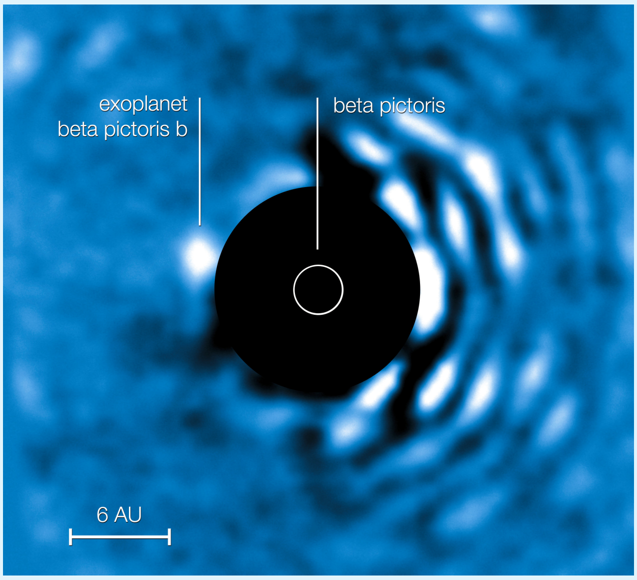

Figure 1.4: Image of Beta Pictoris b taken on 3 April 2010 by the VLT's NACO instrument. It is estimated that the planet is 6.5 AU away from its host star at the time of the image.
Credit: ESO.

---

[a] The most stable is PSR J0437–4715 with an error in predicting the next pulse of only 130 nano seconds (Hartnett & Luiten, 2011).

[b] Each element in the periodic table absorbs a different frequency of light and as such by looking at the frequency of gaps in the spectrum one can determine the abundances of material the light has interacted with.

[c] For Jupiter and the Sun the flux ratio is $f_{\mathrm{Jup}}/f_{\mathrm{Sun}} \approx 10^{-9}$.

Fig. 1.2 displays the mass-period (in Jupiter mass) of all discovered exoplanets (that have suitable data recorded for them) with each case coloured by its eccentricity. The HJ's are located in the top left of the diagram. One clear feature of HJ's is that they are typically found on low eccentricity orbits, which may be the result of tidal circularisation, although it is worth noting the formation pathways for HJ's are still a matter of some debate (see Dawson & Johnson 2018 and references therein). Regardless of the formation pathway these planets are expected to undergo tidal migration due to dissipation of tidal energy within the host star (this process will be described more thoroughly in § 1.2). Indeed, there is compelling evidence of tidally-driven orbital decay for the HJ WASP-12 b (Maciejewski et al. 2016; Patra et al. 2017; Maciejewski et al. 2018; Bouma et al. 2019; Yee et al. 2019; Turner et al. 2020) based on transit timing variations over decadal timescales, and similar observations have been attempted for some other HJ planets[4] (see for example Birkby et al. 2014; Wilkins et al. 2017; Petrucci et al. 2019). The inspiral of HJ's has also been inferred in Hamer & Schlaufman (2019) by exploring the occurrence rate of HJ's as a function of stellar age (estimated from measurements of the stellar Galactic velocity dispersion). They observed that HJ's are more commonly found around stars with smaller Galactic velocity dispersion (younger) and hence conclude that the planets around older stars must have been destroyed within the star's lifetime. These observations motivate theoretical studies to understand the mechanisms of tidal dissipation in stars.

1.1.3 Binary stars

The interaction between tidal flows and convection has long been thought to be the dominant mechanism for producing circularisation and synchronisation of late-type binaries with convective envelopes (e.g. Zahn & Bouchet 1989; Meibom & Mathieu 2005; Meibom et al. 2006; Mazeh 2008), the enhanced rates of orbital circularisation in cool-cool and hot-cool binaries over hot-hot binaries (Van Eylen et al., 2016), and in low-mass binary systems containing fully convective stars (e.g. Triaud et al. 2017; Von Boetticher et al. 2019). The clearest observational example indicating the efficacy of this mechanism is in binary systems containing giant stars (e.g. Verbunt & Phinney 1995; Price-Whelan & Goodman 2018; Sun et al. 2018; Beck et al. 2019). In the first case, that of late-type binaries, the trend towards circularisation can be seen in Fig. 1.5 which shows the mass-period-eccentricity relationships, where the mass is taken as that of the primary[5] (the object with the greatest mass). Tidal effects can also be more directly observed in some binary stars. A good example is the tidally-excited oscillations of heartbeat stars[6] (Welsh et al., 2011; Zimmerman et al., 2017; Guo et al., 2020).

It is clear that an improved understanding of tidal interactions in binary stars is essential as these systems are far from rare. Table 1.1 shows the occurrence rates of main-sequence binary systems as well as the expected number of companions a star of a given mass is expected to have.

Class	Mass range ($M_\odot$)	MF
BD	< 0.1	$22^{+6}_{-4}\%$
M	$0.1 - 0.5$	$26^{+3}_{-3}\%$
FGK	$0.7 - 1.3$	$44^{+2}_{-2}\%$
A	$1.5 - 5$	$> 50\%$
B	$8 - 16$	$> 60\%$
O	> 16	$> 80\%$

Table 1.1: The Multiplicity frequency (MF), which is the fraction of multiple systems in a population for various classes of star (where BD is Brown dwarfs or very low mass stars). Note that a multiple system could have one or many companions but in either case would be counted once. This data is taken from Duchêne & Kraus (2013).

---

[4] Note that in Wilkins et al. (2017) they found no evidence for the inspiral of WASP-18 b, which orbits an F star, to within observational limits (supporting some theories e.g. Barker & Ogilvie 2010). This highlights the dependence of tidal dissipation on stellar spectral type.

[5] These plots was produced from the data contained in Meibom & Mathieu (2005).

[6] Heartbeat stars obtained their name due to the radial velocity curve being similar to that of a heartbeat measured by electrocardiography, see for example figure 5 in Hambleton et al. (2018).

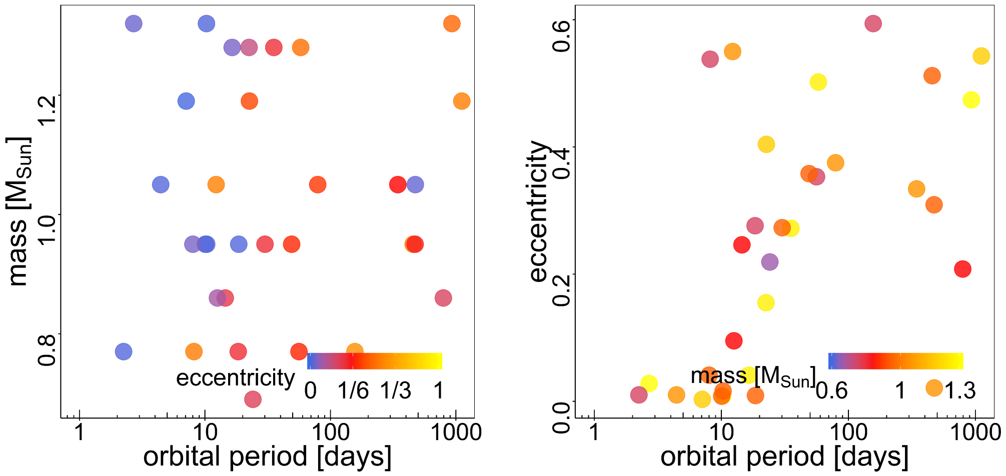

Figure 1.5: (left) Mass-period diagram of short-period binary stars where the mass displayed is for the primary. The eccentricity of the orbits is denoted by the colour of the symbol. (right) Eccentricity-period diagram and coloured by primary mass. The data is the same in each plot and has been taken from Meibom & Mathieu (2005) for binary stars in the M35 cluster. These data show that short-period binaries with sub 10 day orbital periods typically have circular orbits, while those with longer orbital periods have a much wider range of eccentricities.

1.2 The tidal mechanism

In this section we consider the tidal response of a fluid body, such as a star or planet, to an orbiting companion. First we will re-derive the tidal potential and tidal force from first principles[7] similar to Murray & Dermott (2000); Souchay et al. (2013); Ogilvie (2014) . We will then study the response of the body, which we will split up into its wave-like (dynamical tide) and non-wavelike (equilibrium tide) components.

We begin by considering the configuration in Fig. 1.6 where the primary, defined as being the most massive object, of mass M_1 and secondary, defined as the second most massive object, which is treated as a point mass, of mass M_2 in mutual orbit about the common centre of mass (barycentre). The vector $\boldsymbol{d}$ points from the centre of the primary to the point mass secondary. The magnitude of this vector is the semi-major axis $|\boldsymbol{d}| = a$. We note that this derivation is performed in an inertial frame of reference, which avoids the need to introduce the Centrifugal force.

We will consider the gravitational potential inside the primary as a result of the secondary at some arbitrary point described by the vector $\boldsymbol{x}$, which originates from the centre of the primary. The Newtonian (gravitational) potential can be described by

$$\begin{aligned}\Phi &= -\frac{GM_2}{|\boldsymbol{d}-\boldsymbol{x}|}\\ &= -\frac{GM_2}{|\boldsymbol{d}|}\left(1-\frac{2\boldsymbol{d}\cdot\boldsymbol{x}}{|\boldsymbol{d}|}+\frac{|\boldsymbol{x}|^2}{|\boldsymbol{d}|^2}\right)^{-1/2}\end{aligned}$$

---

[7] One motivation for this re-derivation is to highlight that even the most fundamental result is more rich in mathematics and physics than is implied by the often used description, "the difference in the force of gravity over distance".

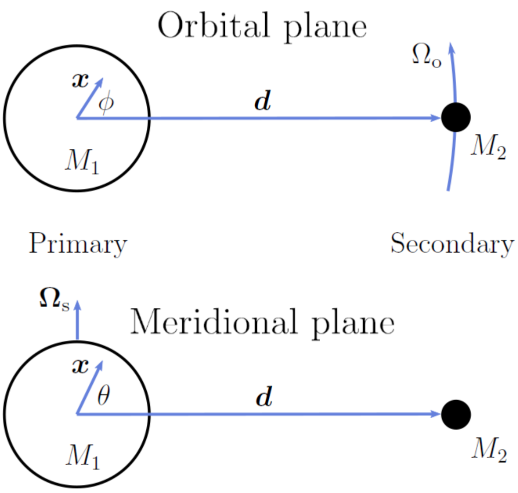

Figure 1.6: Schematic of a binary system to highlight the physical meaning of various quantities. The primary and secondary masses satisfy $M_1 \gg M_2$ with the secondary treated as a point mass. The spin vector of the primary is denoted by $\boldsymbol{\Omega}_\mathrm{s}$ (with magnitude Ω_s) assuming an aligned spin and orbit (for the purposes of this picture), the orbital frequency of the secondary Ω_o, $\boldsymbol{x}$ is a vector pointing from the centre of mass to an arbitrary point within the primary and $\boldsymbol{d}$ is the vector pointing from the centre of mass of the primary to the secondary. Finally, ϕ and θ denotes the azimuthal and polar angles which vanish on the line of centres and direction of the spin vector respectively.

$$= -\frac{GM_2}{|\boldsymbol{d}|}\left(1 + \frac{\boldsymbol{d}\cdot\boldsymbol{x}}{|\boldsymbol{d}|^2} + \frac{3(\boldsymbol{d}\cdot\boldsymbol{x})^2 - |\boldsymbol{x}|^2|\boldsymbol{d}|^2}{2|\boldsymbol{d}|^4} + \mathcal{O}\left(\frac{|\boldsymbol{x}|^3}{|\boldsymbol{d}|^3}\right)\right), \tag{1.1}$$

where in the intermediate step a Taylor expansion has been applied to the bracketed term and G is the gravitational constant. From this, the first two terms do not contribute to the tidal potential. Note that the force which results from this potential can be obtained by evaluating its gradient. The first term is constant in the potential and hence cannot contribute to a tidal force. The second terms gives

$$-\nabla\frac{GM_2}{|\boldsymbol{d}|}\frac{\boldsymbol{d}\cdot\boldsymbol{x}}{|\boldsymbol{d}|^2} = -\frac{GM_2\boldsymbol{d}}{|\boldsymbol{d}|^3}, \tag{1.2}$$

which simply causes the uniform acceleration responsible for orbital motion of the bodies about the centre of mass. The tidal potential is defined to be the remaining terms in the potential, thus we can define

$$\Psi = -\frac{GM_2}{|\boldsymbol{d}|}\left(\frac{3(\boldsymbol{d}\cdot\boldsymbol{x})^2 - |\boldsymbol{d}|^2|\boldsymbol{x}|^2}{2|\boldsymbol{d}|^4} + \mathcal{O}\left(\frac{|\boldsymbol{x}|^3}{|\boldsymbol{d}|^3}\right)\right). \tag{1.3}$$

Due to the increasing exponent on $|\boldsymbol{x}|/|\boldsymbol{d}|$ the quadrupole tidal potential (leading order term that is quadratic in $|\boldsymbol{x}|/|\boldsymbol{d}|$) is usually dominant and so we can approximate the tidal potential with

$$\Psi \approx -\frac{GM_2}{|\boldsymbol{d}|}\left(\frac{3(\boldsymbol{d}\cdot\boldsymbol{x})^2 - |\boldsymbol{d}|^2|\boldsymbol{x}|^2}{2|\boldsymbol{d}|^4}\right). \tag{1.4}$$

At this stage it is worth highlighting that this formulation has kept the orbit, as represented by $\boldsymbol{d}$, general. Let us consider a simple case of the secondary having a circular orbit about the primary's equator. Defining coordinates (and time) such that the orbit lies along x at $t = 0$, we have that

$$\boldsymbol{d} = (a\cos(\Omega_\mathrm{o}t), a\sin(\Omega_\mathrm{o}t), 0), \tag{1.5}$$

where we have written $|\boldsymbol{d}| = a$ (this is the conventional semi-major axis), the orbital frequency Ω_o and the time t. It is also useful to introduce the spherical polar co-ordinate system (r, θ, ϕ) (θ is the polar angle and ϕ is the azimuthal angle, see Fig. 1.6) and with origin centred on the primary's centre of mass[8],

$$\boldsymbol{x} = (r \sin\theta \cos\phi, r \sin\theta \sin\phi, r \cos\theta) \,. \tag{1.6}$$

These can be substituted into eq. 1.4 to give, after some rearrangement,

$$\Psi \approx \frac{GM_2 r^2}{4a^3} \left(2 - 3\sin^2\theta - 3\sin^2\theta \cos(2\phi - 2\Omega_\text{o} t) \right) , \tag{1.7}$$

where we have used $|\boldsymbol{d}| = a$. The first two terms are static and only lead to a time-independent deformation of the body, and no time-dependent flow. Since we are interested in studying the dissipation of tidal flows, we consider the time-dependent portion, which we define as

$$\begin{aligned} \Psi_{2,2} =& \Re\left(-\frac{3GM_2 r^2}{4a^3} \sin^2\theta \; e^{i(2\phi - 2\Omega_\text{o} t)} \right) \\ =& \Re\left\{ \mathcal{A} \left(\frac{r}{R_1} \right)^2 Y_2^2(\theta,\phi)\, e^{-2i\Omega_\text{o} t} \right\} . \end{aligned} \tag{1.8}$$

where we have rewritten the latter part of $\Psi_{2,2}$ in terms of a $l = m = 2$ orthonormalised spherical harmonic[9], which we denote with Y_l^m, and introduced a tidal amplitude

$$\mathcal{A} = -\sqrt{\frac{6\pi}{15}} \frac{GM_2 R_1^2}{a^3} \tag{1.9}$$

for later use (note that R_1 is the radius of the primary). This potential, due to the orbiting secondary, acts to deform and excite tidal flows inside the primary, the result of which is a perturbation to its potential. This perturbation then acts back on the secondary. Since we are considering the secondary as a point mass this mutual interaction only modifies the spin of the primary and the orbits of both bodies about the centre of mass. The misalignment of the tidally excited deformation of the primary exerts a torque on the orbital motion of the secondary, as shown in Fig. 1.7.

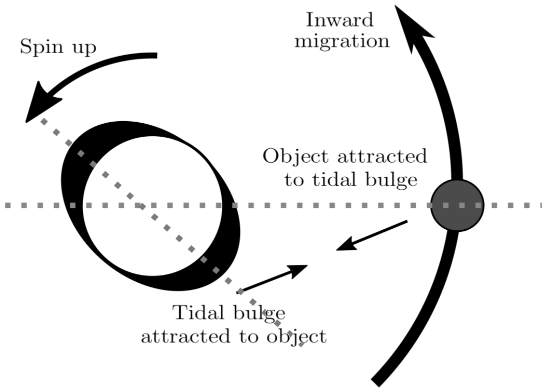

Figure 1.7: Schematic of the tidal deformation which in this case is lagging behind the line of centres, which is generally the case for HJ's but the opposite is the case for the Earth-Moon system. The primary is torqued due to the attraction of the secondary resulting in the primary's spin up where, in this configuration, the torque vector is directed into the page. Due to Newton's third law, conservation of angular momentum and the rate of change of orbital energy, this results in an acceleration of orbital velocity and inwards migration. See aside 1.3 for a more detailed description.

---

[8] We currently have neglected the spin of the primary, but this could be included into the definition of $\boldsymbol{d}$. Further, addition of rotation only changes the tidal frequency from $2\Omega_\text{o}$ to $2(\Omega_\text{o} - \Omega_\text{s})$.

[9] Spherical harmonics were invented by Laplace to be used in his tidal theory.

Aside 1.3: Tidal migration: A physical description

The tidal force due to the secondary causes a tidally excited deformation (bulge) of the primary. In the absence of any dissipation the primary would have an instantaneous response to the tidal force and hence the bulge would align with the line of centres. However, physical systems do have dissipative properties and this results in a misalignment of the tidally excited deformation which will either precede or lag the line of attraction depending on spin and orbital periods of the primary and secondary, respectively, as well as internal effects. In general the bulge will lag (precede) the line of centres if the secondary has a smaller (larger) orbital period than the primary's spin period[a].

If the bulge lags (precedes) behind the line of centres it imposes a negative (positive) torque to the secondary's orbit and, due to Newton's second law, an equal magnitude and opposite sign torque to the primary's spin. This then results in an exchange of angular momentum between the primary and secondary where we have, from the sign of the torque, that the angular momentum of the secondary's orbit decreases (increases) while the angular momentum of the primary's spin increases (decreases). However, while the total angular momentum in the system is conserved, the orbital energy is not (we must have dissipation in order to have a misalignment!). These two facts can be used to find an expression for the rate of change of the orbital energy which tells us that the semi-major axis decreases (increases) and hence by Kepler's laws the orbital velocity increases (decreases).

This effect is basically an imperfect exchange of rotational and orbital energy between the two bodies where some kinetic energy is converted to heat (through dissipation). Some fraction of this heat is then lost to space by radiation leading to a net loss of energy in the system. This conversion from kinetic energy due to friction is known as tidal heating[b]. As the system advances through time the secondary has its orbital distance reduced (increased) while the primary will experience spin-up (spin-down). But remember that it is the mismatch in spin period of the primary and orbital period of the secondary that causes the tidal evolution of the system and so there is a somewhat obvious end point being that after some time there will no longer be a mismatch. This end point (providing there is enough angular momentum to reach this state Hut 1980) is known as tidal locking and results in one side of the secondary always facing the primary. It is important to note however that tidal locking is not the end point of the evolution of the entire system as in the case described, the secondary would be locked to the primary but the primary does not have to be locked to the secondary. Due to tidal locking being a gravitational effect it is typical that the smaller body in the system will lock to the larger one first[c] which is what we observe in the Solar system.

As previously mentioned tidal locking is not the end of migration in a system, as evident from the Moon's migration away from Earth. From the work of Hut (1980) it was found that as long as three quarters of the total angular momentum in the system is orbital angular momentum then the end result is the tidal equilibrium. If this is not the case then there are two possible fates for the planet, it migrates towards the star until it is destroyed, or, it is ejected from the system. Tidal equilibrium is where both bodies are tidally locked to each other, they orbit the barycentre (common centre of mass) with zero eccentricity, they are coplanar and their spin axes are aligned. However this is thought to be an asymptotic process. Indeed from numerical integrations using simple tidal models it has been found that stellar obliquity (also known as inclination and spin-orbit misalignment) evolution timescales can be much longer than circularisation timescales (Barker & Ogilvie, 2009), which might be supported by observations of highly inclined HJ's on circular orbits (Albrecht et al., 2012). It is worth noting that it is also possible for the misalignment to be damped much faster than the orbital migration (Lai, 2012; Barker, 2016b; Lin & Ogilvie, 2017; Damiani & Mathis, 2018).

---

[a] Alternatively, based on frequencies, the bulge will lag (precede) the line of centres if the secondary has a larger (smaller) orbital frequency than the primary's spin frequency.

[b] A number of moons within the solar system show evidence of tidal heating such as Europa and Enceladus which both feature outgassing from geysers (Fairén 2017 and references therein).

[c] This depends on the efficiency of dissipation in each of the bodies.

What we are really interested in is the external potential of the tidally deformed primary as gravity is the only way the two bodies interact. An expression for this can be obtained by considering the solution to Laplace's equation

$$\sum_{l=0}^{\infty}\sum_{m=-l}^{l}\left(A_l r^l + B_l r^{-l-1}\right) Y_l^m(\theta,\phi)\,, \tag{1.10}$$

where we note that the boundary condition is that the potential vanishes at $r \to \infty$. This means we can write the quadrupolar ($l = 2$) part of the external potential as

$$\Phi' = \Re\left\{\mathcal{B}\left(\frac{R}{r}\right)^3 Y_2^2(\theta,\phi)\,e^{-2i\Omega_\mathrm{o}t}\right\}\,, \tag{1.11}$$

where $\mathcal{B}$ must now contain information about the modification of the potential due to the tidal perturbation[10]. Now, we could derive an external potential due to the deformation[11] and sum with the potential due to the spherical interior (see Murray & Dermott (2000) for details of this), however, we would quickly run into problems. The main issue is, in general, we do not know the tidal response of the interior of the primary (which could be a planet, star or other object).

We now introduce the (tidal) Love number[12] (Love 1892, 1909) $k_l^m \in \mathbb{C}$. Formally, it is defined by the ratio of the perturbed gravitational potential to the imposed one. The interior and exterior potentials are related by use of the Love number in the relation

$$k_l^m(\Omega_\mathrm{o}) = \frac{\mathcal{B}_l^m}{\mathcal{A}_l^m} \tag{1.12}$$

---

[10] In fact, $\mathcal{B}$ is at the heart of the tidal problem as it contains all the unknown information about how the body responds to the tidal potential (such as the body's rheology for a terrestrial planet).

[11] In principle this could include the rotational deformation (Barker et al., 2016).

[12] There is a second tidal Love number, h, which defines the constant of proportionality between the perturbing potential and the tidal displacement on the surface of the primary. Further, there is the fluid Love number which parametrises how much a fluid body is deformed by rotation.

for each harmonic component. We have then that $\Re(k_l^m)$ describes the elastic part of the response which is in phase with the imposed potential (from here on we will simply refer to this as the Love number) which is a measure of the central concentration of a body which depends on its mass distribution as well as its rigidity (for solid bodies). Considering two bodies of equal rigidity (or no rigidity in the case of a fluid body) the one with the denser core will have a smaller Love number. We also have that $\Im(k_l^m)$ is out of phase with the imposed tidal potential and is associated with tidal dissipation and the associated torques. In most applications it is k_2^2 that is of primary concern as it related to the dominant tidal response[13].

We also introduce the tidal quality factor Q which describes how efficiently an object can dissipate the tidal energy. This is analogous to the well studied problem of a damped harmonic oscillator which admits an in and out of phase response to a forcing (see for example Feynman 1970). For a damped harmonic oscillator a useful quantity is the quality factor Q which is a measure of how underdamped the oscillator is and defined as the ratio of the energy stored to the energy dissipated in one cycle. Similarly, the tidal quality factor is defined in the same way, as (Goldreich, 1963)

$$Q = \frac{2\pi E_0}{\oint -\dot{E}\mathrm{d}t}, \tag{1.13}$$

which is the ratio of the maximum (at peak oscillation) energy in the deformation to the energy dissipated in one tidal period. The Love number and the quality factor can be related through the complex nature of k_l^m. Thus, much like for the harmonic oscillator, where the quality factor describes the out of phase response, we have a relation between the tidal Love number and tidal quality factor for the $l = m = 2$ component (noting that each l,m harmonic can have different values of Q) as (Ogilvie, 2014)

$$\Im(k_2^2) = \sigma\frac{k_2^2}{Q} = \sigma\frac{3}{2Q'}, \tag{1.14}$$

where $\sigma = \mathrm{sgn}(\omega)$, which is the sign of the tidal forcing frequency $\omega = 2(\Omega_\mathrm{o} - \Omega_\mathrm{s})$, noting that we have introduced Ω_s for the spin frequency of the primary[14]. In eq. 1.14 we have introduced the modified tidal quality factor Q' which is simply merging $\Re(k_2^2)$ and Q into one parameter for convenience[15], as these two terms frequently appear together in tidal evolution equations. We can also write the imaginary part of the Love number in terms of the tidal forcing frequency and the time-lag τ (which is yet another way of parametrising the dissipation) in the tidal response to the forcing by $\Im(k_2^m) = k_2^2\tau\omega$.

Before we continue it is worth highlighting the subtle yet important point of this discussion on the tidal mechanism. Although it is gravity that causes the tides, without dissipation of the tidal energy there can be no exchange of spin/orbital energy and angular momentum between the bodies. As such, if we wish to understand the consequences of tides on the orbital and spin evolution of astrophysical systems, it is essential to understand the mechanisms behind the dissipation of tidal energy.

---

[13] Although much physics is hidden in $\Re(k_l^m)$ it is still of great interest as the k_2^2 harmonic can be measured with current observational instruments Ragozzine & Wolf (2009); Batygin et al. (2009); Ni (2018).

[14] We have, until now, largely neglected to mention the spin of the primary for simplicity.

[15] Note that Q' is the Q of a homogeneous body, where $k_2^2 = 3/2$ in this case.

1.2.1 The equilibrium tide

We now consider the components of the tide and in particular the large-scale non-wavelike equilibrium tide which is essentially the quasi-hydrostatic large-scale motion of the tidal deformation. Following the approach taken by Zahn (1966, 1977), we start with the equation for a body in hydrostatic equilibrium in the unperturbed case with no tidal potential

$$\mathbf{0} = -\frac{1}{\rho}\nabla p - \nabla\Phi\,, \tag{1.15}$$

where Φ is the body's gravitational potential, ρ is the density and p is the pressure. If we take the curl of this expression we get

$$\mathbf{0} = -\frac{1}{\rho}\nabla\times\nabla p - \nabla\frac{1}{\rho}\times\nabla p - \nabla\times\nabla\Phi\,, \tag{1.16}$$

where we note that the curl of a gradient vanishes, and we are left with, upon application of the chain rule,

$$\mathbf{0} = \frac{1}{\rho^2}\nabla\rho\times\nabla p\,. \tag{1.17}$$

This implies $\nabla\rho$ and ∇p must be parallel, and hence be functions of a single variable, and so from eq. 1.15 it must be the case that Φ is also a function of this single variable (either of ρ, p or Φ are suitable choices of the single variable).

Next we can define the perturbed quantities

$$\Phi^* = \Phi + \Phi' + \Psi\,, \tag{1.18a}$$

$$\rho^* = \rho + \rho'\,, \tag{1.18b}$$

$$p^* = p + p'\,, \tag{1.18c}$$

where we note that $\bullet^*$ are the full quantities, $\bullet'$ are perturbed quantities and regular symbols are the background (basic state) quantities. We also note that Ψ is the imposed tidal potential from the secondary which satisfies $\nabla^2\Psi = 0$ within the body of the primary. Here we are considering the linear tides regime and so assume small perturbations, which is justified if the tidal amplitude is small. Since we are looking at the equilibrium tide, which is a quasi-hydrostatic deformation of the body, and its associated flow, we can substitute these into the momentum equation, and assume the body maintains hydrostatic balance, which gives

$$\begin{aligned}
\mathbf{0} &= -\frac{1}{\rho^*}\nabla p^* - \nabla\Phi^*\,,\\
&= -\frac{1}{\rho}\left[1 - \frac{\rho'}{\rho} + \mathcal{O}\left(\left(\frac{\rho'}{\rho}\right)^2\right)\right](\nabla p + \nabla p') - \nabla\Phi - \nabla\Phi' - \nabla\Psi\,,\\
&= \frac{p'}{\rho'^2}\nabla p - \frac{1}{\rho}\nabla p' - \nabla\Phi' - \nabla\Psi\,,
\end{aligned} \tag{1.19}$$

where we have used a Taylor expansion for the leading term, followed by substitution of eq. 1.15. Now we note by application of the chain rule twice, and the fact that $\rho = \rho(p)$, we can write

$$-\nabla\frac{p'}{\rho} = -\frac{1}{\rho}\nabla p' + \frac{p'}{\rho^2}\frac{\mathrm{d}\rho}{\mathrm{d}p}\nabla p\,. \tag{1.20}$$

Thus we can write eq. 1.19 as

$$\mathbf{0} = -\nabla W + \frac{1}{\rho^2}\left(\rho' - p'\frac{\mathrm{d}\rho}{\mathrm{d}p}\right)\nabla p\,, \tag{1.21}$$

$$W = \frac{p'}{\rho} + \Phi' + \Psi\,. \tag{1.22}$$

We can now take the curl of eq. 1.21 to obtain

$$\begin{aligned}
\mathbf{0} &= -\nabla\times\nabla W + \frac{1}{\rho^2}\left(\rho' - p'\frac{\mathrm{d}\rho}{\mathrm{d}p}\right)\nabla\times\nabla p + \nabla\left[\frac{1}{\rho^2}\left(\rho' - p'\frac{\mathrm{d}\rho}{\mathrm{d}p}\right)\right]\times\nabla p\,,\\
&= \nabla\left[\left(\rho' - p'\frac{\mathrm{d}\rho}{\mathrm{d}p}\right)\nabla\frac{1}{\rho^2} + \frac{1}{\rho^2}\nabla\left(\rho' - p'\frac{\mathrm{d}\rho}{\mathrm{d}p}\right)\right]\times\nabla p\,,\\
&= \nabla\left[-\frac{2}{\rho^3}\left(\rho' - p'\frac{\mathrm{d}\rho}{\mathrm{d}p}\right)\nabla\rho\times\nabla p\right] + \left[\frac{1}{\rho^2}\nabla\left(\rho' - p'\frac{\mathrm{d}\rho}{\mathrm{d}p}\right)\right]\times\nabla p\,,\\
&= \frac{1}{\rho^2}\nabla\left(\rho' - p'\frac{\mathrm{d}\rho}{\mathrm{d}p}\right)\times\nabla p\,,
\end{aligned} \tag{1.23}$$

where we have used, in order, the product rule, the curl of a gradient rule, the distributive law, the chain rule and finally the fact that ∇p and $\nabla\rho$ are parallel (and hence the cross product is zero). From this we see that $\rho' - p'\frac{\mathrm{d}\rho}{\mathrm{d}p}$ is parallel to ∇p and hence both can be written as functions of Φ only. Further, due to eq. 1.21, W can also be written as a function of Φ only.

Now, all perturbed quantities (ρ', p' Φ' and W) can be written in the form $e^{-i\omega t}$ and so average to zero over a complete cycle and in particular we note that, for an oscillatory component with $\omega \neq 0$,

$$\rho' - p'\frac{\mathrm{d}\rho}{\mathrm{d}p} = 0\,. \tag{1.24}$$

From this we can write

$$0 = W = \frac{p'}{\rho} + \Phi' + \Psi \implies p' = -\rho(\Phi' + \Psi)\,, \tag{1.25}$$

$$0 = \rho' - p'\frac{\mathrm{d}\rho}{\mathrm{d}p} \implies \rho' = -\rho(\Phi' + \Psi)\frac{\mathrm{d}\rho}{\mathrm{d}p}\,. \tag{1.26}$$

Now we linearise the full Poisson's equation using eq. 1.18

$$\begin{aligned}
\nabla^2\Phi^* &= 4\pi G\rho^*\\
\implies \nabla^2\Phi' &= 4\pi G\rho'\,,
\end{aligned} \tag{1.27}$$

where we have used Poisson's equation for the background $\nabla^2\Phi = 4\pi G\rho$ and the fact that $\nabla^2\Psi = 0$ inside the body. We can then use eq. 1.26 to write the linearised Poisson's equation as

$$\nabla^2\Phi' = -4\pi G\rho(\Phi' + \Psi)\frac{\mathrm{d}\rho}{\mathrm{d}p}\,. \tag{1.28}$$

This is a linear differential equation[16] of a single variable and is valid everywhere inside the body of the primary (outside of the primary we have $\nabla^2\Phi' = 0$). The solution to this equation can be found for a given Ψ and the result is the gravitational potential perturbation due to the equilibrium tide. We have thus obtained expressions for the Eulerian gravitational potential

---

[16] This equation is of the inhomogeneous Helmholtz type.

perturbation and the associated pressure and density perturbations for the equilibrium tide. We are now in a position to compute the resulting tidal flow within the primary.

We consider the tidal displacement vector $\boldsymbol{\xi}$ from the compressible form of the continuity equation. We have

$$\begin{aligned} 0 &= \frac{\partial \rho^*}{\partial t} + \nabla \cdot (\rho^* \mathbf{u})\,, && (1.29) \\ 0 &= \frac{\partial \rho}{\partial t} + \frac{\partial \rho'}{\partial t} + \nabla \cdot \left[\rho \frac{\partial \boldsymbol{\xi}}{\partial t}\right] + \nabla \cdot \left[\rho' \frac{\partial \boldsymbol{\xi}}{\partial t}\right]\,, \\ 0 &\approx \frac{\partial \rho'}{\partial t} + \nabla \cdot \left[\rho \frac{\partial \boldsymbol{\xi}}{\partial t}\right]\,, && (1.30) \end{aligned}$$

where in the last step we have linearised[17] using eq. 1.18 and used the fact that the background density is constant. We can put all terms in this expression inside the time derivative, using the definition of the Eulerian displacement $\boldsymbol{\xi}$ (which is equivalent to the Lagrangian displacement in this case) to get

$$\rho' = -\rho \nabla \cdot \boldsymbol{\xi} - \boldsymbol{\xi} \cdot \nabla \rho\,. \tag{1.31}$$

A similar expression can be obtained for p' by expanding out the energy equation if we assume adiabatic perturbations

$$\begin{aligned} 0 &= \frac{\mathsf{D}}{\mathsf{D}t}\left[\frac{p^*}{\rho^{*\gamma}}\right] \\ &= \frac{1}{\rho^{*\gamma}}\left[\frac{\partial p^*}{\partial t} + \mathbf{u} \cdot \nabla p^*\right] - \frac{\gamma p^*}{\rho^{*\gamma+1}} \underbrace{\left[\frac{\partial \rho^*}{\partial t} + \mathbf{u} \cdot \nabla \rho^*\right]}_{-\rho^* \nabla \cdot \mathbf{u} \text{ by eq. 1.29}} && (1.32) \\ 0 &= \frac{\partial p^*}{\partial t} + \frac{\partial \boldsymbol{\xi}}{\partial t} \cdot \nabla p^* + \gamma p^* \nabla \cdot \frac{\partial \boldsymbol{\xi}}{\partial t} \\ &= \frac{\partial p'}{\partial t} + \frac{\partial \boldsymbol{\xi}}{\partial t} \cdot \nabla p + \gamma p \nabla \cdot \frac{\partial \boldsymbol{\xi}}{\partial t}\,, && (1.33) \end{aligned}$$

where in the last step we have linearised[17] using eq. 1.18 and used the fact that the background pressure is constant in time (due to our hydrostatic assumption). We can put all terms in this expression inside the time derivative, using the definition of the Eulerian displacement $\boldsymbol{\xi}$ (which is equivalent to the Lagrangian displacement in this case) to get

$$p' = -\gamma p \nabla \cdot \boldsymbol{\xi} - \boldsymbol{\xi} \cdot \nabla p\,. \tag{1.34}$$

We can substitute eq. 1.31 and eq. 1.34 into eq. 1.24 to get

$$\begin{aligned} 0 &= \rho' - \frac{\mathsf{d}\rho}{\mathsf{d}p} p'\,, \\ &= -\rho \nabla \cdot \boldsymbol{\xi} - \boldsymbol{\xi} \cdot \nabla \rho - \frac{\mathsf{d}\rho}{\mathsf{d}p}\left(-\gamma p \nabla \cdot \boldsymbol{\xi} - \boldsymbol{\xi} \cdot \nabla p\right)\,, \\ &= -\left(\rho - \gamma p \frac{\mathsf{d}\rho}{\mathsf{d}p}\right) \nabla \cdot \boldsymbol{\xi}\,, && (1.35) \end{aligned}$$

where we have used $\boldsymbol{\xi} \cdot \nabla \rho = \boldsymbol{\xi} \cdot \frac{\mathsf{d}\rho}{\mathsf{d}p} \nabla p$. This can be written in terms of the buoyancy

---

[17] We drop products of ρ' or p' and $\boldsymbol{\xi}$

(Brunt–Väisälä) frequency N^2 as

$$0 = N^2 \frac{\gamma p \rho^2}{|\nabla p|^2} \nabla \cdot \boldsymbol{\xi} \,, \tag{1.36}$$

where the buoyancy frequency can be written as $N^2 = -\boldsymbol{g} \cdot \nabla \ln \left(\frac{p^{1/\gamma}}{\rho}\right)$. We can demonstrate this as follows: first we have that

$$N^2 = -\boldsymbol{g} \cdot \nabla \ln \left(\frac{p^{1/\gamma}}{\rho}\right) \quad \text{and} \quad \boldsymbol{g} = \frac{1}{\rho} \nabla p \,, \tag{1.37}$$

$$\implies N^2 = -\frac{1}{\rho} \nabla p \cdot \nabla \ln \left(\frac{p^{1/\gamma}}{\rho}\right) \,, \tag{1.38}$$

and so

$$\begin{aligned} \frac{N^2 \gamma p \rho^2}{|\nabla p|^2} &= -\frac{\gamma p \rho}{|\nabla p|^2} \nabla p \cdot \nabla \ln \left(\frac{p^{1/\gamma}}{\rho}\right) \\ &= -\frac{\gamma p \rho}{|\nabla p|^2} \nabla p \cdot \frac{\rho}{p^{1/\gamma}} \nabla \frac{p^{1/\gamma}}{\rho} \\ &= -\rho + \frac{\gamma p}{|\nabla p|^2} \nabla p \cdot \frac{\mathrm{d}\rho}{\mathrm{d}p} \nabla p \\ &= -\left(\rho - \gamma p \frac{\mathrm{d}\rho}{\mathrm{d}p}\right) \,. \end{aligned} \tag{1.39}$$

If we consider eq. 1.36 it is clear that $N^2 \neq 0 \implies \nabla \cdot \boldsymbol{\xi} = 0$ and hence the displacement is incompressible[18]. From eq. 1.34 we can then use the incompressibility of $\boldsymbol{\xi}$ and then substitute for eq. 1.25 making use of $\boldsymbol{g} = -\nabla \Phi = 1/\rho \nabla p$ in order to get

$$p' = -\boldsymbol{\xi} \cdot \nabla p \,, \tag{1.40}$$

$$\Phi' + \Psi = \boldsymbol{\xi} \cdot \boldsymbol{g} \,. \tag{1.41}$$

This gives the radial displacement of the tide. The displacement perpendicular to $\boldsymbol{g}$ can then be obtained from $\nabla \cdot \boldsymbol{\xi} = 0$.

Let us now pause to take stock of what we have just derived. We have considered the tidal potential in the so-called linear tides regime[19]. From this we have derived a solvable expression for the tidally excited displacement of the primary. This pioneering description of the equilibrium tide was first derived by Jean Paul Zahn in his PhD thesis which was later published Zahn (1966, 1977) and subsequently refined by Zahn (1989) and Remus et al. (2012). It was not until 1998 when two independent groups (Terquem et al., 1998; Goodman & Dickson, 1998) discovered an important problem with applying this description of tidal flows. As such we draw attention to one important assumption we have made, that is $N^2 \neq 0$. This is true in radiative regions of stars where the fluid is stably stratified (as well as in stably stratified regions of giant planets), however, in convective regions of stars $N^2 < 0$ and since

---

[18] This can be made stricter by not making the assumption the left hand side of eq. 1.15 is zero. This leads to $N^2 > \omega^2$.

[19] This is valid providing perturbations to the potential result in deformations which are very small in comparison to the primary's radius. This is typically the case for the equilibrium tide in stars, but not in all short-period planets.

convection is usually efficient then $N^2 \approx 0$. In particular, if the tidal frequency ω^2 is not much smaller than N^2, then our prior results cannot be applied to infer that the equilibrium tide is incompressible. This raises the question of the validity of these findings in convectively unstable regions.

In order to address this we can consider a non-rotating adiabatically stratified region of an inviscid fluid which satisfies the equation

$$\frac{\mathrm{D}\mathbf{u}^*}{\mathrm{d}t} = -\frac{1}{\rho^*}\nabla p^* - \nabla\Phi^* \,. \tag{1.42}$$

We can then substitute for the perturbed quantities eq. 1.18 to get

$$\begin{aligned}
\frac{\mathrm{D}\mathbf{u}}{\mathrm{d}t} + \frac{\mathrm{D}\mathbf{u}'}{\mathrm{d}t} &= -\frac{1}{\rho+\rho'}\nabla(p+p') - \nabla\Phi - \nabla\Phi' - \nabla\Psi \\
&= -\frac{1}{\rho}\left[1 - \frac{\rho'}{\rho} - \mathcal{O}\left(\left(\frac{\rho'}{\rho}\right)^2\right)\right]\nabla(p+p') - \nabla\Phi - \nabla\Phi' - \nabla\Psi \,, && (1.43)\\
\frac{\mathrm{D}\mathbf{u}'}{\mathrm{d}t} &= -\frac{1}{\rho}\nabla p' + \frac{\rho'}{\rho^2}\nabla p - \nabla\Phi' - \nabla\Psi \\
&= -\nabla\frac{p'}{\rho} - \nabla\Phi' - \nabla\Psi \,, && (1.44)\\
\frac{\mathrm{D}\mathbf{u}'}{\mathrm{d}t} &= -\nabla W \,, && (1.45)
\end{aligned}$$

where we have used the Taylor expansion for the fractional term, eq. 1.15 and $\partial_t \mathbf{u} = 0$ (since we are considering a hydrostatic background). We take the curl of this expression to get

$$\begin{aligned}
\nabla \times \frac{\mathrm{D}\mathbf{u}'}{\mathrm{d}t} &= -\nabla \times \nabla W \,, && (1.46)\\
\implies \nabla \times \mathbf{u}' &= 0 \,, && (1.47)\\
\therefore \nabla \times \frac{\mathrm{D}\boldsymbol{\xi}}{\mathrm{d}t} &= 0 \,, && (1.48)\\
\implies \nabla \times \boldsymbol{\xi} &= 0 \,. && (1.49)
\end{aligned}$$

This tells us that the tidal flow and displacement must be irrotational and so we can write $\boldsymbol{\xi} = \nabla\zeta$ for some potential ζ. We note that the irrotational property is not generally satisfied when $N^2 \neq 0$. In order to make progress we can combine eq. 1.24, eq. 1.26 and eq. 1.31 to get

$$\nabla \cdot (\rho\boldsymbol{\xi}) = \frac{\mathrm{d}\rho}{\mathrm{d}p}\rho(\Phi' + \Psi) \,, \tag{1.50}$$

which can be solved to determine the tidal displacement and hence the tidal flow by assuming appropriate boundary conditions. This is the correct description for the equilibrium tide within a convectively unstable region of a star (and in fluid regions of planets). This equilibrium tide is often referred to as the "non-wavelike equilibrium tide"[20] Ogilvie (2013).

---

[20] Leaving "equilibrium tide" to be associated with the radiative zone.

1.2.2 The dynamical tide

As well as the equilibrium tide there is the possibility for a dynamical tide which consists of wave-like behaviour within the primary[21], as well as their own mechanisms to dissipate energy. The two main flavours of dynamical tide[22] come in the form of inertial waves (which are restored by the Coriolis force) and internal gravity waves (restored by gravity) as tidal frequencies are often too low to excite sound waves and surface gravity modes.

Inertial waves

We first consider inertial waves which require the planet or star to be forced by sufficiently low-frequency tidal forcing (relative to the rotation of the body) that Coriolis forces represent the dominant restoring force. This type of wave occurs in convective regions of stars and planets (if we neglect buoyancy forces, $N^2 = 0$). The starting point is the addition of the Coriolis term into eq. 1.45

$$\frac{\partial \mathbf{u}'}{\partial t} + 2\boldsymbol{\Omega}_{\rm s} \times \mathbf{u}' = -\nabla W \,. \tag{1.51}$$

To examine some of the properties of this system, we can now seek plane wave solutions of the form

$$\mathbf{u}' = \Re\left(\hat{\mathbf{u}}' e^{i(\mathbf{k}\cdot\boldsymbol{x} - \omega t)}\right) \quad \text{and} \quad W = \Re\left(\hat{W} e^{i(\mathbf{k}\cdot\boldsymbol{x} - \omega t)}\right) , \tag{1.52}$$

where ω is the frequency and $\mathbf{k}$ is the wavemode vector (k_x, k_y, k_z). This gives, in the simplest case in which $\boldsymbol{\Omega}_{\rm s}$ lies along the z (rotation) axis and we assume $\nabla \cdot \mathbf{u}' = 0$, the dispersion relation

$$\omega^2 = 4\Omega_{\rm s}^2 \left(\frac{k_z^2}{k_x^2 + k_y^2 + k_z^2}\right) . \tag{1.53}$$

If the star or planet rotates and is forced by a sufficiently low-frequency tidal forcing such that $|\omega| \leq 2\Omega_{\rm s}$, then the solution admits inertial waves[23] which act in addition to the non-wavelike equilibrium tide and any other forms of dynamical tide.

Typically inertial waves in a full sphere, spheroid or ellipsoid form global modes resulting in very little dissipation when non-resonantly forced. However, in spherical shells they are focused into wave attractors (thin beams) that can enhance dissipation for $|\omega| < 2\Omega_{\rm s}$. The width of the rays are determined by a balance between the wave energy and the lateral (cross beam) viscous diffusion. Inertial waves in shellular or fully spherical convective regions can be a source of significant tidal dissipation (Ogilvie & Lin, 2004; Wu, 2005b,a; Ogilvie & Lin, 2007; Ivanov & Papaloizou, 2010; Rieutord & Valdettaro, 2010; Ogilvie, 2013; Mathis, 2015; Bolmont & Mathis, 2016; Barker, 2020).

Inertial waves are likely to be particularly important in the tidal synchronisation and circularisation of binaries, because then $|\omega| < 2\Omega_{\rm s}$ for the relevant tidal frequencies. These waves are unimportant in the slowly rotating host stars of HJs since then $\omega > 2\Omega_{\rm s}$ but could have been important in young rapidly rotating stars.

---

[21] For terrestrial planets with surface oceans there is also the possibility of surface gravity waves (Lamb, 1994). Surface gravity waves (or f-modes) can be excited by tidal forcing in eccentric systems also e.g. HJ formation (for a review of HJ formation pathways see Dawson & Johnson 2018).

[22] Of course there are other sources of wavelike behaviour such as surface gravity, Alfvén waves etc., each requiring independent and combined study.

[23] In the interests of clarity it is worth highlighting that if $|\omega| \geq 2\Omega_{\rm s}$ holds then inertial waves are not excited.

Internal gravity waves

In this case we again consider a similar Cartesian model to eq. 1.45 but this time we include the restorative force to be from gravity, which under the Boussinesq approximation leads to (Chandrasekhar, 1961)

$$\frac{\mathrm{d}\mathbf{u}'}{\mathrm{d}t} = -\nabla W + B\mathbf{e}_z\,, \tag{1.54}$$

where $B = g\rho'/\rho_0$ is the buoyancy variable with ρ_0 as the background density and ρ' the density perturbation. We will, however, relate the buoyancy variable to the buoyancy (Brunt–Väisälä) frequency by

$$N^2 = \frac{\mathrm{d}B}{\mathrm{d}z}\,. \tag{1.55}$$

Upon performing a similar plane wave solution as in § 1.2.2, but also including the thermal energy equation ($\mathrm{D}_t B + N^2 u_z = 0$), we get the dispersion relation as

$$\omega = N^2 \left(\frac{k_x^2 + k_y^2}{k_x^2 + k_y^2 + k_z^2} \right)\,. \tag{1.56}$$

One requirement of these waves is the stable stratification of the fluid and hence $N^2 > 0$ and so for stars these are largely limited to the radiative zone where they are excited by the interface between the radiative and convective zones by tidal forcing (or convective forcing). There are then two configurations that can be considered. The first relates to massive stars with radiative envelopes and convective cores. In this configuration the internal gravity waves are dissipated by radiative damping or nonlinear effects near the surface (Zahn, 1975; Goldreich & Nicholson, 1989). The second relates to Sun-like stars with convective envelopes and radiative cores. These waves then propagate inwards where they can reflect, in which case they can become standing waves (g-modes), and can be dissipated by radiative diffusion, but in many applications this source of dissipation is negligible (Goodman & Dickson, 1998). However, these waves can break if they exceed a critical amplitude, which leads to very efficient dissipation of tidal energy[24] (Ogilvie & Lin, 2007; Barker & Ogilvie, 2010; Barker, 2011; Barker, 2020).

Summary: The equilibrium and dynamical tides

The tidal displacement (and velocity) in the linear tides regime can be obtained by considering the linearised potential equation, eq. 1.34. In the case of radiative regions where the fluid is stably stratified (no convection) the correct description of the equilibrium tide is that of Zahn (1966), eq. 1.41. In this case we find that the tidal displacement/velocity is incompressible and this is what we call the equilibrium tide. In convective regions the fluid displacement/velocity no longer needs to be incompressible but instead it must be irrotational and we must follow the descriptions detailed by Terquem et al. (1998); Goodman & Dickson (1998); Ogilvie (2014); Barker (2020), which is what we call the non-wavelike equilibrium tide, eq. 1.50. The purpose of this section is to provide a more detailed account of the two derivations than those in the literature and also to highlight the importance of using the correct description of the equilibrium tide depending on the application.

---

[24] This source of dissipation may explain the observed orbital decay rate of WASP-12b.

As well as the equilibrium tide we also have the dynamical tide which consists of the wavelike behaviour due to some restoring force. Two well studied restoring forces are the Coriolis force, which results in inertial waves, and buoyancy forces, which result in internal gravity waves. Inertial waves may be relevant in convective regions providing the tidal frequency is at most twice the primary's spin frequency. While internal gravity waves occur in radiative regions and, in the case of an interior radiative zone surrounded by a convective envelope, can result in efficient dissipation of tidal energy due to wave breaking.

1.3 Dissipation of tidal energy

We now return to the problem of the dissipation of tidal energy, which is the main subject of this work. In particular we are interested in the dissipation of the quadrupolar equilibrium tide (§ 1.2.1) as parameterised by the tidal Love number k_2^2 and/or the (modified) tidal quality factor Q (Q').

The most obvious source of dissipation we could consider is that of molecular viscosity of the fluid. We can estimate the viscous timescale by

$$\tau_{\text{visc}} \approx \frac{d^2\rho}{\mu}\,, \tag{1.57}$$

where d is a characteristic length-scale which can be taken as the radius of the star (for equilibrium tides) and μ is the viscosity coefficient, which for an ionised plasma is of order $1\,\text{cm}^{-1}\,\text{g}\,\text{s}^{-1}$. The typical values for the viscous timescale in a star can be found to be $\approx 10^6$ Gyr which is many orders of magnitude longer than even the age of the universe! As such viscous processes acting on global scale motions can, in general, be neglected inside stars.

A second form of dissipation can occur in stars due to radiative diffusivity which occurs in the transport of momentum by photons. The timescale for the radiative diffusion (also known as radiative damping or thermal diffusion) can be estimated by

$$\tau_{\text{rad}} \approx \frac{d^2\rho^2 c\kappa}{aT^4}\,, \tag{1.58}$$

where we have introduced c for the speed of light, κ for the mean absorption coefficient, a for the radiation density constant and T for the temperature. The typical values for the radiative diffusion timescale can be found to be ≈ 10 Gyr[25] which is at least on the order of the age of the universe but is significantly longer than the main sequence lifetimes of most classes of stars with the exception of low mass M-class stars. So we can neglect effects of radiative diffusion even in low mass stars providing we have a source of dissipation which occurs on timescales faster than this. Both of these mechanisms are weak, as evident by the dissipative processes being extremely slow and therefore cannot explain the observations already discussed (see § 1.1).

---

[25] Note that we are considering radiative diffusion for length-scales on the order of the stellar radius on which the equilibrium tide acts. In general, thermal diffusion has shorter timescales for shorter wavelength motions.

Aside 1.4: Heat transport in the Mixing-Length Theory

Much like the transport of momentum (Fig. 1.8), heat transport can be described by MLT. In this case we can again consider the schematic below where time advances from left to right. The bottom of the domain is hotter than the top and so a fluid parcel at the base of the domain is lifted through the buoyancy force over some distance l^{mlt} before being destroyed whereby it releases its thermal energy. Hence, the parcel has transported energy from the lower region to the cooler upper layer.

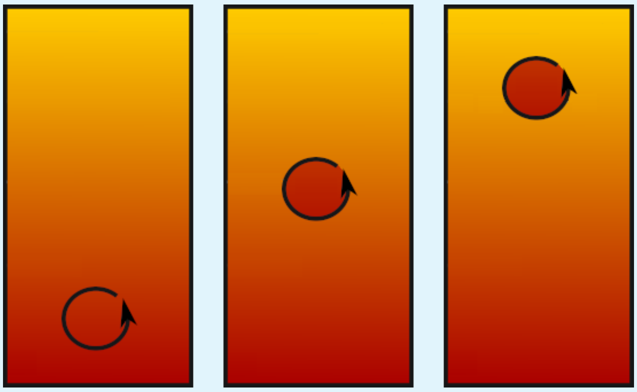

Another source of dissipation is through the interaction between the tidal flow, which acts as a background shear flow, and turbulent convection. One of the earliest descriptions of the interaction between mean flows and turbulence is the mixing-length theory (MLT) of Ludwig Prandtl (Prandtl, 1925; Kippenhahn et al., 2012; Davidson, 2015) which is routinely used in stellar models. MLT uses a local parcel argument to describe the motion of eddies and their transport of some property of the fluid, in our case momentum[26], which is best described with the aid of a diagram, as in Fig. 1.8. The parcel, which can be considered to be a single eddy, is advected by the flow (which can include the turbulent motion as well as the background) over some distance l^{mlt} (the mixing length) before dissolving and depositing its heat and momentum at this location. If the eddy came from a region with lower (higher) background momentum then, since the background momentum is imprinted into the eddy (neglecting molecular viscosity), then it will act against (with) the background flow at the deposition location. This impediment of the background momentum can be considered as simply another source of viscosity which can be added to the regular molecular viscosity. As such this interaction has been called an eddy viscosity or effective viscosity[27] although physically the process is better understood as an exchange of energy between the tidal flow and the turbulent convection (see aside 1.5). In this simple picture, the timescale for this form of dissipation can be evaluated similarly to that of the molecular viscosity by replacing μ in eq. 1.57 with a turbulent viscosity μ_e. This turbulent (dynamic) viscosity is estimated from $\mu_e \approx \rho l^{\mathrm{mlt}} u^{\mathrm{mlt}}$ where we can take $\rho \approx 10^2\,\mathrm{g\,cm^{-3}}$, $l^{\mathrm{mlt}} = H_p \approx 5 \times 10^9\,\mathrm{cm}$ (where H_p is the pressure scale height) and we can take $u^{\mathrm{mlt}} \approx 4000\,\mathrm{cm\,s^{-1}}$ (with all values taken near the base of the convection zone of the Sun). We can then estimate the timescale by using

---

[26] In stellar applications it is more common to use the model for heat transport rather than momentum, see aside 1.4.

[27] There are unfortunately a number of names that have been attributed to this phenomena such as "turbulent viscosity" or "eddy viscosity" which can be a source of confusion.

$\tau_{\mathrm{mlt}} \approx d^2\rho/\mu_e$ where we take $d \approx 10^{11}$ cm as the radius of the Sun. This gives the timescale for turbulent dissipation as $\tau_{\mathrm{mlt}} \approx 16$ yrs. With such a comparatively short timescale it is likely that turbulent viscosity is much more important than molecular or radiative viscosity, and may be the dominant mechanism of dissipation of the large-scale non-wavelike equilibrium tide. This is promising. However, in the above picture, the tidal shear was assumed to be steady. In many applications of tides, tidal flows are rapidly oscillatory relative to convective timescales. As a result, the tidal flow may not be damped as efficiently as in these simple arguments.

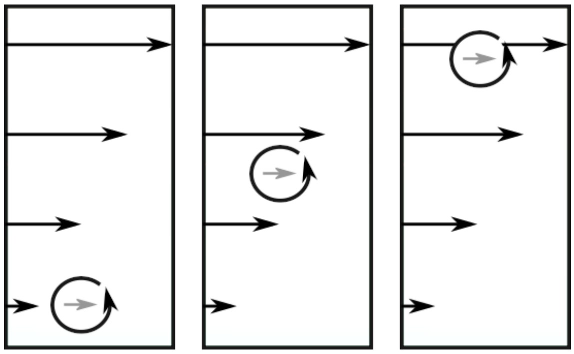

Figure 1.8: This cartoon demonstrates the basic principle of mixing-length theory for momentum transport within a fluid subject to a background shear. In this picture we have that time is advancing from left to right and the vertical direction is defined as perpendicular to the shear flow. At some initial time an eddy is imprinted with the background shear momentum before being advected by the flow which, for convection, results in the eddy being lifted vertically by the buoyancy force. The eddy will carry its momentum from the location of its formation over a distance l^{mlt} where it is then deposited. In this case since the momentum is smaller at the initial location the eddy will act to impede the shear flow at the deposition location. This is the physical idea behind the eddy viscosity of the MLT model.

Aside 1.5: Differences between effective viscosity and molecular viscosity

Molecular viscosity has strictly a positive value (or zero) by the second law of thermodynamics. However, it turns out that the effective viscosity does not have this same limitation. In the case of molecular viscosity kinetic energy is converted into heat. In the case of the effective viscosity kinetic energy is transferred between the turbulent motion and the mean flow. In principle this transfer can occur in either direction and thus negative effective viscosity can occur. One example of the occurrence of negative effective viscosity is in the atmospheric phenomenon of the quasi-biennial oscillation (McIntyre, 1994) which involves gravity waves.

This may seem like a positive step forward, however, while we have a good understanding of molecular viscosity (further benefited by the near monatomic nature of stellar material) and we also have a good understanding of radiative diffusion, what we do not have is a very good understanding of turbulent convection. A number of models have been developed, to try to model the dissipation and we now give a brief description of the most commonly used. We will discuss the shortcomings of these models towards the end of this chapter.

1.3.1 The weak friction approximation and the constant time lag model

We first describe the so-called weak friction approximation for tidal interactions which was mentioned in § 1.2. This approximation originates from G. H. Darwin[28] (Darwin, 1879a,b,c,d) but was not clearly described until Alexander (1973).

The basic idea can be illustrated as follows. The steady state part of the solution to the damped harmonic oscillator problem contains a phase lag component

$$\tan(\phi) = \frac{2\lambda\omega}{\omega_0^2 - \omega^2} \approx \frac{2\lambda\omega}{\omega_0^2} \,,$$

where ϕ is the phase lag angle (which corresponds to the angle between the line of centres and the tidal deformation), λ is the damping coefficient, ω_0 is the natural frequency of the oscillator[29] (free mode) and we have also used the fact that for planets and stars $\omega_0 \gg \omega$.

The weak friction approximation then assumes that ϕ is small[30] which means we can use the small angle approximation to write $\tan\phi \approx \phi \approx \Delta t_{\mathsf{disp}}\omega$ where Δt_{disp} has units of time[31] and is associated with the lag time between the perturbing potential and the response. Now recall that $\Im(k_2^m) \propto Q'^{-1}$ is the phase lag then we can write

$$Q' \propto \frac{1}{\Delta t_{\mathsf{disp}}\omega} \,, \tag{1.59}$$

which is the expression for the weak friction approximation of the tidal dissipation. More thorough explanations of this model can be found in Alexander (1973); Hubbard (1974, 1984); Zahn (2008); Souchay et al. (2013).

The weak friction approximation does not determine the dissipation and merely gives a useful expression for how the dissipation is related to the lag angle of the deformation. One way of modelling the dissipation is then to assume that the lag time Δt_{disp} is constant (frequency independent), and hence $\phi \sim \omega$, in what is known as the constant time lag model (Alexander, 1973; Hut, 1981). The constant time lag model is an approximation made in order to deal with the nature of the dissipation which is still a problem in the weak friction approximation. This results in an expression for the frequency dependence of the tidal dissipation as

$$Q' \propto \omega^{-1} \,. \tag{1.60}$$

It is useful to note that this model is equivalent to assuming a constant kinematic (or effective) viscosity. It should also be pointed out that Darwin also derived a simple model which is consistent with the constant time-lag model. His approach was to model an incompressible viscous fluid in which the response has a phase lag with the perturbing tidal potential. The result being that the lag was proportional to the tidal forcing frequency due to viscosity

The power in this simple model comes from the ability to derive closed-form expressions for

---

[28] George Howard Darwin was the fifth child of the great Charles Darwin who was responsible for the theory of evolution by natural selection.

[29] In stars this could be taken as the dynamical frequency $\omega_{\mathsf{dyn}} = 1/\tau_{\mathsf{dyn}} = \sqrt{GM/R^3}$, where τ_{dyn} is known as the dynamical timescale. In essence this timescale is a measure of how quickly the star in hydrostatic equilibrium can adjust to a perturbation to the pressure gradient and/or gravity.

[30] This is a reasonable assumption for planets and stars. In fact it has been measured for the Earth that $\phi \approx 2^\circ$ (Hubbard, 1984) which is, in general, a more dissipative system than stars and giant planets.

[31] This can be seen from dimensional arguments, $[\tan(\phi)] = 1$ and $[\omega] = T^{-1} \implies [\Delta t_{\mathsf{disp}}] = T$.

tidal evolutionary processes for any (not just small values) eccentricity or inclination (Alexander, 1973; Hut, 1981; Eggleton et al., 1998). This is partly why this model has been widely adopted in the literature, even though it may in fact not be valid to describe tidal interactions. We will revisit this issue later.

1.3.2 Zahn's linear reduction

It was almost a century after Darwin's model for tides to be considered in more detail in stars with convection zones. The largest development in this area came in the form of a model developed by Jean Paul Zahn (Zahn, 1966) and stems from some details about MLT which we neglected in § 1.3. It is equivalent to a constant Q model[32], for reasons which will become obvious. It is interesting to note that the constant Q model was first used in Goldreich (1963) to simply parametrise tidal dissipation for the purposes of computing tidal evolutionary processes, however, the outcome of the linear reduction model that we will describe here happens to give a constant Q.

The main additional consideration is to recognise that the fluid in the star or giant planet would be turbulent, then assume a Kolmogorov turbulent cascade to describe this. Using this description of turbulence we can then explore the length and timescales of the flow. Consider turbulence in the convection zone of a star with an integral scale (energy injection scale) l. First we note that if the eddies on all scales fill the domain then the total effective viscosity should be approximately equal to the effective viscosity at the integral scale l, that is $\nu_e \approx \nu_l$. However, eddies with turnover timescale longer than half the tidal period, i.e. $\tau_l > \tau_\omega/2$, will not be able to transfer their momentum before the tide has changed direction and thus should have their contributions reduced. The eddies will be limited to travelling a distance of $(\tau_\omega/2\tau_l)\, l$ over this timescale and so the contribution of these eddies should be reduced by the same factor. Thus we can write the effective viscosity at an arbitrary length-scale λ as

$$\nu_\lambda \propto \begin{cases} \lambda u_\lambda & \text{if} \quad \tau_\omega > \tau_\lambda\,, \\ \dfrac{\lambda u_\lambda \tau_\omega}{2\tau_\lambda} & \text{if} \quad \tau_\omega < \tau_\lambda\,, \end{cases} \tag{1.61}$$

where u is the velocity of eddies with a scale λ. Goldreich & Nicholson (1977) then argue that the integral scale dominates the contribution to the effective viscosity (which actually may not always be the case, see aside 1.6 for details of this subtlety) which allows us to write the effective viscosity as

$$\nu_\lambda \approx \nu_E \propto \begin{cases} l u_l & \text{if} \quad \tau_\omega > 2\tau_l\,, \\ \dfrac{l u_l \tau_\omega}{2\tau_l} & \text{if} \quad \tau_\omega < 2\tau_l\,, \end{cases} \tag{1.62}$$

which can be written in terms of frequencies as

$$\nu_E \propto u^{\text{mlt}} l^{\text{mlt}} \min\left[1, \frac{\omega_c}{2\omega}\right]\,, \tag{1.63}$$

where ω_c is the convective frequency ($\tau_l = 1/\omega_c$) of the dominant eddies and we have used the mixing-length velocity/length which is typically regarded as that of the integral scale.

---

[32] It is important to highlight that the constant Q model is not unique to convective regions of stars. In fact the model is used in other applications such as for terrestrial planets Dehant (1991).

One important point about this is that eq. 1.63 contains a constant of proportionality which actually consists of two constants. The first is taken to be $1/3$ without rigorous justification. In fact, the only real reason for this value is that MLT is analogous to the kinetic theory of gasses which has $\nu = 1/3\, l\bar{v}$ where l is the mean free path and $\bar{v}$ is the mean velocity of the molecules (Davidson, 2015). The second is the mixing-length parameter α^{mlt} (Böhm-Vitense, 1958; Kippenhahn et al., 2012) which relates the mixing length to the pressure scale height H_p through the relation $l^{\mathsf{mlt}} = \alpha^{\mathsf{mlt}} H_p$. As such a more complete form of eq. 1.63 is

$$\nu_E = \frac{1}{3}\alpha^{\mathsf{mlt}} u^{\mathsf{mlt}} H_p \min\left[1, \frac{\omega_c}{2\omega}\right] . \tag{1.64}$$

We will return to this in Ch. 6.

Aside 1.6: Dominance of the largest scale

Consider an eddy which has length-scale such that $l > \lambda$ which is allowed to travel its full distance before dissipating its energy. We can take the ratio of the contributions from the integral scale to that of our smaller eddy (λ). By making use of the following Kolmogorov relation (see Landau & Lifshitz 1987; Davidson 2015), between eddies of length-scale λ and the integral scale l,

$$u_\lambda \approx u \left(\frac{\lambda}{l}\right)^{1/3} , \tag{1.65}$$

we can obtain an expression for this ratio as

$$\frac{\nu_l}{\nu_\lambda} = \left(\frac{l}{\lambda}\right)^{4/3} . \tag{1.66}$$

Hence the contribution from the integral scale is always larger than that due to a smaller eddy.

We must also consider the ratio of the reduced contribution from the integral scale to the unreduced contribution of a smaller eddy. Note that in this case the dominant unreduced eddy must be that with τ_ω. We can use another Kolmogorov relation (see Landau & Lifshitz 1987; Davidson 2015),

$$\tau_\lambda \approx \tau_l \left(\frac{\lambda}{l}\right)^{2/3} , \tag{1.67}$$

along with the previous to write

$$\begin{aligned} \frac{\nu_l}{\nu_\omega} &= \frac{l u_l}{2}\left(\frac{\lambda_\omega}{l}\right)^{2/3} \frac{1}{\lambda_\omega u_l}\left(\frac{l}{\lambda_\omega}\right)^{1/3} \\ &= \frac{1}{2}\left(\frac{l}{\lambda_\omega}\right)^{2/3} . \end{aligned} \tag{1.68}$$

Which suggests that the integral scale is only dominant over a reduced eddy if $l > 2\sqrt{2}\lambda_\omega$ using Zahn's linear reduction factor.

We can relate eq. 1.63 to Q' by writing $\Delta t_{\mathsf{disp}} \propto \omega^{-1}$ and substituting this into eq. 1.59

which means that $Q' \propto$ const., i.e that this model is equivalent to a constant Q model. It has been claimed that the application of these ideas in stellar models can explain the circularisation of solar-type binary stars (e.g. Zahn 2008), but there is an important theoretical objection which we will now describe.

1.3.3 Goldreich and Nicholson's quadratic reduction

The work of Goldreich & Nicholson (1977) developed the ideas of § 1.3.2 for the small scale eddies with $2\tau_\lambda < \tau_\omega$. However, the authors believed the reduction factor of § 1.3.2 was insufficient and should in fact be significantly stronger leading to a smaller ν_E.

Their main argument stems from the fact that although an eddy with $2\tau_\lambda > \tau_\omega$ will move a distance of $l\omega_c/\omega$ in a single tidal period, the eddy does not exchange momentum with the tidal flow on this timescale. In order to follow the argument we begin with $\nu_\lambda \approx \lambda u_\lambda$ and make use of eq. 1.65 to get

$$\begin{aligned}\nu_\lambda &\approx \lambda u_\lambda \\ &= \frac{l\lambda u_l}{l}\left(\frac{\lambda}{l}\right)^{1/3} \\ &= l u_l \left(\frac{\tau_\lambda}{\tau_l}\right)^2 .\end{aligned} \tag{1.69}$$

For eddies with $\tau_\lambda \leq \tau_\omega$ the most important are those with $\tau_\lambda \approx \tau_\omega$ (i.e. the resonant eddies) as they provide the largest contribution. So Goldreich & Nicholson (1977) argue that

$$\nu_E \approx l u_l \left(\frac{\tau_\omega}{\tau_l}\right)^2 , \tag{1.70}$$

since they claim that the contribution of the largest eddies is at most comparable to those of the resonant eddies (eddies with timescales similar to the tidal period). In essence what this is saying is that ν_E is dominated by the contribution from the largest eddies with turnover timescales shorter than a tidal period. We note that this can be written in a form equivalent to eq. 1.63 as

$$\nu_E \propto u^{\mathrm{mlt}} l^{\mathrm{mlt}} \min\left[1, \left(\frac{\omega_c}{\omega}\right)^2\right] . \tag{1.71}$$

Both of Zahn (1966) and Goldreich & Nicholson (1977) use crude phenomenological arguments and it is worth highlighting the subtle difference between them. In Zahn (1966) the largest scale (longest timescale) i.e. the integral scale convective eddies provide the dominant contribution but that contribution must be reduced by truncating the length-scale they typically travel before they deposit their momentum. In Goldreich & Nicholson (1977) the dominant contribution is from convective eddies with timescales approximately the same as a tidal period. Essentially their disagreement comes down to which eddy size/timescale you select as the most important. As such each prescription predicts different scales of dominant contribution. One criticism of these ideas is that the use of eq. 1.65 may not be valid as if one were to look at all eddies of size λ then it would be unlikely that they would share the same value of u_λ or τ_λ, that is, eddies of a given size admit a spectrum of turnover times[33]. Another

---

[33] The use of eq. 1.65 may be appropriate if one is considering statistical properties of turbulence.

subtlety is that while Zahn (1966) makes use of simple mixing length arguments the results of Goldreich & Nicholson (1977) hinge on the spectrum of Kolmogorov turbulence (and more explicitly the scaling relations between velocities/timescales of eddies of some arbitrary size λ and the integral scale eddies l).

1.3.4 State of the art simulations

To determine which of these viscosity reduction prescriptions should be applied to dissipate the equilibrium tide (or whether such a prescription based on crude MLT arguments can be applied at all) when the tidal frequency exceeds the convective frequency has long been considered as the Achilles heel of tidal theory (e.g. Zahn 1989, Zahn 2008). Further progress is difficult with the kind of phenomenological arguments that we have just discussed and so much of the recent progress has been made by way of numerical experiments.

It is now possible to tackle this problem directly using hydrodynamic simulations of convection. Pioneering work in this direction was undertaken by Penev et al. (2007); Penev et al. (2009b) and Penev et al. (2009a). Penev et al. (2009b) directly simulated the interaction between convection (in a deep layer, adopting the anelastic approximation) and a large-scale flow driven by an oscillatory body force in a Cartesian domain. Their simulations (and the associated perturbative calculations[34] in Penev et al. 2007 based on Goodman & Oh 1997) measured the effective viscosity and found support for a frequency-reduction that is more consistent with the linear scaling of Zahn (1966) over a limited range of tidal frequencies, with some evidence of a weak anisotropy in the components of the eddy viscosity tensor. Motivated by this work, as well as the deficiency of mixing-length theory in predicting the observational-inferred dissipation in binary stars (Mazeh, 2008), Goldman (2008) explored the problem analytically using an idealised turbulence model. The resulting expression found agreement with a -2 power law as well as finding an increased efficiency of dissipation above the standard mixing-length theory, particularly for low frequencies. A further important contribution was subsequently made by Ogilvie & Lesur (2012), who performed a high-frequency asymptotic analysis in a local Cartesian model to understand the fluid response to an imposed oscillatory tidal (shear) flow. They elucidated the viscoelastic nature of the response, and performed complementary simulations to probe the interaction between this flow and convection in a triply-periodic Cartesian box (so-called "homogeneous convection"). Their analysis and simulations were both consistent with a quadratic reduction in the effective viscosity for high-frequency tides. They also obtained tentative evidence suggesting the surprising result that ν_E can become negative at high frequencies, indicating the possibility of tidal anti-dissipation (where energy is transferred from the convective flow). However, their negative values of ν_E contained substantial error bars, partly as a result of the bursty nature of homogeneous convection and the computational expense of running long-duration simulations. Braviner (2015) continued this work further by simulating the interaction between an oscillatory tidal shear flow and a convective-like flow (ABC flow) in laminar and weakly turbulent regimes. He found support for both the asymptotic analysis of Ogilvie & Lesur (2012) and a quadratic reduction in the effective viscosity at high frequencies for this flow.

The independent studies of Penev et al. (2009b) and Ogilvie & Lesur (2012) obtained apparently contradictory results regarding the nature of the effective viscosity in the regime

---

[34] It is worth noting that these perturbative calculations are likely to be invalid (Ogilvie & Lesur, 2012).

of high-frequency tidal forcing. The former work simulated multiple pressure scale heights, whereas the latter assumed a Boussinesq fluid but explored a wider range of tidal frequencies. The two sets of simulations exhibit different turbulent temporal power spectra, which may be responsible for the different frequency scalings in the effective viscosity, but these differences have not yet been explained. This motivates further work to understand the interaction between tidal flows and convection. The approach taken in this thesis follows Penev et al. (2009b) and Ogilvie & Lesur (2012) in simulating the dynamics of convection in a local Cartesian model that represents a small patch of a convection zone of a star or planet. We differ from these works by adopting the well-studied Rayleigh-Bénard setup to model (Boussinesq) convection, which allows us to overcome some of the peculiar properties of “homogeneous convection” (as studied by Ogilvie & Lesur 2012). To drive convection in this system, we impose different temperatures on two boundaries in the vertical direction, with a hot plate underlying a cool one. We wish to understand the fundamental fluid dynamical interactions between convection and tidal flows in this model, using a combination of a hydrodynamical simulations and asymptotic theory.

The advantages of adopting a local Cartesian model that represents a small patch of the convection zone of a star or planet are that these simulations are much less computationally expensive, and this model is much simpler to set up and to analyse than a corresponding global model. The former allows us to simulate more turbulent convection (at higher Rayleigh numbers), and for these simulations to be run for much longer. This allows us to average over long times to form reliable estimates of mean quantities such as the energy and the Reynolds stress, and to estimate the magnitude of the fluctuations. This is likely to be essential to accurately determine the effective viscosity, particularly in the regime of high-frequency tides. The disadvantage of a local model is that global aspects, including the structure of the convection zone and spatial variations in the stellar or planetary properties are not considered. In this study, we have chosen to focus on Boussinesq convection, since it is simpler to analyse and more efficient to simulate than compressible (or anelastic) convection. This allows us to undertake a wider parameter survey, and to run our simulations for longer to reduce noise.

Summary: Dissipation Prescriptions

It is thought that an important mechanism of tidal dissipation in the convective regions of stars and planets is due to the interaction between convective turbulence and the tidal flow. The key takeaways of the discussion on tidal dissipation of the large-scale non-wavelike equilibrium tide are now summarised, where, besides the disagreement between the frequency reduction power laws, some shortcomings have been highlighted.

- $\omega_c > \omega$:
  - no frequency dependence on the effective viscosity,
  - largest scales dominate the contribution,
  - This regime is largely assumed, based on expectations from MLT, without confirmation.
- $\omega_c < \omega$ and following Zahn (1966):

  - $\nu_e \propto \omega^{-1}$,
  - largest scales dominate the contribution to ν_e,
  - supported by simulations of Penev et al. (2007) (fully compressible based on perturbative calculations) and Penev et al. (2009b) (anelastic).
- $\omega_c < \omega$ and following Goldreich & Nicholson (1977):
  - $\nu_e \propto \omega^{-2}$,
  - largest scales with $\tau_\lambda \lesssim \tau_\omega$ (the resonant eddies) dominate the contribution to ν_e,
  - supported by simulations of Ogilvie & Lesur (2012) (homogeneous convection) and Braviner (2015) (ABC flow),
  - supported by theoretical arguments of Ogilvie & Lesur (2012) (using multiscale asymptotics) and Goldman (2008) (using turbulence modelling),
  - Phenomenological arguments have not been tested.

1.4 What would we like to know?

The fluid dynamical mechanisms responsible for tidal dissipation in stars and giant planets remain incompletely understood (e.g. Mathis & Remus 2013; Ogilvie 2014). In this work we focus on tidal dissipation resulting from the interaction of large-scale (non-wavelike) equilibrium tides and convection inside stars or giant planets. This is a classical tidal mechanism that is commonly believed to be important in stars (or giant planets) with convective envelopes (Zahn, 1966; Zahn, 1989, 2008). The interaction between the tide and convection is thought to act like an effective viscosity ν_E (which is much larger than the microscopic viscosity) in damping the large-scale tidal flow. However, the efficiency of this mechanism is expected to be reduced when the tidal shear frequency ω exceeds that of the relevant convective frequency ω_c, but the power law of this reduction has long been a matter of debate (e.g. Goodman & Oh, 1997), and this issue is still often considered as "the Achilles' heel of tidal theory" (Zahn, 2008).

The crux of the problem is to what extent the convection should become less efficient at dissipating the tidal flow when $\omega > \omega_c$? Based on ideas from mixing-length theory, Zahn (1966) (see also Zahn 1989) proposed $\nu_E \propto \omega^{-1}$ when $\omega \gg \omega_c$. Goldreich & Nicholson (1977) suggested that this reduction is insufficient and argue that $\nu_E \propto \omega^{-2}$, which would imply much less efficient tidal dissipation at high frequencies. Prior work on this problem has largely focused on which prescription is true rather than tackling the principles by which the predictions have been made. The question of which prescription is correct is the general theme of this thesis, however, the validity of the phenomenological arguments of Zahn (1966); Zahn (1989) and Goldreich & Nicholson (1977) will also be addressed.

Aside 1.7: A taste of other problems

There are currently many aspects of tidal interactions that are active areas of research, and in particular, mechanisms relating to the dissipation of tidal energy. For example, tidal excitation of internal gravity waves (e.g. Goodman & Dickson, 1998; Ogilvie & Lin, 2007; Barker & Ogilvie, 2010; Barker, 2011; Weinberg et al., 2012; Essick & Weinberg, 2016) can be important in stellar radiation zones, and this mechanism may be responsible for the observed orbital decay of WASP-12 b (Maciejewski et al., 2016; Patra et al., 2017; Chernov et al., 2017; Weinberg et al., 2017; Bailey & Goodman, 2019; Yee et al., 2019). The excitation of inertial waves is being studied in the convective envelopes of rotating stars or giant planets (e.g. Wu, 2005c; Ogilvie & Lin, 2007; Goodman & Lackner, 2009; Papaloizou & Ivanov, 2010; Favier et al., 2014; Barker, 2016a), and this mechanism may be important for tidal circularisation and spin synchronisation. In giant planets, the role of stably-stratified (or semi-convective) layers is also being explored (Fuller et al., 2016; André et al., 2017; André et al., 2019; Pontin et al., 2020) with possible application to the orbital migration of the moons of Jupiter and Saturn (e.g. Lainey et al., 2009, 2012, 2017, 2020).

Why does it matter which of these prescriptions, if any, are correct? To give just one example, a crude estimate for the inspiral time of a hot Jupiter orbiting a Sun-like star in a one day orbit suggests that if there is no frequency-reduction in the effective viscosity the planet would decay in tens of Myr. On the other hand, if $\nu_E \propto \omega^{-1}$, the planet would decay in of order 1 Gyr, and if $\nu_E \propto \omega^{-2}$, the planet would decay in tens to a hundred Gyr. It is clearly essential to determine which of these (if any) are correct before we can predict the orbital decay (or otherwise) of hot Jupiters, and so that we can interpret existing observations. We will return to the astrophysical implications after presentation of relevant results in both Ch. 3 and 6.

Despite much attention being given to the fast tides regime, little has been given to the situation when $\omega < \omega_c$. It has been the general assumption that in this case the effective viscosity would be frequency independent and that the constant time lag model would then be appropriate. This has, however, been largely untested and we will begin to address this in Ch. 6.

Chapter 2

Preliminaries

Contents

Before we explore the frequency dependence of the effective viscosity acting on tidal flows, as well as the fundamental fluid dynamics involved, we first describe the approach used in this work. In this chapter we will describe the model for the convective fluid as well as the approximation used for the tidal flow. Some brief details of the numerical methods used will be given with attention focused on non-standard techniques. Finally, expressions for quantities we are interested in computing in the simulations will be derived.

2.1 Local Cartesian model: small patch of a convection zone

We consider a local Cartesian representation of a small patch of a convection zone of a star or giant planet subjected to gravitational tidal forcing from a companion (see Fig. 2.1). We note that in Ch. 1 the tidal frequency typically included the rotation of the primary, $\omega = 2(\Omega_\mathrm{o} - \Omega_\mathrm{s})$. In the interests of simplifying the model everything that follows will assume the non-rotating case, $\Omega_\mathrm{s} = 0$. Doing this means that we are not considering the influence of the Coriolis force. We ignore the Coriolis term in the equation of motion, as we wish to study the simplest model of the interaction between tidal flows and convection. The effects of including the Coriolis term are a natural further development of this thesis. We use Cartesian coordinates[1] (x, y, z), and simulate a Cartesian domain with $x \in [0, L_x d]$, $y \in [0, L_y d]$ and $z \in [0, d]$, where z is the local radial direction and d is the layer depth (which strictly must be small relative to the local pressure scale height) and x and y represent the two horizontal directions. A local model has the significant advantage that it is much simpler to set up and to analyse, and the numerical methods are also computationally more efficient, than in a corresponding global model. Our approach is similar to, and builds upon, the pioneering works of Penev et al. (2007), Penev et al. (2009b) and Ogilvie & Lesur (2012).

---

[1] The physical interpretation of this coordinate system is not obvious. One simple example is to consider the domain to be located along the rotation axis with $\mathbf{e}_x$ pointing towards the secondary.

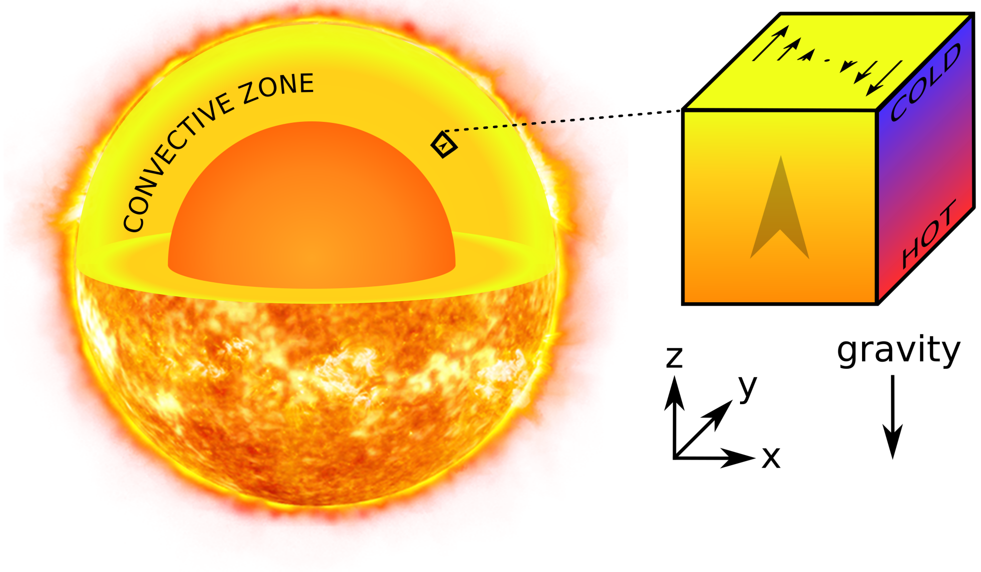

Figure 2.1: Local Cartesian model to study the interaction between tidal flows and convection. The tidal flow is modelled as an oscillatory shear flow in y that varies linearly in x, which represents one component of the large-scale non-wave-like tidal flow in a star (or planet). The local vertical direction is z.

Aside 2.1: The Boussinesq approximation

The Boussinesq approximation essentially linearises the ideal gas law for small departures from a reference state and ignores density differences in all but the gravity terms of the momentum equation (Spiegel & Veronis, 1960). In physical terms the anelastic approximation is saying that the timescales for sound waves to travel one unit of distance is significantly shorter than for the fluid flow. This assumption is likely to be the case in the convective interiors of gas giants and stars where we have that $u \ll u_s$, where u is the fluid velocity and u_s the sound speed, except near the surface. The Boussinesq approximation further requires that $d \ll H_p$ and $d \ll H_\rho$ where H_p is the pressure scale height and H_ρ is the density scale height, that is the domain height is much less than the pressure and density scale heights[a] The Boussinesq approximation results in the mass conservation equation taking the form of an incompressibility condition.

---

[a] For an ideal gas the pressure and density scale heights, along with the temperature scale height H_T, can be related through the equation of state to give $H_p^{-1} = H_\rho^{-1} + H_T^{-1}$.

We model convection using the Boussinesq approximation (Spiegel & Veronis, 1960) (see aside 2.1) and adopt the well-studied Rayleigh-Bénard setup (e.g. Chandrasekhar 1961). The Boussinesq approximation is appropriate for studying small-scale convection with short length-scales that are much smaller than a pressure or density scale height, and with flows that are slow compared with the sound speed. Our approach is similar to Ogilvie & Lesur (2012), except that they studied convection with periodic boundary conditions in the vertical (so-called "homogeneous convection"). That model is peculiar due to the existence of exact convection solutions ("elevator modes"), which lead to bursty temporal dynamics. We have chosen to instead adopt impenetrable, stress-free and fixed temperature walls at the top and bottom of our domain in z. These walls are strictly artificial for stellar convection, but they prevent the occurrence of elevator modes and allow a statistically steady turbulent state to be attained more readily.

2.1.1 Tidal flow description

In order to explore the interaction between convection and the tidal flow we must first find what the tidal flow looks like (following descriptions of Ogilvie 2009, 2013; Barker 2020) so that the relevant components of it can be studied. We do this by considering eq. 1.50

$$\nabla\cdot(\rho\nabla\zeta)=\frac{\mathrm{d}\rho}{\mathrm{d}p}\rho\Psi\,, \tag{2.1}$$

where we have replaced the tidal displacement vector with its associated potential, $\boldsymbol{\xi}=\nabla\zeta$ and we have neglected the perturbation to the primary's potential, Φ', as this simply adjusts the magnitude of the overall potential (we only care about the structure of the flow). The tidal and displacement potentials can be expanded in terms of the spherical harmonics (see aside 2.2 for a minor detail about the chosen notation)

$$\zeta=\sum_{l,m}\zeta_l(r)Y_l^m(\theta,\phi)\,, \tag{2.2}$$

$$\Psi=\sum_{l,m}\Psi_l(r)Y_l^m(\theta,\phi)\,. \tag{2.3}$$

Aside 2.2: A note about notation

In linear theory for an axisymmetric star, the azimuthal wavenumbers are all uncoupled. That means that if only one m is forced, only one m contributes to the linear solution. In general, the response of each m will be different, however, since we will only be considering a single mode, and in the interests of reducing clutter in the equations, we write $\zeta_l(r)$ rather than $\zeta_l^m(r)$ (similarly for $\Psi_l(r)$).

Substitution of the spherical harmonic expansions into eq. 2.1 and considering only the $l=m=2$ component[2], results in

$$\nabla\cdot(\rho\nabla\zeta_2Y_2^2)=\frac{d\rho}{dp}\rho Y_2^2\Psi_2\,. \tag{2.4}$$

We can now expand the LHS as

$$\nabla\cdot(\rho\nabla\zeta_2Y_2^2)=\frac{\mathrm{d}\rho}{\mathrm{d}r}\frac{\mathrm{d}\zeta_2}{\mathrm{d}r}Y_2^2+\frac{\rho Y_2^2}{r^2}\frac{\partial}{\partial r}\left(r^2\frac{\partial\zeta_2}{\partial r}\right)-\frac{6\rho}{r^2}Y_2^2\zeta_2\,, \tag{2.5}$$

where we have expanded the divergence, split the Laplacian into its radial and horizontal (polar

---

[2] There will also be a contribution to the tidal response from the $l=2$, $m=0$ component. However, this component is static and so does not contribute to the dissipation. Also note that the $l=2$, $m=1$ mode only contributes if there is a spin-orbit misalignment.

and azimuthal) components and used the fact that $\rho = \rho(r)$. Using this we can write eq. 2.4 as

$$\frac{1}{r^2}\frac{\partial}{\partial r}\left(r^2\rho\frac{\mathrm{d}\zeta_2}{\mathrm{d}r}\right) - \frac{6\rho}{r^2}\zeta_2 = \frac{\mathrm{d}\rho}{\mathrm{d}p}\rho\Psi_2\,. \tag{2.6}$$

For simplicity we can consider a uniform density sphere[3] but note that to do this we must write $\rho = \rho_0 H(R_1 - r)$ where ρ_0 is some reference density which we can set to unity and $H(R_1 - r)$ is the Heaviside step function (which defines the density as ρ_0 within the body and zero outside). We can now write eq. 2.6 as

$$\frac{1}{r^2}\left[2rH\frac{\mathrm{d}\zeta_2}{\mathrm{d}r} - r^2\delta\frac{\mathrm{d}\zeta_2}{\mathrm{d}r} + r^2H\frac{\mathrm{d}^2\zeta_2}{\mathrm{d}r^2}\right] - \frac{6H}{r^2}\zeta = \frac{\mathrm{d}\rho}{\mathrm{d}p}H\mathcal{A}\left(\frac{r}{R_1}\right)^2, \tag{2.7}$$

where we have made use of eq. 1.8 ($\Psi_2(r) = \mathcal{A}(r/R_1)^2$) and $\mathrm{d}H/\mathrm{d}r = -\delta(R_1 - r)$ where δ is the Dirac delta function. This equation can be simplified by considering the potential only inside the primary, that is when $r < R_1$, which means, since $\delta = 0$ everywhere but at $r = R_1$. This leads to

$$\frac{\mathrm{d}^2\zeta_2}{\mathrm{d}r^2} + \frac{2}{r}\frac{\mathrm{d}\zeta_2}{\mathrm{d}r} - \frac{6}{r^2}\zeta_2 = \frac{\mathrm{d}\rho}{\mathrm{d}p}\mathcal{A}\left(\frac{r}{R_1}\right)^2. \tag{2.8}$$

The RHS can be simplified by considering the derivative term and noting that due to the delta function this term vanishes[4],

$$\frac{\mathrm{d}\rho}{\mathrm{d}p} = \frac{\mathrm{d}\rho}{\mathrm{d}r}\frac{\mathrm{d}r}{\mathrm{d}p} = -\delta(R_1 - r)\frac{\mathrm{d}r}{\mathrm{d}p} = 0\,, \quad r < R_1\,. \tag{2.9}$$

Thus we are left with a simple homogeneous Cauchy-Euler equation in the interior

$$r^2\frac{\mathrm{d}^2\zeta_2}{\mathrm{d}r^2} + 2r\frac{\mathrm{d}\zeta_2}{\mathrm{d}r} - 6\zeta_2 = 0\,, \tag{2.10}$$

with general solution

$$\zeta_2 = C_1 r^{-3} + C_2 r^2\,, \tag{2.11}$$

for some constants C_1 and C_2. These constants can be evaluated by use of appropriate boundary conditions,

$$\left.\frac{\mathrm{d}\zeta_2}{\mathrm{d}r}\right|_{r=0} = 0\,, \tag{2.12}$$

$$\left.\frac{\mathrm{d}\zeta_2}{\mathrm{d}r}\right|_{r=R_1} = -\frac{\Psi_2(R_1,t)}{g}\,, \tag{2.13}$$

where $g = GM_1/R_1^2$ is the surface gravity. Physically the first of these maintains regularity of the radial displacement (ζ_2) at the origin ($r = 0$) while the second is from the assumption of a free-surface at the outer boundary (for a quasi-hydrostatic equilibrium) which is subject to a low-frequency forcing (Ogilvie, 2009).

---

[3] In the case of a uniform density body the equations for the equilibrium tide and non-wavelike equilibrium tide are identical.

[4] This can also be seen by considering this is $\mathrm{d}\rho/\mathrm{d}p = 1/c_s^2$ where c_s^2 is the sound speed. However, since we are considering an incompressible medium we have an infinite sound speed and thus this term vanishes. Alternatively, given we are considering an incompressible case ($\nabla \cdot \boldsymbol{\zeta} = 0$) it follows from eq. 1.31.

This gives the $l = m = 2$ component of the radial tidal potential as

$$\zeta_2 = -\frac{\Psi_2(R_1,t)}{2R_1 g} r^2 \,, \quad \text{for} \quad r < R_1 \,, \tag{2.14}$$

where we note that $\Psi_2(R_1,t)$ consists of only the time dependent parts and the constant term of eq. 1.8. Hence, the tidal displacement is

$$\zeta_{2,2}(r,\theta,\phi,t) = -\frac{\Psi_2(R_1,t)}{2R_1 g} r^2 Y_2^2(\theta,\phi) \,. \tag{2.15}$$

This can be written in global Cartesian coordinates[5] as

$$\zeta_{2,2}(x,y,z,t) = -\frac{\mathcal{A}}{8R_1 g}\sqrt{\frac{15}{2\pi}}(x+iy)^2(\cos\omega t - i\sin\omega t) \,, \tag{2.16}$$

where we have used eq. 1.8 (for the constant and time dependent part of Ψ_2) and made the substitution $2\Omega_\mathrm{o} = \omega$ since we are considering the non-rotating case ($\Omega_\mathrm{s} = 0$). In order to obtain the velocity field we now take the time derivative of the gradient of the displacement potential, noting that we are interested in the real part of the solution, this gives

$$\Re\left(\frac{\partial}{\partial t}\nabla\zeta_{2,2}\right) = \mathcal{A}^\dagger\omega\Big[(-x\sin\omega t + y\cos\omega t)\mathbf{e}_x + (y\sin\omega t + x\cos\omega t)\mathbf{e}_y\Big] \,, \tag{2.17}$$

where we have combined the constants as

$$\mathcal{A}^\dagger = -\frac{\mathcal{A}}{4R_1 g}\sqrt{\frac{15}{2\pi}} = \frac{\sqrt{3}}{4}\left(\frac{M_2}{M_1}\right)\left(\frac{R_1}{a}\right)^3 \,. \tag{2.18}$$

Note that given $R_1 < a$ and under our assumptions that $M_1 \gg M_2$ it must be the case that $\mathcal{A}^\dagger \ll 1$. We can rewrite the above expression as

$$\mathbf{u}_0 = \mathcal{A}^\dagger\omega \begin{bmatrix} -\sin\omega t & \cos\omega t & 0 \\ \cos\omega t & \sin\omega t & 0 \\ 0 & 0 & 0 \end{bmatrix} \boldsymbol{x} \,. \tag{2.19}$$

This flow can be seen in Fig. 2.2 for a slice through the equatorial plane of the primary. Note that since we are exploring only the $l = m = 2$ component of the tidal flow there is no z dependence or flow in the $\mathbf{e}_z$ direction.

Let us first recap what eq. 2.19 represents before a description of how this will be approximated. Eq. 2.19 describes the tidal flow within the primary excited by the orbiting secondary on a non-spin-synchronised, spin-orbit aligned, circular and equatorial orbit. In the interests of simplicity we have neglected rotation of the primary as well as the perturbation to the potential of the secondary. The primary has been approximated as a constant density sphere in quasi-hydrostatic equilibrium for illustration here. Finally, it is important to note that this considers only the $l = m = 2$ component of the tide[6]. This gives us the simplest possible

---

[5] In the global coordinate system the $\mathbf{e}_x$, $\mathbf{e}_y$ and $\mathbf{e}_z$ unit vectors are fixed in space. A physical way of understanding this is that in the global system the unit vector $\mathbf{e}_x$ might point towards some reference star that is effectively at infinity, however, in the local system the vector pointing to said star depends on the location of the local domain within the global domain (this can be understood by considering that the $\mathbf{e}_x$ vector in the local coordinates always points radially outwards).

[6] For justifications of each approximation see the relevant section in the text.

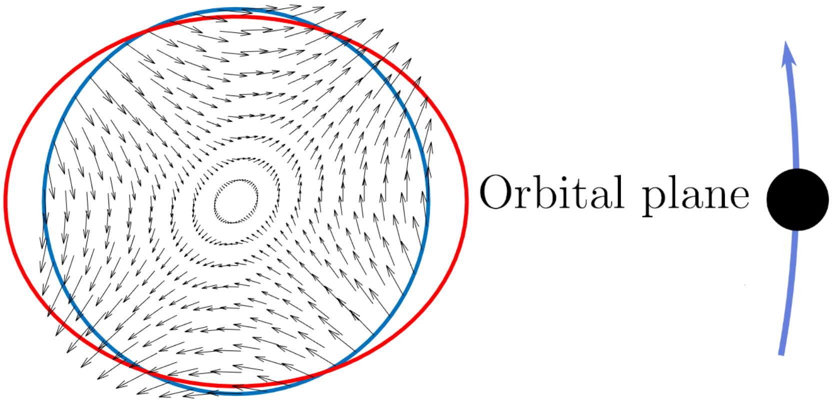

Figure 2.2: Plot of the tidal flow from eq. 2.19 (where we note that $\mathcal{A}^{\dagger}\omega$ has been set to 0.01) in the orbital plane. The plot is for $t = 0$ and it should be reminded that this flow is in the absence of dissipation. The blue circle represents the unperturbed primary's shape while the red ellipse represents how the body would deform from the tidal force. (not to scale)

stellar/planetary model for the equilibrium tidal flow.

2.1.2 Approximation to the tidal flow

Since tidal deformations of stars are typically small, it is sensible to explore the regime of linear tides[7], in which the fluid response to each component of the tidal potential can be studied separately. We will follow Ogilvie & Lesur (2012) in modelling the large-scale tidal flow as an oscillatory shear flow that is linear in the local Cartesian coordinates. In particular, we model the tidal flow as a "background flow" which consists of one component of the flow described by eq. 2.19. Thus our background flow is

$$\mathbf{u}_0 = Sx\cos(\omega t)\mathbf{e}_y = \frac{\dot{a}x}{d}\mathbf{e}_y\,, \tag{2.20}$$

where ω is the tidal frequency, $S = a_0\omega/d$ is the amplitude of the tidal shear, a_0 is the amplitude of the tidal displacement, and $\dot{a}$ is the time-derivative of the displacement $a(t) = a_0 \sin\omega t$. Note that this is only one component of the non-wave-like tidal flow even in the simplest case of a circular aligned orbit (e.g.Ogilvie 2014) which we described in § 2.1.1.

In our simulations we will typically assume $a_0 \ll d$ (with a typical value $a_0 = 0.05d$), so that the tidal displacement is much smaller than a density or pressure scale height. This is reasonable for studying tides in solar-type stars interacting with the convective eddies in the majority of the convection zone (and in particular near the base), for example (the tidal amplitude is typically smaller than 10^{-4} stellar radii, whereas the pressure scale height is of the order of 0.1 stellar radii except near the surface). Since planet-hosting stars are usually slow rotators, we ignore rotation in this initial study, but we note that sufficiently rapid rotation is expected to affect the resulting effective viscosity (Mathis et al., 2016). This is because rotation modifies convective velocities and length-scales (e.g. Stevenson 1979; Jones 2007;

---

[7] Since we assume $\mathcal{A}^{\dagger} \ll 1$, we neglect nonlinear tidal effects such as the elliptical instability in convection zones (Barker & Lithwick, 2013; Barker, 2016a), which might be important for tides in the shortest-period hot Jupiters.

King et al. 2013; Barker et al. 2014), but we relegate the incorporation of rotation to future work.

2.1.3 Convection

Along with the approximation of the tidal flow described in § 2.1.2 we require a model for the convection within the star or giant planet. Within the Boussinesq approximation the flow is governed by

$$\frac{\partial \mathbf{u}^*}{\partial t} + \mathbf{u}^* \cdot \nabla \mathbf{u}^* = -\nabla p^* + \theta \mathbf{e}_z + \nu \nabla^2 \mathbf{u}^* + \boldsymbol{f}\,, \tag{2.21a}$$

$$\frac{\partial \theta}{\partial t} + \mathbf{u}^* \cdot \nabla \theta = N^2 u_z + \kappa \nabla^2 \theta\,, \tag{2.21b}$$

$$\nabla \cdot \mathbf{u}^* = 0\,, \tag{2.21c}$$

where $\mathbf{u}^*$ is the total velocity, p is a pressure variable, ν is the (constant) kinematic viscosity, $\boldsymbol{f}$ is the forcing required to excite the tidal flow, κ is the (constant) thermal diffusivity and we note that the background reference density has been set to unity. We define our "temperature perturbation" (see aside 2.3) by $\theta = \alpha_{\text{th}} g T$, where α_{th} is the thermal expansion coefficient, g is the acceleration due to gravity and T is the usual temperature perturbation, so that θ has the units of an acceleration. The above equations describe perturbations to a linear background temperature profile $T(z)$, with uniform gradient $\alpha_{\text{th}} g \partial_z T = N^2$, where N^2 is the square of the buoyancy (Brunt–Väisälä) frequency, which is negative in a convection zone. This describes fluid that is hotter at the bottom of the domain than at the top.

We can consider the tidal flow to be a background flow which is coupled to the convective motion through the total velocity $\mathbf{u}^* = \mathbf{u} + \mathbf{u}_0$ (note that we also must have $p^* = p + p_0$). On substitution into the governing equations this gives

$$\frac{\partial \mathbf{u}}{\partial t} + \mathbf{u} \cdot \nabla \mathbf{u} + \mathbf{u} \cdot \nabla \mathbf{u}_0 + \mathbf{u}_0 \cdot \nabla \mathbf{u} = -\nabla p + \theta \mathbf{e}_z + \nu \nabla^2 \mathbf{u}\,, \tag{2.22a}$$

$$\frac{\partial \theta}{\partial t} + \mathbf{u} \cdot \nabla \theta + \mathbf{u}_0 \cdot \nabla \theta = N^2 u_z + \kappa \nabla^2 \theta\,, \tag{2.22b}$$

$$\nabla \cdot \mathbf{u} = 0\,, \tag{2.22c}$$

$$\frac{\partial \mathbf{u}_0}{\partial t} + \mathbf{u}_0 \cdot \nabla \mathbf{u}_0 = -\nabla p_0 + \nu \nabla^2 \mathbf{u}_0 + \boldsymbol{f}\,, \tag{2.22d}$$

$$\nabla \cdot \mathbf{u}_0 = 0\,, \tag{2.22e}$$

where we note that the background flow $\mathbf{u}_0$ and perturbed flow $\mathbf{u}$ can be separated. Since we prescribe the background flow we will not explicitly solve the equations for the background flow (eq. 2.22d and 2.22e), instead this will be considered to be externally imposed (and hence $\mathbf{u}_0$ will be prescribed). As such the system of equations which we seek to study are

$$\frac{\partial \mathbf{u}}{\partial t} + \mathbf{u} \cdot \nabla \mathbf{u} + \mathbf{u}_0 \cdot \nabla \mathbf{u} + \mathbf{u} \cdot \nabla \mathbf{u}_0 = -\nabla p + \theta \mathbf{e}_z + \nu \nabla^2 \mathbf{u}\,, \tag{2.23a}$$

$$\frac{\partial \theta}{\partial t} + \mathbf{u} \cdot \nabla \theta + \mathbf{u}_0 \cdot \nabla \theta = N^2 u_z + \kappa \nabla^2 \theta, \tag{2.23b}$$

$$\nabla \cdot \mathbf{u} = 0\,. \tag{2.23c}$$

Aside 2.3: Temperature perturbation

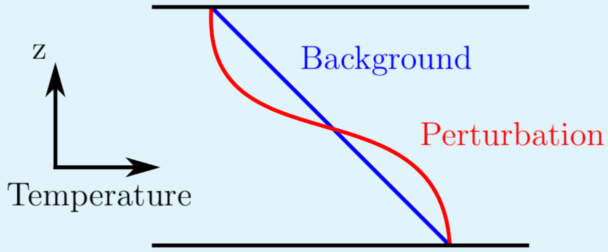

We consider a problem where the temperature is fixed at $z \in \{0, 1\}$ and proceed to split the actual temperature T into a linear background state (conductive profile) and a perturbation about this background. This perturbation, θ, is assumed to be small and has nondimensional form $T = 1 - N^2 z + \theta$ where N^2 describes the gradient of the linear background. On substituting this into the energy equation (eq. 2.21b) we get

$$\frac{\partial \theta}{\partial t} - \kappa \nabla^2 \theta = N^2 u_z - \mathbf{u} \cdot \nabla \theta \,. \tag{2.24}$$

Note that the perturbation to the linear background is defined such that the boundary conditions $\theta(z) = 0 \ \forall z \in \{0, 1\}$ are satisfied.

We choose units such that d is our unit of length and the thermal timescale d^2/κ is our unit of time (so that velocities are measured in units of κ/d). The latter is chosen to enable a direct comparison with the linear theory of convection (e.g. Chandrasekhar 1961), though we will later interpret our results in terms of the convective turnover timescale of the dominant eddies (or "free-fall" timescale), since this is the most relevant physical timescale in this problem. The resulting non-dimensional equations are

$$\frac{\partial \mathbf{u}}{\partial t} + \mathbf{u} \cdot \nabla \mathbf{u} + \mathbf{u}_0 \cdot \nabla \mathbf{u} + \mathbf{u} \cdot \nabla \mathbf{u}_0 = -\nabla p + \mathrm{Ra}\,\mathrm{Pr}\,\theta \mathbf{e}_z + \mathrm{Pr} \nabla^2 \mathbf{u} \,, \tag{2.25a}$$

$$\frac{\partial \theta}{\partial t} + \mathbf{u} \cdot \nabla \theta + \mathbf{u}_0 \cdot \nabla \theta = u_z + \nabla^2 \theta \,, \tag{2.25b}$$

$$\nabla \cdot \mathbf{u} = 0 \,, \tag{2.25c}$$

where we have avoided introducing new "hatted" dimensionless variables to avoid confusing the presentation.

We adopt periodic boundary conditions in the horizontal and in the vertical that of stress-free, impenetrable, fixed temperature boundary conditions such that

$$\left.\begin{aligned} \partial_z u_x = \partial_z u_y &= 0 \\ u_z &= 0 \\ \theta &= 0 \end{aligned}\right\} \quad \text{on} \quad z = 0 \quad \& \quad z = 1 \,. \tag{2.26}$$

The key dimensionless parameters describing the convection are the Rayleigh number (which measures the strength of convective driving to diffusive processes)

$$\mathrm{Ra} = \frac{-N^2 d^4}{\nu\kappa}\,, \tag{2.27}$$

and the Prandtl number (the ratio of viscous to thermal diffusion)

$$\mathrm{Pr} = \frac{\nu}{\kappa}\,. \tag{2.28}$$

We also define a scaled Rayleigh number

$$R = \frac{\mathrm{Ra}}{\mathrm{Ra}_c}\,, \tag{2.29}$$

where $\mathrm{Ra}_c = 27\pi^4/4$ is the critical Rayleigh number for the onset of convection in a horizontally-unbounded domain (in the absence of shear) with our adopted boundary conditions in the vertical (Chandrasekhar, 1961). In principle, the shear could affect the onset of convection, but we find no evidence that this occurs for the adopted values of a_0 (which are $a_0 \leq 1$).

With this non-dimensionalisation, according to mixing-length theory, the convective velocity in the limit of large Ra should be independent of the microscopic diffusivities, meaning that it should scale as $\sqrt{\mathrm{Ra}\,\mathrm{Pr}}$ (see aside 2.4), and therefore the dominant convective frequency (ω_c) should similarly scale as $\sqrt{\mathrm{Ra}\,\mathrm{Pr}}$. In the simulations, we will compute a convective frequency

$$\omega_c = \frac{\bar{u}_z^{\mathrm{rms}}}{d}\,, \tag{2.30}$$

where the overbar denotes a time average and we define the rms vertical velocity as

$$u_z^{\mathrm{rms}} = \sqrt{\langle u_z^2 \rangle}\,, \tag{2.31}$$

where angled brackets denote a volume average. We show that this is observed to scale as $\sqrt{\mathrm{Ra}\,\mathrm{Pr}}$, as expected, later in the text (Ch. 6, Fig. 6.1).

Aside 2.4: Convective velocity scaling

The scaling for the convective velocity can be crudely obtained from the following arguments. We first consider the dispersion relation (Chandrasekhar, 1961) in the limit of $\{\nu\,,\kappa\} \rightarrow 0$ which is

$$\sigma^2 = -N^2 \frac{k_\perp^2}{k^2}\,, \tag{2.32}$$

where σ is the growth rate of the convective instability, $k_\perp^2 = k_x^2 + k_y^2$ is the horizontal wavenumber and $k^2 = k_\perp^2 + k_z^2$. Considering $k_\perp^2 \gg k_z^2$ this gives

$$\sigma^2 \approx -N^2\,. \tag{2.33}$$

Now if we consider from our choice of nondimensionalisation that

$$\mathrm{Ra}\,\mathrm{Pr} = -\frac{N^2 d^4}{\nu\kappa}\frac{\nu}{\kappa} = -N^2\left(\frac{d^2}{\kappa}\right)^2 , \tag{2.34}$$

then[a], from eq. 2.33, we can write

$$\sigma \sim \sqrt{\mathrm{Ra}\,\mathrm{Pr}}\,, \tag{2.35}$$

which follows from the nondimensionalisation of eq. 2.33.
Next we consider the following relations

$$\mathbf{u}\cdot\nabla\mathbf{u} \sim \mathrm{Ra}\,\mathrm{Pr}\,\theta\mathbf{e}_z \implies \frac{u^2}{d} \sim \mathrm{Ra}\,\mathrm{Pr}\,\theta\,, \tag{2.36}$$

$$\frac{\partial\theta}{\partial t} \sim u_z \sim u \implies \sigma\theta \sim u \ . \tag{2.37}$$

The first of these (eq. 2.36) is from the momentum equation by considering a statistical steady state where the injection of energy (the growth of the instability due to the buoyancy term) is balanced by the transfer of energy down to smaller scales (the advective nonlinear term). The second expression (eq. 2.37) is obtained from the linearised temperature equation.
We now substitute for θ from eq. 2.37 into eq. 2.36 and then substitute for the growth rate σ using eq. 2.35. This gives $u \sim d\sqrt{\mathrm{Ra}\,\mathrm{Pr}}$ $(= \sqrt{\mathrm{Ra}\,\mathrm{Pr}}$ since $d = 1)$ as claimed.

---

[a] Note that $-N^2$ has units of T^{-2} and the fractional term is the square of our chosen nondimensional time (thermal time) and hence has units T^2 and so this is dimensionally consistent with the LHS of the expression.

In this work we will first explore laminar cases close to the onset of convection, with $R \leq 10$ and $\mathrm{Pr} = 1$, in order to understand the physics behind the interaction between tides and convection. An advantage of this laminar regime is that we can compare our results with a complementary asymptotic analysis. We then move on to explore more turbulent cases with $R \geq 100$, which are more relevant for convection in stars. However, in a Sun-like star we expect $\mathrm{Ra} \in [10^{21}, 10^{24}]$ and $\mathrm{Pr} \in [10^{-7}, 10^{-3}]$ in the convection zone (Hanasoge et al., 2016). Reaching such extreme parameter regimes with simulations (even those adopting the Boussinesq approximation) is unfeasible, and we are inevitably restricted to modest values of these parameters, such that $R \leq 10^4$ and $\mathrm{Pr} \gtrsim 10^{-2}$. We hope that our simulations can be used to understand the interaction between tides and convection in stars, but this inevitably requires us to extrapolate our results to the astrophysical parameter regime.

Summary: Model setup and assumptions

The system we wish to numerically integrate is

$$\frac{\partial\mathbf{u}}{\partial t} + \mathbf{u}\cdot\nabla\mathbf{u} + \mathbf{u}_0\cdot\nabla\mathbf{u} + \mathbf{u}\cdot\nabla\mathbf{u}_0 = -\nabla p + \mathrm{Ra}\,\mathrm{Pr}\,\theta\mathbf{e}_z + \mathrm{Pr}\nabla^2\mathbf{u}\,, \tag{2.38a}$$

$$\frac{\partial \theta}{\partial t} + \mathbf{u}\cdot\nabla\theta + \mathbf{u}_0\cdot\nabla\theta = u_z + \nabla^2\theta\,, \tag{2.38b}$$

$$\nabla\cdot\mathbf{u} = 0\,, \tag{2.38c}$$

$$\mathbf{u}_0 = \frac{a_0\omega x}{d}\cos(\omega t)\mathbf{e}_y\,, \tag{2.38d}$$

with the boundary conditions

$$\left.\begin{aligned} \partial_z u_x = \partial_z u_y &= 0 \\ u_z &= 0 \\ \theta &= 0 \end{aligned}\right\} \quad \text{on} \quad z=0 \quad \& \quad z=1\,, \tag{2.39}$$

and horizontal periodicity (shearing-periodic in x).

Some key features of this model are:

- We adopt the Boussinesq approximation (hence the flow is incompressible),
- We have non-dimensionalised using the thermal timescale, d^2/κ,
- The velocity field has been decomposed into a background shear flow (which acts as our tidal flow) and the convective flow, so that the total flow is, $\mathbf{u}^* = \mathbf{u}+\mathbf{u}_0$.

2.2 Numerics

We use a modified version of the Cartesian pseudo-spectral[8] (see aside 2.5 for justifications for using this numerical method) code SNOOPY for our simulations (Lesur & Longaretti, 2005; Lesur & Ogilvie, 2010). This uses a basis of shearing waves with time-dependent horizontal wavevector components to deal with the linear spatial variation of $\mathbf{u}_0$. This is equivalent to using shearing-periodic boundary conditions in x. In the y-direction we assume periodic boundary conditions, and in the vertical (z), variables are expanded as either sines or cosines so that they satisfy the boundary conditions given by eq. 2.26 (e.g. Cattaneo et al. 2003; Lesur & Ogilvie 2010). Flow variables are expanded such that

$$u_x(\boldsymbol{x},t) = \Re\Big(\sum_{k_x,k_y,n} \hat{u}_x(t)\mathrm{e}^{i\mathbf{k}_\perp(t)\cdot\boldsymbol{x}}\cos n\pi z\Big)\,, \tag{2.40}$$

where $\mathbf{k}_\perp(t) = (k_x(t),k_y)$, and the sum is over

$$k_i = \left\{\frac{2\pi k_i^*}{L_i} : k_i^* \in \left[\frac{-N_i}{2}, \frac{N_i}{2}-1\right]\cap\mathbb{Z}\right\} \tag{2.41}$$

and

$$n = \{n\in\mathbb{Z} : n = [0, N_z-1]\}, \tag{2.42}$$

---

[8] For a more detailed account of spectral methods see Trefethen (2000); Boyd (2001).

where N_i is the number of modes in each dimension and $i \in \{x, y\}$ denotes the dimension[9]. A similar expansion is used for $u_y(\boldsymbol{x}, t)$ and $p(\boldsymbol{x}, t)$, but we also have

$$[u_z(\boldsymbol{x},t),\theta(\boldsymbol{x},t)] = \Re\Big(\sum_{k_x,k_y,n}[\hat{u}_z(t),\hat{\theta}(t)]\mathrm{e}^{i\mathbf{k}_\perp(t)\cdot\boldsymbol{x}}\sin n\pi z\Big)\,. \tag{2.43}$$

Aside 2.5: Why spectral methods?

The foundations of spectral methods is the use of series expansions of the relevant quantities in order to solve (systems of) partial differential equations. The expansions take the form

$$f(x) \approx f_N(x) = \sum_{n=0}^{N} f_n \Upsilon_n(x)\,, \tag{2.44}$$

where $\Upsilon_n(x)$ are a set of N orthonormal basis functions and this approximation is exact in the limit of $N \to \infty$. Of course due to computational limitations N must be truncated to some finite value. In this formulation we have a set of basis functions $\Upsilon_n(x)$ which in spectral methods span the entire domain, that is, computation of any given point in the domain depends on the state of every other point in the domain. The spectral method algorithm then solves for the unknown basis coefficients f_n. The major strength of this comes from what is known as ‘spectral convergence’ which means that the approximations converge towards a solution more rapidly (for smooth solutions), for increasing N, than other commonly used methods[a] (finite element, finite volume, finite difference).

It is worth addressing some of the significant weaknesses of spectral methods.

Complex geometry: Due to the global nature of spectral methods this makes complex geometries at best difficult and at worst impossible. Simple cuboid shaped domains are suitable for spectral methods and so for the problem we are considering this is not an issue.

Basis functions choice: The choice of basis functions depends on the geometry and boundary conditions of the problem. In our problem we are considering horizontal periodic boundary conditions which can be dealt with efficiently with Fourier basis functions and application of the Fast Fourier Transform[b] (FFT) to deal with converting to and from spectral space. In the vertical our equations and boundary conditions admit a decomposition of the Fourier series basis functions such that the horizontal velocity components can be decomposed into a cosine series while the vertical velocity component and temperature perturbation takes the form of a sine series. This is known as a sine-cosine decomposition. Both of these basis types are computationally cheap.

Discontinuities/shocks: A significant problem with spectral methods occurs if the solution admits discontinuities (shocks). Such situations result in Gibbs instabilities (a type of numerical error) which do not die out as N increases (instead approaching a finite limit) and can result in divergence of computed quantities. Since we are considering

---

[9] In general we have N_x, N_x and N_x as the discrete resolution in the $\mathbf{e}_x$, $\mathbf{e}_y$ and $\mathbf{e}_z$ directions respectively.

subsonic flow this is of no concern for our problem.

Since the major weaknesses of spectral methods do not cause us problems due to our simple geometry, we can employ spectral methods and take advantage of the spectral convergence.

---

[a] The other commonly used numerical methods have polynomial convergence which is strictly slower than the exponential convergence (spectral) convergence of spectral methods.

[b] The FFT is typically attributed to the work of Cooley & Tukey (1965), however, efficient algorithms to compute Fourier co-efficients can be traced back to some unpublished work of the eminent mathematician Carl Friedrich Gauss (Heideman et al., 1985).

In order to account for the linearity in x of $\mathbf{u}_0$ (see aside 2.6), the horizontal wavevector evolves according to

$$\dot{\mathbf{k}}_\perp = -Sk_y\cos(\omega t)\mathbf{e}_x\,. \tag{2.45}$$

so that

$$k_x(t) = k_{x,0} - a_0 k_{y,0}\sin(\omega t)\,, \tag{2.46}$$

$$k_y(t) = k_{y,0}\,, \tag{2.47}$$

where

$$\mathbf{k}_\perp(t=0) = (k_{x,0}, k_{y,0})\,. \tag{2.48}$$

The code uses a 3rd order Runga-Kutta time-stepping scheme and deals with the diffusion terms using an integrating factor. To accurately integrate (and analyse) high-frequency shear, we impose an additional time-step constraint such that the timestep $\delta t \ll 1/\omega$ (in addition to the usual time-step constraint due to the CFL condition). Further details regarding the code can be found in e.g. Lesur & Longaretti (2005) or Lesur & Ogilvie (2010). The nonlinear terms are fully de-aliased using the 3/2 rule (Orszag, 1971; Boyd, 2001).

Aside 2.6: Why do we need time dependent wavevectors?

In our numerical formulation we have used time dependent wavevectors which may raise the question as to why add this complication. To answer this, consider the $\mathbf{e}_y$ component of the term $\mathbf{u}_0\cdot\nabla\mathbf{u}$ in eq. 2.25a,

$$u_0\left(\frac{\partial u_y}{\partial x}+\frac{\partial u_y}{\partial y}+\frac{\partial u_y}{\partial z}\right) = x\frac{a_0\omega\cos\omega t}{d}\left(\frac{\partial u_y}{\partial x}+\frac{\partial u_y}{\partial y}+\frac{\partial u_y}{\partial z}\right)\,, \tag{2.49}$$

which is linear in x. There are no other terms in eq. 2.25a with an x dependence and hence this term can not be simply balanced by another term without having a time-dependent $\mathbf{k}$. This in principle would not be a problem if it was not for our choice of horizontally periodic boundary conditions which this term does not satisfy! The solution is then to use time dependent wavevectors which in essence means the domain deforms with the shear[a].

This technique is often used in models of astrophysical discs subject to a Keplerian shear where it is known as a *shearing sheet*. In such cases the shear is non-oscillatory and so the domain gets continually stretched and there are techniques to deal with this problem. In our model the oscillatory nature of the shear means that this is less of a problem.

Note that a similar approach has been used by Barker & Lithwick (2013) to study the elliptical instability.

---

[a] A geometric description would be that our domain does not remain in the shape of a cuboid (right square prism) but is in general a rhombohedron (or more specifically a right rhombic prism).

2.3 Quantities of interest

In this section we detail the quantities which we will compute from our simulations. As a reminder, the dissipation as a result of the interaction between the tidal flow and convection is the quantity we are most interested in evaluating. In particular the frequency dependence of this form of dissipation.

2.3.1 Reynolds stress

We wish to explore the interaction between the background tidal flow $\mathbf{u}_0$ and convectively-driven flows. To do this we are essentially wanting to consider the energy transfer between the background flow and the convective motion and so we look at the energy equation. The energy equation can be obtained by applying $\mathbf{u}\cdot$ to the (dimensional) momentum equation eq. 2.23a and then taking the volume average, which gives, after some manipulation and applying our boundary conditions[10],

$$\frac{1}{2V}\int_V \frac{\mathrm{D}}{\mathrm{D}t}|\mathbf{u}|^2\,\mathrm{d}V = \frac{1}{V}\int_V \mathbf{u}\cdot\theta\mathbf{e}_z\,\mathrm{d}V - \frac{\nu}{V}\int_V |\nabla\times\mathbf{u}|^2\,\mathrm{d}V - \frac{1}{V}\int_V \mathbf{u}\cdot(\mathbf{u}\cdot\nabla)\mathbf{u}_0\,\mathrm{d}V\,. \quad (2.50)$$

The last term on the RHS is the energy transfer term we are interested in. It can be written as

$$\begin{aligned} -\frac{1}{V}\int_V \mathbf{u}\cdot(\mathbf{u}\cdot\nabla)\mathbf{u}_0\,\mathrm{d}V &= -\frac{1}{V}\int_V S u_x u_y \cos(\omega t)\,\mathrm{d}V \\ &= -\frac{S\cos(\omega t)}{V} R_{xy}(t)\,. \end{aligned} \quad (2.51)$$

The Reynolds stress, $R_{xy}(t)$, determines the energy transfer rate between the tidal (shear) flow and the convection, which can in principle operate in either direction (see Ogilvie & Lesur 2012 and aside 1.5), transferring energy from (to) the convection to (from) the shear, and is defined from eq. 2.51 as

$$R_{xy}(t) = \frac{1}{V}\int_V u_x u_y\,\mathrm{d}V\,, \quad (2.52)$$

where $V = L_x L_y d$ (and $d = 1$ with our non-dimensionalisation) is the volume of our domain. We are interested in the response of this Reynolds stress component at the frequency of the tidal forcing.

---

[10] The $\mathrm{D}_t|\mathbf{u}|^2$ can also be written as $\partial_t|\mathbf{u}|^2$ since $\mathbf{u}\cdot\nabla\mathbf{u}$ vanishes when applying our boundary conditions

2.3.2 Effective viscosity

We are most interested in exploring the effective viscosity ν_E, which can be related to the modified tidal quality factor Q' (see § 1.3), which quantifies the rate of energy transfer between the tidal and convective flows. The value of ν_E represents the viscosity that is required to produce the same energy transfer rate from/to the convective flow to/from the tidal flow as the simulated flow, which may be turbulent. Following Goodman & Oh (1997); Ogilvie & Lesur (2012); Braviner (2015), we may define ν_E by equating the mean rate at which the shear does work on the flow with the mean rate at which energy is dissipated by a viscosity ν_E acting on the background tidal flow.

The mean rate at which the shear does work on the flow can be obtained from the volume averaged energy equation ($\mathbf{u}\cdot$ of eq. 2.23a) by considering the term

$$-\frac{1}{V}\int_V \mathbf{u}\cdot(\mathbf{u}\cdot\nabla)\mathbf{u}_0\,\mathrm{d}V = -\frac{1}{V}\int_V S u_x u_y \cos(\omega t)\,\mathrm{d}V\,. \tag{2.53}$$

For the mean rate at which the energy is dissipated by viscosity we consider the volume averaged energy equation for eq. 2.22d ($\mathbf{u}_0\cdot$ of this equation). The term we are interested in is the dissipation term

$$\frac{2\nu}{V}\int_V e^0_{ij}e^0_{ij}\,\mathrm{d}V = \frac{2\nu_{\text{mol}}}{V}\int_V e^0_{ij}e^0_{ij}\,\mathrm{d}V + \frac{2\nu_E}{V}\int_V e^0_{ij}e^0_{ij}\,\mathrm{d}V\,, \tag{2.54}$$

where we have split the dissipation of the background flow into a molecular and turbulent term ($\nu = \nu_{\text{mol}} + \nu_E$) and

$$e^0_{ij} = \frac{1}{2}(\partial_i u_{0,j} + \partial_j u_{0,i})\,, \tag{2.55}$$

is the rate-of-strain tensor for the background flow. The turbulent viscosity in the background can then be written, after application of a few vector identities and the boundary conditions, as

$$\begin{aligned}\frac{2\nu_E}{V}\int_V e^0_{ij}e^0_{ij}\,\mathrm{d}V &= -\frac{\nu_E}{V}\int_V |\nabla\times\mathbf{u}_0|^2\,\mathrm{d}V\\ &= -\nu_E\dot{a}^2\,,\end{aligned} \tag{2.56}$$

where $\nabla\times\mathbf{u}_0$ is the vorticity of the background flow (note that given our shear[11] that $|\nabla\times\mathbf{u}_0|^2 = \dot{a}^2$). We now assume that the energy transfer between the background flow and the convective turbulence is entirely dissipated by the effective viscosity. As such we can equate eq. 2.53 and eq. 2.56 to obtain[12] the viscous balance as

$$\nu_E\dot{a}^2 = -\frac{1}{V}\int_V a_0\omega u_x u_y \cos(\omega t)\,\mathrm{d}V\,. \tag{2.57}$$

In order to eliminate the transient nature, particularly in turbulent cases, we take the time

---

[11] Reminder that our shear has the form $\mathbf{u}_0 = a_0\omega x\cos(\omega t)\mathbf{e}_y = \dot{a}x\mathbf{e}_y$.

[12] Note that both of these terms appear on the same side of the full system and so when they are equated this introduces a sign change for one of them.

average over many cycles[13] and average to give

$$\frac{\nu_E}{(T-T_0)}\int_{T_0}^{T}\dot{a}^2\,\mathrm{d}T = -\frac{a_0\omega}{(T-T_0)}\int_{T_0}^{T}\cos(\omega t)\frac{1}{V}\int_V u_x u_y\,\mathrm{d}V\,\mathrm{d}T\,, \tag{2.58}$$

$$\nu_E\frac{a_0^2\omega^2}{2} = -a_0\omega\int_{T_0}^{T}R_{xy}(t)\cos(\omega t)\,\mathrm{d}T\,, \tag{2.59}$$

$$\nu_E = -\frac{2}{a_0\omega}\int_{T_0}^{T}R_{xy}(t)\cos(\omega t)\,\mathrm{d}T\,, \tag{2.60}$$

where we have used

$$\lim_{(T-T_0)\to\infty}\int_{T_0}^{T}\dot{a}^2\,\mathrm{d}T = \frac{\omega}{2\pi}\int_0^{2\pi/\omega}\dot{a}^2\,\mathrm{d}T$$
$$= \frac{a_0^2\omega^2}{2}\,, \tag{2.61}$$

by using $T = 2\pi/\omega$. Note that T_0 is some appropriate initial time and $T - T_0$ is (strictly) an integer number of periods of the shear flow $2\pi/\omega$.

For clarity, the effective viscosity at the frequency of the shear can be evaluated by computation of

$$\nu_E(\omega) = \frac{-2}{a_0\omega(T-T_0)}\int_{T_0}^{T}R_{xy}(t)\cos(\omega t)\,\mathrm{d}t\,. \tag{2.62}$$

This gives the response that is out of phase with the tidal displacement (and in phase with the tidal shear). In our more turbulent simulations we will typically integrate for hundreds or thousands of tidal periods to get well-converged values for ν_E, and $T - T_0$ will not necessarily be taken to be an integer number of tidal periods. In practice we compute the integral in eq. 2.62 as a cumulative integral[14] and then a linear fit is taken. A more thorough description of this process can be found in aside 2.7.

Aside 2.7: Evaluation of cumulative integrals and error

To get converged results for $\nu_E(\omega)$, it is important to integrate these simulations for long enough. In order to check this we plot the integral that arises in the expression for ν_E (eq. 2.62) for various end times T, excluding terms outside of the integral, and plot its variation with time T. We then determine the linear regression line for this quantity over a time interval, $[T_0, T]$, such that the exponential convective growth phase is omitted (thus $T_0 > 0$). This linear fit provides the value of the integral in eq. 2.62, allowing ν_E to be calculated. We evaluate error bars conservatively at 2σ (where σ is the standard deviation) from the regression line.
The same technique is used for the elasticity which is defined in § 2.3.4 where the integral in question is that in eq. 2.73.

In the limit of low frequencies (and small a_0) the tidal flow becomes quasi-steady as the tidal period becomes very long compared with the convective timescale, and so ν_E might be

---

[13] In principle, laminar cases could be averaged over a single cycle. However, it is technically easier to average over many cycles.

[14] The integral is computed as a time series where the time variable is the end time T.

thought to represent represent the "eddy viscosity" of convection, and we therefore expect it to scale as a convective velocity multiplied by a length-scale, as predicted by mixing-length theory. This would give the prediction[15], $\nu_E \propto \sqrt{\mathrm{Ra}\,\mathrm{Pr}}$ for $\omega \ll \omega_c$. We will explore the frequency dependence of ν_E, as a function of ω/ω_c. Note that ν_E can be related to the potential Love number or (modified) tidal quality factor Q', and is therefore the most relevant quantity for tidal dissipation. We will discuss this later in Ch. 7 and 8. For example, the orbital period derivative $\dot{P}/P$ due to tidal dissipation is proportional to ν_E. The effective viscosity is related to the misalignment angle between the tidal bulges and the line of centres of the star and planet.

2.3.3 Scaled effective viscosity

When the tidal frequency is much smaller than the convective frequency, $\omega \ll \omega_c$, the effective viscosity is often calculated using $\nu_E^{\mathsf{mlt}} \propto u^{\mathsf{mlt}} l^{\mathsf{mlt}}$, where u^{mlt} is the convective velocity (which is typically some relevant statistic of the vertical/radial component of velocity), l^{mlt} is the mixing length (in stellar convection this is typically a multiple of the pressure scale height, see § 1.3.2) and there exists a constant of proportionality. In our simulations, we define this constant of proportionality so that

$$\alpha = \frac{\nu_E}{u_z^{\mathsf{rms}} d}\,, \tag{2.63}$$

which we will determine in simulations. Note that this strictly differs from the usual mixing-length "α" parameter, since it combines the usual parameter with the coefficient involved in converting $u^{\mathsf{mlt}} l^{\mathsf{mlt}}$ to a viscosity – which is commonly assumed to be 1/3 without rigorous justification. Eq. 2.63 will be of most use in Ch. 6.

2.3.4 Effective elasticity

It can be shown (e.g. Ogilvie & Lesur 2012 and § 4.2) that the fluid responds viscoelastically to high-frequency shear, and that the dominant response is elastic (with a weaker viscous component). To explore this component, and to compare with asymptotic theories (in Ch. 4), we will also compute the effective elasticity of the flow. This is less directly relevant for tidal dissipation than the effective viscosity, but is important for quantifying the amplitude of the tidal response, and could be important for e.g. modifying the rates of non-dissipative tidally-driven apsidal precession. We can obtain an effective elasticity S_E by considering the ratio of tidal shear stress to shear strain, which is a measure of the deformation (e.g. Braviner 2015).

In solid mechanics the shear modulus (also known as the modulus of rigidity) is defined as[16]

$$G_{\mathsf{rig}} = \frac{\tau_{xy}}{\gamma_{xy}} = \frac{F/A}{\Delta x/l}\,, \tag{2.64}$$

where τ_{xy} is the shear stress, defined as the ratio of force F over area A, and γ_{xy} is shear strain, defined as the ratio of transverse displacement Δx to non-sheared length l. Analogous quantities for our fluid problem can be evaluated in order to quantify the effective (fluid) elasticity.

---

[15] If we consider MLT we have, $\nu_E \propto u^{\mathsf{mlt}} l^{\mathsf{mlt}}$ (see §. 1.3) which on replacing the mixing-length velocity using $u^{\mathsf{mlt}} \sim \sqrt{\mathrm{Ra}\,\mathrm{Pr}}$ (see aside 2.4) we get $\nu_E \propto \sqrt{\mathrm{Ra}\,\mathrm{Pr}}$.

[16] In solid mechanics this is thought of as a real valued quantity, unlike the complex shear modulus we use in the asymptotic theory described in Ch. 4.

The typical displacement is related to the shear velocity through integration and considering the displacement only around the mean, that is

$$\begin{aligned} \mathbf{u}_0 =& \dot{a}(t)x\mathbf{e}_y\,, && (2.65)\\ \implies \Delta x \propto \int \mathbf{u}_0\,\mathrm{d}t =& \int \dot{a}x\mathbf{e}_y\mathrm{d}t = (a(t)x + C_1)\mathbf{e}_y\,, && (2.66)\end{aligned}$$

for some arbitrary constant C_1. Thus we have that the typical displacement magnitude $\Delta x \propto a$ about x. We also consider the non-sheared length-scale to be the domain size in the direction of the transverse displacement, that is $l = L_x$. Hence we have for the fluid strain $\gamma_{xy} = a/L_x$.

Aside 2.8: Alternative methods for evaluating ν_E and S_E

An equivalent way of evaluating ν_E and S_E is by using the Fourier transform of $R_{xy}(t)$ (Ogilvie & Lesur, 2012) as

$$\begin{aligned} \nu_E(\omega) &= \Re\left(\frac{\hat{R}_{xy}(\omega)}{S\pi}\right)\,, && (2.67)\\ S_E(\omega) &= \Im\left(\frac{\hat{R}_{xy}(\omega)}{a_0\pi}\right)\,, && (2.68)\end{aligned}$$

where we select the value of the Fourier transformed quantity at the shear frequency. We prefer to use the integral forms given above, since we found this alternative approach to be very sensitive to the precise frequencies chosen, and the numerical errors obtained were considerably larger, even if they should be formally equivalent.

The shearing force is applied along x and so the surface area of the application of the tidal force is L_yL_z. It is left to determine the force term F. To do this we consider the rate at which the force does work on the flow, $FL_x\dot{a}$, and relate it to the rate at which the shearing term does work on the flow $-\dot{a}R_{xy}L_xL_yL_z$. Equating these two quantities gives

$$\begin{aligned} FL_x\dot{a} =& -\dot{a}R_{xy}L_xL_yL_z\,, && (2.69)\\ \implies F =& -R_{xy}L_yL_z && (2.70)\end{aligned}$$

and so we get for the effective shear modulus, which is related to G_{rig}, as

$$S_E = \frac{-R_{xy}L_yL_z}{L_yL_za(t)} = -\frac{R_{xy}}{a(t)}\,. \qquad (2.71)$$

To evaluate eq. 2.71 we multiply this through by a^2 and time average over one cycle, noting that $a = -a_0\sin(\omega t)$, and make use of

$$\begin{aligned} \lim_{(T-T_0)\to\infty} a_0^2\int_{T_0}^{T}(\sin(\omega t))^2\,dt &= -\frac{a_0^2\pi}{\omega}\\ &= -\frac{a_0^2T}{2}\,, && (2.72)\end{aligned}$$

to get

$$S_E(\omega) = -\frac{2\int_{T_0}^{T} R_{xy}\sin(\omega t)\,\mathrm{d}\,t}{a_0(T-T_0)}\,, \tag{2.73}$$

which we will also compute in our simulations. This measures the response that is in phase with the tidal displacement (out of phase with the tidal shear). Note that, in the same way as for the effective viscosity, in our simulations we will evaluate S_E by using a large time interval $T - T_0$ such that these quantities are adequately converged (see aside 2.7).

Summary: What we wish to compute

The quantity we are most interested in computing is the dissipation of tidal energy in this model. This has been defined as (§. 2.3.2)

$$\nu_E(\omega) = \frac{-2}{a_0\omega(T-T_0)}\int_{T_0}^{T} R_{xy}(t)\cos(\omega t)\,\mathrm{d}t\,. \tag{2.74}$$

We will also be interested in computation of the effective elasticity (which will be useful for comparisons with the asymptotic computations, see Ch. 3 and 4). This is defined as (§. 2.3.4)

$$S_E(\omega) = -\frac{2\int_{T_0}^{T} R_{xy}\sin(\omega t)\,\mathrm{d}\,t}{a_0(T-T_0)}\,. \tag{2.75}$$

The computation of both of these requires the calculation of the volume averaged Reynolds stress defined as (§. 2.3.1)

$$R_{xy}(t) = \frac{1}{V}\int_V u_x u_y\,\mathrm{d}V\,. \tag{2.76}$$

In Ch. 6 we will find it useful to define the scaled effective viscosity (§. 2.3.3)

$$\alpha = \frac{\nu_E}{u_z^{\mathsf{rms}} d}\,, \tag{2.77}$$

to allow comparison with MLT.
It is also important to note our definition of the convective velocity (§. 2.1.3)

$$\omega_c = \frac{\bar{u}_z^{\mathsf{rms}}}{d}\,, \tag{2.78}$$

where the overbar denotes a time average and we define the rms vertical velocity as

$$u_z^{\mathsf{rms}} = \sqrt{\langle u_z^2\rangle}\,. \tag{2.79}$$

Chapter 3

Interaction between tides and laminar convection in small domains

Contents

In this chapter, we will explore results from the model described in Ch. 2. For now we will focus on laminar convection which can be loosely defined as having a Rayleigh number Ra close to the onset number Ra_c (so R close to 1). Another way of thinking about this is that the resulting flow will be non-turbulent and so is not expected to exhibit a Kolmogorov cascade. These results will also be compared with a complementary asymptotic analysis which will be described in Ch. 4.

The purpose of exploring laminar convection is primarily to explore the simplest cases first, which we can complement with analytical theory. With this approach we can gain insight into the fundamental fluid dynamical behaviour of the interaction between our prescribed oscillatory (tidal) flow and the convection. We then build on this by considering more turbulent cases (in small domains) in Ch. 5.

3.1 Parameter survey

In this chapter we will vary the scaled Rayleigh number which measures the strength of the convection, in the range $1 < R \leq 10$. The amplitude a_0 varies from 0.01 to 0.1, but with these small values the shear does not affect the convection significantly. The tidal frequency ω is varied over a wide range, $0.1 \leq \omega \leq 10^4$. Unless otherwise stated we will take the dimensions of the box to be[1] $(L_x, L_y, 1) = (2, 2, 1)$, though L_x and L_y will be varied in a number of cases below. In all simulations in this chapter we have set $\mathrm{Pr} = 1$. The initial conditions will be small amplitude, solenoidal, homogeneous random noise for the velocity field. This is initialized using the system clock so that each simulation has unique initial conditions (to high probability).

---

[1] As a reminder, the layer depth d is our unit of length, § 2.1.3.

3.2 Laminar convection with $R = 2, 5$ and 10

We begin our investigation by exploring the interaction between tidal flows and laminar convection with $R = 2, 5$ and 10. Chandrasekhar (1961) shows that with our stress-free boundaries the critical Rayleigh number for the onset of convection is $\mathrm{Ra}_c = 27\pi^4/4$ with a critical wavenumber of $\pi/\sqrt{2}$. Because of our small shear amplitudes, this is not significantly changed when the shear is added. By considering the critical Rayleigh number for each mode (e.g. Chandrasekhar 1961), we can show that the modes that are first unstable with $L_x = L_y = 2$ have the vertical wavenumber $n = 1$ and are 2D y-aligned rolls with $n_x = \pm 1, n_y = 0$ or 2D x-aligned rolls with $n_x = 0, n_y = \pm 1$ (these modes first onset when $R \gtrsim 1.05$), where we have defined integers n_x and n_y by taking $n_x = 2\pi n_x/L_x$ and $n_y = 2\pi n_y/L_y$. With the larger box $L_x = L_y = 4$, convection occurs when $R > 1$ by exciting 3D modes with $n_x = \pm 1$ and $n_y = \pm 1$ (which have a horizontal wavenumber magnitude of $\pi/\sqrt{2}$). The advantage of simulating laminar convection when only a small number of modes are unstable is that it allows us to explore the dependence of the effective viscosity on the nature of the flow most easily. We can also compare our results with a complementary asymptotic analysis (see Ch. 4). As R is increased, additional modes become linearly unstable.

3.2.1 Rolls aligned with y with $L_x = L_y = 2$

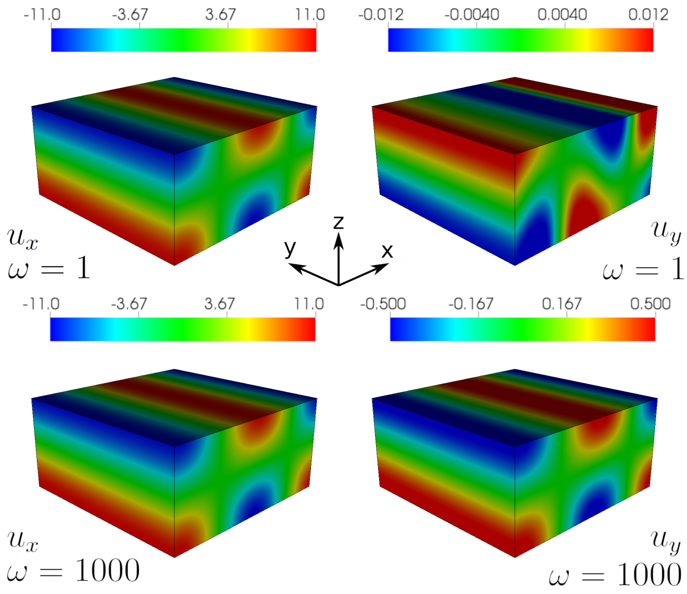

Figure 3.1: Flow structure for y-aligned rolls in a snapshot with $R = 2$, with $\omega = 1$ and $\omega = 1000$ (top and bottom respectively), both with $a_0 = 0.05$. The plotted quantities are u_x (left) and u_y (right). Note that only u_y differs noticeably between low and high-frequency cases.

We first select simulations with initial conditions such that 2D y-aligned convection rolls are preferentially excited, which saturate nonlinearly with an approximately steady amplitude. These simulations were performed with a resolution of at least $(N_x, N_y, N_z) = (64, 64, 16)$, which was found to be adequate. In the absence of shear, such a linear mode would have nonzero u_x and u_z velocity components (but $u_y = 0$) and be independent of y. The shear (plus weak nonlinearity) induces an additional oscillatory u_y component of the velocity, which is typically much smaller than that of the unperturbed convection roll. We present the horizontal flow structure for u_x and u_y in a snapshot from two simulations with $R = 2$, with $\omega = 1$ (top panels) and $\omega = 1000$ (bottom panels) in Fig. 3.1 at times $t = 100$ and 29.9, respectively. In these simulations the convective frequency $\omega_c \approx 5.5$ (see eq. 2.30) which means that $\omega = 1$ is in the low-frequency regime ($\omega/\omega_c < 1$), and $\omega = 1000$ is in the high-frequency regime

($\omega/\omega_c \gg 1$). The shear does not strongly modify the convection in these simulations, and u_x is similar in both cases. On the other hand, the spatial structure of u_y differs between the low and high-frequency regimes, as shown in the right panels of Fig. 3.1, indicating that we might expect the Reynolds stresses to differ. The flow is qualitatively similar in simulations with $R = 5$ and 10.

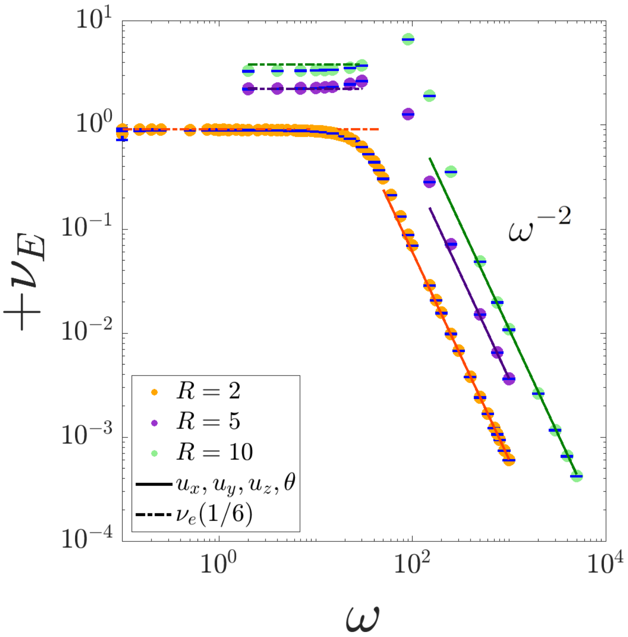

Figure 3.2: Frequency-dependence of $\nu_E(\omega)$ for laminar y-aligned convection rolls with $R \in \{2, 5, 10\}$, indicating that ν_E is reduced at high frequencies such that $\nu_E \propto \omega^{-2}$. The mixing-length theory prediction for ν_E, with a constant of proportionality of $1/6$, such that $\nu_E = \frac{1}{6}\nu_e$, is plotted as the horizontal line, which matches the data for low frequencies. We also plot the prediction from an independent asymptotic analysis (Ch. 4) as the solid lines at high frequency. These are all proportional to ω^{-2} and are in excellent agreement with the data. Error bars for ν_E are plotted, but these are very small since the flow is laminar.

We compute ν_E using eq. 2.62, and this is plotted as a function of ω for these simulations with $R = 2, 5$ and 10 in Fig. 3.2. Each value of R exhibits two distinct behaviours. For $\omega < 20$ i.e. "low frequencies", we find ν_E to be independent of ω. For $\omega > \{30, 90, 200\}$ (for $R = 2, 5, 10$, respectively), we find that the effective viscosity is reduced and decays with frequency such that $\nu_E \propto \omega^{-2}$. This matches the results of Ogilvie & Lesur (2012) for homogeneous convection and Braviner (2015) for ABC flow. In Ch. 4 we provide an asymptotic analysis which explains why laminar convection gives $\nu_E \propto \omega^{-2}$. We also provide a simpler mathematical derivation of this result for steady y-aligned rolls in Ch. 4. Such a high-frequency scaling is in accordance with Goldreich & Nicholson (1977), but their model was based on Kolmogorov turbulence rather than laminar flow (see § 1.3.3), and it disagrees with Zahn (1966) (see § 1.3.2). Note that the amplitude of the u_y component increases with ω (e.g. Fig. 3.1), following the behaviour of the oscillatory shear flow $\mathbf{u}_0$, but this component becomes increasingly in phase with the tidal displacement at high frequencies, thereby reducing ν_E. On this figure, we have included simulations with several different values of $a_0 = \{0.01, 0.02, \ldots, 0.09, 0.1\}$, but these are not highlighted in the figure since our results were observed to be independent of a_0 for these values. This is consistent with us probing the regime of linear tides.

Note that in laminar simulations with small R, we find that calculating the integral in eq. 2.62 directly gives similar results to the technique described[2] (and more specifically aside 2.7). The reason for this is the variation in the cumulative integral about the regression line[3] for laminar cases has magnitude proportional to ω^{-1} for $\omega > \omega_c$ or to a_0 for $\omega < \omega_c$ (which in both cases

---

[2] In more turbulent runs with larger R the approach in § 2.3.2 in § 2.3.2 was found to give cleaner results.

[3] Note that the variation in the cumulative integral about the regression line for S_E does not have any clear trend. However, the variation is found to also be small.

is small).

For low frequencies, and in particular as $\omega \to 0$ such that the tidal shear becomes quasi-steady, we expect ν_E to be approximated well by the mixing-length theory of convection if the flow is turbulent, i.e. by $\nu_E \propto \nu_e = u^{\mathrm{mlt}}\ell$. We define ν_e to be an effective viscosity from MLT (without any constant multiplicative factors), u^{mlt} to be the mixing-length velocity, which we can approximate by $u^{\mathrm{mlt}} \approx \bar{u}_z^{\mathrm{rms}}$, defined in eq. 2.31, after a suitable time averaging, and $\ell \sim d$ is a length-scale. We also expect $\nu_e \propto u^{\mathrm{mlt}} \propto \sqrt{\mathrm{Ra}\,\mathrm{Pr}}$ (see aside 2.4) when $R \gg 1$. Even in laminar convection, where we might not expect mixing-length theory to apply, we find the simulations to be described very well by $\nu_E \approx \frac{1}{6}\nu_e$ for $\omega \lesssim \omega_c$, as is shown in Fig. 3.2. Note that a frequency-independent ν_E is consistent with a constant tidal lag-time for this tidal component (e.g. Alexander 1973; Mignard 1980; Hut 1981, also see § 1.3.1).

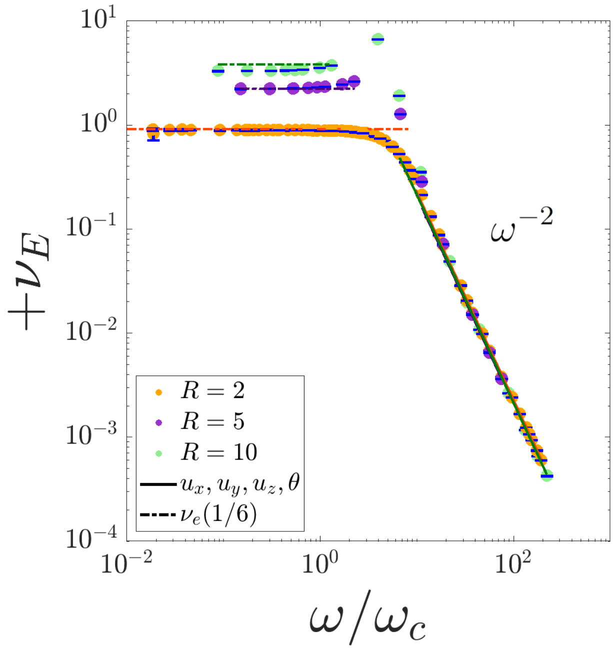

Figure 3.3: Same as Fig 3.2, showing $\nu_E(\omega)$ for laminar convection with $R = 2, 5, 10$, but with frequencies scaled by the convective frequency, ω_c. This clearly highlights the transition from frequency-independent ν_E to $\nu_E \propto \omega^{-2}$ occurs when $\omega \approx 5\omega_c$ in these cases.

In Fig. 3.2, to conveniently separate results with different R, the unit of time is kept as the thermal timescale for both the x and y axes, therefore cases with larger R values have larger convective velocities and frequencies in these units, and we expect the ν_E to increase with R. In Fig. 3.3, we instead scale frequencies with a convective frequency ω (without re-scaling the y-axis), where $\omega_c = \bar{u}_z^{\mathrm{rms}}/d$ where $\bar{u}_z^{\mathrm{rms}}$ is the time-averaged rms value of u_z (see § 2.1.3). This figure shows clearly that the transition from constant ν_E to $\nu_E \propto \omega^{-2}$ occurs when $\omega \approx 5\omega_c$. Note that there is also an enhancement in ν_E for $\omega \approx \omega_c$ in the simulations with $R = 5$ and 10.

For high frequencies such that $\omega \gtrsim \omega_c$, we expect the rapid oscillatory nature of the tidal shear to inhibit the effective viscosity. In Ch. 4, we present an asymptotic linear analysis using the method of multiple scales to calculate ν_E (and S_E) in the high-frequency regime in which $\omega \gg \omega_c$. This calculation builds upon prior work by Ogilvie & Lesur (2012) by extending their formalism so that it applies to Rayleigh-Bénard convection. For further details of how the asymptotic method is applied see § 4.2.

The asymptotic analytical prediction is shown as the solid lines at high ω in Figs. 3.2 and 3.3. The theory is in excellent agreement with our simulations for each R value considered.

For y-aligned rolls, we also obtain good agreement between each of the methods of evaluating the magnitudes of the velocity components. This provides an independent check that our simulations are correctly probing the high-frequency regime.

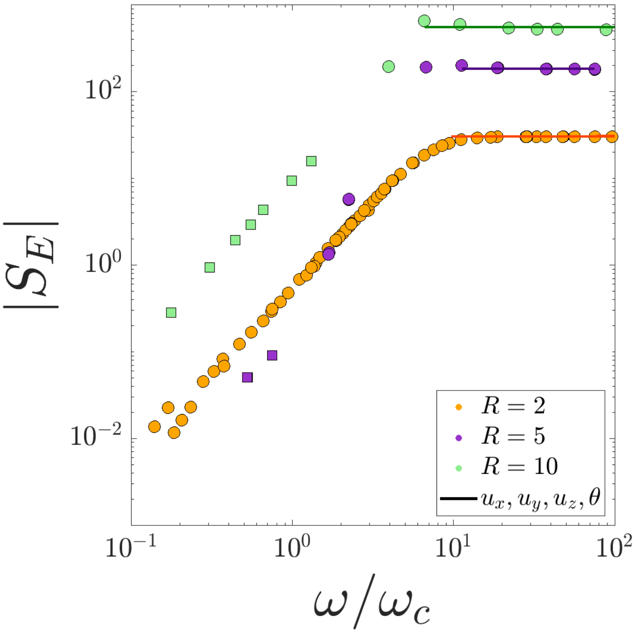

Figure 3.4: Frequency-dependence of $S_E(\omega)$ for laminar y-aligned convection rolls with $R \in \{2, 5, 10\}$, where frequencies have been scaled by the convective frequency, ω_c. Theoretical predictions of S_E for $\omega \gg \omega_c$ are computed using the theory presented in Ch. 4 and are plotted here as solid lines. Square symbols denote negative values of S_E while circles denote positive values. We have omitted error bars since they are small, but they typically fit within the symbol plotted except for small ω ($\omega/\omega_c \lesssim 0.1$).

We show the corresponding results for the effective elasticity (eq. 2.3.4), S_E, in Fig. 3.4, where we have scaled frequencies by the convective frequency. We find that $S_E \propto \omega^{1.77}$ for $\omega \lesssim 5\omega_c$, which is an empirical scaling, with a transition to a frequency-independent S_E for $\omega \gtrsim 5\omega_c$. This frequency independence is in qualitative agreement with the findings of Braviner (2015) for the related problem of ABC flow. The value of S_E in the high-frequency regime from the theoretical prediction in Ch. 4 is shown as the solid lines. Error bars are omitted from this figure for clarity. As with ν_E we observe that S_E is independent of a_0 for the values of a_0, R and ω simulated here (so we do not explicitly show this). One interesting feature is that for $R \in \{5, 10\}$ we observe a statistically significant sign change in S_E, going from negative at low ω to positive at high ω, at $\omega \approx \omega_c$, which does not occur for $R = 2$. We have also observed that S_E appears to transition from increasing with ω to being flat at approximately the same frequency (as opposed to scaled frequency ω/ω_c) in each case. The case with $R = 5$ is intermediate between the case with $R = 2$, where S_E is always positive, and the case with $R = 10$, which exhibits a change in sign. As a consequence we observe a more pronounced transition between positive and negative values for $R = 5$.

Note that $S_E \gg \nu_E$ at high frequencies, emphasizing that the response is primarily elastic, with a weaker viscous component.

3.2.2 Rolls aligned with x with $L_x = L_y = 2$

In this section we analyse similar simulations to § 3.2.1 except that the initial conditions select x-aligned convection rolls[4]. For these cases we use the same box size and set of R values but the resolution is chosen to be $(N_x, N_y, N_z) = (64, 64, 32)$, which was found to be sufficient

---

[4] The amplitude of the corresponding mode in the initial conditions determines which roll orientation is selected.

in all cases. In the absence of shear such linear convection solutions would have nonzero u_y and u_z velocity components, with $u_x = 0$, and they would saturate nonlinearly with a steady amplitude. The flow is similar to that shown in Fig. 3.1 except that the roll is aligned with x rather than y. The u_x component behaves differently in the high and low frequency cases however.

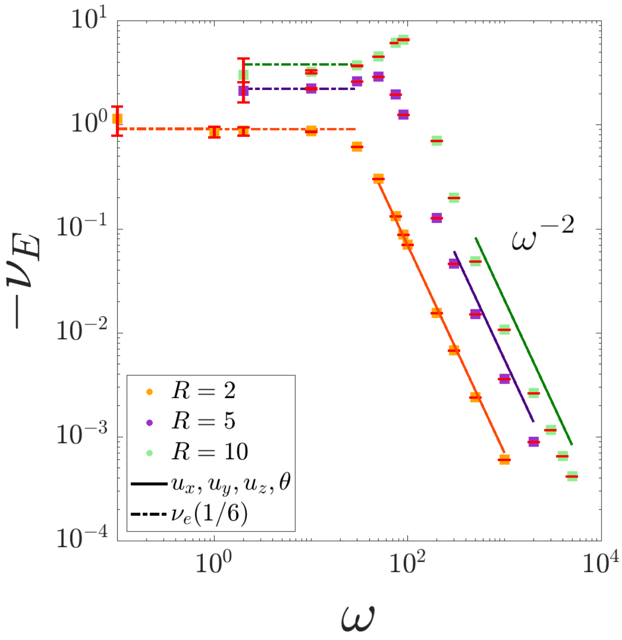

Figure 3.5: Frequency-dependence of $\nu_E(\omega)$ for laminar x-aligned convection rolls with $R \in \{2, 5, 10\}$. This demonstrates the surprising result that ν_E is negative in these cases. ν_E is also reduced at high frequencies such that $\nu_E \propto \omega^{-2}$. The mixing-length theory prediction for $|\nu_E|$, with a constant of proportionality of $1/6$, such that $|\nu_E| = \frac{1}{6}\nu_e$, is plotted as the horizontal line, which matches the magnitude of the data for low frequencies. We also plot the prediction from an independent asymptotic analysis (Ch. 4) as the solid lines at high frequency, which confirms our observation of negative ν_E. These predictions are proportional to ω^{-2} and are in excellent agreement with the data. Error bars for ν_E are plotted, but these are very small in most cases as the flow is laminar.

We show ν_E as a function of ω (not scaled by ω_c so as to separate data with different R) in Fig. 3.5, using the same method as for the y-aligned simulations in the previous section. The most surprising feature is that ν_E is negative for all ω. This indicates that the convective flow is transferring energy to the tidal flow. Negative values were previously obtained in the (more turbulent) simulations of Ogilvie & Lesur (2012) (§ 1.3.4), though only at high frequency and with error bars that could not conclusively rule out positive values. Our results in Fig. 3.5 conclusively demonstrate that statistically significant negative values[5] are attained in laminar convection consisting of rolls aligned with x.

As in the previous section, the value of $|\nu_E|$ is approximately independent of frequency until $\omega \approx 5\omega_c$ (this is most clearly shown by scaling frequencies with ω_c, but we have omitted this figure to save space), above which it falls off with frequency such that $|\nu_E| \propto \omega^{-2}$. We have also analysed simulations with $R = 2$ in which we vary the tidal amplitude such that $a_0 \in \{0.0005, 0.005, 0.05\}$, finding that our results for ν_E (and S_E) are independent of a_0 for the simulated values.

As in the previous section, we have extended the theory of Ogilvie & Lesur (2012) to also apply to x-aligned convection rolls, as explained in Ch. 4. This allows us to independently

---

[5] We have also performed preliminary simulations to explore whether ν_E remains negative for very small ω, and we find some evidence of a possible transition to positive values for $\omega \lesssim 10^{-4}$, although exceptionally long run times were required and the error bars were large in these cases.

predict ν_E (and S_E) in the high-frequency regime by fitting the amplitude of the convection roll. Our results are shown as the solid lines in Fig. 3.5. These results are in good agreement with our simulation data, which provides independent confirmation of the negative values for ν_E, as well as the quadratic fall-off with ω. Note that the asymptotic prediction departs most strongly from the simulation results for $R = 10$, presumably because we have adopted a single mode in the analysis, which is no longer strictly applicable.

Figure 3.6: Frequency-dependence of $S_E(\omega)$ for laminar x-aligned convection rolls with $R \in \{2, 5, 10\}$, where frequencies have been scaled by the convective frequency, ω_c. The lines connect the data points with each value of R and highlight the sign change in S_E as ω is varied. Note that the high-frequency behaviour is not predicted according to the theory in Ch. 4, since it requires the computation of higher-order terms. In this plot negative (positive) values of S_E are denoted by red error bars on square symbols (blue error bars on round symbols).

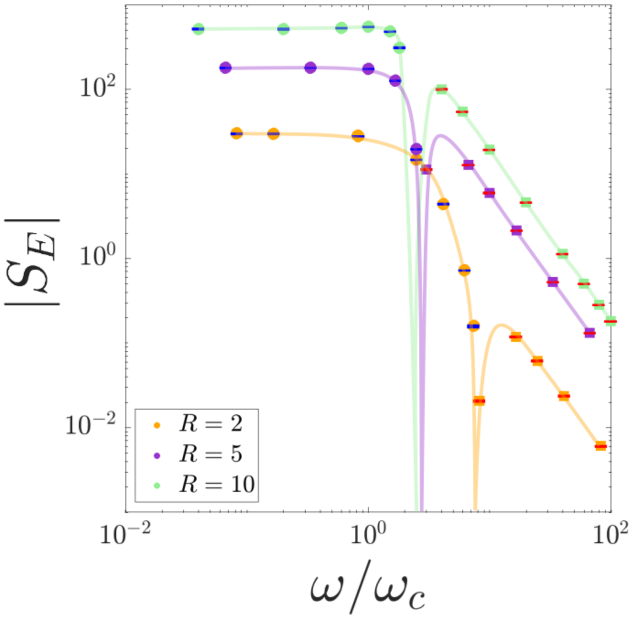

We show S_E as a function of ω in Fig. 3.6, where we have scaled the frequencies with ω_c. For y-aligned rolls, we previously found that S_E increased for small ω and was independent of frequency for large ω, similar to the results of Braviner (2015) for ABC flow (§ 1.3.4). However, for x-aligned rolls, we instead find S_E to be independent of frequency for small ω and to fall off rapidly with frequency such that $S_E \propto \omega^{-2}$ at high frequencies. For each of the R values considered, S_E also changes sign at a certain frequency, transitioning from positive at low ω to negative at high ω. This again differs from y-aligned rolls, where S_E was instead negative for small ω. In both x and y-aligned cases, S_E is negative when it is small and varying with ω, and is positive when it is larger in magnitude and independent of ω.

The asymptotic theory presented in Ch. 4 predicts $S_E = 0$, and so is unable to explain the high-frequency behaviour of S_E for x-aligned rolls shown in Fig. 3.6. However, this is consistent with our observation that $S_E \sim \omega^{-2}$ at high frequency, since this implies we must consider higher order terms (in ω^{-1}) to explain this with theory.

3.2.3 $R = 2$ with larger boxes such that $L_x = L_y = 4$

Our final set of simulations to explore the interaction between tidal shear and laminar convection have $R = 2$ but with a larger box such that $L_x = L_y = 4$ using a resolution of $(N_x, N_y, N_z) = (64, 64, 16)$. In this case, we expect multiple convective modes to be excited, including 3D modes with $n_x = \pm 1$, $n_y = \pm 1$ as well as the quasi-2D x and y-aligned convection rolls that we have studied in the previous two sections. Each mode is expected to provide its own contribution to the effective viscosity (and elasticity), which we can quantify

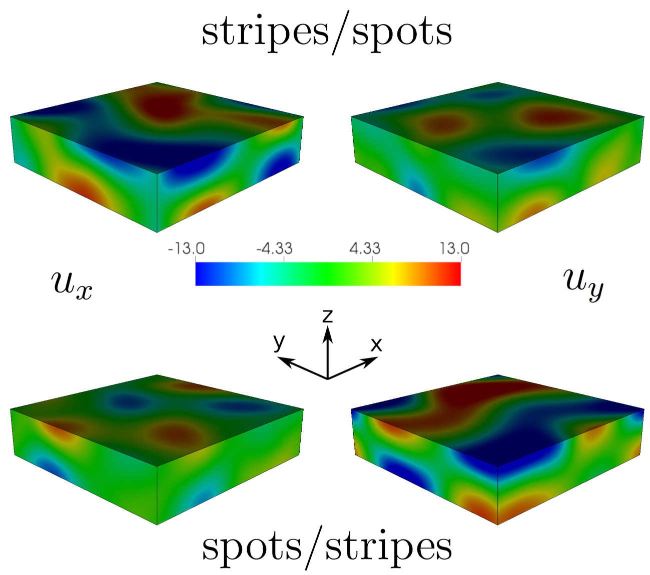

Figure 3.7: Snapshots of the flow for two cases with different initial conditions that we refer to as stripes/spots and spots/stripes (top and bottom, respectively) with $\omega = 1000$ at $t = 97$ and 290 (respectively). These have $R = 2$ and $(L_x, L_y, L_z) = (4, 4, 1)$. The plotted quantities are u_x (left) and u_y (right).

and compare with theory. Since 3D modes are preferentially excited in these cases, unlike those with $L_x = L_y = 2$, we can use this set of simulations to probe the contribution of 3D modes to ν_E.

We show a snapshot of u_x and u_y in two simulations with $\omega = 1000$ in Fig. 3.7, which indicates that the flow consists of a superposition of a number of convective modes. We explored different random initial conditions and determined that there were two main flow configurations, as shown in the top and bottom panels of this figure. We will refer to these as stripes/spots (corresponding to the patterns in u_x and u_y) and spots/stripes, respectively. These cases provide a more robust test of the asymptotic theory in Ch. 4, since many of the terms in the theory are identically zero when only an x or y-aligned convection roll is considered.

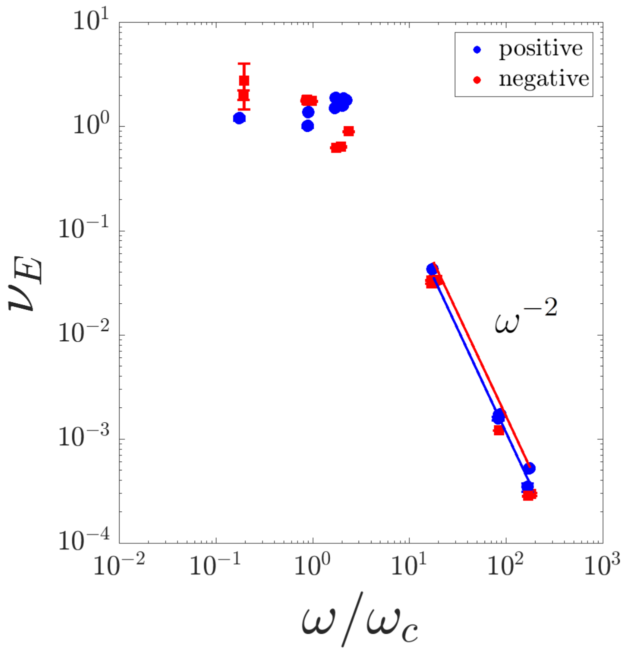

Figure 3.8: Frequency-dependence of $\nu_E(\omega)$ for laminar convection with $R = 2$ in a box with $L_x = L_y = 4$ for two different flow configurations. The asymptotic high-frequency prediction (shown as the solid lines), is computed by incorporating multiple modes in the theory in Ch. 4. We obtain very good agreement with the values and sign of ν_E in each case, corresponding with the two flows in Fig. 3.7, where the stripes/spots flow has $\nu_E > 0$ and spots/stripes flow has $\nu_E < 0$.

We show the frequency-dependence of ν_E for each of these cases in Fig. 3.8. As in § 3.2.1 and 3.2.2, both cases exhibit an approximately frequency-independent ν_E for $\omega \lesssim \omega_c$, and for

$\omega \gtrsim \omega_c$, $|\nu_E| \propto \omega^{-2}$. Interestingly, the different flow configurations shown in Fig. 3.7 exhibit different signs for ν_E, which remain the same for all ω. The case with stripes/spots (top panels of Fig. 3.7) has $\nu_E > 0$ for all ω and the case with spots/stripes (bottom panels of Fig. 3.7) has $\nu_E < 0$. This agrees with what we might expect based on § 3.2.1 and 3.2.2, since the stripes/spots flow contains a larger amplitude y-aligned roll component, and the spots/stripes flow contains a larger amplitude x-aligned roll component. These examples illustrate once more that for laminar convection, the effective viscosity can be negative.

We show our prediction for the high-frequency behaviour of ν_E as the solid lines in Fig. 3.8, where each of the two flow configurations have been treated separately. These agree well with the simulation data, and are found to correctly predict the magnitude and sign of ν_E in each case, such that the spots/stripes case is negative and the stripes/spots case is positive. The case with negative values is slightly less well predicted by theory, probably because this depends more strongly on the θ component of the flow, which is more strongly modified by nonlinearity.

These simulations agree with the asymptotic theory in Ch. 4 in cases where multiple modes contribute, and we have also shown that 3D laminar convection can exhibit a negative effective viscosity. Next, it is essential to determine how robust these results are to increasing R, allowing us to explore more turbulent convective flows.

3.3 Discussion

In this chapter we have presented an analysis of the frequency dependence of the effective viscosity and effective elasticity. For laminar convection with low R values for fixed Pr and with a domain sizes of $(L_x, L_y, L_z) = \{(2,2,1),(4,4,1)\}$.

We defer a more in depth discussion until after presentation of more turbulent convection in similarly sized domains, in Ch. 5.

Summary: Key findings

For laminar convection we find two quasi-stable flow configurations with either convective cells aligned in the $\mathbf{e}_y$ or $\mathbf{e}_x$ directions.

- $\mathbf{e}_y$ and $(L_x, L_y, L_z) = (2,2,1)$,
  - ν_E is constant for $\omega/\omega_c \lesssim 5$ (consistent with the constant time lag, § 1.3.1),
  - $\nu_E \propto (\omega/\omega_c)^{-2}$ for $\omega/\omega_c \gtrsim 5$ (consistent with the quadratic reduction model, § 1.3.3),
  - ν_E is strictly positive,
  - S_E is constant for $\omega/\omega_c \gtrsim 5$,
  - $S_E \propto (\omega/\omega_c)^{-1.77}$ $\omega/\omega_c \lesssim 5$.
- $\mathbf{e}_x$ and $(L_x, L_y, L_z) = (2,2,1)$,
  - ν_E is constant for $\omega/\omega_c \lesssim 5$ (consistent with the constant time lag, § 1.3.1),
  - $\nu_E \propto (\omega/\omega_c)^{-2}$ for $\omega/\omega_c \gtrsim 5$ (consistent with the quadratic reduction model, § 1.3.3),

  - ν_E is strictly negative,
  - S_E is constant for $\omega \lesssim 1$,
  - S_E follows a polynomial power law decay (which is close to, and might be, quadratic) for $\omega \gtrsim 1$.

- $(L_x, L_y, L_z) = (4, 4, 1)$,
  - two observed flow configurations (which we classify as stripes/spots and spots/stripes),
  - ν_E is constant for $\omega/\omega_c \lesssim 5$ (consistent with the constant time lag, § 1.3.1),
  - $\nu_E \propto (\omega/\omega_c)^{-2}$ for $\omega/\omega_c \gtrsim 5$ (consistent with the quadratic reduction model, § 1.3.3),
  - stripes/spots have $\nu_E > 0$ for all ω values explored,
  - spots/stripes have $\nu_E < 0$ for all ω values explored.

The asymptotic analysis performed in the following chapter (Ch. 4) is in good agreement with the high-frequency regimes ($\omega \gtrsim \omega_c$) for all cases, excluding S_E for $\mathbf{e}_x$ aligned rolls where higher orders are likely required to obtain quantitative agreement.

Chapter 4

Multi-scale asymptotic analysis

Contents

In this chapter we outline a simple description of the high-frequency ν_E scaling for $\mathbf{e}_y$ aligned rolls, which was discussed in Ch. 3. We will then go through the details of our extension to the more rigorous multi-scale asymptotic analysis of Ogilvie & Lesur (2012). Our goal is to provide further understanding and a complementary asymptotic analysis for the results of Ch. 3.

4.1 Simple derivation of ν_E scaling for y-aligned convection rolls

Here we provide a simple explanation (rather than the formal analysis we will go through in § 4.2) for why $\nu_E \propto \omega^{-2}$ for high-frequency shear in the specific case of y-aligned laminar convection rolls (as described in § 3.2.1). We consider the $\mathbf{e}_y$ component of the momentum equation (using the dimensionless variables described in Ch. 2),

$$\partial_t u_y = -S u_x \cos(\omega t) + \nabla^2 u_y - \mathbf{u}\cdot\nabla u_y - \mathbf{u}_0\cdot\nabla u_y - \partial_y p\,. \tag{4.1}$$

For a steady y-aligned roll, u_x is approximately time-independent, u_y is small in the absence of shear, and $\partial_y \approx 0$. For high-frequencies and laminar flows, the dominant balance in eq. 4.1 is (see aside 4.1)

$$\partial_t u_y \approx -S u_x \cos(\omega t), \tag{4.2}$$

which implies $u_y \approx -a_0 u_x \sin\omega t$, such that the response is primarily elastic (out of phase with the shear). We have confirmed that the amplitude of u_y matches this prediction, and is indeed approximately independent of ω in our simulations in this high-frequency regime. The resulting effective viscosity (eq. 2.62)

$$\nu_E \propto \frac{1}{\omega}\int \langle u_x u_y\rangle \cos(\omega t)\,\mathrm{d}t \tag{4.3}$$

therefore vanishes to leading order[1].

---

[1] Since the $\int \sin(\omega t)\cos(\omega t)\,\mathrm{d}t = 0$ when integrated over an integer number of cycles and $\langle u_x u_y\rangle \sim \langle u_x\rangle\langle u_y\rangle$ since $\langle u_x\rangle$ is constant.

Aside 4.1: Dominant balance for high-frequency shear

In order to obtain the dominant balance in eq. 4.1 in the high-frequency regime we consider the following. Since the flow is laminar we can neglect the nonlinear term, since we are considering an $\mathbf{e}_y$ aligned roll there is no variation in this direction and so we can neglect the pressure term and the term which represents advection of u_y by the background. This leaves us with

$$\frac{\partial u_y}{\partial t} =\nu\nabla^2 u_y - S u_x \cos(\omega t)\,. \tag{4.4}$$

Let us consider the balance between the time derivative and the shear term, since these are the terms we claim are the dominant balance. We can then write

$$\frac{\partial u_y}{\partial t} = - u_x a_0 \omega \cos(\omega t)\,, \tag{4.5}$$

$$\int \frac{\partial u_y}{\partial t}\,\mathrm{d}t = - u_x a_0 \omega \int \cos(\omega t)\,\mathrm{d}t \tag{4.6}$$

$$\implies u_y \propto u_x a_0 \cos(\omega t - \pi/2)\,, \tag{4.7}$$

where we note that u_x can be treated as constant. First we note that this predicts that in the high-frequency limit that u_y does not depend on ω which is consistent with results from the simulations. We now have that $R_{xy} \propto u_y \propto \cos(\omega t - \pi/2)$ which predicts that in the high-frequency limit that the Reynolds stress is out of phase by $\pi/2$ with the shear and has been found to agree with results from the simulations.

In order to ensure that this balance is indeed the correct one for the high-frequency regime we must also consider the case when the viscous term balances with the shear. Let us consider

$$u_x S \cos(\omega t) = \nu \nabla^2 u_y\,, \tag{4.8}$$

and convert to Fourier space by using

$$u_y = \hat{u}_y e^{i(\mathbf{k}\cdot\boldsymbol{x})} \cos n\pi z \quad \text{and} \quad u_x = \hat{u}_x e^{i(\mathbf{k}\cdot\boldsymbol{x})} \cos n\pi z\,, \tag{4.9}$$

where $k_x = n\pi$ and we note that $\hat{u}_x$ is constant in time, to get

$$\hat{u}_x a_0 \omega \cos(\omega t) = - \nu k^2 \hat{u}_y\,, \tag{4.10}$$

$$\implies \hat{u}_y \propto \frac{a_0 \omega \hat{u}_x}{\nu k^2} \cos(\omega t)\,. \tag{4.11}$$

This predicts that u_y scales linearly with ω which is in fact what we observe in the low ω limit. Also, this has no phase lag with the shear which again is behaviour we observe in the low ω limit rather than high ω. Finally, we have that $R_{xy} \propto u_y \propto \cos(\omega t)$ and so

$$\nu_E \propto \int_{\text{cycle}} \cos^2(\omega t)\, dt\,, \tag{4.12}$$

which has a finite value independent of ω and hence in agreement with the low ω results.

From this we can say that the leading order balance in the low-frequency regime for $\mathbf{e}_y$ aligned rolls is that of eq. 4.8 while the high-frequency leading order balance is that of eq.4.4.

To obtain the frequency scaling for the effective viscosity, we must therefore consider the next largest terms in eq. 4.1. We may write[2] $u_y = u_{y,0} + u_{y,1} + \dots$, where $u_{y,0}$ is the dominant contribution just obtained, and $u_{y,1}$ is the leading order correction. For laminar convection, we suppose that $u_{y,1}$ is dominated by the viscous term acting on the $u_{y,0}$ component, and hence

$$\partial_t u_{y,1} \approx \nabla^2 u_{y,0}, \tag{4.13}$$

where $u_{y,0}$ is given by eq. 4.7, implying $u_{y,1} \propto \frac{1}{\omega}\cos\omega t$. We thus obtain

$$\nu_E \propto \frac{1}{\omega}\int \langle u_x u_y \rangle \cos(\omega t)\,\mathrm{d}t \propto \frac{1}{\omega^2} \tag{4.14}$$

for the largest nonzero contribution. This scaling would also be expected if the nonlinear and pressure terms (involving $u_{y,0}$) were instead dominant in eq. 4.13 for $u_{y,1}$ (instead of the viscous term).

One weakness of this analysis is it is not directly applicable to $\mathbf{e}_x$ aligned rolls. In order to explore this problem further we instead turn to a more rigorous asymptotic analysis.

4.2 Asymptotic linear analysis for high-frequency tidal flows

We now extend upon the linear asymptotic analysis of Ogilvie & Lesur (2012) for high-frequency oscillatory shear. We set out to provide a complementary analysis to explore further the response at high frequency, and to validate the results of our simulations of laminar convection, particularly the surprising appearance of negative effective viscosities. Our primary extension is to incorporate buoyancy forces and to consider perturbations to the temperature field. This was found to be necessary since Ogilvie & Lesur (2012) considered a flow driven by an imposed body force that is divergence-free, but buoyancy forces in Rayleigh-Bénard convection do not satisfy this property.

In order to aid comparisons with our modification and the original work of Ogilvie & Lesur (2012), notes will be provided which reference equations from the Ogilvie & Lesur (2012). The convention we will adopt in this section is to say ‘OL#’ to refer to the equation numbered # from the unmodified version[3] in Ogilvie & Lesur (2012). Since not all equations are numbered we will adopt the convection that a decimal place will indicate counting from the last labelled equation.

This section builds upon section 3 in Ogilvie & Lesur (2012) (see also Braviner 2015 who corrects some typographical errors), and we adopt their notation and use the dimensional equations for ease of comparison with their work. The momentum equation is (OL18 but

---

[2] This can be obtained formally by expanding in the small parameter $\epsilon = 1/\omega$, as is done in the next section.

[3] In the interests of clarity, one would read ‘OL12’ to mean ‘equation 12 in Ogilvie & Lesur (2012) and ‘OL4.2’ would be read as ‘the second non-numbered equation after equation 4 in Ogilvie & Lesur (2012).

replacing f_j with the buoyancy term)

$$(\partial_t + u_i\partial_i)u_j = -\partial_j p + \theta\delta_{j3} + \nu\Delta u_j \,, \tag{4.15}$$

where $\Delta \equiv \nabla^2$. The velocity field satisfies $\partial_i u_i = 0$, and we incorporate the heat equation

$$(\partial_t + u_i\partial_i)\theta = N^2 u_z + \kappa\Delta\theta \,. \tag{4.16}$$

We define horizontally-sheared coordinates (OL4)

$$x' = x \,, \quad y' = y - a(t)x \,, \quad t' = t \,, \quad a(t) = a_0 \sin(\omega t) \,, \tag{4.17}$$

so that partial derivatives transform according to (OL5 with inclusion of z derivatives)

$$\partial_x = \partial'_x - a\partial'_y \,, \quad \partial_y = \partial'_y \,, \quad \partial_z = \partial'_z \,, \quad \partial_t = \partial'_t - \dot{a}x\partial'_y \,, \tag{4.18}$$

and define the velocity components (OL6 with inclusion of u_z)

$$u_x = v_x \,, \quad u_y = v_y + \dot{a}x \,, \quad u_z = v_z . \tag{4.19}$$

Eq. 4.16 gives us an extra equation to be used with OL7 and OL8. In sheared coordinates we obtain the system

$$\begin{aligned}
\left(\partial'_t + v_j(\partial'_j - a\delta_{j1}\partial'_y)\right) v_i + \dot{a}v_x\delta_{i2} &= -\left(\partial'_i - a\delta_{i1}\partial'_y\right) p \\
&\quad +\nu(\partial'_j - a\delta_{j1}\partial'_y)(\partial'_j - a\delta_{j1}\partial'_y)v_i + \theta\delta_{i3}, && (4.20)\\
\left(\partial'_t + v_j(\partial'_j - a\delta_{j1}\partial'_y)\right) \theta &= N^2 u_z + \kappa(\partial'_j - a\delta_{j1}\partial'_y)(\partial'_j - a\delta_{j1}\partial'_y)\theta, && (4.21)\\
\left(\partial'_t - a\delta_{i1}\partial'_y\right) v_i &= 0 \,. && (4.22)
\end{aligned}$$

Since we are interested in small amplitude shear, we linearise the above equations in the shear amplitude. The basic convective flow in the absence of the shear satisfies (our new versions of OL18 and OL19 with an additional equation)

$$\begin{aligned}
(\partial'_t + v_j\partial'_j)v_i &= -\partial'_i p + \nu\Delta' v_i + \theta\delta_{i3}, && (4.23a)\\
(\partial'_t + v_i\partial'_i)\theta &= N^2 u_z + \kappa\Delta'\theta, && (4.23b)\\
\partial'_i v_i &= 0 \,, && (4.23c)
\end{aligned}$$

and the pressure satisfies (which now contains an extra term in comparison to OL20)

$$\Delta' p = \partial'_z\theta - (\partial'_i v_j)(\partial'_j v_i), \tag{4.24}$$

where the linear operator[4] Δ' is defined by (OL8.1)

$$\Delta' = \Delta + 2a\partial'_x\partial'_y - a^2\partial'^2_y \,. \tag{4.25}$$

The presence of buoyancy forces here is the key difference compared with Ogilvie & Lesur (2012).

---

[4] Note that this is the Laplacian operator but in the sheared coordinates.

We also linearise in terms of v_i, p_i and θ (for example we write $\theta = \bar{\theta} + \delta\theta$) which means the system eq. 4.23 becomes (OL21 but including the temperature equation and buoyancy term in the momentum equation)

$$\begin{aligned}(\partial'_t + \bar{v}_j\partial'_j)\delta v_i + (\delta v_j\partial'_j - a\bar{v}_x\partial'_y)\bar{v}_i + \dot{a}\bar{v}_x\delta_{i2} =& -\partial'_i\delta p + a\delta_{i1}\partial'_y\bar{p} - 2\nu a\partial'_x\partial'_y\bar{v}_i \\ &+ \nu\Delta'\delta v_i + \delta\theta\delta_{i3}\,, \end{aligned} \tag{4.26a}$$

$$\left[\partial'_t + \bar{v}_i\partial'_i\right]\delta\theta + \left[\delta v_i\partial'_i - a\bar{v}_x\partial'_y\right]\bar{\theta} = N^2\delta v_z + \kappa\Delta\delta\theta\,, \tag{4.26b}$$

$$\partial'_i\delta v_i - a\partial'_y\bar{v}_x = 0\,. \tag{4.26c}$$

Note that in the interests of making expressions easier to read we drop the bar notation from now on.

4.2.1 Application of the asymptotic expansion

We use the method of multiple scales, introducing a fast time variable to represent the rapid shear, $T' = t'/\epsilon$, where $\epsilon \ll 1$ is a small parameter that characterises the ratio of convective to shear frequencies[5]. We pose the asymptotic expansions (OL22 and OL23 with the inclusion of an expansion for θ) for the perturbed parts of the linear expansion[6] for each of v_i, p_i and θ

$$\delta v_i = \delta v_{i0} + \epsilon\delta v_{i1} + \epsilon^2\delta v_{i1} + \dots\,, \tag{4.27a}$$

$$\delta p_i = \frac{1}{\epsilon}\delta p_0 + \delta p_1 + \epsilon\delta p_2 + \dots\,, \tag{4.27b}$$

$$\delta\theta = \frac{1}{\epsilon}\delta\theta_0 + \delta\theta_1 + \epsilon\delta\theta_2 + \dots\,. \tag{4.27c}$$

On substitution of eq. 4.27 into the momentum equation (eq. 4.26a) we find that the leading order, $\mathcal{O}(\epsilon^{-1})$, is

$$\partial'_T\delta v_{i0} + \dot{a}v_x\delta_{i2} = -\partial'_i\delta p_0 + \delta\theta_0\delta_{i3}\,. \tag{4.28}$$

Similarly for the continuity equation (eq. 4.26c) results in the leading order balance, $\mathcal{O}(1)$, of

$$\partial'_i\delta v_{i0} - a\partial'_y v_x = 0\,. \tag{4.29}$$

Finally for the temperature equation (eq. 4.26b) the leading order balance, $\mathcal{O}(\epsilon^{-2})$, is

$$\partial'_T\delta\theta_0 = 0 \implies \delta\theta_0 = \text{constant} \tag{4.30}$$

but due to the boundary conditions we must have that

$$\delta\theta_0 = 0\,. \tag{4.31}$$

So the leading order equations are

$$\partial'_T\delta v_{i0} + \dot{a}v_x\delta_{i2} = -\partial'_i\delta p_0\,, \tag{4.32a}$$

---

[5] Note that this means that quantities such as $\delta\theta$ and δv_i are now functions of t' and T' and so time derivatives require application of the chain rule, i.e. $\partial'_T\delta\theta \to \partial'_t\delta\theta + \epsilon^{-1}\partial'_T\delta\theta$.

[6] For example we write $\theta = \bar{\theta} + \delta\theta$.

$$\delta\theta_0 = 0\,, \tag{4.32b}$$

$$\partial'_i \delta v_{i0} - a\partial'_y v_x = 0\,, \tag{4.32c}$$

which are identical to OL24 and OL25.

We now consider the next order for the momentum equation and temperature equation[7]. We have for the momentum equation at next order, $\mathcal{O}(\epsilon^0)$,

$$\begin{aligned} \partial'_T \delta v_{i1} + (\partial'_t + v_j \partial'_j)\delta v_{i0} + (\delta v_{j0}\partial'_j - a v_x \partial'_y) v_i = &- \partial'_i \delta p_1 + a\delta_{i1}\partial'_y p \\ &+ \nu(\Delta' \delta v_{i0} - 2a\partial'_x \partial'_y v_i) + \delta\theta_1 \delta_{i3}\,, \end{aligned} \tag{4.33}$$

which is the same as OL32 except for the addition of the $\delta\theta_1$. Similarly for the temperature equation to next order, $\mathcal{O}(\epsilon^{-1})$, gives

$$\partial'_t \delta\theta_0 + \partial'_T \delta\theta_1 + \bar{v}_i \partial'_i \delta\theta_0 = \kappa \Delta \delta\theta_0 \tag{4.34}$$

but we have that $\delta\theta_0 = 0$ and so this is just

$$\partial'_T \delta\theta_1 = 0 \implies \delta\theta_1 = 0\,. \tag{4.35}$$

On careful examination of the temperature equation it becomes clear that $\delta\theta_n = 0 \,\forall\, n \in \mathbb{N}$. Hence perturbations to the temperature field do not enter at any order with this choice of asymptotic ordering.

4.2.2 An alternative θ expansion

We could also choose the expansion of θ in eq. 4.27 to be

$$\delta\theta = \delta\theta_0 + \epsilon\delta\theta_1 + \epsilon^2 \delta\theta_2 + \ldots \tag{4.36}$$

to match the expansion of the velocity term. To leading order in the momentum equation[8] (eq. 4.26a), $\mathcal{O}(\epsilon^{-1})$, using this expansion gives

$$\partial'_T \delta v_{i0} + \dot{a} v_x \delta_{i2} = -\partial'_i \delta p_0\,, \tag{4.37}$$

where an important point to note is that neither θ or $\delta\theta_n, \forall n \in \mathbb{N}_0$, appear in the momentum at leading order (this will be important shortly). Since the continuity equation[8], eq. 4.26c, is unchanged and does not include θ or $\delta\theta$ we can immediately write the continuity equation to leading order, $\mathcal{O}(\epsilon^{-1})$, as

$$\partial'_i \delta v_{i0} - a\partial'_y v_x = 0\,. \tag{4.38}$$

From the temperature equation[8], eq. 4.26b, the leading order, $\mathcal{O}(\epsilon^{-1})$, gives

$$\partial'_T \delta\theta_0 = 0 \implies \delta\theta_0 = \text{constant} \tag{4.39}$$

---

[7] We need not examine the continuity equation any further as it is clear that our modification does not affect it, thus the continuity equation will not differ from Ogilvie & Lesur (2012).

[8] Reminder that the bar notation is dropped to make the equations easier to read.

but due to the boundary conditions we must have that

$$\delta\theta_0 = 0\,. \tag{4.40}$$

Thus we have the same as OL24 and OL25 and hence the same as eq. 4.32 using the other expansion of $\delta\theta$.

The next order, $\mathcal{O}(\epsilon^0)$, in the momentum equation gives

$$\begin{aligned}\partial'_T\delta v_{i1} + (\partial'_t + v_j\partial'_j)\delta v_{i0} + (\delta v_{j0}\partial'_j - a v_x\partial'_y)v_i = &-\partial'_i\delta p_1 + a\delta_{i1}\partial'_y p \\ &+ \nu(\Delta'\delta v_{i0} - 2a\partial'_x\partial'_y v_i) + \delta\theta_0\delta_{i3}\,,\end{aligned} \tag{4.41}$$

where we have left in $\delta\theta_0$ so it is clear that it enters at this order, and continuity (at $\mathcal{O}(\epsilon^0)$) gives

$$\partial'_i\delta v_{i1} = 0\,. \tag{4.42}$$

Finally (although as we will see this is not required), the temperature equation at $\mathcal{O}(\epsilon^0)$ gives

$$\partial'_T\delta\theta_1 + \partial'_t\delta\theta_0 + \delta v_{i,0}\partial'_i\theta - a v_x\partial'_y\theta = N^2\delta v_{z,0} + \kappa\Delta\delta\theta_0\,, \tag{4.43}$$

where the viscous term and the ∂'_t terms are clearly zero since $\delta\theta_0 = 0$. Hence at first order our equations are

$$\begin{aligned}\partial'_T\delta v_{i1} + (\partial'_t + v_j\partial'_j)\delta v_{i0} + (\delta v_{j0}\partial'_j - a v_x\partial'_y)v_i = &-\partial'_i\delta p_1 + a\delta_{i1}\partial'_y p \\ &+ \nu(\Delta'\delta v_{i0} - 2a\partial'_x\partial'_y v_i)\,, &\text{(4.44a)}\\ \partial'_T\delta\theta_1 + \delta v_{i,0}\partial'_i\theta - a v_x\partial'_y\theta =& N^2\delta v_{z,0}\,, &\text{(4.44b)}\\ \partial'_i\delta v_{i1} =& 0\,. &\text{(4.44c)}\end{aligned}$$

The key things to notice is that $\delta\theta_n, \forall n \in \mathbb{N}_0$, does not enter into the momentum at this order and hence the result is identical to OL32. Thus, since this is the highest order we are considering we know that we do not need to consider $\delta\theta$ with this expansion.

4.2.3 Calculating the effective viscosity and elasticity

The key result of both § 4.2.1 and § 4.2.2 is that we need not consider $\delta\theta$. In fact the inclusion of thermal effects only manifests in a modification to the pressure term, OL20. We will now derive the modifications to Ogilvie & Lesur (2012) that are required to take into account buoyancy.

As we have seen in § 4.2.1 and § 4.2.2, to leading order we obtain OL24 and OL25. The linearised shear stress $\delta R_{xy0} = \langle v_x\delta v_{y0} + \delta v_{x0}v_y\rangle$, therefore satisfies (OL29)

$$\partial'_T(-\delta R_{xy0}) = -\dot{a}\langle v_x^2 - 2(v_x\partial'_y + v_y\partial'_x)\partial'_y\Delta'^{-1}v_x\rangle, \tag{4.45}$$

where angled brackets denote a volume average. To obtain the perturbed shear stress at the next order, which is necessary to obtain the effective viscosity, we note that since both of the expansions in § 4.2.1 and § 4.2.2 agree with the first order expansion (OL32) we can start from OL33.1:

$$\begin{aligned}\partial'_T(-\delta R_{xy1}) =& \langle v_x(\partial'_t + v_j\partial'_j)\delta v_{y0} + v_y(\partial'_t + v_j\partial'_j)\delta v_{x0}\\ &+ v_x(\delta v_{j0}\partial'_j - av_x\partial'_y)v_y + v_y(\delta v_{j0}\partial'_j - av_x\partial'_y)v_x\\ &+ (v_x\partial'_y + v_y\partial'_x)\delta p_1 \underbrace{-av_y\partial'_y p}\\ &- \nu v_x(\Delta'\delta v_{y0} - 2a\partial'_x\partial'_y v_y)\\ &- \nu v_y(\Delta'\delta v_{x0} - 2a\partial'_x\partial'_y v_x),\end{aligned} \tag{4.46}$$

where $\delta R_{xy1} = \langle v_x\delta v_{y1} + \delta v_{x1}v_y\rangle$, and where we have highlighted the only term that requires modification due to our inclusion of buoyancy. The pressure is determined by

$$p = \Delta'^{-1}\partial'_z\theta - \Delta'^{-1}(\partial'_j v_j)(\partial'_j v_i)\,, \tag{4.47}$$

which we can substitute into eq. 4.46 (note this is our modified version of OL20). The new contribution to the highlighted term is $\Delta'^{-1}\partial'_z\theta$, which becomes $-av_y\Delta'^{-1}\partial'_y\partial'_z\theta$ in eq. 4.46. A second term arises from OL33.2 that has the form

$$-\Delta'^{-1}(\partial'_y v_x - \partial'_x v_y)(a\partial'_x\partial'_y p)\,, \tag{4.48}$$

which on considering only the additional contribution due to buoyancy forces we obtain

$$-a\Delta'^{-1}(\partial'_y v_x - \partial'_x v_y)(\Delta'^{-1}\partial'_x\partial'_y\partial'_z\theta)\,, \tag{4.49}$$

thus, equation OL33.3 will have additional terms of

$$-av_y\Delta'^{-1}\partial'_y\partial'_z\theta - a\Delta'^{-1}(\partial'_y v_x - \partial'_x v_y)(\Delta'^{-1}\partial'_x\partial'_y\partial'_z\theta)\,, \tag{4.50}$$

which need to be followed until OL33.6. The first step is to apply ∂'_T which gives

$$\begin{aligned}-\dot{a}\left(v_y\Delta'^{-1}\partial'_y\partial'_z\theta + \Delta'^{-1}(\partial'_y v_x - \partial'_x v_y)(\Delta'^{-1}\partial'_x\partial'_y\partial'_z\theta)\right)\\ \equiv -\dot{a}\mathcal{G}_1^\theta\,.\end{aligned} \tag{4.51}$$

We can write eq. 4.45 and OL33.6 with the new term in eq. 4.51 in the form

$$\partial'_T(-\delta R_{xy0}) = \dot{a}\mathcal{G}_0\,, \tag{4.52a}$$

$$\partial'^2_T(-\delta R_{xy1}) = -\dot{a}\left(\mathcal{G}_1 + \mathcal{G}_1^\theta\right)\,, \tag{4.52b}$$

where $\mathcal{G}_0$ and $\mathcal{G}_1$ are the same as OL40 and OL41 (see aside 4.2). These are the final results required to obtain the effective elasticity and viscosity of the flow. These are straightforward in principle to evaluate for laminar flows since the $\mathcal{G}$ quantities on the right hand side depend only on the basic convective flow. Note that

$$S_E = \mathcal{G}_0\,, \tag{4.53}$$

$$\nu_E = \frac{1}{\omega^2}(\mathcal{G}_1 + \mathcal{G}_1^\theta)\,, \tag{4.54}$$

to this order. These equations therefore indicate that for high-frequency shear, the leading order response is a frequency-independent effective elasticity, and a weaker (effective) viscous response that scales quadratically with (inverse) frequency. In principle, the $\mathcal{G}$ coefficents can take either sign, depending on the basic flow. This is therefore a mathematical derivation to justify why $\nu_E \propto \omega^{-2}$ for high-frequency shear. Note that this agrees with the Goldreich & Nicholson (1977) scaling law, but the reasons are very different.

Aside 4.2: Complete forms of OL41 and OL41

For completeness we include the full expressions for $\mathcal{G}_0$ and $\mathcal{G}_1$ from Ogilvie & Lesur (2012) accounting for the correction of a sign error highlighted in Braviner (2015). We have that

$$\mathcal{G}_0 = A_{1jj1} - 2A_{1221} - 2A_{2121} \tag{4.55}$$

and

$$\begin{aligned}\mathcal{G}_1 =& - \left(B_{1jj1} - B_{1221} - B_{1122} + C_{1jj1} - C_{1221} + 3C_{1122}\right.\\ & - 2D_{1jj221} - 2D_{2jj121} + 3D_{1jj221} + 3D_{1jj212}\\ & \left. - D_{ijij1221} - D_{ijij1212} + D_{ijij22} + 4E_{2121} + 4E_{2112}\right) ,\end{aligned} \tag{4.56}$$

where

$$A =\langle v_i \partial'_j \partial'_k \Delta'^{-1} v_l \rangle \, , \tag{4.57}$$

$$B_{ijkl} =\langle (\partial'_t v_i) \partial'_j \partial'_k \Delta'^{-2} v_l \rangle \, , \tag{4.58}$$

$$C_{ijkl} =- \nu \langle v_i \partial'_j \partial'_k v_l \rangle \, , \tag{4.59}$$

$$D_{ijklmn} =\langle v_i v_j \partial'_k \partial'_l \partial'_m \Delta'^{-2} v_n \rangle \, , \tag{4.60}$$

$$D_{ijklmnpq} =\langle v_i v_j \partial'_k \partial'_l \partial'_m \partial'_n \partial'_p \Delta'^{-2} v_q \rangle \, , \tag{4.61}$$

$$E_{ijkl} =\langle v_m (\partial'_m \partial'_n \Delta'^{-1} \partial'_i v_j) \partial'_n \Delta'^{-1} \partial'_k v_l \rangle \, . \tag{4.62}$$

In all there are 4 distinct terms for $\mathcal{G}_0$ that need to be evaluated and 62 for $\mathcal{G}_1$ (not including our $\mathcal{G}_1^\theta$ term). While in general this is highly complex, in the cases we explore it turns out that the majority of these terms do not contribute.

4.3 Implementation of the asymptotic method

To evaluate these quantities (eq. 4.52) for a given convective flow for comparison with simulations, we assume a set of individual convective modes which each satisfy

$$u_x(k_x,k_y) = \Re\Big(\hat{u}_x \mathrm{e}^{ik_x x + ik_y y} \cos(\pi z) e^{\sigma t}\Big) \, , \tag{4.63a}$$

$$u_y(k_x,k_y) = \Re\Big(\hat{u}_y \mathrm{e}^{ik_x x + ik_y y} \cos(\pi z) e^{\sigma t}\Big) \, , \tag{4.63b}$$

$$u_z(k_x,k_y) = \Re\Big(\hat{u}_z \mathrm{e}^{ik_x x + ik_y y} \sin(\pi z) e^{\sigma t}\Big) \, , \tag{4.63c}$$

$$\theta(k_x,k_y) = \Re\Big(\hat{\theta} \mathrm{e}^{ik_x x + ik_y y} \sin(\pi z) e^{\sigma t}\Big) \, , \tag{4.63d}$$

$$p(k_x, k_y) = \Re\Big(\hat{p}e^{ik_xx+ik_yy}\cos(\pi z)e^{\sigma t}\Big)\,. \tag{4.63e}$$

We can linearise eq. 2.22a-2.22c to get

$$\frac{\partial u_x}{\partial t} = -\frac{\partial p}{\partial x} + \nu\nabla^2 u_x\,, \tag{4.64a}$$

$$\frac{\partial u_y}{\partial t} = -\frac{\partial p}{\partial y} + \nu\nabla^2 u_y\,, \tag{4.64b}$$

$$\frac{\partial u_z}{\partial t} = -\frac{\partial p}{\partial z} + \nu\nabla^2 u_z + \theta\,, \tag{4.64c}$$

$$\frac{\partial \theta}{\partial t} = -N^2 u_z + \kappa\nabla^2\theta\,, \tag{4.64d}$$

$$\nabla\cdot\mathbf{u} = 0\,,$$

which we can then substitute for eq. 4.63 to eliminate[9] $\hat{u}_x$, $\hat{u}_y$, $\hat{\theta}$ and $\hat{p}$. We then have that

$$u_x(k_x, k_y) = \Re\Big(-\frac{ik_xk_zN^2}{k^2\sigma_\kappa\sigma_\nu}\hat{u}_z e^{i(k_xx+k_yy)}\cos(\pi z)e^{\sigma t}\Big)\,, \tag{4.65a}$$

$$u_y(k_x, k_y) = \Re\Big(-\frac{ik_yk_zN^2}{k^2\sigma_\kappa\sigma_\nu}\hat{u}_z e^{i(k_xx+k_yy)}\cos(\pi z)e^{\sigma t}\Big)\,, \tag{4.65b}$$

$$u_z(k_x, k_y) = \Re\Big(\hat{u}_z e^{i(k_xx+k_yy)}\sin(\pi z)e^{\sigma t}\Big)\,, \tag{4.65c}$$

$$\theta(k_x, k_y) = \Re\Big(-\frac{N^2}{\sigma_\kappa}\hat{u}_z e^{i(k_x+k_yy)}\sin(\pi z)e^{\sigma t}\Big)\,, \tag{4.65d}$$

where $\sigma_\nu = (\sigma + \nu k^2)$, $\sigma_\kappa = (\sigma + \kappa k^2)$, $k^2 = k_x^2 + k_y^2 + \pi^2$ and the growth rate σ can be obtained from the dispersion relation for each case[10]. We can fit the amplitudes of each of u_x, u_y, u_z and θ separately, but still assuming a single linear mode for each variable, by taking $\max(u_x)$ (and similarly for other variables) within the domain. This in essence means we use

$$u_x(k_x, k_y) = \Re\Big(i\hat{u}_x^{\mathsf{sim}} e^{i(k_xx+k_yy)}\cos(\pi z)\Big)\,, \tag{4.66a}$$

$$u_y(k_x, k_y) = \Re\Big(i\hat{u}_y^{\mathsf{sim}} e^{i(k_xx+k_yy)}\cos(\pi z)\Big)\,, \tag{4.66b}$$

$$u_z(k_x, k_y) = \Re\Big(\hat{u}_z^{\mathsf{sim}} e^{i(k_xx+k_yy)}\sin(\pi z)\Big)\,, \tag{4.66c}$$

$$\theta(k_x, k_y) = \Re\Big(\hat{\theta}^{\mathsf{sim}} e^{i(k_x+k_yy)}\sin(\pi z)\Big)\,, \tag{4.66d}$$

where $\hat{\bullet}^{\mathsf{sim}} = \max\left[\Re(\hat{\bullet})\right]$ for each wavemode (k_x, k_y) of a given simulation. It should be noted that in practice we take the average in time of the maximum. An alternative method is briefly described in aside 4.3. Once the amplitudes of the quantities in eq. 4.66 have been evaluated they can simply be plugged into the appropriate expressions eq. 4.53 to obtain S_E and ν_E for each wavemode. There are some subtleties to this method which are best described by relevant examples.

---

[9] In order to obtain the expressions we consider the $\mathbf{e}_z$ component of the divergence of the momentum equation to obtain an expression for $\hat{p}$ in terms of $\hat{u}_z$ as well as the temperature equation to obtain $\hat{\theta}$ in terms of $\hat{u}_z$. Both of these are then substituted into the $\mathbf{e}_x$ and $\mathbf{e}_y$ components of the momentum equation to get $\hat{u}_x$ and $\hat{u}_y$ in terms of $\hat{u}_z$.

[10] The dispersion relation in its nondimensional form can be found to be $(k^2+\sigma)(k^2+\sigma/\mathrm{Pr})k^2 = \mathrm{Ra}k_\perp^2$ where $k_\perp^2 = k_x^2 + k_y^2$. This can be evaluated simply for each given simulation, note that since this is a quadratic in σ we get two solutions and we take the fastest growing case (that with the greatest magnitude real part).

Aside 4.3: An alternative method

Since the results in Ch. 3 are just above onset, we can use eq. 4.65 so that only a single value is needed for this fit (we chose to use the amplitude of $\hat{u}_z$).
Note that this has also been tried, although not reported, as it obtains very similar results for our cases. It might be expected that the chosen method would also be more stable to increasing strength of non-linearities as it partly avoids the application of linear theory when relating the amplitudes of the components (but still neglects generation of any other k_x, k_y or $n\pi$ components).

In the cases presented in § 3.2.1 and § 3.2.2 the flow primarily consists of only a single convective mode[11]. As such we can use our simulation snapshots (e.g. Fig. 3.1) to fit the amplitude of the flow (such as $\hat{u}_z$) and input this into a Mathematica script that calculates the asymptotic predictions for ν_E and S_E following § 4.2.

In the larger domain sizes of § 3.2.3, computing the asymptotic predictions using the approach outlined here is more difficult due to the presence of multiple modes that could each contribute to ν_E. We can calculate the contribution from the most important modes by taking a horizontal Fourier transform of a set of flow snapshots to determine the amplitude of each Fourier k_x, k_y mode in the flow (selecting the maximum value over all z). The amplitude of each mode may vary in time and so we use a suitable time-average to obtain these values. We also convert quantities like N^2 and ν to the forms used in the simulations. Once we have the amplitude of u_x, u_y, u_z and θ for each mode, we compute their contributions to ν_E separately using the approach outlined above, and then sum up their contributions to obtain a prediction for ν_E. We consider all modes which have a contribution within 3 orders of magnitude of the dominant (typically the largest scale) mode, and we find large wavenumber modes contribute less to ν_E. This approach is only expected to work for steady laminar convection near onset (because the theory contains terms that depend on the derivative of the convective flow with respect to time). However, the asymptotic theory in principle applies to more complex flows if they can be adequately represented.

We have found that the new term $\mathcal{G}_1^\theta$ is essential to obtain negative effective viscosities for laminar convection. Note that it vanishes for y-aligned rolls, since $\partial_y' = 0$. On the other hand, for x-aligned rolls, $\partial_x' = 0$, so only the first term in $\mathcal{G}_1^\theta$ contributes. It turns out if we substitute the form of each wavemode, eq. 4.66, into $\mathcal{G}_1^\theta$ then we obtain

$$\mathcal{G}_1^\theta = v_y \nabla'^{-1} \partial_y' \partial_z' \theta = -\frac{\pi k_y}{k^2} \hat{u}_y \hat{\theta} < 0 \,, \tag{4.67}$$

since we take $\hat{u}_y$ and $\hat{\theta}$ as $\max(\Re[\hat{u}_y])$ and $\max(\Re[\hat{\theta}])$ respectively. This demonstrates that any purely x-aligned roll ($k_x = 0$; $k_y = 2\pi n_y / L_y, \forall n_y \in \mathbb{N}_0$) will always result in a negative contribution to the total $\mathcal{G}_1^\theta$. For a 3D convective mode, all terms in $\mathcal{G}_1$ could be important in principle.

---

[11] Note that for x-aligned rolls, $k_x = 0$, and for y-aligned rolls, $k_y = 0$.

4.4 Discussion

In order to help understand the results in Ch. 3 we have first outlined a simple derivation using force balances to obtain crude explanations for the observed ω^{-2} scaling for an $\mathbf{e}_y$ aligned roll. This has also provided insight as to which terms in the momentum equation are dominant in each of the low and high-frequency regimes. We have also extended the asymptotic analysis of Ogilvie & Lesur (2012) to include buoyancy effects. This allows us to quantitatively predict the amplitude and sign of the effective viscosity and elasticity for a given steady laminar convection flow. We have obtained the important result that $\nu_E < 0$ is a robust result obtained in both theory and simulations (particularly for x-aligned rolls).

Summary: Key findings

In cases with $\mathbf{e}_y$ aligned rolls we find that considering the balance of the time derivative of the y-component of velocity and the shear term we are able to explain the $\nu_E \sim \omega^{-2}$ result of § 3.2.1. We also have that this is the leading order balance in the high-frequency regime, while in the low-frequency regime it has been shown that the leading order balance is between the shear terms and the viscous term (for u_y component of the momentum equation). This analysis is not applicable to $\mathbf{e}_x$ aligned roll cases and so we appeal to the multi-scale asymptotic method of Ogilvie & Lesur (2012) which we modify to include buoyancy effects. Some important points about the method are as follows:

- perturbations of θ are unimportant,
- the inclusion of the heat equation and buoyancy effects only acts to modify the pressure gradient,
- expressions for S_E and ν_E can be obtained which can be readily evaluated for steady laminar flows,
- the inclusion of the buoyancy is able to predict the observed negative values of ν_E and we have therefore confirmed our numerical results in Ch. 3 are robust.

Chapter 5

Interaction between tides and turbulent convection in small domains

Contents

We will now expand on the study of Ch. 3 to consider more turbulent cases such that $R \gg 1$. In such cases the flow can be described as turbulent and may exhibit a Kolmogorov cascade, although this inertial range may be short. With more complex flow patterns we will also turn our attention to more statistical approaches such as examination of kinetic energy spectra.

5.1 Parameter survey

In this chapter we will vary the scaled Rayleigh number $R \gg 1$, which measures the strength of the convection, the tidal frequency ω and amplitude a_0. All cases in this chapter will have domain sizes of $(L_x, L_y, d) = (2, 2, 1)$. The Prandtl number will be $\mathrm{Pr} = 1$ except where it has been explicitly stated (§ 5.2.2). Everything else, such as initial conditions, will be the same as described in § 3.1.

These simulations are much more computationally demanding than those that only aim to explore the dynamics of the convection, since we must integrate them for multiple tidal periods and for many convective timescales to accurately probe the interaction between tides and convection. This is the reason that we have limited our study to modest values of $R \leq 10^3$ in this chapter.

5.2 More turbulent convection with $R = 100$ and $R = 1000$

The simulations of laminar convection described in Ch. 3 provide a starting point to explore the interaction between tidal flows and convection. Those cases had the significant advantage that the flow was sufficiently simple that we could compare our results with the independent asymptotic analysis of Ch. 4. Since convection in stars is highly turbulent, it is important to study more astrophysically relevant cases with much larger values of R. We begin by studying cases with $R = 100$, both with $\mathrm{Pr} = 1$ and then with different Pr, before moving on to cases with $R = 1000$.

5.2.1 $R = 100$ with $L_x = L_y = 2$

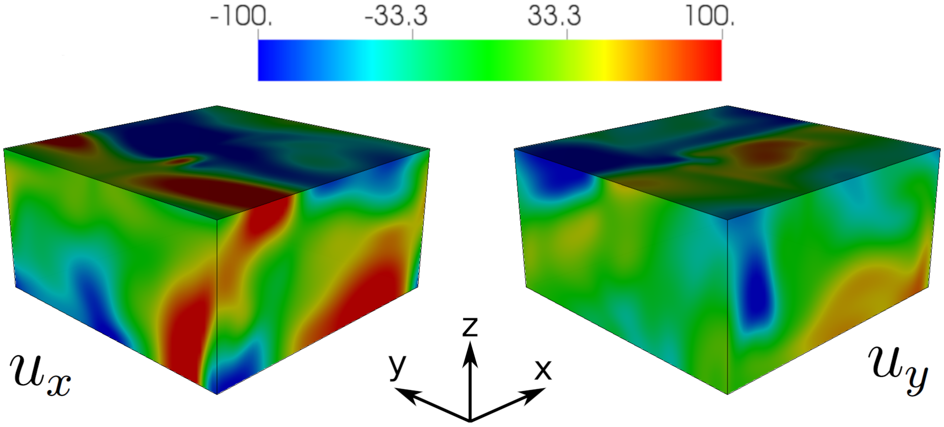

Figure 5.1: Flow in weakly turbulent simulations with $R = 100$, with $\omega = 5000$ and $a_0 = 0.05$, where u_x is plotted in the left panel and u_y in the right panel at $t = 90$. The flow is three-dimensional but is dominated by x and y-aligned convection rolls, which can be seen by the tendency for u_x to align with y and u_y to align with x.

We now present results with $R = 100$, which corresponds with a weakly turbulent regime. These simulations have $(L_x, L_y, L_z) = (2, 2, 1)$, are run with $(N_x, N_y, N_z) = (64, 64, 64)$, and result in a fully three-dimensional time-dependent convective flow. We show this in a snapshot with $\omega = 5000$ at $t = 90$ in Fig. 5.1. The flow is qualitatively similar for all ω considered, and consists of several modes, including both x and y-aligned rolls. This can be seen in Fig. 5.1 by observing that u_x preferentially aligns with y and u_y aligns with x, indicating the dominance of these rolls in the flow, even if other components are also present.

Aside 5.1: Computation of spectral flow structure

In order to compute the results of Fig. 5.2 we use

$$u_i(n_x, n_y) = \frac{1}{2(T - T_0)} \int_{T_0}^{T} \int_0^1 \hat{u}_i(n_x, n_y, z, t)\hat{u}_i^*(n_x, n_y, z, t)\, \mathrm{d}z\, \mathrm{d}t\,, \tag{5.1}$$

where $*$ denotes the complex conjugate, hats represent horizontally (2D) Fourier transformed quantities, $n_i = L_i k_i / 2\pi$ and $i \in \{x, y\}$. In practice the temporal resolution is not as high as the one we use for global quantities (such as ν_E), however the integration is performed over many time snapshots to reduce any bias.

We can determine the dominant (k_x, k_y) wavenumbers in the flow by evaluating the vertically integrated and temporally-averaged horizontal power spectrum of $|\hat{u}_x|^2$ and $|\hat{u}_y|^2$, which we plot in Fig. 5.2 for two different frequencies with $\omega = 10$ and $\omega = 10000$. We plot the integer wavenumbers on each axis i.e. $n_x = L_x k_x / 2\pi$ and $n_y = L_y k_y / 2\pi$. This shows that the flow at both low and high frequencies contains multiple modes, but that the x and y-aligned

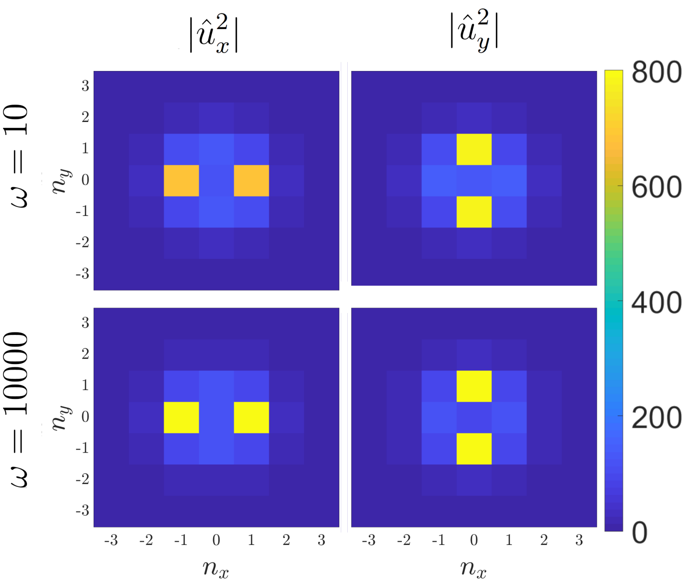

Figure 5.2: Vertically integrated and temporally averaged horizontal power spectrum of $|\hat{u}_x|^2$ (left) and $|\hat{u}_y|^2$ (right) as a function of (k_x, k_y) in simulations with $R = 100$ and $a_0 = 0.05$, for two different frequencies with $\omega = 10$ and $\omega = 10000$ (top and bottom, respectively). We plot the integer wavenumbers on each axis i.e. $n_x = L_x k_x/2\pi$ and $n_y = L_y k_y/2\pi$. The flow is fully three dimensional but is dominated by a small number of large-scale modes.

convection rolls with $(k_x, k_y) = (0, 2\pi/L_y)$ or $(2\pi/L_x, 0)$ are dominant. We have run several simulations with the same parameters with different random initial conditions and the flow has a similar spectrum in each case with $(L_x = L_y = 2)$.

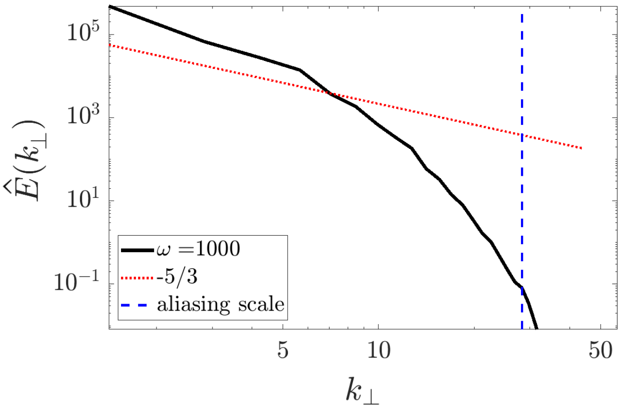

Figure 5.3: Temporally-averaged kinetic energy spectrum $\hat{E}(k_\perp)$ as a function of $k_\perp$ in a simulation with $R = 100$, $a_0 = 0.05$ and $\omega = 1000$. This is representative of all simulations with $R = 100$. The red line represents the Kolmogorov scaling ($k^{-5/3}$) and the blue line shows the de-aliasing scale.

In Fig. 5.3, we show the time-averaged and vertically-integrated kinetic energy spectrum[1] $\hat{E}(k_\perp)$ as a function of horizontal wavenumber $k_\perp$ (computed by summing up the mode energy in wavenumber rings of unit width in the (k_x, k_y)-plane, where $k_\perp^2 = \sqrt{k_x^2 + k_y^2}$). This is computed using the horizontal Fourier transform of the velocity field. A more thorough description of the computation of this spectrum will be given in Ch. 6 where the results will be explored in more depth. This shows that the energetically dominant scales are those on the size of the box, but that smaller scales are also present with non-negligible amplitudes. With $R = 100$, the flow has a short inertial-like range, which can be seen by comparing the data (black line) with the Kolmogorov (-5/3) scaling (red line). This figure also demonstrates that our simulations are well-resolved horizontally, since the energy in wavenumbers close to the de-aliasing scale (blue dashed vertical line) is more than 6 orders of magnitude smaller than the peak.

Since the convective flow with $R = 100$ is non-steady, accurately computing the effective viscosity (and elasticity) in this case is more challenging than for the laminar simulations.

---

[1] This is a spatial spectrum. We will frequently refer to spatial spectra through the terminology of "wavenumber spectrum"

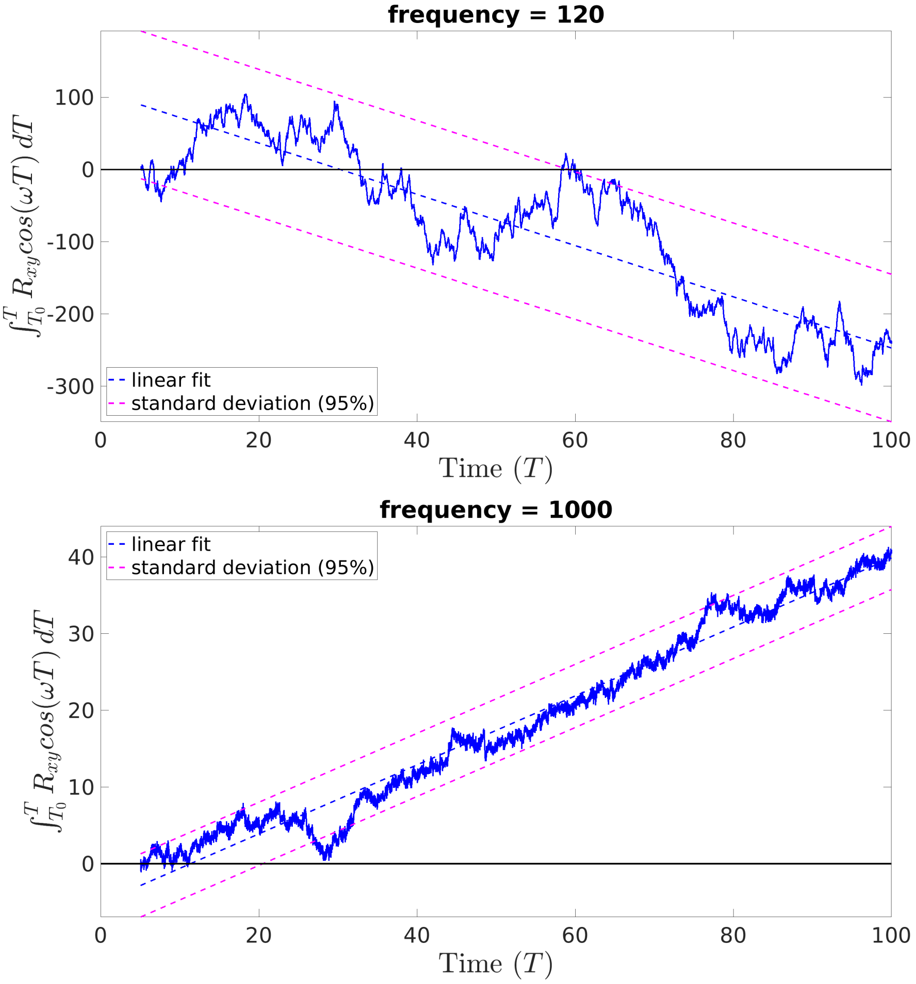

Figure 5.4: Cumulative integrals used to compute ν_E based on eq. 2.62, ignoring the factors outside the integral. Decreasing (increasing) behaviour indicates positive (negative) ν_E. The blue dashed line shows the linear fit used to compute ν_E, and the magenta dashed lines highlight the error, defined by 2σ from the mean trend. Top: an example case in the low-frequency regime ($\omega \lesssim \omega_c$) with $\omega = 120$ where the effective viscosity is such that $\nu_E > 0$. Bottom: an example case in the high-frequency regime ($\omega \gtrsim \omega_c$) with $\omega = 1000$ where the effective viscosity is such that $\nu_E < 0$.

We previously outlined our approach to determine ν_E in § 2.3.2 (also in aside 2.7), and in Fig. 5.4 we show the results of computing the cumulative integral required to calculate ν_E as a function of the end-times T, omitting the constant multiplicative factors outside the integral in eq. 2.62. This figure shows an example with low frequency ($\omega = 120$) and another with high frequency ($\omega = 1000$), along with the linear fit as the dashed blue line. The magenta dashed lines denote the error bars defined at two standard deviations (σ) from the mean. Both cases show temporal variability but exhibit a well-defined linear slope, indicating that the resulting values for ν_E are well-converged. In this figure, since we have omitted the numerical factors outside the integral in eq. 2.62, including the sign, a trend that is decreasing (increasing) in Fig. 5.4 represents a positive (negative) effective viscosity. This means that the case with $\omega = 120$ has $\nu_E > 0$ and $\omega = 1000$ has $\nu_E < 0$. The error bars are smaller for $\omega = 1000$ since the simulation has been run for more tidal periods. We have analysed similar plots in all of our simulations to ensure that ν_E is always well-converged.

Figure 5.5: Plot of ν_E versus ω scaled by the convective frequency ω_c in simulations with $R = 100$. Positive values are indicated by blue symbols and negative values by red. There is a clear transition from positive to negative values at $\omega/\omega_c \approx 10$. At high ω ($\omega/\omega_c \gtrsim 5$), we again find $|\nu_E| \propto \omega^{-2}$.

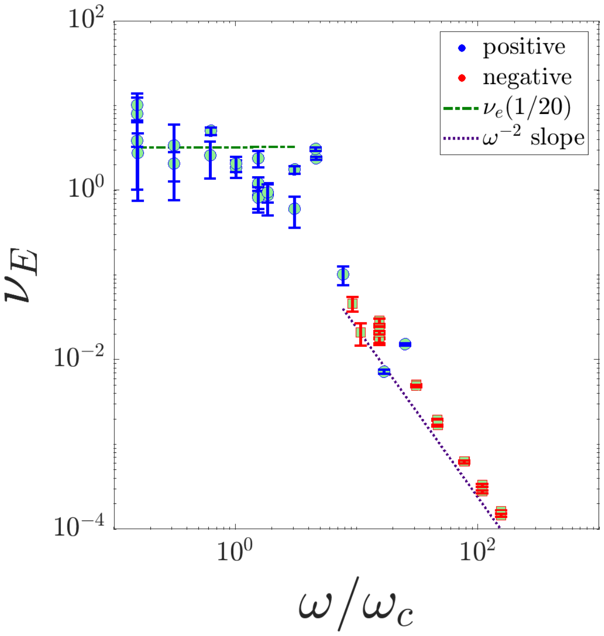

The results for ν_E are shown in Fig. 5.5, where we have scaled ω by the convective frequency. Similar to the laminar simulations presented in Ch. 3, this case also has a frequency-independent effective viscosity at low frequencies, with a transition to $\nu_E \propto \omega^{-2}$ at high frequencies. The transition occurs at $\omega/\omega_c \approx 5$ (where $\omega_c \approx 64$ in this case). The most surprising feature in Fig. 5.5 is that the sign of ν_E changes at $\omega/\omega_c \approx 10$, with low ω having positive ν_E (plotted using blue symbols) and large ω having negative ν_E (plotted using red symbols). The negative effective viscosities at high frequencies are highly statistically significant. Indeed, the error bars – obtained in the same way as those plotted in the bottom panel in Fig. 5.4 – on the points with $\omega/\omega_c > 1$ are very small because these simulations have been run for many hundreds of tidal periods, indicating that the values of ν_E are very robust. This corroborates the tentative finding that negative effective viscosities are possible at high frequencies obtained by Ogilvie & Lesur (2012).

Also shown on Fig. 5.5 is a low-frequency fit based on mixing-length theory, where we have used $\frac{1}{20}\nu_e$. The constant of proportionality is clearly smaller than the value $(1/6)$ required to fit our laminar results in Ch. 3, possibly because the convective length-scales are reduced at higher Ra. It is possible that larger box sizes would permit larger wavelength convective modes, which can enhance ν_E and lead to a constant of proportionality that is more consistent with our laminar simulations. We will explore this issue in Ch. 6.

To explore further the occurrence of negative ν_E at high frequencies, we have also performed a set of simulations in which the amplitude a_0 is varied. These allow us to explore whether the sign change in ν_E is related to the increasing amplitude of the tidal flow relative to the convective flow i.e. to check whether we are still exploring the regime of linear tides at high frequencies. We focus on simulations varying a_0 near the transition, taking $\omega = 1000$ (so that $\omega/\omega_c \approx 15$). The resulting values for ν_E are shown in Fig. 5.6 as a function of a_0. This shows that $\nu_E < 0$ for all $a_o \leq 0.1$, but that $\nu_E > 0$ when $a_0 \geq 0.1$. The occurrence of negative values with very similar magnitude for all cases with $a_0 \leq 0.1$, suggests that, for these values, we are probing the regime of linear tides, since ν_E depends only very weakly on a_0. However,

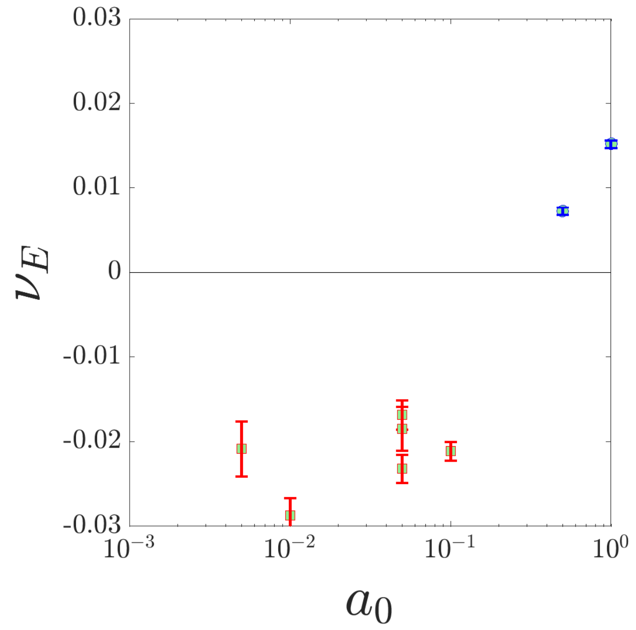

Figure 5.6: Plot of ν_E versus a_0 for $R = 100$ and $\omega = 1000$ (so that $\omega/\omega_c \approx 15.6$) to explore the dependence of our results on a_0. Since ν_E is approximately independent of a_0 for $a_0 \leq 0.1$, this suggests that the simulations in Fig. 5.5 are primarily exploring the regime of linear tides. For large amplitudes, the sign is observed to change, potentially indicating a departure from the linear regime.

for larger amplitudes we obtain different results, with positive ν_E, suggesting that the largest amplitude cases are no longer probing the regime of linear tides. Note that Ogilvie & Lesur (2012) instead fix the shear ($a_0\omega$) in their simulations, so the concurrence of our results with their observation of negative values at high frequencies also suggests that the transition to $\nu_E < 0$ in Fig. 5.5 is not caused by a transition out of the regime of linear tides.

Our observation of negative effective viscosities suggests the intriguing possibility of tidal anti-dissipation due to the interaction between tides and convection. This means that energy is transferred from the convective flow to the tidal flow, in opposition to the standard picture in which the tidal flow is damped by its interaction with the convection. Unlike molecular viscosity, there is nothing in principle preventing the effective viscosity from being negative, even if this result is surprising (see aside 1.5).

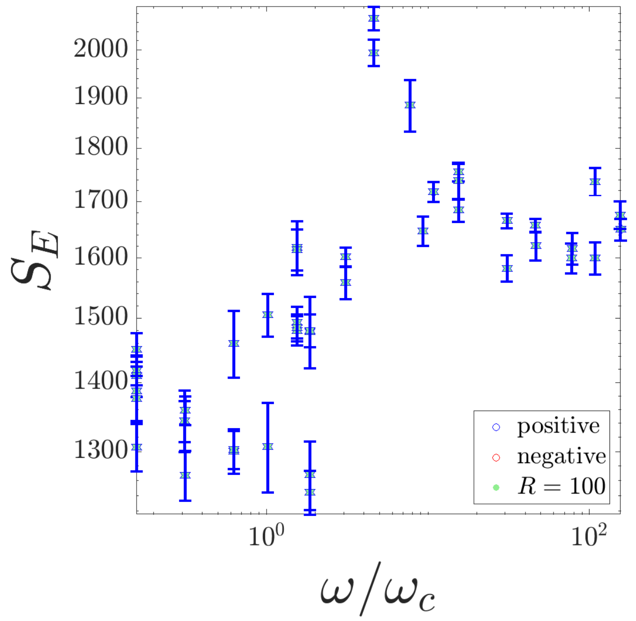

Figure 5.7: Plot of the frequency dependence of $S_E(\omega)$ scaled by the convective frequency ω_c for simulations with $R = 100$ and $a_0 = 0.05$. For all values of ω we obtain positive values.

We plot the effective elasticity S_E in Fig. 5.7. Similar to our laminar results in Fig. 3.4, S_E increases with ω until $\omega \approx 5\omega_c$, above which there is a transition to a regime in which S_E is independent of ω, with a possible enhancement for $\omega \sim \omega_c$. Note that there is no change in sign and S_E remains positive for all ω, unlike what we have observed in our laminar simulations.

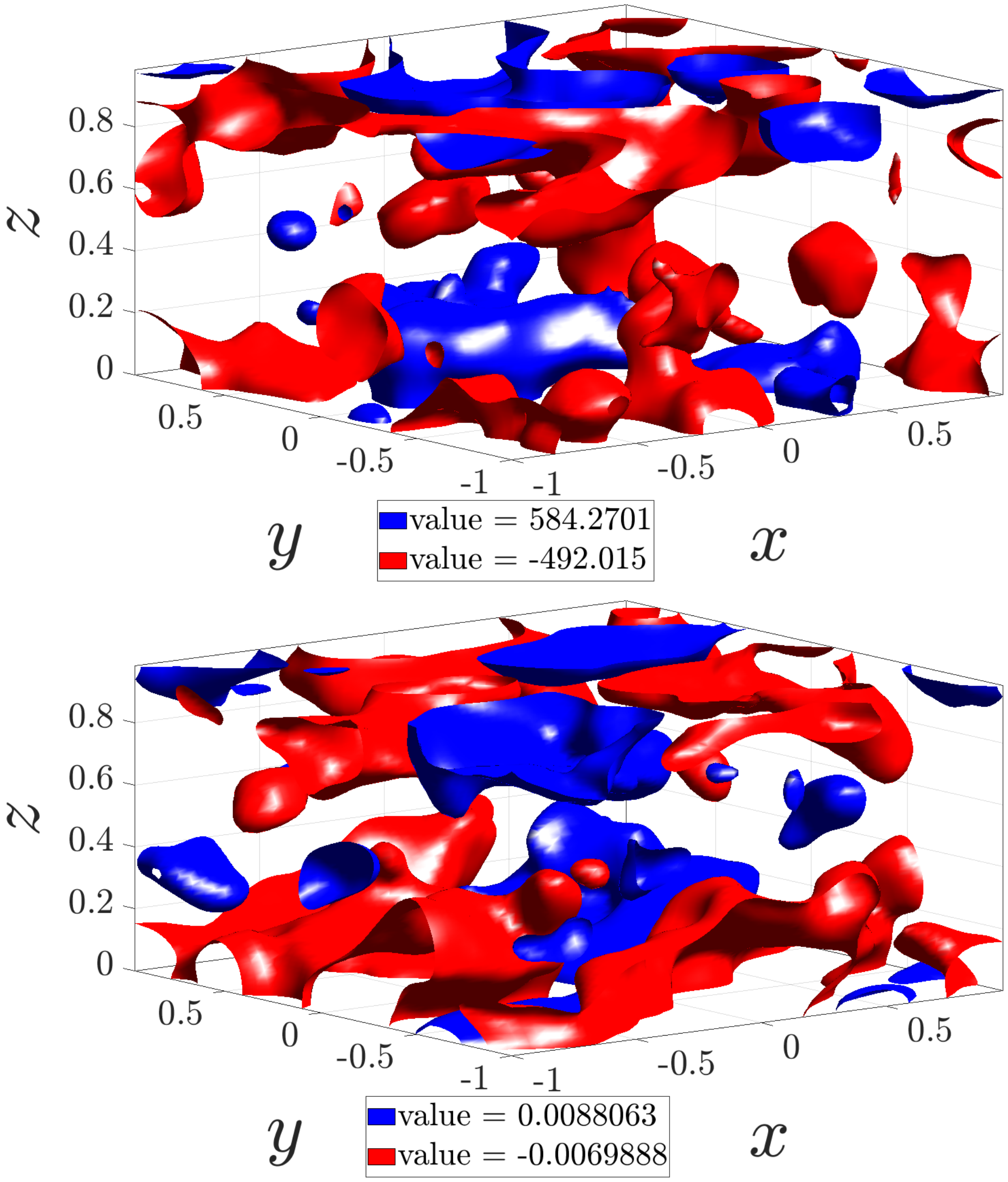

Figure 5.8: Iso-surfaces showing $\tilde{\nu}_E$, the spatial contribution to ν_E based on eq. 5.2, where 80% of the maximum (blue) and minimum (red) values are shown in two simulations $\omega \in \{10, 10000\}$ (top to bottom respectively) with $R = 100$ and $a_0 = 0.05$. The maximum values are distributed in space but are primarily localised near to the boundaries in z.

We would like to understand where in the domain the flow contributes the most to the effective viscosity and also which scales are important. To explore this, we recorded the spatial structure using at least ten snapshots per ω^{-1} in simulations with $R = 100$, $a_0 = 0.05$ and

$\omega \in \{10, 100, 1000, 10000\}$. Fig. 5.8 shows the result from evaluating

$$\tilde{\nu}_E(x, y, z) = \frac{-2}{a_0\omega(T - T_0)} \int_{T_0}^{T} u_x(x, y, z, t)u_y(x, y, z, t)\cos(\omega t)\,\mathrm{d}t \tag{5.2}$$

for the cases $\omega = 10$ and 10000, where T_0 and T are the start and end times of our simulation. This is effectively evaluating eq. 2.62 in a point-wise sense before volume-averaging. Note that $\nu_E = L_x L_y d\langle\tilde{\nu}_E\rangle$ where we note that $\langle\bullet\rangle$ is a volume average[2]. We plot iso-surfaces representing 80% of the maximum positive (blue) and negative (red) values of $\tilde{\nu}_E$ within the domain. This allows us to identify where in the domain contributes the most to both the positive and negative values of ν_E.

The regions near to the boundaries in z clearly provide the dominant contribution to both the positive and negative values of ν_E, at both low and high frequency. This is what we might have expected based on the linear modes because we have adopted stress-free boundary conditions and the convection is only weakly turbulent. There is no obvious pattern in the spatial distribution of negative and positive contributions, nor is there an obvious change in the spatial distribution between the low and high-frequency cases.

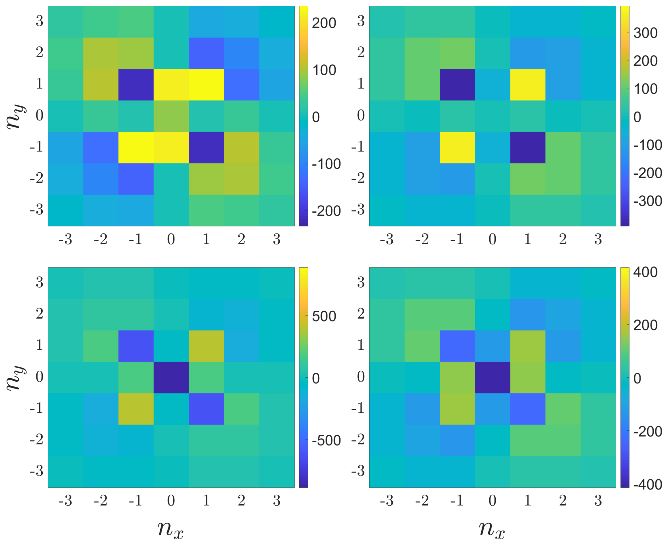

Figure 5.9: Temporally-averaged and vertically-integrated $\hat{R}_{xy}(k_x, k_y)$ spectrum as a function of integer wavenumbers $n_x = L_x k_x/2\pi$ and $n_y = L_y k_y/2\pi$ in four simulations with $\omega = 10, 100, 1000, 10000$ (top left, top right, bottom left, bottom right, respectively), all with $R = 100$ and $a_0 = 0.05$. This shows that the dominant scales for the Reynolds stress are the box-scale x and y-aligned convection rolls, but that other modes also contribute.

In order to determine the dominant spatial scales contributing to both positive and negative values of ν_E, we performed a horizontal Fourier transform of the point-wise Reynolds stress. The contribution to ν_E due to each (k_x, k_y) mode is given by

$$\hat{\nu}_E(k_x, k_y) = \frac{-1}{2a_0\omega(T - T_0)} \int_{T_0}^{T} \hat{R}_{xy}\cos(\omega t)\,\mathrm{d}t\,, \tag{5.3}$$

where T_0 and T are the start and end times of our simulation. We have defined

$$\hat{R}_{xy}(k_x, k_y, t) = \frac{1}{4}\int_0^1 \hat{u}_x(k_x, k_y, z, t)\,\hat{u}_y^*(k_x, k_y, z, t) + \text{c.c.}\ \mathrm{d}z\,, \tag{5.4}$$

where c.c. denotes the complex conjugate and hats denote a horizontal Fourier transform. Note that ν_E is obtained by summing up $\hat{\nu}_E(k_x, k_y)$ over all of the modes, and we have used this to verify our method (some small differences remain due to the timestep being larger in

---

[2] Eq. 2.62 is computed from the volume averaged Reynolds stress and hence the equivalence.

the data used to compute the spatial structure).

First we show a temporal average of $\hat{R}_{xy}$ on the (k_x, k_y)-plane in Fig. (5.9), where the axis values represent the integer wavenumbers. The largest-scale modes provide the dominant contribution to ν_E, particularly the box-scale x and y-aligned convection rolls, though smaller scales also contribute non-negligibly.

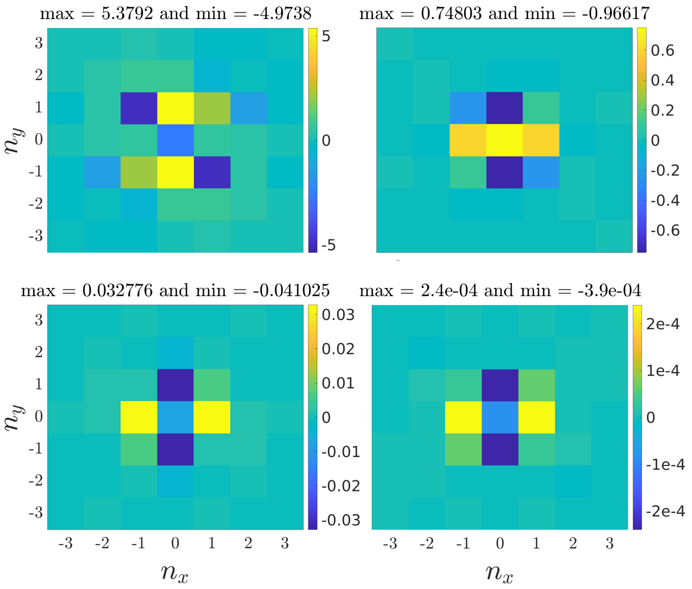

Figure 5.10: Spatial spectrum of $\hat{\nu}_E$ (eq. 5.3) as a function of the integer wavenumbers $n_x = k_x L_x/2\pi$ and $n_y = k_y L_y/2\pi$, which represents the dominant contributions to ν_E due to different horizontal wavenumber modes. The cases shown are all for $R = 100$ and $a_0 = 0.05$, with $\omega = 10, 100, 1000, 10000$ (top left, top right, bottom left, bottom right, respectively).

We plot $\hat{\nu}_E(k_x, k_y)$ on the integer (k_x, k_y)-plane in Fig. 5.10, which shows the contributions due to each mode to ν_E. The higher frequency cases with $\omega \in \{100, 1000, 10000\}$ show that the x-aligned roll $(n_x = 0, n_y = 1)$ provides a negative contribution to ν_E, and the y-aligned roll $(n_x = 1, n_y = 0)$ provides a positive contribution. This is in accord with our expectations based on laminar convection in § 3.2.1 and 3.2.2, as well as the theory in Ch. 4. The lowest frequency case with $\omega = 10$ behaves differently however, but this is a case where the theory does not apply. In that case, the x-aligned roll component provides a positive contribution to ν_E.

Finally, we show the temporal Fourier transform[3], which we will refer to as the frequency spectrum, of the volume-averaged Reynolds stress, $\tilde{R}_{xy}$ and kinetic energy $\tilde{E}$ as a function of frequency $\tilde{\omega}$, where $\tilde{\omega}$ is the angular frequency $2\pi f$, in Fig. 5.11. These quantities are shown for one low-frequency simulation with $\omega = 100$ (with $\nu_E > 0$) and one high-frequency case with $\omega = 1000$ (with $\nu_E < 0$). The forcing frequency ω is indicated by the grey dashed vertical line. This shows that when $R = 100$, the flow contains a wide range of frequencies, and that there is a peak at the forcing frequency ω. We observe that $\omega = 100$ coincides with a part of the $\tilde{E}$ spectrum with a shallow negative slope for a decade or so in $\tilde{\omega}$, potentially coinciding with an inertial range. On the other hand, $\omega = 1000$ lies above a transition in $\tilde{E}$ to a steeper decay with $\tilde{\omega}$, potentially indicating frequencies in the dissipation range. We speculate that the sign of ν_E may be related to whether ω lies in the inertial (positive ν_E) or dissipative (negative ν_E) frequency range. If this is true then higher R would result in an inertial range that extends to higher frequencies, hence we would require a larger value of ω to obtain negative ν_E. Although our findings of negative ν_E values are robust for high frequencies, it would be worth simulating more turbulent cases with larger R to explore this further. Indeed, we will explore this issue further in Ch. 6.

---

[3] A more in depth description of the temporal Fourier transform will be given in Ch. 6.

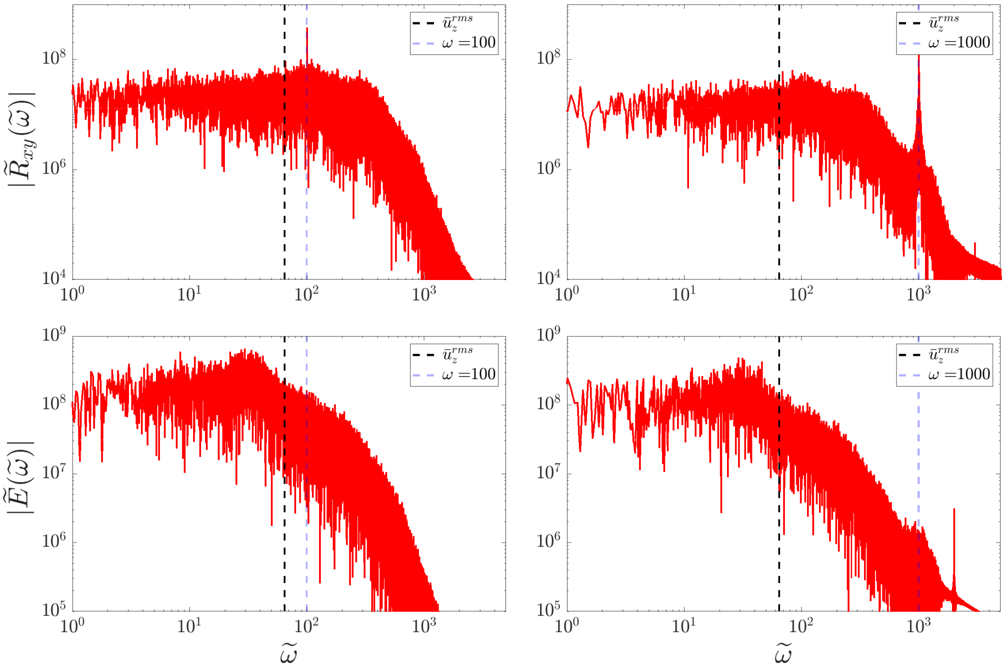

Figure 5.11: Temporal power spectrum of Reynolds stress $\tilde{R}_{xy}$ (top row) and kinetic energy $\tilde{E}$ (bottom row) as a function of frequency $\tilde{\omega}$ for one low-frequency case with $\omega = 100$ (left column) and one high-frequency case with $\omega = 1000$ (right column). The black dashed line highlights the respective convective frequency while the dashed grey/blue line highlights the shear frequency.

5.2.2 Effects of varying Pr

Our simulations until now have all adopted $\mathrm{Pr} = 1$, which is the most convenient choice computationally. In stellar interiors however, $\mathrm{Pr} \ll 1$ (e.g. 10^{-6} at the base of the solar convection zone), and in the mantles of terrestrial planets, $\mathrm{Pr} > 1$. It is therefore important to determine how changing Pr modifies our results. This is particularly important because the theory in Ch. 4 identifies the key role of the temperature perturbation in producing negative values for ν_E. To do this, we have performed two sets of additional simulations with $R = 100$ with both $\mathrm{Pr} = 0.1$ and $\mathrm{Pr} = 10$. We show the u_x and u_y velocity field in a snapshot from an illustrative simulation with each Pr in Fig. 5.12, which can be compared with the $\mathrm{Pr} = 1$ case in Fig. 5.1.

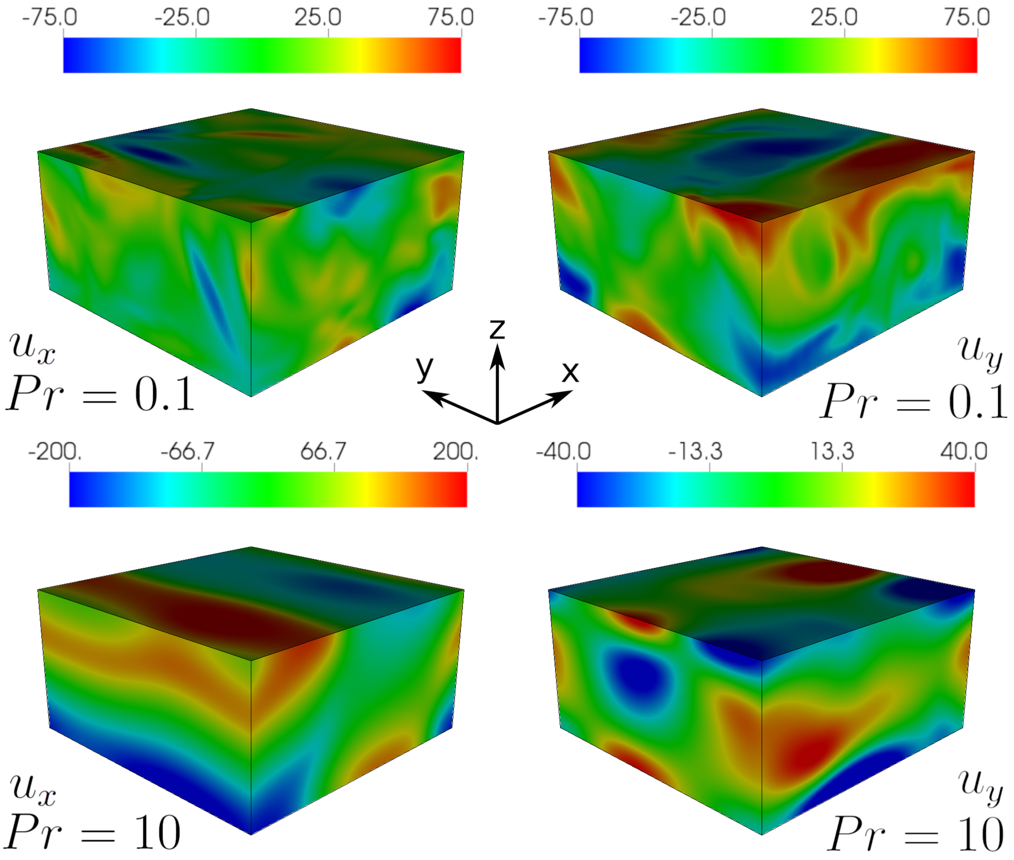

Figure 5.12: Snapshot of u_x (left) and u_y (right) for $R = 100$, $a_0 = 0.05$, $\omega = 1000$, at time $t = 175$, with $\mathrm{Pr} = 0.1$ and $\mathrm{Pr} = 10$ (top and bottom, respectively). This can be compared with Fig. 5.1 and shows the effects of varying Pr on the flow.

Aside 5.2: The Prandtl number

As is clear from eq. 2.28, the Prandtl number is the ratio of viscous to thermal diffusion. What is less obvious is what this means for the behaviour of the fluid. The first important thing to note is that this quantity is a material measure which does not depend on the geometry or boundary conditions of the problem.

For flows with large Prandtl number, $\mathrm{Pr} \gg 1$, the flow is dominated by the viscous term while small Prandtl number, $\mathrm{Pr} \ll 1$, the flow is dominated by the advective and convective nonlinearities. For a fixed Rayleigh number an increase of the Prandtl number tends to lead to weaker fluctuations in the velocity (flow structures larger than thermal structures) while a decrease tends to lead to more turbulent flows (flow structures smaller than thermal structures). Astrophysical examples of a high and low Prandtl number flow is that of the mantles of terrestrial planets and the interiors of stars respectively.

For more detail on the effects of Prandtl number see Goluskin (2016); Verma (2018).

We show the frequency-dependence of the effective viscosity from these simulations in Fig. 5.13. This figure can be compared with the simulations with $\mathrm{Pr} = 1$ in Fig 5.5. To

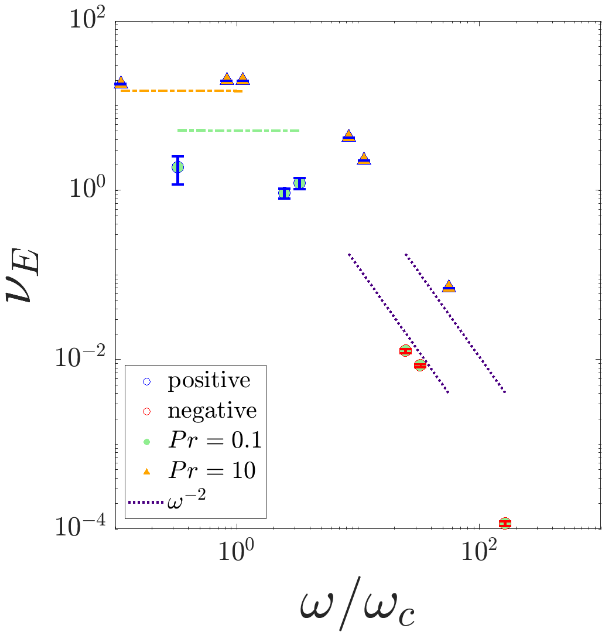

Figure 5.13: $\nu_E(\omega)$ as a function of frequency using the convective frequency scaling ω_c for two cases with $\mathrm{Pr} \in \{0.1, 10\}$ with $R = 100$ and $a_0 = 0.05$. This shows qualitatively similar behaviour to Fig. 5.5. Positive values are indicated by blue symbols and negative quantities by red. We have used $\alpha = 1/6$ for the low-frequency constant of proportionality.

allow these simulations to be most clearly distinguished, we have not re-scaled the y-axis ν_E values, and our use of the thermal timescale as our unit of time in the governing equations means that ν_E is expected to move upwards as we increase Pr if this scales in the way predicted by mixing-length theory ($\nu_E \propto \sqrt{\mathrm{Ra}\,\mathrm{Pr}}$, see aside 2.4). We also plot the mixing-length scaling that fits our laminar simulations ($\frac{1}{6}u_z^{rms}$) as the horizontal dashed lines in this figure.

For both $\mathrm{Pr} = 0.1$ and 10 we also obtain a frequency-independent ν_E for $\omega/\omega_c \lesssim 5$, which transitions to $\nu_E \propto \omega^{-2}$ at higher frequencies. At low frequencies, the simulations with $\mathrm{Pr} = 10$ most closely agree with the mixing-length scaling obtained in our laminar simulations, in comparison with the simulations with $\mathrm{Pr} = 0.1$, which has slightly smaller values of ν_E. This is presumably because the velocity field in the case with $\mathrm{Pr} = 0.1$ contains more smaller scale eddies, as we can see by comparing the top and bottom panels of Fig. 5.12. When $\mathrm{Pr} = 0.1$, ν_E transitions to negative values for $\omega \gtrsim 10\omega_c$, similar to our previously-presented cases with $\mathrm{Pr} = 1$. On the other hand, our simulations with $\mathrm{Pr} = 10$ do not exhibit a transition to negative values in this range of ω. The occurrence of negative effective viscosities at high frequencies may provide support that such values could be possible in stellar interiors, where Pr is small.

5.2.3 $R = 1000$ with $L_x = L_y = 2$

We now move on to analyse more turbulent simulations with $R = 1000$ and $a_0 = 0.05$ with $\mathrm{Pr} = 1$. We use a resolution of $(N_x, N_y, N_z) = (128, 128, 64)$, which was found to be sufficient for the flow to be well-resolved. In these cases, the flow is fully three dimensional and time-variable. We show the u_x and u_y components of the flow in a snapshot at $t = 175$ in a simulation with $\omega = 50000$ in Fig. 5.14. We also plot the wavenumber (horizontal power) spectrum of the kinetic energy $\hat{E}(k_\perp)$ as a function of $k_\perp$ in Fig 5.15. The flow consists of many modes, though the box-scale rolls are still energetically dominant.

The effective viscosity is plotted as a function of frequency in Fig. 5.16. This shows very similar behaviour to $R = 100$ (Fig. 5.5) in that ν_E remains approximately independent of

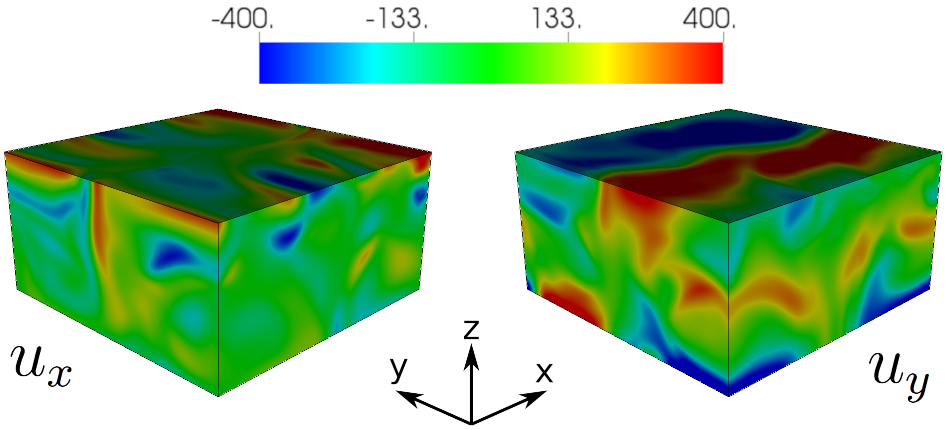

Figure 5.14: Plots of the u_x (left) and u_y (right) components of velocity for the cases $R = 1000$, $a_0 = 0.05$, $\omega = 50000$ and $t = 21$.

Figure 5.15: Kinetic energy spectrum for a simulation with $R = 1000$, $a_0 = 0.05$ and $\omega = 1000$. The Kolmogorov scaling $(-5/3)$ is shown as the red dotted line and the aliasing scale is shown as the blue dashed vertical line.

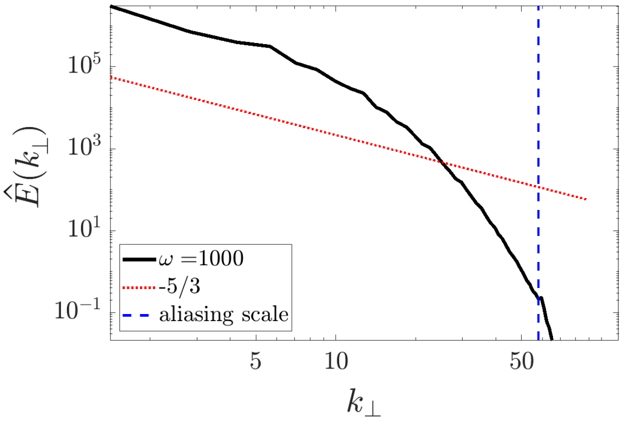

ω for $\omega \lesssim 5\omega_c$. When $\omega \gtrsim 10\omega_c$, there is a transition to negative values with magnitudes falling off such that $|\nu_E| \propto \omega^{-2}$. As with the simulations in § 5.2.1, we find that ν_E is smaller than we would expect based on extrapolating the mixing-length scaling that applies to our laminar simulations. Indeed, ν_E is less efficient than $(d/6)u_z^{\mathrm{rms}}$ (where $d = 1$ in our nondimensionalization), which was previously found to describe the laminar simulations. This is potentially due to the dominant length-scales being smaller than d. It is unclear whether larger horizontal boxes would lead to larger ν_E values, and this will be explored in Ch. 6.

We show the effective elasticity (S_E) as a function of frequency in Fig. 5.16. This shows similar behaviour to the results for $R = 100$ shown in Fig. 5.7, in that for $\omega \gtrsim \omega_c$ we find that S_E becomes independent of frequency. However, in the low-frequency regime, when $\omega \lesssim \omega_c$, S_E exhibits non-monotonic behaviour in this case. It is worth noting that the evaluation of S_E for low frequencies is increasingly sensitive to error[4], making this regime difficult to probe.

We show the spectrum of $\hat{\nu}_E(k_x, k_y)$ on the integer (k_x, k_y)-plane for the simulation with $\omega = 1000$ (with $\omega_c \approx 178$) in Fig. 5.17, which shows the contributions to the effective viscosity due to the various modes. Multiple modes contribute to the effective viscosity in this case, but the x-aligned (y-aligned) roll continues to provide a dominant negative (positive) contribution.

---

[4] This sensitivity comes from considering the integral used in evaluation of S_E, eq. 2.73, where in cases with small ω we require time averaging over many tidal periods. This is exasperated by the small values of S_E in this regime.

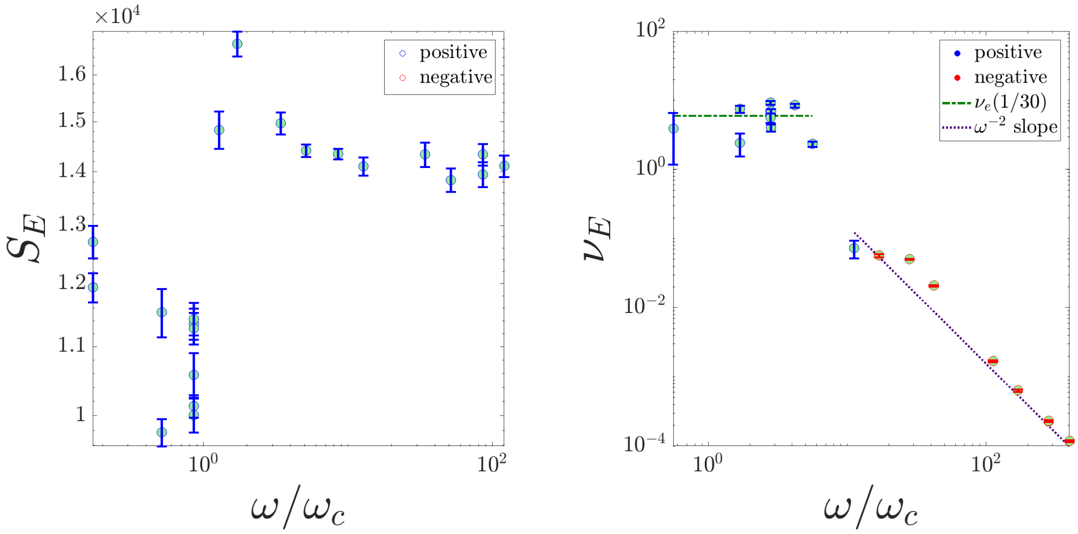

Figure 5.16: Plots of $S_E(\omega)$ (left) and ν_E (right) scaled by the convective frequency ω_c for various simulations with $R = 1000$ and $a_0 = 0.05$. The effective elasticity is found to be positive for all values of ω explored. For the effective viscosity, positive quantities are indicated by blue symbols and negative quantities by red. We also denote an ω^{-2} power law to the high-frequency regime where $\omega > \omega_c$ by a purple dotted line.

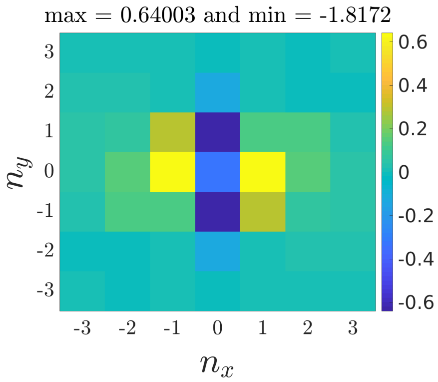

Figure 5.17: Spectrum of $\hat{\nu}_E$ as a function of integer (k_x, k_y) for a simulation with $R = 1000$, $a_0 = 0.05$ and $\omega = 1000$. The largest and smallest amplitude is indicated above the figure.

In this case the 3D modes also contribute appreciably.

Our simulations with $R = 100$ and $R = 1000$, and those with $R = 100$ with smaller Pr, indicate broadly similar results. Further work is required to explore more turbulent regimes with larger values of R, as well as simulations with larger boxes (see Ch. 6), to explore the robustness of these results.

5.3 Discussion

We will now discuss the results of Ch. 3 and this chapter which explore laminar and turbulent convection and its interaction with a prescribed tidal flow in a small domain.

Our simulations have demonstrated that the effective viscosity describing the damping (or otherwise) of large-scale tidal flows through their interaction with convection exhibits two (or possibly three) regimes. For low tidal frequencies such that $\omega \lesssim 5\omega_c$, we obtain a frequency-independent ν_E, which approximately agrees with the eddy viscosity from the mixing-length theory of convection (to within a constant factor e.g. Böhm-Vitense 1958; Zahn 1989). When

$\omega \gtrsim 5\omega_c$, we observe that $\nu_E \propto \omega^{-2}$, implying a significant reduction in the effective viscosity at high frequencies (e.g. Goldreich & Nicholson 1977). In the high-frequency regime, we also observe ν_E to become negative, indicating the intriguing possibility of tidal anti-dissipation. Broadly, our results are consistent with Ogilvie & Lesur (2012) and Braviner (2015), but we used a different setup to model the convection.

R	$\alpha = \overline{\left(\frac{\nu_E}{\bar{u}_z^{\rm rms}}\right)}$	$\beta = \overline{\nu_E \omega^2}$	$\bar{u}_z^{\rm rms}$
2_x	0.160	674	5.50
2_y	0.163	631	5.47
$2\ (4 \times 4 \times 1)$	0.355	360	4.25
5_x	0.174	5079	13.44
5_y	0.174	3691	13.44
10_x	0.146	13882	22.86
10_y	0.150	10921	22.88
100	0.051	17002	64.44
$100\ (4 \times 4 \times 1)$	0.193	20842	48.87
1000	0.033	622001	178.09

Table 5.1: Table listing values and scalings for the effective viscosity as a function of R in both the low and high-frequency regimes, as well as the typical rms vertical velocity. For the laminar simulations, in the first column we use a subscript on the R value to indicate whether the flow consists of x or y-aligned convection rolls. The values of $\bar{u}_z^{\rm rms}$ are obtained by taking an average over all simulations with this value of R (and roll orientation) for $\omega < \omega_c$.

In Table 5.1, we list the values of α and β used to fit $\nu_E = \alpha \bar{u}_z^{\rm rms} d$ in the low-frequency regime, and $\nu_E = \beta\omega^{-2}$ in the high-frequency regime. In Fig. 5.18 we also show a comparison of the vertical convective velocity with the mixing-length scaling as a function of R (taking an average over all simulations with this value of R). This shows that the convective velocity approaches a diffusion-free mixing-length scaling ($\bar{u}_z^{\rm rms} \propto \sqrt{R}$) for $R \gtrsim 10$. On the other hand, we observe a departure in ν_E from the mixing-length expectation, with α depending on R, tending to decrease as R is increased. We speculate that this may be due to the convection being constrained by the horizontal box size in the simulations with the largest R. Evidence in favour of this hypothesis includes the value of α increasing in simulations with $R = 100$ as we increase the box size from $L_x = L_y = 2$ to $L_x = L_y = 4$, as listed in Table 5.1, in addition to the energy spectrum in e.g. Fig. 5.15. Simulations with larger L_x and L_y are required to explore this issue further, and these will be described in Ch. 6.

Our observation that $\nu_E \propto \omega^{-2}$ when $\omega \gg \omega_c$ is robust as to whether we simulate laminar convection, with only one scale, or turbulent convection with many (spatial and temporal) scales. Furthermore, our results demonstrate that the largest spatial scales (locally) are those that primarily contribute to the effective viscosity. The phenomenological arguments of Goldreich & Nicholson (1977), which extended Zahn (1966) to a turbulent flow with a Kolmogorov spectrum, assumed that only eddies with turnover times faster than the tidal period, corresponding with short spatial scales, contribute to the effective viscosity (see § 1.3.3). This argument is at odds with our finding that it is the largest spatial scales that dominate this interaction. Therefore, even though we obtain a quadratic frequency reduction like Goldreich & Nicholson (1977), our simulations do not support their theoretical arguments for the reason

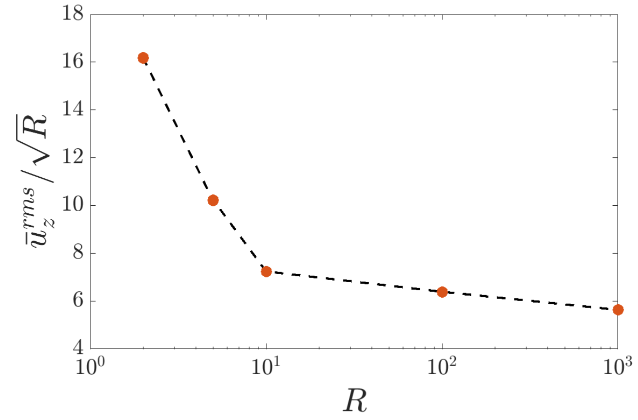

Figure 5.18: Comparison of the rms vertical convective velocity with the mixing-length scaling, plotting $\bar{u}_z^{\mathrm{rms}}/\sqrt{R}$ as a function of R. This indicates a trend towards $\bar{u}_z^{\mathrm{rms}} \propto \sqrt{R}$ for large enough R.

behind this scaling. It would be worth exploring further the fundamental mechanism that results in the attenuation of the effective viscosity, perhaps by building upon the theory in Ch. 4. We will revisit this issue in Ch. 6.

It is worth pointing out that in our more turbulent simulations the magnitude of the negative values of ν_E is smaller than the molecular viscosity ν_{mol} (which is equal to one in each of the figures with $\mathrm{Pr} = 1$) in the high-frequency regime. Whether or not the negative values would become important in reality for tidal evolution depends partly on whether ν_E increases with R in the high-frequency regime so that it exceeds ν_{mol}. In our cases with larger R the negative values of ν_E increase as R is increased (see Table 5.1), but these values remain smaller than ν. If this remains the case at larger R, the negative ν_E values would not be astrophysically significant for tidal evolution. In our limited exploration into the effects of changing Pr we found that decreasing Pr results in similar negative values for ν_E at high frequencies to the case with $\mathrm{Pr} = 1$, but this remains to be confirmed in a more extensive parameter survey.

Our simulations adopted the Boussinesq approximation, which means that they are strictly applicable to studying the local interaction between convection and tidal flows on scales that are much smaller than a pressure scale height. In stars, the convective velocities (and length-scales) vary with radius, typically increasing (decreasing) as we approach the stellar surface, where the validity of a Boussinesq model will eventually break down. However, our results do indicate that the effective viscosity will be maximised, and therefore tidal dissipation will be dominated, by radii for which $\omega \lesssim 5\omega_c$, which typically involve radii closer to the stellar surface than to the base of the convection zone. This issue will be explored further in Ch. 7.

Another caveat of our model is that we have followed Ogilvie & Lesur (2012) in only simulating one component of the tidal flow, corresponding with an oscillatory shear flow. In reality (even in a non-rotating homogeneous body with a circular companion), the tidal flow would contain additional components as we discussed in Ch. 2. We have not demonstrated in this thesis whether these other components would behave in a similar manner to produce negative values for ν_E, and this would be worth exploring further.

Summary: Key findings

Note that this summary is for the turbulent cases only and can be combined with that of the laminar cases presented in Ch. 3.

- Low ω regime ($\omega < \omega_c$),
    - ν_E is frequency independent (consistent with the constant time lag, § 1.3.1),
    - ν_E is strictly positive,
    - S_E follows a polynomial power law.
- High ω regime ($\omega > \omega_c$),
    - $\nu_E \propto \omega^{-2}$ (consistent with the quadratic reduction model, § 1.3.3),
    - ν_E transitions from positive to negative with increasing ω,
    - S_E is frequency independent.
- In both regimes the largest scales dominate the contribution to ν_E,
- S_E follows the laminar findings for $\mathbf{e}_y$ aligned rolls.

Chapter 6

Interaction between tides and turbulent convection in large domains

Contents

The purpose of this study is to build upon previous chapters, which explored the interaction between Rayleigh-Bénard convection and an oscillatory tidal-like flow in Cartesian domains, by exploring larger domain sizes and by performing a much wider parameter survey. Despite the results of Ch. 3-5 agreeing with the power law proposed by Goldreich & Nicholson (1977) for high frequencies, our observation that the largest scales dominated the effective viscosity differs from the mechanism proposed in their theory. Indeed, in Ch. 5, we found that the largest scales were comparable with the domain size, and thus an investigation into the impact of any constraints of adopting such a limited domain size is important. Our wider parameter survey will also enable us to explore the effective viscosity not just for the highest forcing frequencies, but over a wide range of astrophysically relevant frequencies. As well as investigating larger domains, and guided by Penev et al. (2009b) and Vidal & Barker (2020b) we explore further the turbulent statistics of the convection, both with and without the tidal shear. This will enable us to determine if the nature of the turbulence, and its statistical properties, is key to understanding the frequency-dependence of the effective viscosity. If so, this would provide an important advance in our understanding of this mechanism.

Between the work presented in Ch. 3-5 and the work in this chapter another relevant paper was published, Vidal & Barker (2020b). The authors explored the effective viscosity dependence within a sphere which was homogeneously heated[1]. The model used studied the full tidal flow in a homogeneous star/planet of eq. 2.19 rather than the single component that we consider. They recovered the $\nu_E \propto \omega^{-2}$ power law in the high-frequency regime. More interestingly they observed hints at a frequency dependence in what was referred to as the “anomalous range” which suggested an ω^{-1} scaling. They also showed hints that this may be connected to the

---

[1] Essentially what this means is that instead of a heat source at some boundary there is heating throughout the domain.

frequency spectra but due to the computational cost of these simulations were not able to probe sufficiently low frequencies to demonstrate this conclusively.

A summary of relevant findings up to the time of the work in this chapter can be found in table. 6.1.

6.1 Preliminaries

As with the work in Ch. 3 and 5 we will find it helpful to evaluate the 1D horizontal wavenumber spectrum (spatial), which we will now provide a more rigorous description of. To obtain this we first Fourier transform the three velocity components in the two horizontal directions to obtain the discrete version of ($j = x, y$ or z)

$$\hat{u}_j(k_x, k_y, z, t) = \int_{-\infty}^{\infty}\int_{-\infty}^{\infty} u_j(x, y, z, t) e^{i(k_x x + k_y y)} \, \mathrm{d}x \, \mathrm{d}y. \tag{6.1}$$

The 1D horizontal energy spectrum is then defined by writing $k_x = k_\perp \cos\theta$, $k_y = k_\perp \sin\theta$, time-averaging and vertically integrating, so that

$$\hat{E}(k_\perp) = \lim_{T\to\infty} \frac{1}{2T} \int_0^T \int_0^1 \int_0^{2\pi} (\hat{u}_x\hat{u}_x^* + \hat{u}_y\hat{u}_y^* + \hat{u}_z\hat{u}_z^*) \, k_\perp \, \mathrm{d}\theta \, \mathrm{d}z \, \mathrm{d}t. \tag{6.2}$$

Here $\hat{\bullet}$ defines Fourier transformed quantities, $\bullet^*$ defines complex conjugates.

In our simulations, k_x and k_y take on the discrete values

$$k_x = \frac{2\pi n_x}{L_x}, \quad k_y = \frac{2\pi n_y}{L_y}, \tag{6.3}$$

where n_x and n_y are integers (smaller than or equal to $N_x/2 = N_y/2$), so we approximate eq. 6.2 by considering rings with fixed width in wavenumber space. In simulations with various $L_x = L_y$ for each R we select the number of $k_\perp$ values $N_\perp = N_x^{\text{largest}}$ where N_x^{largest} is the number of k_x values in the largest domain with length[2] L_x^{largest}. We also pick the maximum k_x value in the largest domain to evaluate $k_\perp$. We then define the set of $k_\perp$ values to be

$$k_\perp = \left\{ \frac{2\pi n_\perp}{L_x^{\text{largest}}} : n_\perp \in \mathbb{N}_0 < N_\perp \right\} \tag{6.4}$$

so that each ring has width $2\pi/L_x^{\text{largest}}$. For each ring we identify the set K of integer pairs (n_x, n_y) such that (k_x, k_y) lies inside the $k_\perp$ ring,

$$K = \left\{ (n_x, n_y) : \frac{2\pi n_\perp}{L_x^{\text{largest}}} \leq 2\pi\sqrt{\frac{n_x^2}{L_x^2} + \frac{n_y^2}{L_y^2}} < \frac{2\pi(n_\perp + 1)}{L_x^{\text{largest}}} \right\}. \tag{6.5}$$

We note that some of the $k_\perp$ bins contain no k_x , k_y values, and in such cases we remove this bin and interpolate between the adjacent bins.

---

[2] This was not required in Ch. 5 where we did not make comparisons of the spectrum between domain sizes, as such in Ch. 5 we simply use $N_\perp = N_x$.

Citation	Theory / Simulation	Power law	conditions	additional
Zahn (1966)	Theory	-1	from MLT type arguments	
Goldreich & Nicholson (1977)	Theory	-2	from MLT assuming Kolmogorov cascade	
Goldman (2008)	Theory	-2	by application of an idealised turbulence model	
Penev et al. (2007)	Simulation	-1	Compressible convection	used an invalid perturbative method based on Goodman & Oh (1997)
Ogilvie & Lesur (2012)	Theory	-2	multi-scale asymptotic analysis	
Ogilvie & Lesur (2012)	Simulation	-2	homogeneous convection	negative ν_E values tentatively obtained within the error
Braviner (2015)	Simulation	-2	ABC flow	
Duguid et al. (2020a) (Ch. 3 and 5)	Simulation	-2	Boussinesq Rayleigh-Bénard convection	negative ν_E values obtained for high frequencies (as well as for certain laminar flows)
Duguid et al. (2020a) (Ch. 4)	Theory	-2	extension to multi-scale asymptotic analysis of Ogilvie & Lesur (2012) to include thermal effects	negative ν_E values predicted for certain laminar flows
Vidal & Barker (2020b)	Simulation	-2	Boussinesq, homogeneously heated, full sphere	in the high-frequency regime
Vidal & Barker (2020b)	Simulation	-1	Boussinesq, homogeneously heated, full sphere	for $\omega \sim \omega_c$
Vidal & Barker (2020a)†	Simulation	-2	Boussinesq, slowly rotating, homogeneously heated, full sphere	in the high-frequency regime
Vidal & Barker (2020a)†	Simulation	~ -0.6	Boussinesq, slowly rotating, homogeneously heated, full sphere	for $\omega \sim \omega_c$

Table 6.1: Summary of findings from the literature that motivated the work in this chapter sorted by chronological order. The table denotes if the findings are obtained analytically or from numerical simulations as well as the relevant power law for the frequency dependence of the effective viscosity. Brief details of the approach for each are provided. The study highlighted by † was performed in parallel to the results in this chapter.

Our numerical approximation to the 1D horizontal energy spectrum is then

$$\hat{E}(k_\perp) = \frac{1}{2(T-T_0)} \sum_{(n_x,n_y)\in K} \int_{T_0}^{T} \int_0^1 \hat{u}_x\hat{u}_x^* + \hat{u}_y\hat{u}_y^* + \hat{u}_z\hat{u}_z^* \, \mathrm{d}z \, \mathrm{d}t. \tag{6.6}$$

Note that every wavenumber pair (k_x, k_y) falls in exactly one ring, so the sum of $\hat{E}(k_\perp)$ over all $k_\perp$ rings exactly equals the sum over all horizontal wavenumber pairs. Our algorithm therefore partitions all of the temporally-averaged and vertically-integrated energy into bins which correspond approximately to a horizontal wavelength $2\pi/k_\perp$. This allows us to examine the energy contained in the various horizontal length-scales.

Ch. 5 as well as previous numerical work (Penev et al. 2009b; Vidal & Barker 2020b) has suggested that the frequency spectrum (temporal) of the kinetic energy, and/or Reynolds stress, may be important for determining the frequency dependence of the effective viscosity. In particular, it appears that for a certain "intermediate" range of frequencies (meaning for an interval around $\omega \sim \omega_c$), the Reynolds stress frequency spectrum may have the same frequency dependence as the effective viscosity (Vidal & Barker, 2020b), though this has not yet been demonstrated for low frequencies, and the spectrum may depend on the nature of the convection (e.g. Penev et al., 2009b). Therefore, we evaluate the frequency spectrum, which is a commonly used diagnostic in turbulent convection (e.g. Ashkenazi & Steinberg 1999; Kumar et al. 2014; Kumar & Verma 2018), by computing

$$\tilde{\Gamma}(\tilde{\omega}) = \int_{-\infty}^{\infty} H_w(t)\,\langle\Gamma\rangle(t)\,e^{i\tilde{\omega}t}\,\mathrm{d}t \quad \text{with} \quad \Gamma = (E, R_{xy})\,, \tag{6.7}$$

where $\langle\Gamma\rangle$ is the volume-averaged kinetic energy E or Reynolds stress R_{xy}, H_w is the Hann window function (Oppenheim & Schafer, 2010) which we have applied in order to reduce spectral leakage, and $\tilde{\omega}$ is the angular frequency. We present the frequency spectra with application of a 20-point moving average in order to clean up the signal. We will later plot these spectra by scaling $\tilde{\omega}$ by the convective frequency ω_c. For completeness we note that the kinetic energy is evaluated using

$$E(t) = \frac{1}{2L_xL_y} \int_0^{L_x} \int_0^{L_y} \int_0^1 \mathbf{u}\cdot\mathbf{u}\,\mathrm{d}z\,\mathrm{d}y\,\mathrm{d}x\,. \tag{6.8}$$

Despite Ch. 3-5 and previous work (see table. 6.1) finding agreement with Goldreich & Nicholson (1977) that $\nu_E \propto (\omega_c/\omega)^2$ for high-frequency tidal forcing, i.e. $\omega \gg \omega_c$, the mechanism they proposed has not been explored in detail. In particular, Goldreich & Nicholson (1977) proposed that with a short tidal forcing timescale τ_T the resonant eddies would have a small length-scale λ and small typical velocity u_λ corresponding to the values expected in a Kolmogorov cascade, $\lambda/l^{\mathrm{mlt}} \sim (\tau_T/\tau_{\mathrm{conv}})^{3/2}$ and $u_\lambda/u^{\mathrm{mlt}} \sim (\tau_T/\tau_{\mathrm{conv}})^{1/2}$ giving an effective eddy viscosity $\nu_E \sim \lambda u_\lambda \sim (\tau_T/\tau_{\mathrm{conv}})^2 \propto (\omega_c/\omega)^2$ (see § 1.3.3). However, Ch. 5 hinted that this argument may not be correct, since the large-scale energetically dominant convective modes appear to contribute the most to the effective viscosity, and the contributions appeared to fall off rapidly with increasing wavenumber. One shortcoming of our previous analysis was that the convection was intentionally simulated in a small horizontal domain (to enable a more straightforward comparison with asymptotic theory), but this artificially constrained the turbulent state, as the most energetically dominant modes were always at the box scale in these simulations. In this chapter, we revisit this issue with simulations in wider horizontal domains that are "more turbulent", and present an analysis of the time-averaged and vertically-integrated wavenumber (spatial) spectrum of the kinetic energy, $\hat{E}(n_x, n_y)$, and Reynolds stress, $\hat{R}_{xy}(n_x, n_y)$, where n_i are the integer wavenumbers $n_i = k_i L_i/\pi$, and $i = x$ or y. With this we are able to evaluate contributions to the effective viscosity from each wavenumber in the flow, enabling us to directly test the mechanism proposed by Goldreich & Nicholson (1977).

6.1.1 Parameter survey

In this work we explore the behaviour of four of the key parameters in the problem. Our main focus is the frequency dependence of the effective viscosity $\nu_E(\omega)$. Our new simulations build upon Ch. 3 and 5 by simulating wider horizontal domains ($L_x, L_y > 2$), leading to "more turbulent" convection for a given R, and by exploring further the low-frequency regime, $\omega < \omega_c$. The parameters of simulations presented in this chapter are summarised in Table 6.3 where the data for $L_x = L_y = 2$ is the same as that presented in Ch. 3 and 5 for cases with $\mathrm{Pr} = 1$. Further, we note that all simulations presented in this chapter have $\mathrm{Pr} = 1$. This brings the total number of simulations performed in this study to be in excess of 700. The strength of the convection is varied by varying R. Due to the demanding nature of these simulations, which for convergence of ν_E are required to be integrated for multiple tidal periods (in some cases this means hundreds of diffusion times), we are again limited to values of $R \leq 1000$, which is much smaller than the values expected in stars[3]. We therefore hope to find robust features in our simulations that can be extrapolated to real stars or planets. We also revisit here the dependence of ν_E on tidal amplitude a_0. Everything else, such as initial conditions, will be the same as described in § 3.1.

6.2 Results

6.2.1 Convection without shear

We begin our investigation by considering convection in the absence of oscillatory shear. In particular, for reasons that will become clear later on, we are interested in the wavenumber (eq. 6.6) and frequency spectra (eq. 6.7) of the kinetic energy (eq. 6.8) and Reynolds stress (eq. 2.52) and how these vary as the strength of the convective driving R, and domain size $L_x = L_y$ are varied.

We compute the wavenumber spectrum of the kinetic energy as described by eq. 6.6 for $R \in \{2, 100, 1000\}$ and various domain sizes $L_x = L_y \in \{2, 4, 8, 12, 16, 24, 32\}$. The results can be seen in Fig. 6.1. We ensure that the resolution per unit length for a given R is held constant in all but the smallest domains, which are slightly better resolved. This ensures that the de-aliasing scale, defined by $k_\perp^{\text{alias}} = 2\pi N_x/(3L_x)$ (where N_x is the number of grid-points in the x direction), occurs for the same value of $k_\perp$. These simulations have been found to be well resolved by comparing the spectra for various resolutions.

From these results we observe an energetically dominant peak in the spectrum at $k_\perp \approx 2$

---

[3] The convection zones of Sun-like stars are expected to have $\mathrm{Ra} \in [10^{21}, 10^{24}]$ and $\mathrm{Pr} \in [10^{-7}, 10^{-3}]$ (e.g. Hanasoge et al., 2016).

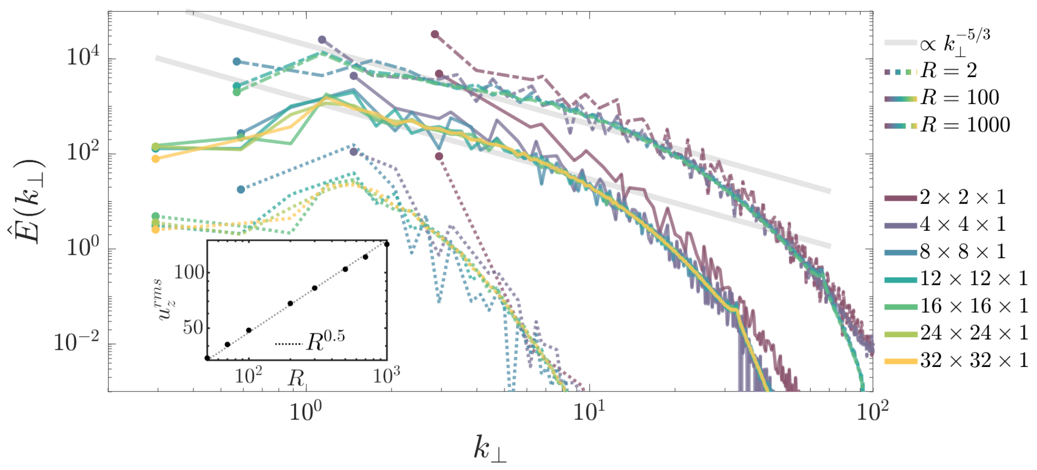

Figure 6.1: Time-averaged and vertically-integrated kinetic energy spectra, $\hat{E}$, as a function of horizontal wavenumber $k_\perp$, for $R \in \{2, 100, 1000\}$ (denoted by dashed, solid and dot-dashed lines, respectively) and various domain sizes (see legend) for convection in the absence of oscillatory shear ($a_0 = 0$). These spectra are visually indistinguishable (above the inherent variability within the convection) when a weak tidal shear is applied. The thick grey lines show the classical Kolmogorov $-5/3$ power law for the turbulent cascade of energy, for reference. The inset panel shows that the vertical convective velocities obey the classical diffusion-free mixing-length scaling derived in Ch. 2, for which $u_z^{\text{rms}} \propto \sqrt{R}$ (Spiegel, 1971). We note this data for the fixed domain size of $(8, 8, 1)$ corresponding to the cases displayed in Fig. 6.2.

(which, we note, is similar to the onset wavenumber $\pi/\sqrt{2}$), which corresponds to a length-scale of $L^{\text{peak}} \approx 3$, for each value of R. In cases with smaller L_x (such as those presented in Ch. 3 and 5), the energy is instead preferentially dominated by the largest wavelengths in the box. The spectrum in smaller domains is similar to those in larger domains except for the smallest $k_\perp$ values.

In the more turbulent cases with $R \in \{100, 1000\}$, we can see from Fig. 6.1 that they possess identifiable inertial ranges that extend from the peak of the spectrum until $k_\perp \approx (20, 30)$, respectively, which are consistent with the classical Kolmogorov $-5/3$ power law (e.g. Kolmogorov, 1941; Davidson, 2015). For even higher $k_\perp$, we observe a dissipation range in which the energy falls off faster with $k_\perp$. The cases with $R = 2$ for all domain sizes are laminar and lack a clear inertial range. We show in the inset panel of Fig. 6.1 that the convective velocities obey the classical diffusion-free scaling of mixing-length theory, such that $u_z^{\text{rms}} \propto R^{0.5}$ (see aside 2.4 noting that we have $\text{Pr} = 1$).

We note that in order to make fair comparisons the spatial resolution has been chosen such that the aliasing scale takes the same value of k_x, k_y. The result of this is that in the larger domains there are more k_x, k_y pairs to be distributed in the $k_\perp$ bins, which we note we have fixed for each R case. As such the smaller domains have lower resolution in $k_\perp$ space than the larger domains despite being equivalently resolved in real space, hence the increased variation in the spectrum for smaller domains. Various statistics for these cases can be seen in Table 6.2, which show that we attain convergence for sufficiently large $L_x = L_y$.

We next compute the frequency spectrum of the kinetic energy, as described by eq. 6.7, for various cases with $R \in \{50, 70, 100, 200, 300, 500, 700, 1000\}$ and a fixed domain size of

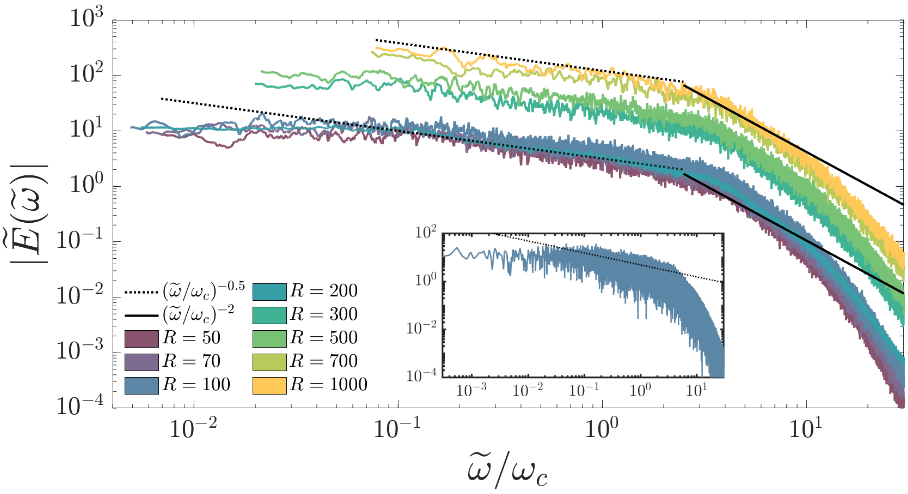

Figure 6.2: Frequency (temporal) spectra of the volume-averaged kinetic energy for various values of R (see legend), with a domain size of $(8, 8, 1)$ in the absence of oscillatory shear. The solid lines highlight the scaling expected in the inertial range of $(\tilde{\omega}/\omega_c)^{-2}$ for a Kolmogorov cascade. For frequencies above those in the inertial range, we observe a power law decay of magnitude greater than -2 which can be attributed to the dissipation range (beyond which lies high-frequency noise). The dotted lines represent the $(\tilde{\omega}/\omega_c)^{-0.5}$ power law that exists at frequencies lower than the inertial range until a flattening of the spectrum at very low frequencies (corresponding with white noise). We note that the displayed spectra represent smoothed 20-point moving averages of the full spectrum to reduce noise. The inset panel is an example of the frequency spectrum for the case of $R = 100$ before smoothing.

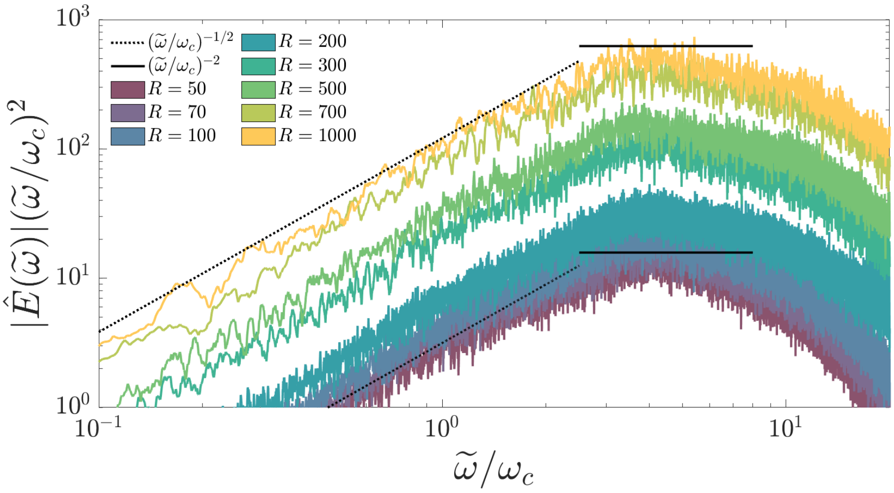

Figure 6.3: The same as Fig. 6.2 but with the spectra scaled by $(\tilde{\omega}/\omega_c)^2$ in order to highlight the short inertial range. The inertial range for the $R = 1000$ case is approximately $(3, 6)$ while it is vanishingly small for $R = 50$.

$(8, 8, 1)$, which has been guided by our analysis of the wavenumber spectrum. These are shown in figure 6.2, which are computed by using a 20-point moving average in order to smooth the original noisy signal (see insert). The angular frequency $\tilde{\omega}$ in each case has been scaled by the convective frequency.

R	$L_x(=L_y)$	u_x^{rms}	u_y^{rms}	u_z^{rms}	$N_x = N_y$	N_z	$E_\perp$
2	2	5.44	0	5.44	32	32	29.6
2	4	3.64	7.2	4.29	64	32	44.4
2	8	8.01	3.43	4.64	64	32	52.6
2	12	5.19	5.59	4.11	128	64	38.7
2	16	5.55	5.33	4.07	256	64	38.3
2	24	5.47	5.5	4.05	512	64	38.6
2	32	5.54	5.45	4.05	512	64	39.1
100	2	47.67	51.11	64.32	64	128	4637
100	4	61.01	59.81	48.98	64	128	4919
100	8	56.99	58.37	48.61	128	128	4527.4
100	12	58.49	58.03	48.11	192	128	4589.9
100	16	58.18	58.49	47.52	256	128	4570.2
100	24	58.29	58.8	47.71	384	128	4591
100	32	58.63	58.68	47.71	512	128	4604.4
1000	2	148.94	146.66	178.74	128	192	38783
1000	4	166.22	173.82	145.43	192	192	39643
1000	8	164.96	164.22	144.64	256	192	37302
1000	12	165.81	167.59	143.7	384	192	37937
1000	16	167.66	165.68	143.29	512	192	37963

Table 6.2: Table listing the time-averaged rms velocity components $u_i^{\text{rms}} : i \in \{x, y, z\}$, and the horizontal $N_x = N_y$ and vertical N_z resolutions, for each R and domain size. We evaluate the energy per horizontal unit area $E_\perp$ in each case. This table is associated with the un-sheared cases of convection reported in Fig. 6.2.

In the Kolmogorov description of turbulence, the inertial range follows a -2 power law in the frequency spectrum (Landau & Lifshitz, 1987; Kumar & Verma, 2018). This power law is highlighted in figure 6.2 by the solid black line. For each value of R, this inertial range begins at $\tilde{\omega}/\omega_c \approx 3$ and extends to higher frequencies with increasing R. In the case of $R = 1000$ this inertial range extends until $\tilde{\omega}/\omega_c \approx 6$ while for $R = 50$ the range is vanishingly small. This can more clearly be seen in Fig. 6.2 where we have re-plotted the data with application of an $(\tilde{\omega}/\omega_c)^2$ scaling factor (as well as zooming in on a narrower range of frequencies) which highlights the short inertial ranges. We observe a dissipation range above the inertial range, as is evident from the more rapid drop-off in the energy for higher frequencies. The key feature of this figure is our observation of a new power-law for intermediate frequencies $\tilde{\omega}/\omega_c \lesssim 3$, with an approximate exponent of -0.5 which extends over approximately two decades to lower frequencies. For very low frequencies, $\tilde{\omega}/\omega_c \lesssim 10^{-2}$, the spectrum then flattens off to indicate frequency-independent white noise. We note that not all of our spectra extend to low enough frequencies to observe the appearance of this white noise due to computational limitations.

Snapshots of the horizontal flow showing the u_x and u_y components of velocity at chosen times are presented in Fig. 6.4 for example simulations with $R \in \{2, 100, 1000\}$, all in $(8, 8, 1)$ domains. We note that these snapshots are also representative of cases including the oscillatory shear, since the flow is not strongly modified by its presence.

In the more turbulent cases, $R \in \{100, 1000\}$, the flow is fully three-dimensional and temporally chaotic for all domain sizes explored. As R is increased ever smaller features in the flow appear, which is consistent with the extension of the inertial range in Fig. 6.1. For

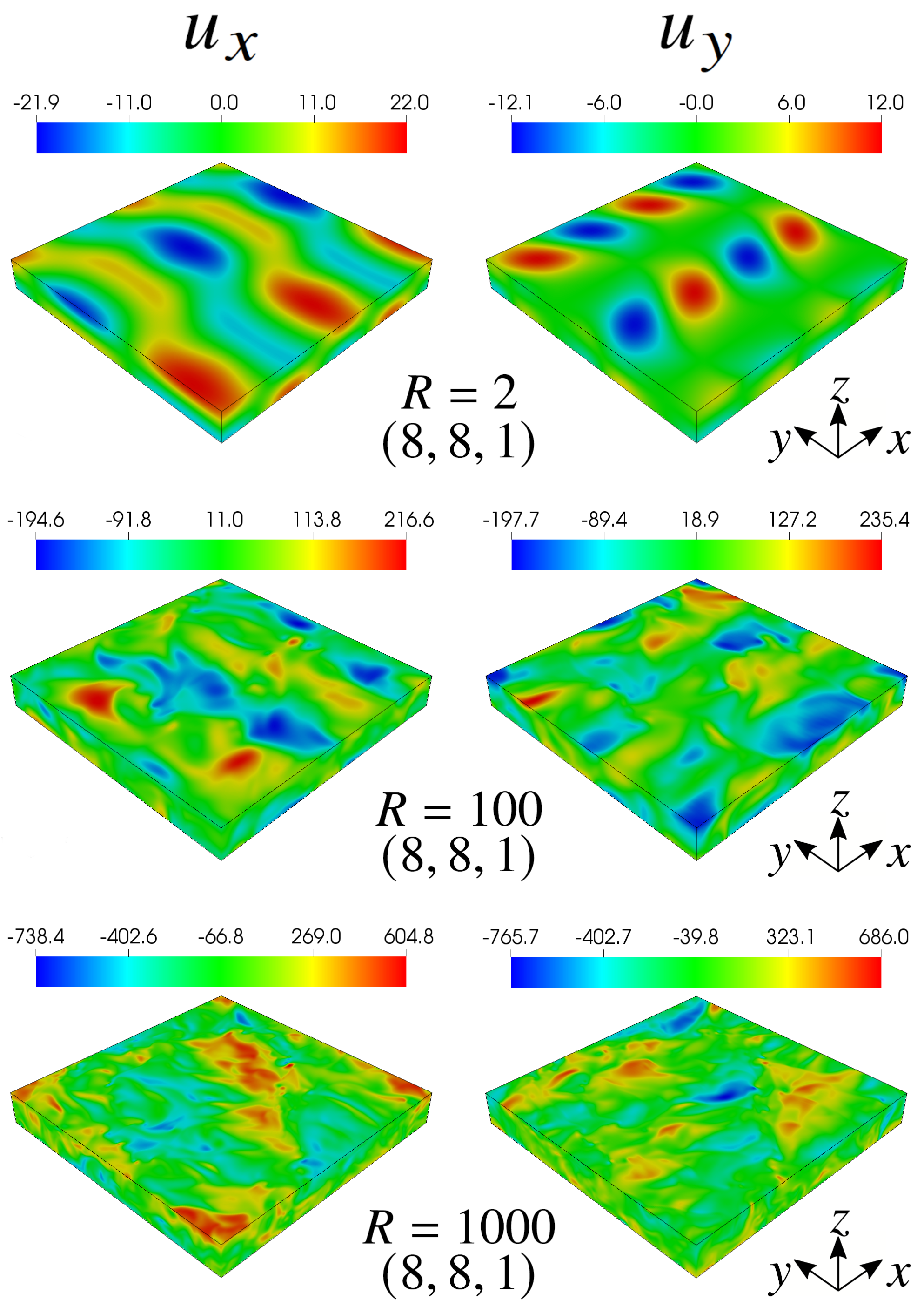

Figure 6.4: Snapshots of the u_x (left) and u_y (right) velocity components for convection in the absence of oscillatory shear. The values of $R \in \{2, 100, 1000\}$ and the domain size are displayed in each panel. As expected, as R is increased, ever smaller scales are manifested in the flow (as seen in the bottom three rows), though large-scale components remain. The flow in the sheared cases is similar.

the laminar cases with $R = 2$ the flow consists of spatially persistent features with temporally-periodic amplitudes that are similar to the results in smaller domains presented in Ch. 3. The frequency spectrum for this laminar case, and in smaller domains, consists of discrete peaks. On the other hand, we comment that $R = 2$ simulations in larger domains with $L_x = L_y \geq 12$ instead exhibit a chaotic flow (which is still non-turbulent due to the lack of an inertial range), with a frequency spectrum that is more similar to those with larger R values.

6.2.2 Frequency dependence of the effective viscosity

We now move on to the main task of this chapter, which is to analyse the interaction between oscillatory tidal (shear) flows and convection. Before we do we would like to make the reader aware that in what follows we will primarily make use of the scaled effective viscosity, α, defined in § 2.3.3 (see eq. 2.63). An important point is that α quantity strictly differs from the usual mixing-length parameter as it combines the usual mixing-length parameter with the constant of proportionality from relating the mixing length to the pressure scale height (see § 1.3.2).

The oscillatory (tidal) shear flow, described by Ch. 2, is now introduced and we begin by presenting results for the magnitude of the scaled effective viscosity α (eq. 2.63) in simulations with various values of $R \in \{2, 100, 1000\}$, $\omega = [0.001, 10000]$, $L_x (= L_y) \in \{2, 4, 8, 12, 16\}$ and $a_0 = [0.05, 1]$. Details of the typical ranges of these parameters for various cases, including further details such as the resolution, are given in Table 6.3. The results are presented in Fig. 6.5, where ω has been scaled by the relevant convective frequency ω_c. The main result here is that ν_E is a frequency-dependent quantity and is strongly attenuated for high-frequency tidal forcing, in agreement with the results in previous chapters and prior works (Ogilvie & Lesur 2012; Vidal & Barker 2020b).

In order to reduce the influence of noise on the computation of ν_E, we evaluate eq. 2.62 by computing the cumulative integral, to which we apply a linear fit to determine ν_E. This method also allows us to define an error in ν_E using two standard deviations from the mean slope, as adopted in Ch. 5. To ensure convergence, the simulations are run for tens to thousands of tidal periods (with the exception of some cases with $\omega < 0.1$ that could only be run for approximately one tidal period). These long-duration simulations were successful in reducing the error in the computation of ν_E, which is demonstrated by the small error bars in Fig. 6.5, which are typically smaller than the symbols plotted.

In the high-frequency regime $\omega/\omega_c \gtrsim 5$, for all values of R, we observe a clear -2 power law (represented by the dotted lines in Fig. 6.5). This corresponds with the high-frequency scaling law ($\nu_E \propto \omega^{-2}$) of Goldreich & Nicholson (1977), and clearly disagrees with the high-frequency scaling law ($\nu_E \propto \omega^{-1}$) of (Zahn, 1966). This result is consistent with Ch. 3-5, as well as prior simulations of similar problems (see Table. 6.1). The theory of Goldreich & Nicholson (1977) assumes a Kolmogorov turbulent cascade to obtain a -2 power law for ν_E. In Ch. 3 we noted that $R = 2$ simulations were laminar and yet still followed the -2 scaling. This remains true for the larger domains considered here, thus demonstrating that a turbulent flow is not required to obtain a -2 power-law scaling for ν_E at high frequencies. The behaviour of laminar convection with $R = 2$ can probably be explained by applying the asymptotic theory developed in Ch. 5, which extends that of Ogilvie & Lesur (2012), providing all convective modes are accounted for, though we do not attempt to do so here as our larger domains would require considering many modes. We will later show (see Fig. 6.8) that the scatter in the high-frequency regime for $R = 100$ can be attributed to an amplitude (a_0) dependence of α.

Fig. 6.5 provides evidence for a previously undiscovered scaling $\nu_E \propto \omega^{-0.5}$ for intermediate frequencies with $\omega/\omega_c \approx (10^{-2}, 1)$. This new regime is clearly observed in the middle panel with $R = 100$ in all domains with $L_x > 2$, and is highlighted by the solid line representing a -0.5 power law (this regime is also present with $R = 2$ in the largest domains $L_x \geq 12$). To the best

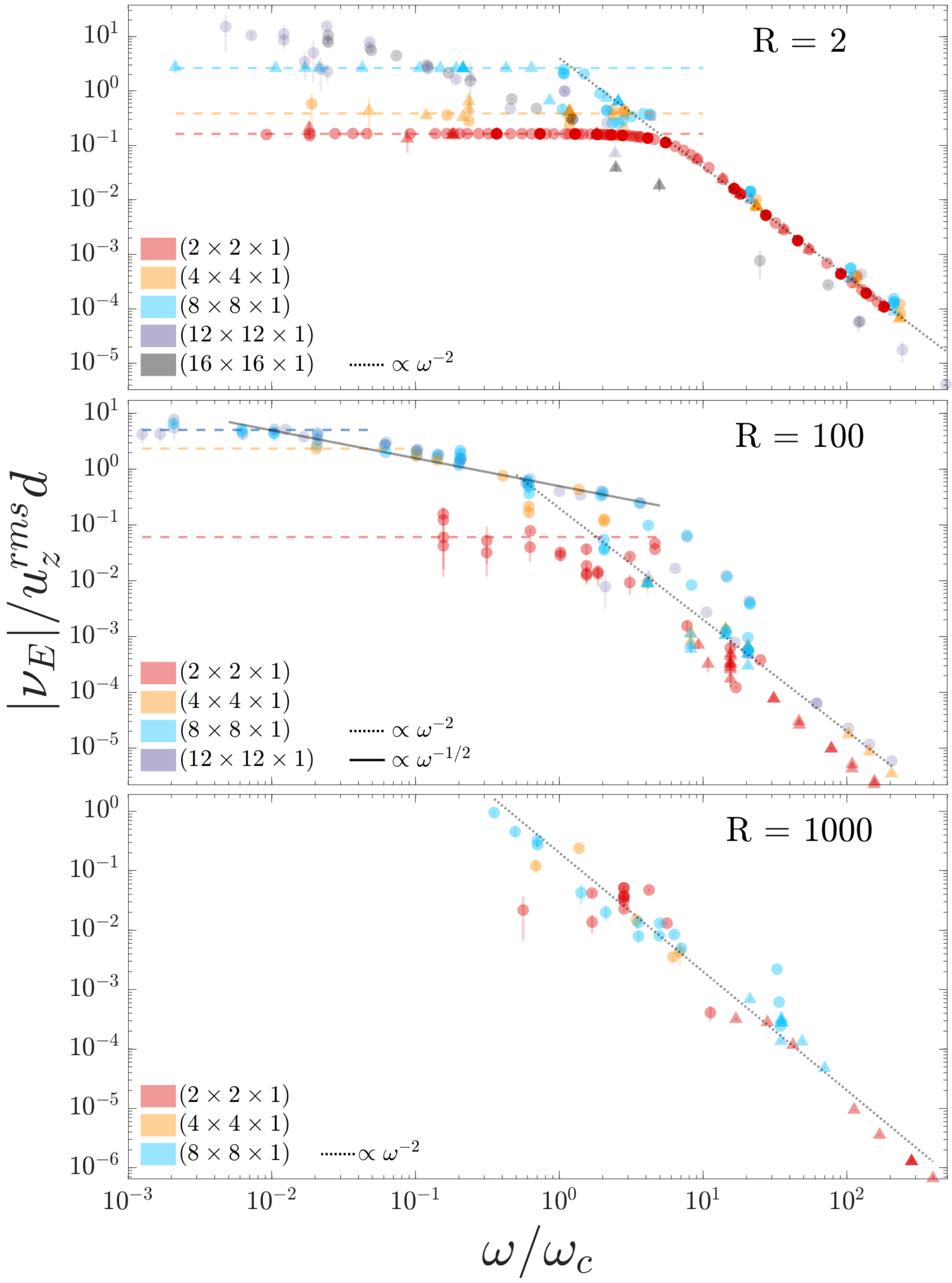

Figure 6.5: Scaled effective viscosity $|\nu_E|/u_z^{\mathrm{rms}}d$ as a function of scaled shear frequency, ω/ω_c, that arises from the interaction between the oscillatory tidal flow and convection. Various shear amplitudes are shown, in the range $a_0 \in [0.05, 1]$, and the effects of a_0 will be discussed later (and shown in Fig. 6.8). The cases shown have $R \in \{2, 100, 1000\}$ (top to bottom respectively) with various domain sizes (see legend). We denote the sign of the effective viscosity using circles for positive and triangles for negative values. Error bars are shown but these are often smaller than the sizes of the symbols. The dashed lines show horizontal fits to the low-frequency regime. The solid lines show the $(\omega/\omega_c)^{-0.5}$ scaling for intermediate frequencies, which is a new result in this work. The dotted lines show the classic $(\omega/\omega_c)^{-2}$ scaling for high-frequency tidal forcing. The scatter of points in the frequency range $\omega/\omega_c = (10^0, 10^2)$ for $R = 100$ and $\omega/\omega_c \approx 40$ for $R = 1000$ can be attributed to a shear amplitude dependence that is shown more clearly later in Fig. 6.8.

of our knowledge, this is the first time this scaling has been observed in simulations, and it has also never been predicted theoretically. The cases with $L_x = 2$ previously presented in Ch. 3 and 5 instead exhibit a frequency-independent ν_E for $\omega \lesssim \omega_c$. This difference demonstrates the importance of resolving the peak of the spatial spectrum (see Fig. 6.1). This new intermediate regime is not evident in the $R = 1000$ simulations, probably because we have not been able to run simulations for sufficiently low frequencies to observe it clearly (these cases are particularly computationally expensive). The lowest frequencies for $R = 1000$ may be starting to transition to this regime, but we are unable to confirm this at present.

For cases exhibiting an intermediate regime with a -0.5 power law, the magnitude of the scaled effective viscosity, α, becomes independent of the domain size and tidal amplitude, as long as the domain size is large enough to resolve the peak of the wavenumber spectrum (Fig. 6.1). We also note that the magnitudes of ν_E in the intermediate and low-frequency regimes are significantly larger than for the cases in smaller boxes. They are also larger, by more than an order of magnitude, from the naive expectation from MLT, which would predict $\alpha = 1/3$ (Zahn, 1989). This suggests that convection is more efficient at damping low-frequency tidal flows than previously expected.

The $R = 2$ case exhibits a change in behaviour in this intermediate frequency range as we increase the domain size, from frequency-independent behaviour in smaller boxes, to following a -0.5 power law in larger boxes. This coincides with our observation that the flow transitions from deterministic to chaotic in the largest boxes, as well as being related to the requirement to resolve the energetically dominant scales (see Fig. 6.1), which we will address further in section 6.2.3. Note that the flow is non-turbulent for $R = 2$, and yet it still exhibits the same -0.5 scaling for ν_E.

In Ch. 3 and 5 we observed a frequency independent regime for $\omega/\omega_c \lesssim 5$, which can be seen in Fig 6.5, in domain sizes of $(2, 2, 1)$ for all R (it also occurs in domains up to $L_x = 8$ for the $R = 2$ cases). In larger domains, this frequency-independent regime is only observed for very low frequencies, $\omega/\omega_c \lesssim 10^{-2}$. We have only observed this regime for $R = 100$ due to the computational expense of probing such low values of ω. Indeed, these typically require approximately 1000 diffusion times to obtain convergence in the evaluation of ν_E. Where possible, we have shown the best fit to the frequency-independent regime with dashed lines in Fig. 6.5.

On physical grounds, there are no restrictions on the sign of the effective viscosity defined by eq. 2.62 (see aside 1.5). Indeed, in Ch. 3-5, as suggested in the earlier simulations of Ogilvie & Lesur (2012), we observed robust negative values for ν_E for very high frequencies in the turbulent cases. In Fig. 6.5 we have denoted positive values with circles and negative by triangles. In Ch. 3, we found that in laminar cases the initial conditions determined the sign of ν_E. This behaviour is again observed in the $R = 2$ cases up to domain sizes of $(8, 8, 1)$. In the $(12, 12, 1)$ and larger cases, where the flow is chaotic, and there is an increase of energy transfer between convective modes, there appears to be a preference towards positive values for ν_E, with negative values only occurring around the transition between the intermediate and high-frequency regimes.

For the more turbulent $R \in \{100, 1000\}$ cases with the domain size $(8, 8, 1)$ we observe the same behaviour as in the smaller box simulations of Ch. 5, in that ν_E transitions from positive ($\omega/\omega_c \lesssim 10$) to negative values ($\omega/\omega_c \gtrsim 10$). However we note that for the $R = 100$ cases in the large domain $(12, 12, 1)$, ν_E is also positive for frequency ratios much larger than 10. We have also conducted simulations in small $(2, 2, 1)$ domains with $R = 10000$ (not presented) where the transition to negative values is shifted to higher frequencies, $\omega/\omega_c \approx 30$, than for $R \in \{100, 1000\}$. This suggests that the transition to negative values occurs for unrealistically high tidal frequencies in convection with astrophysically relevant values of R.

Convection in stars is much more turbulent, with much larger values of R, than we can explore in our simulations. One of our key goals is to determine if there are robust features or scaling laws as R is varied. In Fig. 6.6, we compare the scaled effective viscosity as a function of the scaled shear frequency for various values of $R \in \{50, 100, 200, 500, 1000\}$ in a fixed domain size $(8, 8, 1)$.

Fig. 6.6 shows the frequency dependence of ν_E in our simulations. We include a range of $R \geq 50$ in this plot, but by plotting $|\nu_E|/u_z^{rms} d$ we collapse the low-frequency data ($\omega/\omega_c < 1$) onto a single "master curve". This collapse is only observed in simulations in large domains that resolve the energetically dominant length-scale, for which further increases in domain size are not observed to strongly affect our results (see Fig. 6.5). The scaling adopted here assumes the convection to approach a diffusion-free mixing-length regime in which convective velocities scale as $\sqrt{R}$ (which is demonstrated in the inset panel in Fig. 6.1; e.g. Spiegel 1971), such that ω_c and ν_E would also be expected to scale as $\sqrt{R}$ (see aside 2.4). We have therefore demonstrated in Fig. 6.6 that the convective velocities (and dominant length-scales) for $R \geq 50$ are essentially in the diffusion-free mixing-length regime for our simulations. At higher frequencies, there is still considerable scatter which comes mainly from dependence on the shear amplitude a_0. In the inset, symbols $+$ correspond to $a_0 = 1$, $\bullet$ to $a_0 = 0.5$ and $\times$ to $a_0 = 0.05$. There is a systematic increase in ν_E with amplitude, which we will explore further below. However, the data for the same values of a_0 collapse reasonably well onto their R-independent curves even for high-frequency tides. For numerical reasons it is difficult to get consistent results for ν_E with low amplitude tides at low frequencies, so the low frequency points $\omega/\omega_c < 0.1$ are mostly for amplitudes above 0.5, but generally we found little evidence for significant variation of scaled effective viscosity with amplitude at low frequency.

The frequency-independent low frequency regime is observed when $\omega/\omega_c < 10^{-2}$, for each of $R = 50$, 100 and 200, though we should point out that there only are few simulations with such low frequencies. The dashed line in this case is the linear fit to the constant slope for the $R = 100$ cases, which also matches those with $R = 50$ and 200.

It is clear from Fig. 6.6 that the new intermediate scaling regime for $\omega/\omega_c \approx (10^{-2}, 1-5)$ holds for all R values explored, highlighting that this new regime is also robust. In the high-frequency regime, when $\omega/\omega_c \gtrsim 1-5$, we observe a robust transition to a -2 power law for all values of R. However, in this regime, there is more scatter in the points from a single "master curve", which can be attributed a shear-amplitude dependence of our results, since here we adopt various $a_0 \in \{0.05, 0.5, 1\}$ (as we will explain further below).

Negative (positive) values of the effective viscosity in Fig. 6.6 are denoted by triangles (circles). If we consider the lowest frequency for each $R \in \{50, 100, 200, 500, 1000\}$ for which ν_E is negative, we find this to occur at approximately $\omega/\omega_c \in \{2, 4, 5, 30, 20\}$, respectively. This shows that with exception of the $R = 500$ case, the larger the value of R the higher frequency required to obtain negative values of the effective viscosity. We also note that the apparent discrepancy in the $R = 500$ case could be the result of the particular discrete values

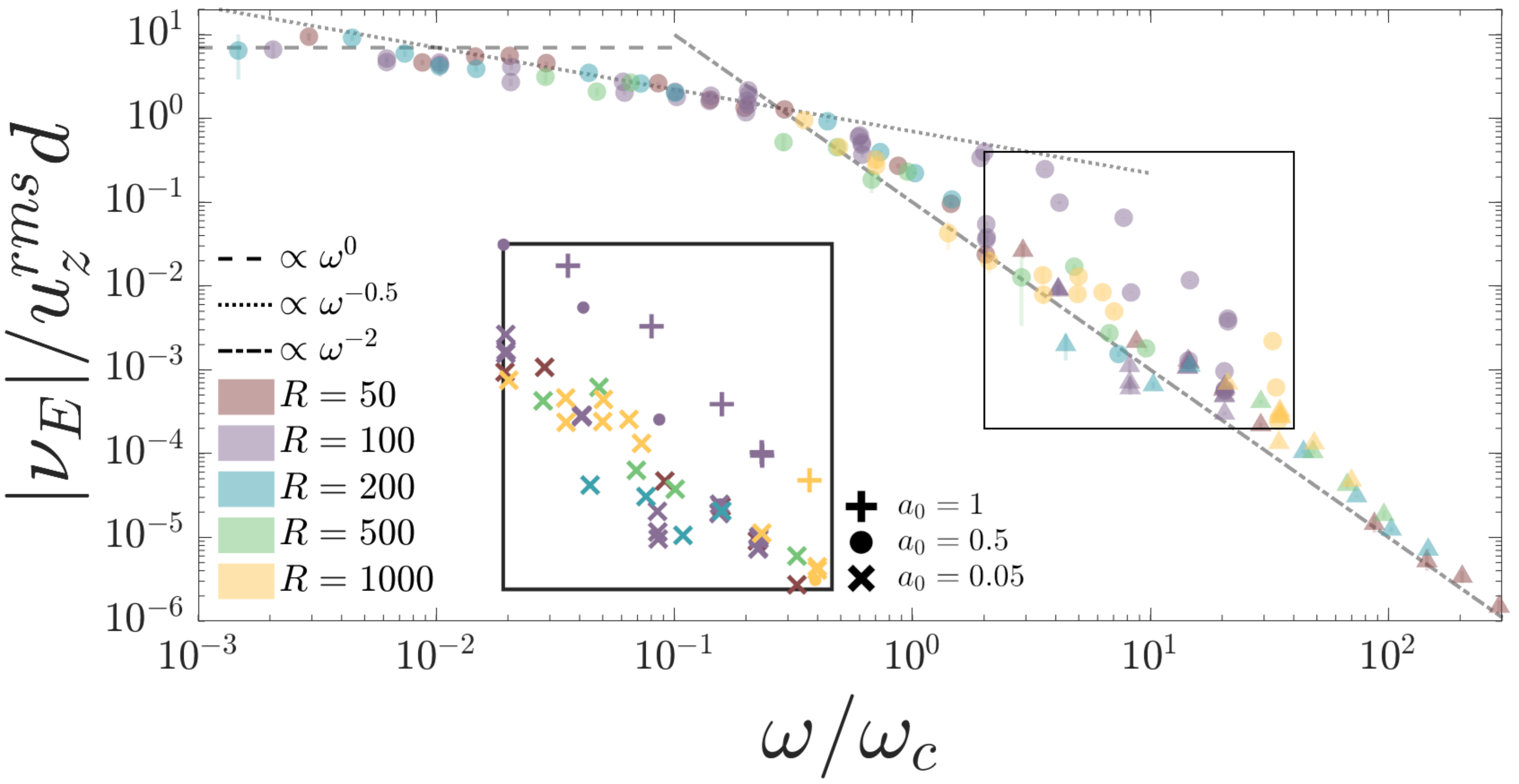

Figure 6.6: Scaled effective viscosity as a function of the scaled shear frequency, similar to figure 6.5. The cases shown here have $R \in \{50, 100, 200, 500, 1000\}$ (see legend) for a fixed domain size of $(8, 8, 1)$ and with shear amplitudes in the range $a_0 = [0.05, 1]$ (not highlighted here to avoid confusion). Power law lines are displayed for exponents of $\{0, -0.5, -2\}$ for low, intermediate and high-frequency cases respectively (see legend). This shows that the frequency-dependence of the scaled effective viscosity is robust to changes in the Rayleigh number over this range. The scatter of points in the frequency range $\omega/\omega_c = (10^0, 10^2)$ can be attributed to a shear amplitude dependence that is illustrated clearly in the inset panel.

of the frequency that have been run.

6.2.3 Comparing the frequency spectra to effective viscosity

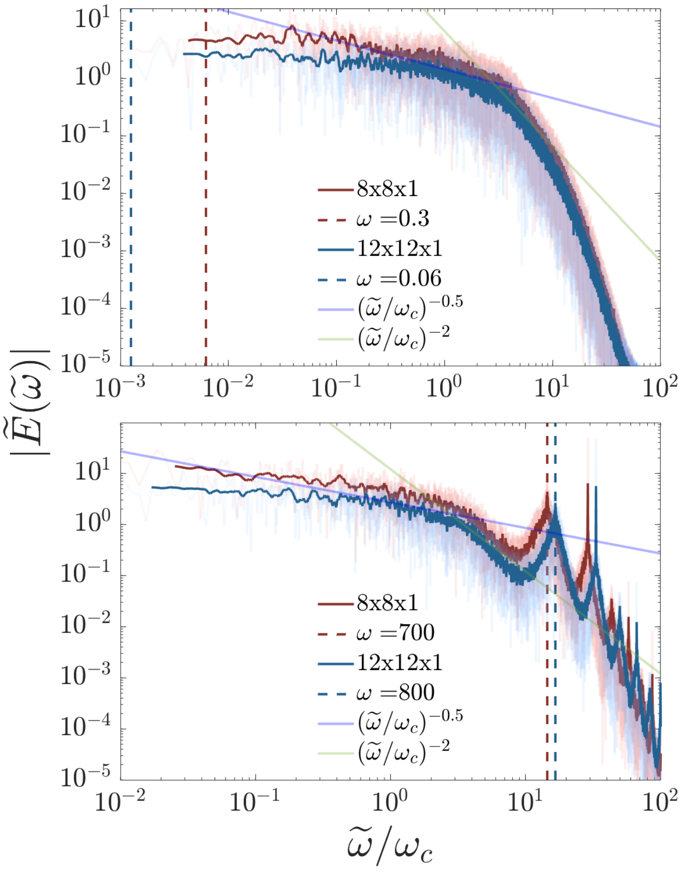

Figure 6.7: Examples of the frequency spectra of the kinetic energy for convection in the presence of oscillatory shear, with $R = 100$, $a_0 = 0.5$, $(L_x, L_y, L_z) \in \{(8, 8, 1), (12, 12, 1)\}$ (red and blue, respectively) and $\omega \in \{0.3, 0.06\}$ (top, with $\omega < \omega_c$) and $\{700, 800\}$ (bottom, with $\omega > \omega_c$). The angular frequency has been scaled by the relevant convective frequency. The solid lines show the 20-point moving average of the full spectrum, which is shown using faded lines. An inertial range is observed, where the spectrum follows an $(\tilde{\omega}/\omega_c)^{-2}$ power law (green line), before entering the dissipation range for the highest $\tilde{\omega}$. We also observe a significant region which features a $(\tilde{\omega}/\omega_c)^{-0.5}$ power law in the spectrum, which matches the scaling observed for ν_E in Figs. 6.5 and 6.6. The vertical dashed lines correspond to the frequency of the oscillatory shear in each case. Similar results are obtained for the frequency spectrum of the Reynolds stress.

Ch. 5 and previous work (Penev et al. 2009b;Vidal & Barker 2020b) have suggested that the frequency (temporal) spectrum of the kinetic energy $\tilde{E}(\tilde{\omega})$ (or Reynolds stress) may play an important role in determining the frequency-dependence of the effective viscosity. In this section we explore more closely the connection between the frequency spectrum of the kinetic energy and the frequency dependence of the effective viscosity. Examples of the frequency spectrum of the kinetic energy (evaluated after applying a Hann window function) can be seen in Fig. 6.7 for the low-frequency tide regime with $\omega \in \{0.3, 0.06\}$ (top) and the high-frequency tide regime with $\omega \in \{700, 800\}$ (bottom). All cases in Fig. 6.7 have $R = 100$ and a shear amplitude $a_0 = 0.5$ covering two cases in each of the high and low-frequency regimes with domain sizes $L_x \in \{8, 12\}$ (dark red and dark blue, respectively) and the tidal frequencies (see legend) denoted by the vertical dashed lines. For these plots we scale the angular frequency $\tilde{\omega} = 2\pi/\tau$ (where τ represents the period of each Fourier component) of the spectrum by the relevant convective frequency (ω_c) in each simulation, so as to make a meaningful comparison between these spectra results and the profiles of ν_E. In Fig. 6.7 the solid lines represent the 20-point moving average of each full kinetic energy spectrum (which are plotted using faded lines). We also note that similar spectra have been obtained for all simulations that have been run for a long enough duration.

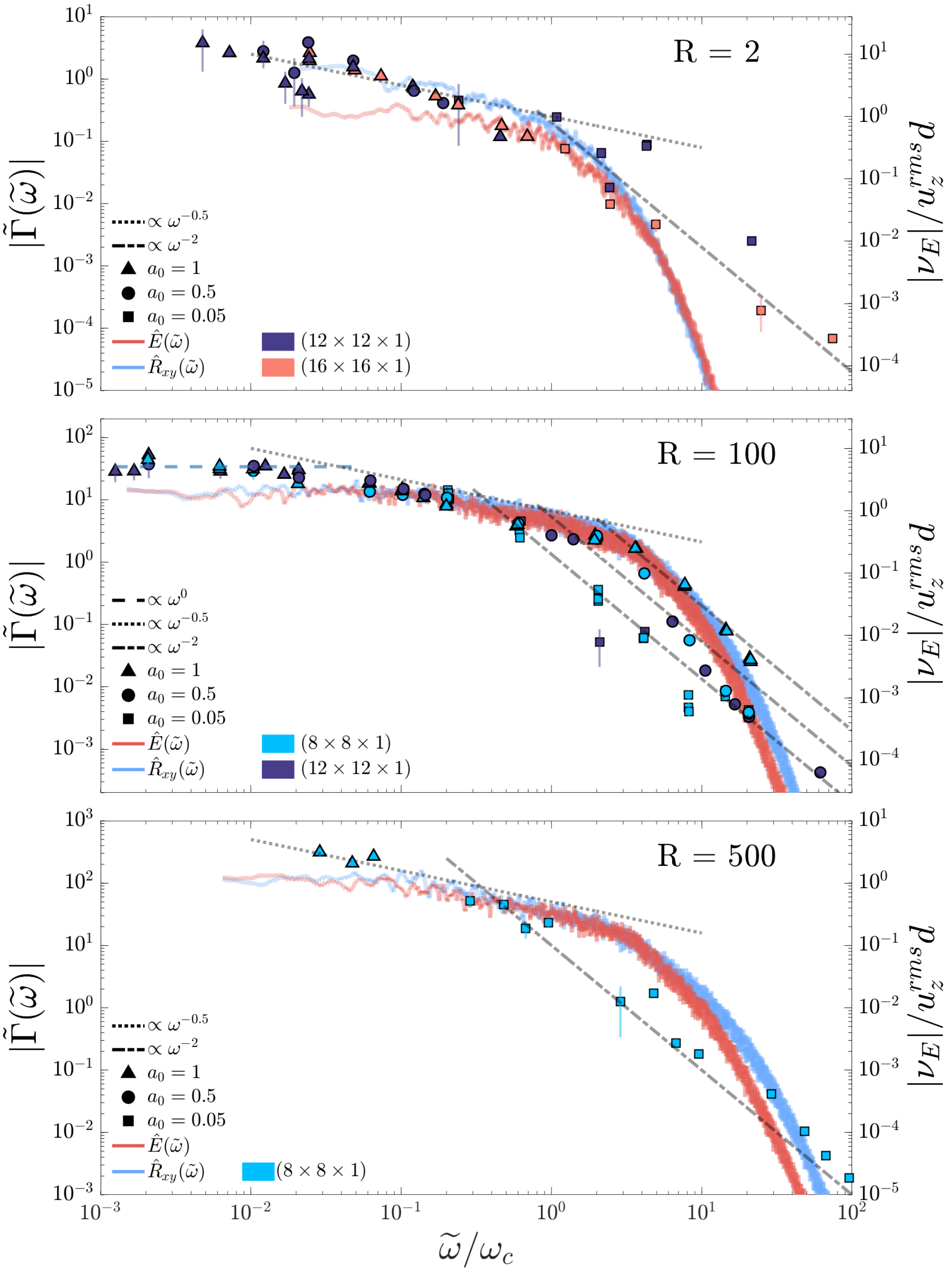

Figure 6.8: Magnitude of the effective viscosity from figure 6.5 (right axis - points) with the frequency spectra of the convection over-plotted, $\tilde{\Gamma}(\tilde{\omega})$ (left axis - lines) where $\Gamma \in \{E, R_{xy}\}$ is either the kinetic energy, E, (blue) or Reynolds stress, R_{xy}, (red). The $R = 1000$ case has been replaced with $R = 500$ due to computational limitations of reaching the lowest frequencies with higher R values. The symbols for the effective viscosity now highlight the amplitude a_0 for each case, while the sign is no longer identified in this figure to clarify the presentation. The symbol colour denotes the domain size (see legend). The 20-point moving average of the frequency spectrum is shown here. Various relevant power laws are denoted by the dotted and dashed lines which are highlighted in the legend. Appendix A shows cases of $R \in \{50, 200, 1000\}$.

In these low tidal frequency example cases (Fig. 6.7 top) we observe a small inertial-like range defined by a -2 power law (green line) (Landau & Lifshitz, 1987; Kumar & Verma, 2018) in the kinetic energy spectra starting at $\tilde{\omega}/\omega_c \approx 4$ and extending to $\tilde{\omega}/\omega_c \approx 10$. Beyond this, we observe a dissipation range where the spectrum transitions to a power law decay with magnitude greater than 2, followed by low-power noise at very high frequencies as a consequence of the finite time-step size. For frequencies lower than the inertial range, we observe a power law exponent that is consistent with -0.5 (light blue line) extending down to $\tilde{\omega}/\omega_c \approx 10^{-1}$ before the spectrum approaches white noise for the lowest observable frequencies. The frequency spectrum of the kinetic energy and Reynolds stress are both consistent with the un-sheared cases presented in section 6.2.1 for all cases where the shear frequency is in the low or intermediate regimes. We note that in the high-frequency regime the shear introduces a strong resonant response in the spectrum at the shear frequency, which is related to the larger shear amplitude $a_0\omega$ at high frequencies. The rapid drop-off in the frequency spectrum then allows the energy injected by the shear to become observable for these high frequencies. Fig. 6.7 also shows that the shape of the frequency spectrum is independent of domain size, providing the energetically dominant convective modes are resolved spatially.

In the high-frequency cases (Fig. 6.7 bottom) the spectrum behaves similarly to the low-frequency cases when $\tilde{\omega}/\omega_c \lesssim 5$. We observe a significant modification of the spectrum in the high-frequency regime beginning with a substantial peak in the spectrum at the shear frequency. The peak is not confined to the discrete frequency of the shear and has a substantial lead and lagging tail. Further, we observe a significant resonant chain of peaks each with the same shape as the main peak.

We now compare the frequency spectra (evaluated after applying a Hann window) of kinetic energy (blue) and Reynolds stress (red) with the scaled effective viscosity in figure 6.8. Note that the symbols denoting the scaled effective viscosity are shown as a function of the scaled tidal frequency, ω/ω_c, whereas the spectrum is plotted as a function of $\tilde{\omega}/\omega_c$. As before, the solid lines for the spectrum represent its 20-point moving average. We demonstrate these comparisons for cases similar to those in figure 6.5, that is, cases with $R \in \{2, 100, 500\}$ (cases with $R = 1000$ were excluded due to the difficulty in reaching the intermediate regime but can be found in Appendix A along with cases with $R \in \{50, 200\}$), domain sizes $L_x = L_y \in \{2, 4, 8, 12, 16\}$ and various amplitudes $a_0 = [0.05, 1]$. For each value of R, we show a representative spectrum of kinetic energy and Reynolds stress, choosing cases with the longest run time to effectively probe the low-frequency regime. As the domain size does not significantly alter the spectrum as long as it is "large enough" (see figure 6.7), we plot a case with a domain size $(8, 8, 1)$ for each R. Similarly, the shear in the low-frequency regime only weakly affects the spectrum, as we can observe from comparing figures 6.2 and 6.7, so we adopt a representative case for each R with $\omega < 1$ that has the longest run time. In figure 6.8 the symbols now denote the amplitude of the shear (see legend for the values).

The key result of figure 6.8 is that for low and intermediate frequencies such that $\omega/\omega_c \lesssim 5$, the frequency dependence of $\nu_E(\omega)$ closely follows the spectrum of the energy and Reynolds stress. This agrees with the global simulations of Vidal & Barker (2020b). It is an important result because it suggests that we can infer the frequency dependence of ν_E in stars if we know the spectrum of the convection.

It is worth highlighting that, although the left and right y-axis values are offset, the range of

R	$L_x(=L_y)$	ω	$\alpha = \overline{\left(\frac{\nu_E}{u_z^{\text{rms}} d}\right)}$	$\gamma = \overline{\nu_E(\omega/\omega_c)^2}$	$u_z^{\text{rms}} = d\omega_c$	typical resolution (N_x, N_y, N_z)	a_0
2	2	$[0.001, 1000]$	0.163	21.071	5.484	$(64, 64, 32)$	$[0.0005, 1]$
2	4	$[0.08, 1000]$	0.386	20.538	4.354	$(64, 64, 32)$	0.05
2	8	$[0.01, 1000]$	2.63	25.629	4.698	$(64, 64, 32)$	0.05
2	12	$[0.01, 2000]$	–	3.923	4.278	$(128, 128, 64)$	$[0.05, 1]$
2	16	$[0.1, 500]$	–	4.888	4.091	$(128, 128, 64)$	$[0.05, 1]$
5	2	$[0.001, 1000]$	0.168	23.663	13.44	$(64, 64, 32)$	0.05
10	2	$[2, 5000]$	0.144	28.450	22.87	$(64, 64, 128)$	0.05
50	8	$[0.1, 10000]$	–	5.761	34.39	$(128, 128, 128)$	$[0.05, 1]$
100	2	$[10, 10000]$	0.061	3.967	63.85	$(64, 64, 128)$	$[0.0005, 1]$
100	4	$[1, 10000]$	2.356	8.318	49.07	$(64, 64, 128)$	$[0.05, 1]$
100	8	$[0.05, 1000]$	5.109	see table 6.4	49.06	$(128, 128, 128)$	$[0.05, 1]$
100	12	$[0.06, 10000]$	5.074	11.794	48.78	$(128, 128, 128)$	$[0.05, 1]$
200	8	$[0.1, 10000]$	–	11.177	68.16	$(128, 128, 128)$	$[0.05, 1]$
500	8	$[30, 10000]$	–	24.785	104.1	$(256, 256, 192)$	0.05
1000	2	$[100, 70000]$	–	23.570	178	$(128, 128, 128)$	0.05
1000	4	$[100, 1000]$	–	–	145.8	$(192, 192, 128)$	0.05
1000	8	$[30, 10000]$	–	39.36	143.1	$(256, 256, 192)$	1
10000	2	$[1000, 50000]$	–	156.577	495.1	$(192, 192, 384)$	0.05

Table 6.3: Table of simulation parameters and output data. The (horizontal) fit to the data for ν_E for very low frequencies is used to obtain $\alpha = \overline{\left(\frac{\nu_E}{u_z^{\text{rms}} d}\right)}$ (which can only be clearly obtained in cases with $R \leq 100$). Also shown is the y-intercept of the fit on a log scale to the data in the high-frequency regime for which $\nu_E \propto (\omega/\omega_c)^{-2}$. We also report the volume-averaged rms convective (vertical) velocity component, $u_z^{\text{rms}} = d\omega_c$. The table features various values of R with a range of different domain sizes and reports the typical resolutions (N_x, N_y, N_z) used for each set of simulations. Effects of the shear amplitude, a_0, are neglected in these results but we report the range of values explored.

values in both is similar. We also note that there is a good agreement between the spectrum of the kinetic energy and the Reynolds stress, though the kinetic energy has slightly smaller amplitude than the Reynolds stress.

We continue our analysis of figure 6.8 by considering the high-frequency regime where $\omega/\omega_c \gtrsim 1$. As alluded to earlier, we observe an amplitude dependence in the magnitude of ν_E, which is most clearly observed in cases with $R = 100$ and shear amplitudes of $a_0 \in \{0.05, 0.5, 1\}$. This amplitude dependence shifts where the transition to the -2 power law begins, which is here observed to occur when $\omega/\omega_c \approx (0.6, 1.5, 3)$, respectively. In the high-frequency regime, $\nu_E \propto \omega^{-2}$ for higher ω. This only agrees with the spectrum for a narrow range of frequencies corresponding to the inertial-like range. For higher frequencies, the spectrum transitions into a dissipation range, where the power law exponent is steeper than -2, whereas the effective viscosity continues to follow the -2 power law. This again suggests that, despite the power law of the inertial range and the frequency dependence of the effective viscosity being the same, this cannot explain the robustness of $\nu_E \propto \omega^{-2}$ for high-frequency tidal forcing.

For intermediate frequencies, $\omega/\omega_c \approx (10^{-2}, 10^{0})$, we observe a strong agreement in the power law of the effective viscosity with both the kinetic energy and Reynolds stress frequency spectra for all R plotted. The transition from intermediate to high-frequency regimes in the effective viscosity does not always coincide with when the spectrum falls off more steeply than a -0.5 power law. In fact, the $R = 100$ cases clearly demonstrate that the amplitude dependence plays a role in deciding when the effective viscosity transitions to the quadratic scaling regardless of the slope of the spectrum.

Although we have shown that there is good agreement with the frequency-dependence of the scaled effective viscosity and the frequency spectrum of kinetic energy (or Reynolds stress) in the intermediate and low-frequency regimes, the relationship between these quantities is a constant of proportionality. That is, we have shown that $\nu_E(\omega/\omega_c) \propto \tilde{E}(\tilde{\omega}/\omega_c)$. Since the intermediate and low-frequency spectrum appears to be approximately amplitude and domain size independent, this constant of proportionality may be some function of R (and possibly Pr which we have not explored in this work).

For the $R = 2$ cases shown in figure 6.8, we only display domain sizes of $L_x = L_y \in \{12, 16\}$, since these are required to obtain a -0.5 power law in the intermediate regime. This may be related to the transition to a chaotic flow and/or the requirement of resolving the energetically dominant scales in larger domains. Cases in smaller domains exhibit a frequency spectrum consisting of discrete peaks, suggesting little energy exchange between eddies with different time-scales. However, in the larger domains the frequency spectrum is more continuous. This suggests that this new -0.5 power law regime is a consequence of the frequency spectrum of chaotic/turbulent flow. In addition, the robustness of this new regime for both laminar and turbulent flows indicates that it may be relevant for understanding the interaction between tidal flows and convection in stars and giant planets.

In Table 6.3 we summarise three key quantities of interest from our simulations and the range of parameters explored. The key quantities are:

- time averaged rms of the vertical component of velocity, u_z^{rms}.
- linear fit values of α in the low-frequency regime, indicating the constant of proportion-

ality between ν_E and $u_z^{\mathrm{rms}} d$.

- $\gamma = \overline{\nu_E(\omega/\omega_c)^2}$, which represents the y-axis crossing of the quadratic fit to the high-frequency regime, for $R = 100$, $a_0 \in \{0.05, 0.5, 1\}$, including only simulations such that $\omega/\omega_c > 1$.

In the interests of examining the amplitude dependence of the effective viscosity in the high-frequency regime, Table 6.4 lists γ and u_z^{rms} for the cases with $R = 100$ in a domain of size $(8, 8, 1)$ for three different amplitudes $a_0 \in \{0.05, 0.5, 1\}$.

R	a_0	$\gamma = \overline{\nu_E(\omega/\omega_c)^2}$	u_z^{rms}
100	0.05	11.403	48.83
100	0.5	29.282	48.47
100	1	133.38	49.93

Table 6.4: Table listing values of $\gamma = \overline{\nu_E(\omega/\omega_c)^2}$, which is the y-intercept of the linear fit to the high-frequency regime assuming a $(\omega/\omega_c)^{-2}$ power law, and the time and volume averaged vertical component of the velocity (the convective velocity), u_z^{rms}, for various shear amplitudes, a_0. All cases are for $R = 100$ and with domain size $(8, 8, 1)$. This shows the effects of varying the tidal amplitude on our high-frequency results for ν_E.

In the larger domains, the low-frequency regime is shifted to significantly lower frequencies than in the cases in Ch. 5 which makes this regime computationally difficult to examine. Where possible we report the linear fit to the low-frequency regime to provide an estimate of α there. It is clear that as the domain size increases then the magnitude of the linear fit to α also increases until we reach an approximate convergence once the energetically dominant modes of the convection are contained in the box. This convergence can be seen most clearly in the cases with $R = 100$ in Table 6.3.

In the high-frequency regime we examine the quantity γ and find that it increases with R in chaotic and turbulent cases but appears to have a smaller value than in the laminar, deterministic cases ($R = 2$ small domains $L_x \leq 8$). In Table 6.4 we see that γ also increases with increasing shear amplitude.

As would be expected the data in Table 6.3 shows that as R increases so does u_z^{rms}. For increasing domain size the values of u_z^{rms} converge once $L_x \approx 4$, which we note is similar to when the peak of the wavenumber spectrum is contained within the box. Table 6.4 shows that the shear amplitude has little, if any, effect on u_z^{rms}, which is used to scale the shear frequency. As such this, the amplitude dependence of γ to be unlikely to be due to the shear significantly modifying the dominant eddies of the convection (in principle the shear could still affect the “resonant eddies” with lower energies).

6.2.4 Spatial structure of the Reynolds stress and effective viscosity

To explore the mechanism governing the interaction between tides and convection in more detail, we analyse the spatial (wavenumber) spectrum of the Reynolds stress $\hat{R}_{xy}(n_x, n_y)$ and effective viscosity $\hat{\nu}_E(n_x, n_y)$ as in Ch. 5 (eq. 5.3 and 5.4). These quantities are vertically-integrated and time-averaged spatial spectra that are computed as a function of the horizontal integer wavenumbers n_x and n_y, as described in section 2.3. The computation of $\hat{\nu}_E(n_x, n_y)$

requires sufficiently good temporal resolution that the time integral (as in eq. 2.62) is accurately computed.

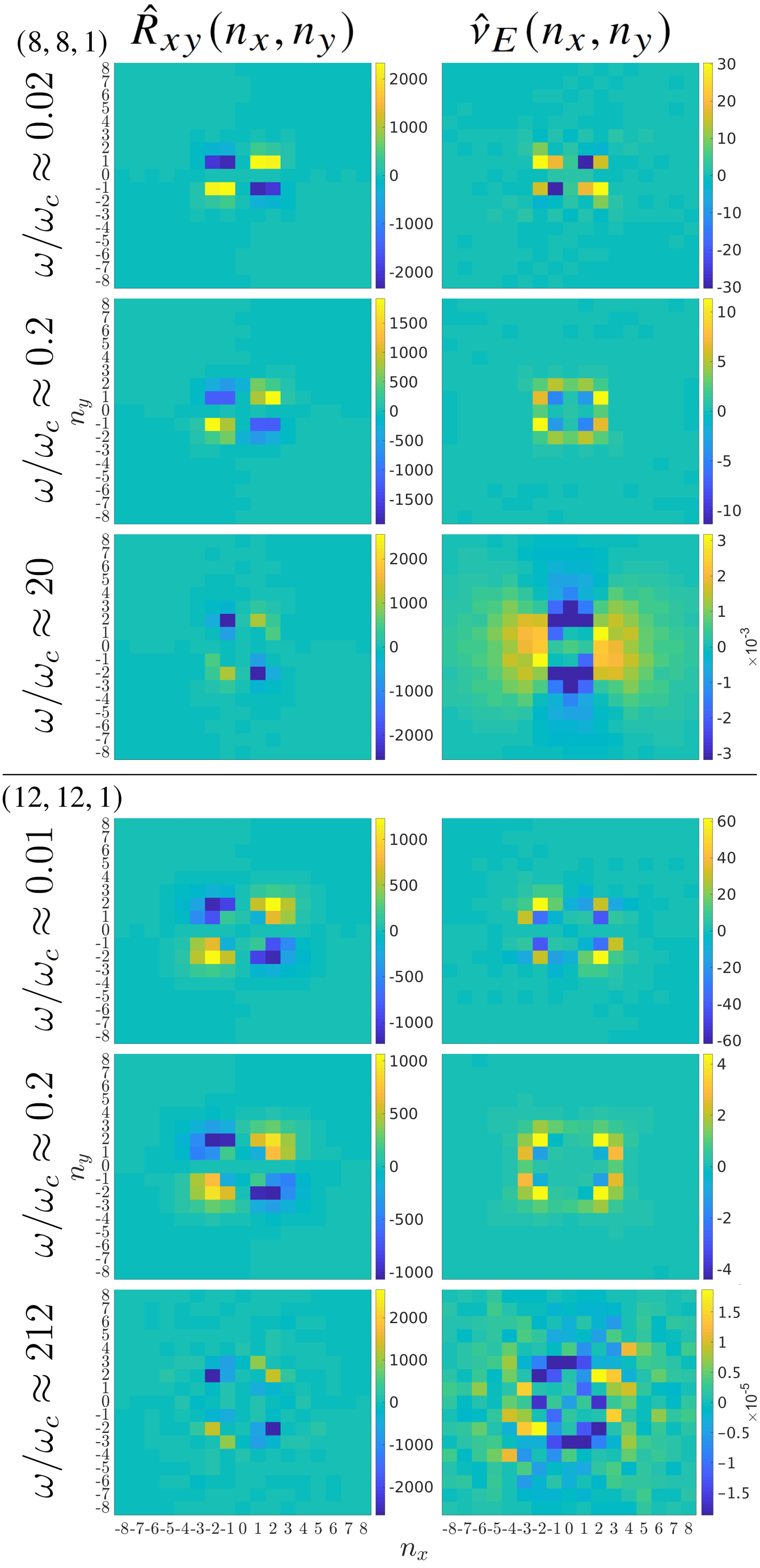

Figure 6.9: Examples of the temporally-averaged and vertically-integrated spatial spectra of the Reynolds Stress $\hat{R}_{xy}(n_x, n_y)$ (left column) and effective viscosity $\hat{\nu}_E(n_x, n_y)$ (right column) as a function of the integer wavenumbers n_x and n_y. The top three rows are for $R = 100$ with $\omega/\omega_c \in \{0.02, 0.2, 20\}$ with a domain size of $(L_x, L_y, L_z) = (8, 8, 1)$. The bottom two rows are also for $R = 100$ but with $\omega/\omega_c \in \{0.01, 0.2, 212\}$, and for the larger domain size of $(L_x, L_y, L_z) = (12, 12, 1)$, which more clearly demonstrate the dominant ring in the spatial spectrum. The frequencies shown correspond to cases in the low, intermediate and high-frequency regimes. Similar results are obtained for all values of R and domain sizes explored.

Example cases are shown in figure 6.9 with $R = 100$ and $a_0 = 0.5$ for two different domain sizes $(8, 8, 1)$ and $(12, 12, 1)$, each demonstrating three cases for each box size which lie in the low, intermediate and high-frequency regimes (the respective frequencies can be seen in the figure). For adequate temporal averaging, we ensured that at least 10 snapshots were taken per tidal period, and the simulations were integrated for many tens of tidal periods. Similar figures have been obtained for a number of other cases that show similar behaviour. We also note that the spectra in Fig. 6.9 have been zoomed in to show the lowest wavenumbers, since we find higher wavenumbers to contribute negligibly.

We observe that $\hat{R}_{xy}(n_x, n_y)$ is maximal in a ring that coincides with the energetically dominant wavenumber in Fig. 6.1, and this quantity then falls off rapidly in magnitude with increasing n_x and n_y. The same wavenumber ring also provides the dominant contribution to $\hat{\nu}_E(n_x, n_y)$. The modes in this ring provides the dominant contribution to the total effective viscosity ν_E, suggesting that the largest (energetically dominant) scales of the convection are the most important. This appears to contradict the main hypothesis of Goldreich & Nicholson (1977), who claim that the resonant eddies dominate the interaction, and that the largest scales could at most contribute a comparable amount as the resonant eddies. There is a peak in the frequency spectrum (e.g. of the Reynolds stress) at the forcing frequency, but this does not appear to be correlated with a ring of modes in the wavenumber spectrum. Instead, it appears that it is the response of the energetically dominant modes at the forcing frequency that dominates the contribution to ν_E. However, we caution that our simulations do not possess a sufficiently long inertial range to clearly test the expectations of Goldreich & Nicholson (1977) solely within the turbulent cascade, which would require much more turbulent simulations.

In the high-frequency cases, the $\hat{\nu}_E(n_x, n_y)$ spectra shows a strong negative contribution from the nearly x-aligned components of the flow, and a slightly weaker contribution from the positive nearly y-aligned components. This is compatible with the predictions of the asymptotic theory in Ch. 4. Note also that more modes provide an observable contribution to ν_E for larger frequencies, which results from the larger shear amplitude $a_0\omega$ in these cases.

6.3 Discussion

In this chapter we have presented a much wider parameter survey than Ch. 3-5, and in particular we have studied convection in wider boxes, allowing the peak of the energy spectrum to be fully resolved. These new simulations support our prior results for high-frequency tidal forcing, in that we find strong evidence in favour of $\nu_E \propto \omega^{-2}$, but they have also uncovered a new intermediate frequency scaling that has not been previously reported (or predicted). This new frequency scaling has $\nu_E \propto \omega^{-0.5}$ for frequencies $10^{-2} \lesssim \omega/\omega_c \lesssim 1 - 5$ (depending on amplitude). In this section we discuss further this new regime, and some of the implications of our results.

Previous simulations of anelastic convection (Penev et al., 2009b), and Boussinesq spherical convection in a model with homogeneous internal heating (Vidal & Barker, 2020b), have observed an intermediate frequency scaling for $\nu_E \propto \omega^{-1}$ for a range of frequencies around $\omega \sim \omega_c$. This is consistent with the -1 slope in the frequency spectrum of the kinetic energy in the simulations of Vidal & Barker (2020b) (and possibly also in Penev et al. 2009b). This differs from our results in this frequency range, where we find $\nu_E \propto \omega^{-0.5}$. In addition, simulations with various strengths of convective driving in spheres are found to give different exponents from -0.5 to -1 in the intermediate regime (Vidal et al., 2020). Further work is required to explore in detail this difference, though we hypothesise that it may result from the radial variation in the heat flux in the spherical model, which is constant in our Cartesian case.

The study of the frequency spectrum of turbulent convection has been primarily directed towards the inertial range in order to make comparisons between the classical theories (Kolmogorov, 1941; Bolgiano, 1959; Obukhov, 1959), which are based on the spatial spectrum, and experiments (Sano et al., 1989; Ashkenazi & Steinberg, 1999; Wu et al., 1990; Shang & Xia, 2001; Liot et al., 2016), where the data is primarily temporal in nature, with the objective of understanding the nature of the turbulence. The low-frequency portion of the spectrum has received far less attention, with the majority of prior interest coming from the classical area of "$1/f$ noise" (Dmitruk & Matthaeus, 2007; Pereira et al., 2019; Vidal et al., 2020). Our results suggest that an understanding of the frequency spectrum of convection may allow us to predict the effective viscosity acting on the equilibrium tide for low and intermediate frequencies (though perhaps not for high frequencies). As such, this provides new motivation for research into the long term dynamics of turbulent convection in more realistic models.

The agreement of the frequency spectrum and the effective viscosity was observed to break down when the high-frequency regime was reached. The transition to the high-frequency regime depends on the tidal amplitude, where larger amplitudes are found to shift the transition to higher frequencies. This may be related to the relative energy in the tidal shear to the convection at these frequencies. However, this should be explored further in a future investigation.

Despite the existence of a -2 power law in the frequency spectrum of convective turbulence Landau & Lifshitz (1987); Kumar & Verma (2018), which the effective viscosity follows, the effective viscosity trend maintains this power law even when the frequency spectrum transitions into the dissipation range with a much faster fall-off. This demonstrates that the effective viscosity does not follow the spectrum at high frequencies (at least in our simulations), and the agreement in the power law may be coincidental. In the theoretical prediction of Goldreich & Nicholson (1977) the -2 power law was predicted by applying Kolmogorov turbulence and assuming that the "resonant eddies" that are resonant with the tidal shear would provide the dominant contributions to the effective viscosity. However, we have shown that a turbulent cascade is not required to obtain a -2 scaling (see also Ogilvie & Lesur 2012; Braviner 2015). For example, $R = 2$ cases possess no inertial range in the wavenumber spectrum, which is hence non-Kolmogorov-like, and yet we still obtain a -2 power law for ν_E. An independent prediction of the -2 scaling was made using asymptotic analysis (Ogilvie & Lesur, 2012) which we extended in Ch. 4 to include thermal effects, which also allows for the prediction of negative effective viscosities.

Goldreich & Nicholson (1977) claimed that the "resonant modes" provide the dominant contributions to the effective viscosity, but the largest scale modes could contribute a comparable amount. We have conducted a Fourier analysis of the spatial structure of the Reynolds stress and of the contributions to the effective viscosity. We found that the effective viscosity is dominated by the energetically dominant ring of modes in wavenumber space. We do not observe any appreciable contribution from resonant eddies. We do however observe a significant temporal resonance observed in the frequency spectrum (which is found to occur for all spatial wavenumber bins above the dissipation length-scale).

In this and Ch. 3-5, we provided robust measurements of negative effective viscosities, as originally found in a slightly different convection model by Ogilvie & Lesur (2012). Here we find that increasing the strength of the convection shifts the transition to higher frequencies, suggesting that for realistic Rayleigh numbers in planets and stars, the frequency required to produce a negative ν_E, and therefore tidal anti-dissipation, would be prohibitively high (see also Vidal & Barker 2020b). The negative values may therefore not be relevant in reality.

Summary: Key findings

This summary is in combination with the previous summaries of Ch. 3-5.

- High-frequency regime ($\omega > \omega_c$),
  - $\nu_E \propto \omega^{-2}$ (consistent with the quadratic reduction model, § 1.3.3),
  - ν_E transitions from positive to negative at higher ω/ω_c for larger R (hence may not be physically relevant in astrophysical applications),
  - shear amplitude, a_0, dependence of $|\nu_E|$,
  - largest scale eddies dominate the contribution to ν_E (not the resonant eddies § 1.3.3),
  - does not follow frequency spectrum for kinetic energy.
- new intermediate frequency regime ($10^{-2} \lesssim \omega < \omega_c$),
  - $\nu_E \propto \omega^{-0.5}$ not previously predicted by any model or simulation,
  - follows the frequency spectrum of kinetic energy,
  - shear amplitude independent,
  - requires energetically dominant mode in the wavenumber spectrum of kinetic energy to fit within the domain,
  - requires chaotic flow.
- low-frequency regime pushed to very low frequencies ($\omega/\omega_c \lesssim 10^{-2}$),
  - ν_E is frequency independent (consistent with the constant time lag, § 1.3.1),
  - scaled effective viscosity has magnitude $\alpha > 1/3$,
  - transition to this regime occurs when the frequency spectrum flattens to white noise,
  - shear amplitude independent.
- in all regimes the largest scales dominate the contribution to ν_E,
- for a single choice of shear amplitude the frequency dependence of the effective viscosity collapses onto a single master curve.

Chapter 7

Astrophysical implications

Contents

In this chapter we consider the astrophysical implications of the results presented in Ch. 3-6. We will first explore a simple example case of a HJ planet around a main sequence sun-like star and estimate the inspiral timescale and modified tidal quality factor (Q') using different prescriptions for the frequency dependence of the effective viscosity. The purpose of exploring this simple case is to highlight the importance of using the correct model for the tidal dissipation that arises from the interaction between the tidal flow and convection, and hence emphasise the importance of our results and motivate further research in this area.

7.1 A simple illustrative calculation

Let us consider a single example to illustrate the importance of considering the correct prescription for ν_E for high frequencies. We can crudely estimate the rate of orbital decay of a Jupiter-mass planet in a one day aligned circular orbit around a slowly rotating Sun-like star. Tidal dissipation in the star usually leads to planetary orbital decay because $\Omega_{\rm s} < \Omega_{\rm o}$ (if $\nu_E > 0$, but not if $\nu_E < 0$), raising the question as to the planet's long-term survival. This example could represent a close-in hot Jupiter such as WASP-12 b (e.g. Maciejewski et al. 2016; Patra et al. 2017). We can use our results to predict the tidal orbital evolution timescale due to the effective viscosity of the convection. We will apply our results in a simplified spherically-symmetric stellar model, which is described by a basic state dependent only on spherical radius r (e.g. Kippenhahn et al. 2012). We will use publicly available stellar models computed using[1] Model S (Christensen-Dalsgaard et al. 1996) or MESA (Paxton et al. 2011, 2013, 2015, 2018, 2019).

---

[1] The Model S stellar model is specifically for the Sun while the MESA code is a more general stellar evolution code to produce realistic models of stars.

7.1.1 Preliminaries

Before we explore this problem let us first derive and define some important quantities which we will use in our analysis. Note that although we will be considering a planet around a star, what follows can also be applied to binary stars where we simply exchange the planet for a star.

Effective viscosity

The most important quantity we wish to evaluate is the effective viscosity which we can use a smoothed version of eq. 1.64 as in Ogilvie & Lin (2007)

$$\nu_E(r) = \alpha_c u^{\mathrm{mlt}}(r) l^{\mathsf{mlt}}(r) \begin{cases} 1 & \text{if} \quad \aleph = 0\,, \\ \left(1 + \left(\frac{|\omega|}{\omega_c(r)}\right)^{\aleph}\right)^{-1} & \text{if} \quad \aleph \in \{1, 2\}\,, \end{cases} \tag{7.1}$$

where[2] $\alpha_c = \alpha/\alpha^{\mathrm{mlt}}$ (see § 2.3.3) can be taken from Table. 6.3 to apply these results of our simulations, $u^{\mathrm{mlt}}(r)$ is a convective (mixing-length) velocity, $l^{\mathsf{mlt}} = \alpha^{\mathsf{mlt}} H_p$ is a mixing length, which consists of the pressure scale height $H_p = H_p(r)$ and the mixing-length parameter which is often taken $\alpha^{\mathsf{mlt}} \approx 2$, and $\omega_c(r)$ is the convective frequency which can be related to the convective velocity by $\omega_c = u^{\mathrm{mlt}}(r)/l^{\mathsf{mlt}}(r)$. Note that we have introduced $\aleph$ to account for the three prescriptions of the frequency reduction[3] and highlight that this neglects any frequency dependence[4] when $\omega < \omega_c$. This leaves us to evaluate $u^{\mathsf{mlt}}(r)$ where we use the expression (rearrangement of equation 9 in Ogilvie & Lin (2007))

$$u^{\mathrm{mlt}}(r) = \left(\frac{3}{8}\alpha^{\mathsf{mlt}} H_p \frac{g\delta F_{\mathsf{lum}}}{\rho c_p T}\right)^{1/3}\,, \tag{7.2}$$

where g is the magnitude of the gravitational acceleration which can be obtained from

$$g(r) = \frac{G M_\star(r)}{r^2}\,, \tag{7.3}$$

and the quantity δ is defined as (where the subscript means evaluation at constant pressure)

$$\delta = -\left(\frac{\partial \log\rho}{\partial \log T}\right)_p\,, \tag{7.4}$$

where G is the gravitational constant, $M_\star = M_\star(r)$ is the stellar internal mass[5], $\rho = \rho(r)$ is the density, $c_p = c_p(r)$ is the specific heat at constant pressure, $T = T(r)$ is the temperature and F_{lum} is the convective luminosity flux. Note that we can compute the convective turnover time as

$$\tau_c = \frac{l^{\mathsf{mlt}}}{u^{\mathsf{mlt}}} = \frac{1}{\omega_c}\,. \tag{7.5}$$

---

[2] Note that our definition of α includes the mixing-length parameter as well as the constant of proportionality. Thus we divide through by the mixing-length parameter as it is already included in the mixing length.

[3] In the interests of clarity, 0 corresponds to no frequency reduction, 1 for the linear reduction and 2 for the quadratic reduction. See Ch. 1 for further details.

[4] For this calculation we ignore the "intermediate regime" as it is not relevant for the frequencies in this problem.

[5] The internal mass is the mass contained within some radius r.

The final ingredient is the evaluation of F_{lum} which can be done by subtracting the radiative luminosity from the total luminosity and integrating over the stellar volume, that is

$$F_{\text{lum}} = \frac{L - L_{\text{rad}}}{4\pi r^2}\,, \tag{7.6}$$

where L_{rad} is the radiative luminosity which is defined by (see Kippenhahn et al. 2012 equation 5.11)

$$L_{\text{rad}} = -\frac{16\pi a_{\text{rad}} c r^2 T^3}{3\kappa_{\text{op}}\rho}\frac{\mathrm{d}T}{\mathrm{d}r}\,, \tag{7.7}$$

where a_{rad} is the radiation density constant, c is the speed of light, $\mathrm{d}T/\mathrm{d}r$ is the temperature gradient, $\kappa_{\text{op}} = \kappa_{\text{op}}(r)$ is the opacity and $L = L(r)$ is the total luminosity. It is worth noting that some of these equations can be bypassed depending on the stellar model that is used, for example, while the convective velocity is an output of the commonly used MESA stellar model it is not for the Model-S for the Sun.

Orbital motion

Another useful expression is the relationship between the semi-major axis and the orbital period, which by Kepler's laws is

$$P_{\mathrm{orb}} = 2\pi\sqrt{\frac{a^3}{G(M_\star + M_p)}}\,, \tag{7.8}$$

where a is the semi-major axis, $M_\star$ is the internal stellar mass and M_p is the planet mass. Note that for an aligned circular orbit the tidal frequency is $\omega = 2(\Omega_{\mathrm{o}} - \Omega_{\mathrm{s}})$, and for $\Omega_{\mathrm{o}} \gg \Omega_{\mathrm{s}}$ (i.e. slowly rotating star with short-period orbit), $\omega \approx 2\Omega_{\mathrm{o}}$ so that $P_{\text{tide}} = P_{\mathrm{orb}}/2$. This can be used, for example, if we wish to consider a planet with a given orbital separation rather than orbital period. It can also be useful for converting orbital distance into orbital frequency.

Crude estimate for the inspiral timescale

The inspiral timescale, τ_a, is an important quantity to evaluate as this gives the time for the inward (or outward) migration of the planet. This timescale can then be compared to the age of the system or the expected lifetime of the system to quantify the importance of whatever mechanism is causing the migration. In our case we are considering the inspiral timescale as a result of tidal dissipation of the equilibrium tide. The timescale for the evolution of the semi-major axis[6] can be estimated from (see Rasio et al. 1996 where we have used our own notation)

$$\frac{a}{|\dot{a}|} = f_{\aleph}\tau_c \frac{M_\star^2}{M_{\text{env}} M_p\left(1 + \frac{M_p}{M_\star}\right)}\left(\frac{a}{R_\star}\right)^8\,, \tag{7.9}$$

where $f_{\aleph}$ is the reduction factor which is a function of the frequency (we will define this more thoroughly soon), τ_c is the convective turnover time (eq. 7.5), M_{env} is the mass of the

---

[6] The evolution of the semi-major axis is defined as $\dot{a}/a$ which has a negative sign for an inspiraling orbit and positive for outspiraling.

convective envelope, M_p is the planet mass and $R_\star$ is the stellar radius. We can write the mass of the convective envelope as

$$M_{\mathsf{env}} = 4\pi \int_{\mathsf{conv}} r^2 \rho \, \mathrm{d}r \, , \tag{7.10}$$

where the integration is taken over the radius of the convective envelope rather than the full stellar radius. An approximation to this can be made by considering that the planet's mass is much lower than that of the star, $M_p \ll M_\star$. This means that the bracket term on the denominator can be neglected and we can write

$$\tau_a \approx f_\aleph \tau_c \left(\frac{M_\star}{M_{\mathsf{env}}} \right) \left(\frac{M_\star}{M_p} \right) \left(\frac{P_{\rm orb}}{P_{\rm dyn}} \right)^{\frac{16}{3}} , \tag{7.11}$$

where we have used eq. 7.8 and the definition of the dynamical timescale[7]

$$P_{\rm dyn} = 2\pi \sqrt{\frac{R_\star^3}{G M_\star}} \tag{7.12}$$

to write the final term. It is worth highlighting that this timescale is the time taken for the planet to migrate from its initial semi-major axis, a, to the centre of the host star, $a = 0$. Although not strictly physical due to the Roche limit, this provides a fair comparison between the cases as well as a reasonable estimate due to the accelerating nature of tidal inspiral.

We now turn to the definition of $f_\aleph$ where $\aleph \in \{0, 0.5, 1, 2\}$. This term contains both a reduction constant associated with time integration of the evolution of the semi-major axis as well as taking account of the reduction factor due to the frequency dependence of the dissipation, which we write as $f_\aleph = f_\aleph^{\mathsf{int}} f_\aleph^{\mathsf{disp}}$. First, the frequency dependence of the dissipation can be written as (our definition is the inverse of equation 5 in Rasio et al. 1996 with inclusion of $\aleph$ which chooses the reduction factor)

$$\begin{aligned} f_\aleph^{\mathsf{disp}} &= \max \left[1, \left(\frac{2\tau_c}{P_{\rm orb}} \right)^{\aleph} \right] \\ &= \min \left[1, \left(\frac{\omega}{\omega_c} \right)^{\aleph} \right] , \end{aligned} \tag{7.13}$$

where we write in terms ot the timescales and frequencies for completeness. Now the constant $f_\aleph^{\mathsf{int}}$ comes from integration of eq. 7.9 with respect to the semi-major axis a. We can evaluate this by considering the 'a' terms in eq. 7.9 (the inverse of equation 3 of Rasio et al. (1996)), so

$$a \frac{\mathrm{d}t}{\mathrm{d}a} \sim f_\aleph^{\mathsf{disp}} a^8 \, , \tag{7.14}$$

$$\int_a^0 \frac{\mathrm{d}t}{\mathrm{d}a} \, \mathrm{d}a \sim \int_a^0 a^{-3\aleph/2} a^7 \, \mathrm{d}a \, , \tag{7.15}$$

where we note that since $f_\aleph^{\mathsf{disp}} \sim P_{\rm orb}^{-\aleph}$ then $f_\aleph^{\mathsf{disp}} \sim a^{-3\aleph/2}$. Now since, $a = a \rightarrow t = 0$ and

---

[7] The dynamical timescale, which is also known as the free-fall timescale, is a measure of time a star takes to respond to a disturbance in the balance between pressure and gravity.

$a = 0 \rightarrow t = \tau_a$ we can write

$$\int_0^{\tau_a} \mathsf{d}a \sim \int_a^0 a^{-3\aleph/2} a^7 \, \mathsf{d}a \,, \tag{7.16}$$

$$\tau_a \sim \frac{2}{16 - 3\aleph} a^{(16-3\aleph)/2} \,. \tag{7.17}$$

This allows us to write for each $\aleph$ the following

$$f_\aleph = \begin{cases} \frac{1}{8} & \text{if} \quad \aleph = 0 \,, \\ \frac{2}{13}\max\left[1, \left(\frac{2\tau_c}{P_{\mathrm{orb}}}\right)\right] & \text{if} \quad \aleph = 1 \,, \\ \frac{1}{5}\max\left[1, \left(\frac{2\tau_c}{P_{\mathrm{orb}}}\right)^2\right] & \text{if} \quad \aleph = 2 \,, \end{cases} \tag{7.18}$$

where we note that this neglects any frequency dependence when $\omega < \omega_c$.

Stellar (modified) tidal quality factor

We will also wish to consider the modified tidal quality factor within the star (as described in Ch. 1). To obtain an expression for this quantity, $Q'_\star$, we compare equation 3 in Rasio et al. (1996) with an equivalent expression, equation 7, in[8] Ogilvie & Lin (2007). We will consider the case where the orbital frequency is greater than the stellar spin frequency and hence $\mathrm{sgn}(\Omega_{\mathrm{o}} - \Omega_{\mathrm{s}}) = 1$, thus equating and rearranging these equations we find that

$$\begin{aligned} Q'_\star &= -9\pi f_\aleph \frac{\tau_c}{P_{\mathrm{orb}}} \frac{M_\star^2}{M_{\mathsf{env}}(M_\star + M_p)} \left(\frac{a}{R_\star}\right)^3 \\ &= -9\pi f_\aleph \tau_c \frac{M_\star^2}{M_{\mathsf{env}}(M_\star + M_p)} \frac{P_{\mathrm{orb}}}{P_{\mathrm{dyn}}^2} \,, \end{aligned} \tag{7.19}$$

where we note that all quantities in this expression have been defined in this section.

7.1.2 Analysis

In our simple problem we are considering a HJ planet orbiting a slowly-rotating Sun-like star on the main sequence. In Fig. 7.1 we plot the convective timescale for the Sun as a function of the normalised stellar radius with a highlighted region to show the relevant tidal timescales for HJ's. We take the timescale for the convection near the base of the convection zone ($r/R_\star \approx 0.77$) with corresponds to approximately 20 days, following Rasio et al. (1996). It is clear that the tidal period of HJ's is always much less than the convective timescale and thus HJ's find themselves in the high-frequency regime[9] (in which $\omega > \omega_c$). Fig. 7.1 also plots the stellar density as a function of the normalised stellar radius for the convection zone with an insert for the density over the full stellar radius. We choose the base of the convection zone for our turnover timescale due to the larger density (which can be seen as approximately constant in comparison to the radiative zone, see insert) which plays a role in the total dissipation,

---

[8] Note that in their symbols n is the orbital frequency which we call Ω_{o}. We also use Ω_{s} to be the spin frequency of the star as opposed to Ω_* in the notation of Ogilvie & Lin (2007).

[9] We have taken the tidal period to be half the orbital period and hence have not taken account of the stellar rotation period. If we take the stellar rotation period as 27 days (the equatorial rotation period of the Sun) then we have the tidal period for our HJ to be $P_{\mathsf{tide}} \approx [0.36, 7.9]$.

although in our analysis in this section we neglect density variation. Note that the density plot in Fig. 7.1 is in units[10] of $\mathrm{g\,cm^{-3}}$.

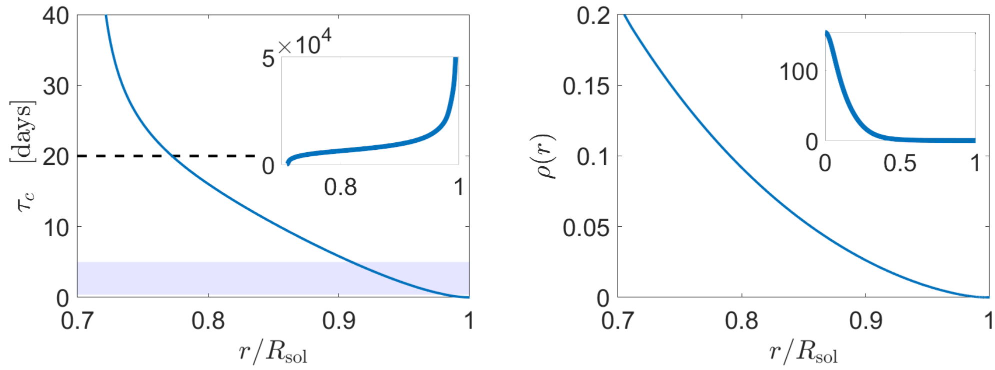

Figure 7.1: Left: The convective timescale (τ_c), calculated from eq. 7.5 using data from Model S, as a function of the stellar radius which is scaled by the total radius. The shaded region highlights the range of tidal periods for HJ's where the upper limit is taken as 5 days (half the upper limit of orbital period of 10 days, see § 1.1.2) while the inner limit is taken as 0.383 days which is taken from the shortest period HJ (as of November 2020 this is NGTS-10b with an orbital period of 0.76 days, McCormac et al. 2020). The dashed line is an approximate timescale at the base of the convection zone. The insert shows the associated convective velocity in cgs units, the point where the velocity is zero defines the edge of the convective zone. Right: The density as a function of radius (using Model S and radius scaled by the total radius) which covers slightly more than the convection zone. The insert is the same but covering the full radius of the Sun.

We show the radial dependence of the effective viscosity in a Sun-like star in Fig 7.2 by computing eq. 7.1 using data from Model S. We have chosen a tidal period 0.5 day, corresponding with a hot Jupiter on a 1 day orbit[11]. Since α is an order 1 parameter we use $\alpha = 1$ rather than the values reported in Table. 5.1 as qualitatively this will not affect our conclusions here. Here we take $\alpha_M \approx 2$ for the usual mixing-length parameter in accordance with Model S. The three lines represent the prediction from assuming $\aleph = 0, 1, 2$, corresponding with no frequency-reduction, the linear frequency-reduction of Zahn (1966), and a quadratic reduction, respectively. The prescriptions clearly give very different predictions for the magnitudes of ν_E, spanning many orders of magnitude, particularly at the base of the convection zone where $\omega \gg \omega_c$. If $\aleph = 2$ (and also for $\aleph = 1$), ν_E is dominated by regions close to the surface, where ω_c is largest.

The data from Model S for the current Sun can be used for a crude estimate of the inspiral timescale (using eq. 7.9), where we assume that the planet orbits faster than the star rotates and hence that tidal dissipation drives inward migration. We take $\tau_c \approx 20$ days which approximately corresponds to the base of the convection zone where the largest convective eddies

---

[10] In astrophysics it is common to use centimetre, grams and seconds (known as cgs) as the units.

[11] This is equivalent to a semi-major axis of $a \approx 0.02AU$.

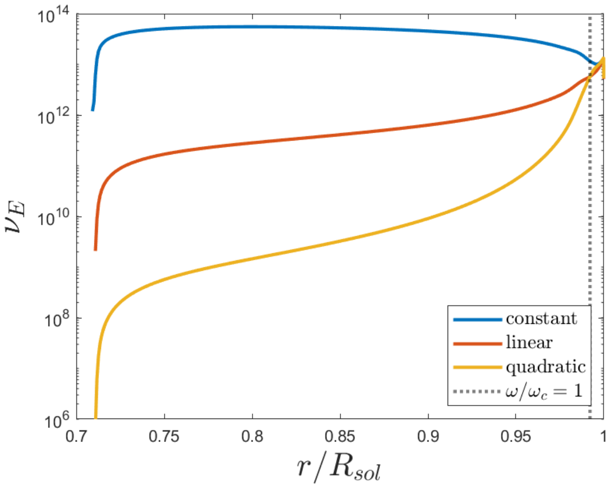

Figure 7.2: Effective viscosity evaluated as a function of radius in the solar convection zone according to mixing-length theory for each prescriptions for its high-frequency behaviour (eq. 7.1). We adopt a tidal period of 0.5 days, corresponding with a hot Jupiter on a 1 day orbit. This demonstrates the importance of using the correct prescription for ν_E (in cgs units).

reside. We thus find

$$\tau_a \approx \begin{cases} 30\,\text{Myr} & \text{if} \quad \aleph = 0, \\ 3\,\text{Gyr} & \text{if} \quad \aleph = 1, \\ 321\,\text{Gyr} & \text{if} \quad \aleph = 2. \end{cases} \tag{7.20}$$

It is worth reminding the reader that this is the timescale for the planet to migrate from its initial semi-major axis to $a = 0$. Since our simulations are consistent only with $\aleph = 2$ (for such tidal periods), this suggests that the orbital decay timescale of the closest hot Jupiters around solar-type stars due to this mechanism would be negligible over the main-sequence lifetime of the star.

This crude estimate is very simplistic, and we have not considered the integrated ν_E due to all eddies throughout the convection zone (e.g. Zahn 1989; Ogilvie & Lin 2007; Remus et al. 2012; Barker 2020), but it illustrates that these prescriptions give significantly different predictions for orbital decay timescales. Note also that a modified stellar tidal quality factor for this mechanism can be defined by (Zahn, 2008; Ogilvie, 2014)

$$Q'_\star \propto \frac{1}{\omega \Delta t} \propto \begin{cases} \omega^{-1} & \text{if} \quad \aleph = 0, \\ \text{const} & \text{if} \quad \aleph = 1, \\ \omega & \text{if} \quad \aleph = 2, \end{cases} \tag{7.21}$$

where $\Delta t \propto 1/\nu_E$ is a tidal lag time[12]. Note that our results imply that Q' is not constant for the interaction between tides and convection. We also find that it does not scale like a constant-time lag $(1/\omega)$ except for very low frequencies according to Ch. 6.

7.2 Effective viscosity and timescales following stellar evolution

In many astrophysical applications, tidal forcing occurs in the high-frequency regime for the dominant convection eddies, such that $\omega/\omega_c \gg 1$. Based on our results, this implies a

---

[12] Using eq. 7.19 we find $Q'_\star$ values of 2×10^5, 2×10^7 and 2×10^9 for $\aleph = 0, 1, 2$ respectively for a Jupiter mass planet around a Sun-like star on a one day orbit. In the interests of clarity, it is important to highlight that this is specifically for a 1 day orbit and as the period changes so too do these values.

significant reduction in the effective viscosity. As stars evolve, their convective velocities and length-scales evolve, leading to large changes in turbulent viscosities predicted by MLT. Here we apply our results to predict planetary orbital decay around an evolving solar-mass star. We compute the dissipation more accurately than in the previous section by integrating over all of the eddies in the convection zone for a particular ν_E prescription that matches our simulations.

7.2.1 Effective viscosity model

To apply the results of Ch. 6, we must adopt an appropriate fit for ν_E. We choose to fit the points in Fig. 6.6 which provide the maximum estimate of the dissipation (here we ignore any possible amplitude dependence for $\omega/\omega_c \gtrsim 1$), such that we define

$$\nu_{\rm FIT} = u^{\rm mlt} l^{\rm mlt} \begin{cases} 5 & \text{if} \quad (\frac{|\omega|}{\omega_c} < 10^{-2}), \\ \frac{1}{2}\left(\frac{\omega_c}{|\omega|}\right)^{\frac{1}{2}} & \text{if} \quad (\frac{|\omega|}{\omega_c} \in [10^{-2}, 5]), \\ \frac{25}{\sqrt{20}}\left(\frac{\omega_c}{|\omega|}\right)^{2} & \text{if} \quad (\frac{|\omega|}{\omega_c} > 5), \end{cases} \tag{7.22}$$

where $u^{\rm mlt}$ is the convective velocity and $l^{\rm mlt}$ is the mixing length, and $\omega_c = u^{\rm mlt}/l^{\rm mlt}$, which are obtained in stellar models computed with MESA. Note that the constant, 5, is obtained from the results of Ch. 6 (see Table. 5.1) while the following constants are determined by ensuring continuity of ν_E at the transition frequencies that are assumed (based on the results of Ch. 6). For the purposes of this crude application (and in the absence of compressible simulations), we have simply replaced d with $l^{\rm mlt}$ and $u_z^{\rm rms}$ with $u^{\rm mlt}$ and calculated these at each radius in the convection zone. To apply this in a stellar model we calculate the correct equilibrium tide in convective envelopes (Terquem et al., 1998; Ogilvie, 2014), and then compute the dissipation integral following the procedure outlined in[13] Barker (2020). The result is then converted into a tidal quality factor $Q'_{\rm eq}$, which is an inverse measure of the dissipation (e.g. Ogilvie, 2014) (see Barker 2020 for further details).

The resulting orbital decay rate for a (circularly orbiting) short-period planet of mass M_p around a slowly rotating star of mass $M_\star$ and radius R can be computed from

$$\frac{\mathrm{d}\ln a}{\mathrm{d}t} = -\frac{9\pi}{Q'_{\rm eq}}\left(\frac{M_p}{M_\star}\right)\left(\frac{M_\star}{M_\star + M_p}\right)^{\frac{5}{3}} \frac{P_{\rm dyn}^{\frac{10}{3}}}{P_{\rm orb}^{\frac{13}{3}}}\,. \tag{7.23}$$

This is subtly different from the inverse of eq. 7.11 (note that $\tau_a \propto a/|\dot{a}|$) as it includes the (modified) tidal quality factor for the equilibrium tide, $Q'_{\rm eq}$, (this will be explained later in this section) and also does not assume $M_p \ll M_\star$.

The expression for the (modified) tidal quality factor for the equilibrium tide[14] can be obtained by considering the viscous dissipation of the equilibrium tide which is defined as

$$D_\nu = \frac{\omega^2}{2}\int r^2 \rho(r)\nu_E(r) D_l(r)\,\mathrm{d}r\,, \tag{7.24}$$

---

[13] See also Zahn (1989) and Remus et al. (2012) for a similar approach using the conventional equilibrium tide, which is strictly invalid in convection zones. This predicts more efficient dissipation than our model by a factor of 2-3 for the same $\nu_{\rm FIT}$.

[14] This is also detailed in Barker (2020).

where $D_l(r)$ is obtained from the viscous fluid stress tensor (in spherical harmonics) for the non-wavelike equilibrium tide as computed in § 1.2.1. This gives $D_l(r)$ to be

$$D_l(r) = 3\left|\frac{\mathrm{d}\xi_r}{\mathrm{d}r} - \frac{\Delta_l}{3}\right|^2 + l(l+1)\left|\frac{\xi_r}{r} + r\frac{\mathrm{d}}{\mathrm{d}r}\left(\frac{\xi_h}{r}\right)\right|^2 + l(l-1)(l+1)(l+2)\left|\frac{\xi_h}{r}\right|^2 , \quad (7.25)$$

where

$$\Delta_l = \frac{1}{r^2}\frac{\mathrm{d}}{\mathrm{d}r}\left(r^2\xi_r\right) - l(l+1)\frac{\xi_h}{r} \quad (7.26)$$

and $\boldsymbol{\xi}$ is the tidal displacement vector for the equilibrium tide in the convective region of the host star (see § 1.2.1 for how this is defined) which can be expanded in terms of spherical harmonics ($Y_l^m e^{-i\omega t}$). Explicitly, for a single harmonic, say $l = m = 2$, the displacement vector can be written as

$$\boldsymbol{\xi} = \Big(\xi_r(r)e_r + r\xi_h(r)\nabla\Big)Y_l^m(\theta,\phi)e^{-i\omega t} , \quad (7.27)$$

where $\mathbf{e}_r$ is radial unit vector and ∇ is the gradient operator. With this definition the tidal quality factor is given by

$$Q'_{\text{eq}} = \frac{3(2l+1)R_\star^{2l+1}|A|^2}{16\pi G}\frac{|\omega|}{D_\nu} , \quad (7.28)$$

where A is the dimensional tidal amplitude[15]. To give a clearer picture of this quantity, in eq. 1.8 we would have that $A = \mathcal{A}/R_1^2$. Note that A is required here as $\xi \propto A$ in linear theory and hence $D_\nu \sim A^2$, thus Q'_{eq} is independent of A in linear theory.

7.2.2 Analysis

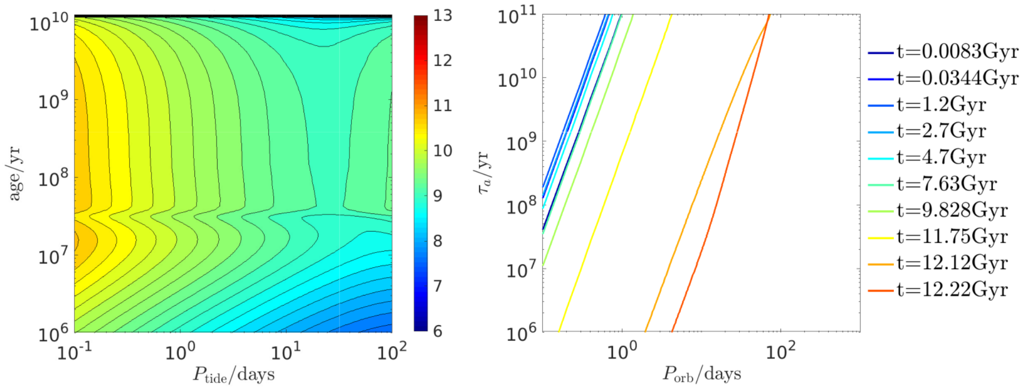

Figure 7.3: Left: Contours of $\log_{10} Q'_{\text{eq}}$ resulting from dissipation of the correct equilibrium tide in the convective envelope of a $1M_\odot$ star (with initial metallicity 0.02) as a function of age and tidal period based on applying ν_{FIT}. Right: inspiral time τ_a as a function of orbital period resulting from this mechanism, for a $1M_J$ planet in circular orbit about a slowly rotating $1M_\odot$ star at various ages prior to the red giant phase ($P_{\text{rot}} = 100$ d for all curves, which may be relevant for later ages).

---

[15] A has units of time^{-2} which can be seen from analysis of eq. 1.8.

We show $Q'_{\rm eq}$ (from eq. 7.28) computed using $\nu_{\rm FIT}$ (eq. 7.22) in models of a $1M_\odot$ star (computed with an initial metallicity 0.02) in the left panel of Fig. 7.3 as function of tidal period $P_{\rm tide} = 2\pi/\omega$ and age (in yrs). The models used are computed using the MESA code and provide 400 snapshots which follow the evolution of the star. This shows that during the main sequence, solar-mass stars have $Q'_{\rm eq} \sim 10^{10}$ for tidal periods of order 1 day, though $Q'_{\rm eq}$ is smaller during pre-main sequence phases (ages prior to approximately 10^7 yr) and as the star evolves off the main sequence (ages approaching 10^{10} yr), indicating more efficient dissipation during these phases[16].

We note that the relevant tidal frequency, assuming $P_{\rm orb} \ll P_{\rm rot}$, is $\omega = 4\pi/P_{\rm orb}$, and that the high-frequency regime is found to be the relevant one for short orbital periods (at all stages in stellar evolution). As a result $\nu_{\rm FIT} \propto P^2_{\rm orb}$, implying that $Q'_{\rm eq} \propto P^{-1}_{\rm orb}$, so that the right hand side of eq. 7.23 is proportional to a^{-5}, indicating accelerating inspiral. The corresponding timescale for orbital decay of a 1 M_J hot Jupiter is

$$\tau_a \approx -\frac{1}{5}\left(\frac{\mathrm{d}\ln a}{\mathrm{d}t}\right)^{-1} \approx 250\,\mathrm{Gyr}\left(\frac{M_J}{M_p}\right)\left(\frac{P_{\rm orb}}{1\,\mathrm{day}}\right)^{\frac{10}{3}}, \tag{7.29}$$

which we have evaluated in a stellar model similar to the current Sun (assuming $P_{\rm rot} = 20$ days). Note that the $1/5$ constant comes from eq. 7.17.

We show similar estimates for τ_a as a function of orbital period $P_{\rm orb}$, computed numerically for a $1M_\odot$ star for a range of ages, in the right panel of Fig. 7.3. We have assumed $P_{\rm rot} = 100$ days for all ages for the purposes of this figure, since the curves shown are unaffected by rotation except for the latest ages when the star is expected to rotate so slowly. This figure, and the estimate in eq. 7.29, indicates that convective damping of equilibrium tides plays a negligible role for planetary orbital decay around main sequence stars, even assuming the most optimistic fit for $\nu_{\rm FIT}$ consistent with our simulations. This is because of the strong reduction in the effective viscosity with the quadratic scaling law. On the other hand, for later evolutionary stages as the star begins to evolve onto the red giant phase, this mechanism becomes more efficient, primarily because the stellar radius becomes much larger. This mechanism thus predicts the destruction of many short-period planets during the later stages in the evolution of solar-mass stars. (We have omitted figures showing even later evolutionary stages for clarity, but planets out to much wider orbits can be rapidly destroyed by this mechanism.)

Our results using $\nu_{\rm FIT}$ (with $\alpha = 5$ at low frequencies) is found to predict more efficient dissipation by approximately a factor of 15, and therefore shorter tidal evolutionary timescales by this factor, than the usual assumption $\alpha = 1/3$ that is usually assumed when applying the Goldreich & Nicholson (1977) reduction (e.g. Ogilvie & Lin, 2007). We note that an enhancement in α is apparently required to explain the results of Hansen (2012), though they employ the linear reduction law, and thus their model predicts much more efficient dissipation at high frequencies. However, we caution that the application here of our results in Fig. 6.6, based on Boussinesq simulations, is very crude. In addition, our simulations find a scatter at high frequencies of approximately an order of magnitude depending on tidal frequency, so the precise results of our application are probably uncertain to within at least such a factor.

---

[16] As a reminder $\nu_E \propto Q'^{-1}$ and so a smaller value of Q' is to be interpreted as more efficient dissipation. This can be seen from eq. 7.28 which has $Q'_{\rm eq} \sim D_\nu^{-1}$.

7.3 A brief word on negative effective viscosities

As mentioned in aside 1.5, negative effective viscosity should be considered as an energy transfer process rather than an analogue of molecular viscosity. In the formalism we have described in this work the definition of a positive effective viscosity is such that the convective motion extracts energy from the tidal flow. In this case the energy being provided to the convection comes at a cost of the orbital or rotational energy. The case of negative effective viscosity can simply be thought of as the inverse of this process, that is, the tidal flow extracts energy from the convection (which is powered by fusion within the star).

One might be tempted think of negative effective viscosities as simply inverting the direction of the evolution of orbital parameters (semi-major axis, eccentricity, etc.). From this perspective the prediction of negative effective viscosity would seem at odds with the observations presented in § 1.1! The problem with this viewpoint is it neglects that we have been considering a local model and it is perhaps the case that the global picture consists of a net positive effective viscosity with locally negative regions. The overall result of this would be a further reduction in the efficiency of this mechanism to dissipate the tide, over and above any frequency scaling, when integrating over the entire convection zone. In principle, a global negative effective viscosity is possible and would indeed drive an inverse tidal evolution. For example, the excitation of eccentricity of the secondary.

Another useful way to consider this problem is through the tidal torque. Much like the problem of the sum total of the effective viscosity, the total torque is the sum of contributions to the tidal torque from all sources. That is, we must consider the turbulent dissipation of the equilibrium tide alongside other sources of tidal dissipation such as inertial waves, internal gravity waves, etc. Thus even if the total effective viscosity was negative it may be that other mechanisms are dominant and have opposing sign of tidal torque. In fact a similar process is thought to be occurring with the retrograde rotation of Venus where the gravitational and atmospheric tides impose torques on the planet with opposite sign (Correia & Laskar, 2001; Correia et al., 2008).

7.4 Summary

In this chapter we have applied the results of the simulations (and theory) presented in Ch. 3-6 to toy problems based on real world physical systems. In particular, in this chapter, we have focused on the problem of the orbital evolution of HJ planets around Sun-like stars. We will discuss some additional implications of this work in Ch. 8.

Summary: Key findings

We have demonstrated through simple models the following:

- the correct prescription for the frequency dependence of the tidal dissipation is essential,
- inspiral timescales span many orders of magnitudes depending on the prescription used (from much shorter than the lifetime of the system to significantly longer),

- the high-frequency regime is the relevant case for 1 M_J HJ planets around Sun-like stars,
- this then suggests that this mechanism is unlikely to be the dominant mechanism for tidal dissipation for HJ's

We have also discussed the consequences and interpretation of negative effective viscosities. Considerations that should be made are:

- negative effective viscosity may be a localised phenomenon,
- we must consider all sources of tidal torque (not just the mechanisms in this work),
- global negative effective viscosity would result in an inverse tidal evolution (such as excitation of eccentricity).

Chapter 8

Conclusions and future work

Contents

The interaction between large-scale equilibrium (non-wavelike) tidal flows, as described in § 1.2, and turbulent convection is believed to act as an effective viscosity (ν_E) in damping these tidal flows. This mechanism has long been thought to be one of the dominant mechanisms of tidal dissipation in stars with convective envelopes[1] (Zahn, 1966, 1977; Zahn, 1989; Zahn & Bouchet, 1989). However, it is probably the most uncertain tidal mechanism, making it difficult to make robust predictions for the resulting spin-orbit evolution in astrophysical systems. In particular, it is thought that the effective viscosity mediating the interaction between the tidal flow and convection depends strongly on the tidal frequency, and its efficiency is expected to be greatly reduced when the tidal frequency is larger than the relevant convective frequency (Zahn, 1966; Goldreich & Nicholson, 1977; Goodman & Oh, 1997). However, the correct frequency scaling that should be applied in the high-frequency regime has been a matter of much controversy (see § 1.3), with the original work of Zahn (1966) proposing $\nu_E \sim \omega^{-1}$ when[2] $\omega \gg \omega_c$, and Goldreich & Nicholson (1977) later proposing $\nu_E \sim \omega^{-2}$ instead. The resolution of this issue is essential before we can apply this mechanism to make robust predictions for tidal evolution in planetary systems and binary stars.

We have presented the results from an extensive parameter survey of numerical simulations, in Ch. 3, 5 and 6, designed to explore the interaction between large-scale equilibrium tidal flows and convection within a star or giant planet. We have used Boussinesq hydrodynamical simulations of a local Cartesian patch of convective fluid, which is modelled within the well-studied Rayleigh-Bénard system (§ 2.1.3), to which we impose a large-scale tidal-like shear flow as a "background flow" (§ 2.1.1). Our analysis of these simulations has primarily focused on the evaluation of the effective viscosity (eq. 2.3.2) which arises as a result of the interaction between the convection and this tidal-like flow. We have presented an in-depth study into the

---

[1] The tidal excitation and dissipation of inertial waves, perhaps through their interaction with convection, may also be important for low tidal frequencies (see e.g. Ogilvie 2014 and references therein).

[2] This regime is relevant in most applications.

relationship between the frequency spectrum of both the energy and the Reynolds stress in the convection and the frequency-dependence of the effective viscosity, in Ch. 5 and 6.

In this parameter survey we have explored a wide range of parameters, to explore the effective viscosity (in Ch. 3, 5 and 6) and the effective elasticity (in Ch. 3 and 5). This has largely focused on the tidal (shear) frequency dependence ω, which is our primary concern, but in order to gain a more complete understanding has also considered effects of shear amplitude (a_0), the strength of convection (parametrised by the scaled Rayleigh number R), the horizontal domain size $(L_x = L_y)$ and a brief look at the effects of changing the ratio of molecular viscosity to thermal diffusivity (through the Prandtl number Pr).

8.1 Main results

We have determined that the effective viscosity governing the interaction between tidal flows and convection exhibits three different regimes depending on the ratio of the tidal and convective frequencies (as shown most clearly in e.g. Fig. 6.6). We refer to these as the low frequency, intermediate frequency and high-frequency regimes, respectively. Our main results are as follows, where we also highlight which of the three regimes each statement applies to:

1. (*low-frequency regime*) For very low tidal frequencies, the effective viscosity becomes frequency-independent. The transition into this regime is observed to occurs at $\omega/\omega_c \lesssim 10^{-2}$, which is a much lower frequency than has been predicted (Zahn, 1966; Goldreich & Nicholson, 1977) or observed in simulations to date (see Table 6.1). Previous work instead expected or observed the transition to occur at approximately the convective frequency. This frequency-independent regime coincides with the commonly-adopted constant tidal time-lag model (e.g. Darwin, 1879d; Mignard, 1980; Hut, 1981; Eggleton et al., 1998), which our results have shown is only valid for a limited range of very low tidal frequencies $\omega/\omega_c \lesssim 10^{-2}$. The constant time-lag model is therefore not appropriate for modelling tidal interactions except for such low frequencies, which are usually not relevant in astrophysical applications.

2. (*low-frequency regime*) We find this mechanism to be considerably more efficient than has been previously proposed at very low frequencies. In particular, we have determined that $\nu_E \approx \alpha u_z^{\mathrm{rms}} d$, where[3] $\alpha \approx 5$. This result appears to be independent of Rayleigh number, suggesting that we might be able to extrapolate this to astrophysical parameter values. Previous work has adopted a naive mixing-length picture based on the analogy with kinetic theory, which instead gives $\alpha = 1/3$ (e.g Zahn, 1989; Ogilvie & Lin, 2007) if d corresponds with the usual mixing length. In our Boussinesq model d is the most natural length-scale to identify with the mixing length, but compressible models are needed before we can be fully confident of the appropriate value of α.

3. (*intermediate regime*) We have discovered a new regime with a different frequency scaling $\nu_E \propto \omega^{-0.5}$, which occurs in the range $10^{-2} \lesssim \omega/\omega_c \lesssim 1-5$ (depending on tidal amplitude), which we refer to as the intermediate-frequency regime. This regime is observed for all Rayleigh numbers considered, suggesting that it might be a robust feature of the interaction between tides and convection. To the best of our knowledge, this

---

[3] We remind the reader that this is strictly different from the usual mixing-length "α" parameter, see § 2.3.3.

regime has never previously been predicted or reported. A similar intermediate regime, but with a different power law of -1 was however observed for spherical convection in Vidal & Barker (2020b) for $1 \lesssim \omega/\omega_c \lesssim 5$. The existence of such an intermediate regime here and in Vidal & Barker (2020b) may explain the disagreement between the results in our Ch. 3, 5 and Ogilvie & Lesur (2012) compared with Penev et al. (2009b). This new regime may be relevant in many astrophysical applications where the constant time-lag model was previously applied.

4. (*low/intermediate regime*) The frequency scaling of the effective viscosity, in both the low and intermediate frequency regimes, appears to follow the corresponding slope of the frequency spectrum of the kinetic energy (and also the Reynolds stress) when $\omega/\omega_c \lesssim 1$ (see also Vidal & Barker, 2020b,a). This is shown in Fig. 6.8. In these regimes, the agreement of the slope of the eddy viscosity points with both the energy and Reynolds stress curves is robust, but the constants of proportionality could depend on the Rayleigh number, the Prandtl number and the tidal amplitude (though the dependence on the latter has been found to be weak). In principle, this could be determined by performing a more extensive parameter survey for larger R for frequencies that lie within the intermediate regime. This would be a challenging task however, since simulations with large R are computationally costly, and we have only been able to robustly find the intermediate regime for ν_E in simulations with $R \leq 500$.

5. (*high-frequency regime*) For $\omega \gtrsim \omega_c$, we provide strong evidence clearly demonstrating that the effective viscosity follows $\nu_E \propto \omega^{-2}$, in agreement with prior simulations (Ogilvie & Lesur 2012; Braviner 2015 and those performed concurrently with this thesis Vidal & Barker 2020b,a) and theoretical expectations (Goldreich & Nicholson, 1977; Goldman, 2008; Ogilvie & Lesur, 2012), see Table 6.1. This mechanism is therefore much less efficient for high-frequency tidal forcing than would be predicted by adopting the less drastic frequency-reduction of Zahn (1966). One implication is that this mechanism is unlikely to cause appreciable orbital decay for hot Jupiters orbiting main-sequence stars (for which dynamical tide mechanisms such as internal gravity wave damping or inertial waves in sufficiently rapidly rotating stars are probably much more important).

6. (*high-frequency regime*) Despite our simulations being in agreement with Goldreich & Nicholson (1977) in finding $\nu_E \propto \omega^{-2}$ in the high-frequency regime, our results do not support their physical explanation. This is most clearly evident from our observation that it is the energetically dominant modes of the convection which contribute the most to the effective viscosity. In fact, we do not observe any significant contribution from the "resonant modes" in the spatial spectrum (see Fig. 6.9), which were predicted by Goldreich & Nicholson (1977) to provide the dominant contribution. However, we do observe resonant behaviour in the frequency spectrum of the kinetic energy, particularly when the shear is in the high-frequency regime. In the absence of a simple mechanism to explain this scaling, the asymptotic analysis in Ogilvie & Lesur (2012), which we have extended in Ch. 4, does however provide a mathematical prediction for this behaviour which highlights that the convection responds viscoelastically to high-frequency shear.

7. (*high-frequency regime*) The sign of the effective viscosity, ν_E, transitions from positive

to negative (anti-dissipation) within the high-frequency regime. The mechanism behind the transition to anti-dissipation is unclear, however, there are signs that the transition is pushed to ever higher frequencies with increasing strength of convection (R). This observation is consistent with the asymptotic theory presented in Ch. 4 and corroborates the tentative detection of negative values in Ogilvie & Lesur (2012). Further, we have demonstrated that laminar convection gives robust negative values in small domains for certain roll alignments (Ch. 3), which depend on the initial conditions. This result is explained by the asymptotic theory in Ch. 4.

8. (*combining all regimes*) From Fig. 6.6 it seems clear that if the appropriate scaling is chosen, that is the scaled effective viscosity (eq. 2.63) and scaled shear frequency (ω/ω_c where ω_c is defined by eq. 2.30) the effective viscosity collapses to a single master curve (for a given a_0) which is independent of R, as far as we are able to probe this. This suggests that we can explore its consequences using stellar models, as we describe in Ch.7 (see also Barker 2020).

Our results confirm that tidal dissipation in convective regions due to this mechanism does not behave like a frequency-independent tidal quality factor. For very low-frequency tidal forcing ($\omega \ll \omega_c$), our results indicate that this mechanism behaves in a similar way to the commonly-adopted constant tidal lag-time model, at least in the simplest cases of either an aligned circular orbit or an aligned, spin-synchronised, weakly eccentric orbit, where there is only one tidal frequency (Darwin, 1879d; Alexander, 1973; Mignard, 1980; Hut, 1981; Eggleton et al., 1998; Ivanov & Papaloizou, 2004). However, we have shown that ν_E is frequency dependent for a range of frequencies even for $\omega \lesssim \omega_c$ and does not attain a constant value until $\omega/\omega_c \lesssim 10^{-2}$. This indicates that the constant time-lag model is strictly inappropriate to model tidal interactions even in (most of) the low-frequency regime. In addition, our result that $\nu_E \propto \omega^{-2}$ when $\omega \gtrsim \omega_c$, clearly indicates in the general case that if any component of the tide has a frequency that is comparable with or larger than the dominant convective frequency, then different components of the tide will be damped at different rates i.e. they will have different lag times (Lai, 2012), and these will no longer be constant (see also Ivanov & Papaloizou 2004; Vick & Lai 2020). The consequences of this should be explored in future work.

Our results disagree with the high-frequency scaling law of Zahn (1966) and Zahn (1989), and apparently also with the prior simulations of Penev et al. (2007) and Penev et al. (2009b) (see § 1.3.2, 1.3.4 and Table 6.1). The reason for this discrepancy has not yet been elucidated, but it is possible that it is due to the narrow range of frequencies they probed being only in the intermediate regime (and hence they would not observe ω^{-2} behaviour). Alternatively, it may be related to differences in the turbulent temporal power spectra between these simulations. Another possibility is that compressible convection responds differently to tidal forcing in an important way compared with the Boussinesq convection that we have modelled. The simulations in Penev et al. (2009a) adopted the anelastic approximation, allowing them to simulate multiple density scale heights, whereas our model is effectively restricted to single scale height. However, our simulations have been run for a much longer duration, over a much wider range of frequencies, and they have also been confirmed for laminar convection with an independent asymptotic analysis. A further difference between our models is that their simulations adopted a body force to drive the tidal flow rather than a background flow in a shearing box.

8.1.1 Secondary results

Our main astrophysically relevant results have been described above, but we have also obtained a number of interesting fluid dynamical results which we will now summarise. We will briefly highlight some of these results which may help shed light on the fundamental physics at play.

1. In small domains $(L_x = L_y = 2,\ L_z = 1)$ with weak convection (low $R \leq 10$) we find convective rolls aligned in either the $\mathbf{e}_x$ or $\mathbf{e}_y$ directions and it has been found that they result in robust values of either negative or positive (respectively) magnitudes of the effective viscosity regardless of frequency. This result is supported by the asymptotic analysis presented in Ch. 4 which extends that of Ogilvie & Lesur (2012). Furthermore, the frequency scaling and sign for the $\mathbf{e}_y$ aligned case, $\nu_E \propto \omega^{-2}$, can be obtained by a simple force balance argument.

2. In small domains $(L_x = L_y = 2,\ L_z = 1)$ with weak convection (low $R \leq 10$) we find that the effective elasticity, S_E, behaves differently for each of the $\mathbf{e}_x$ or $\mathbf{e}_y$ configurations. In the $\mathbf{e}_x$ aligned cases S_E demonstrates frequency independence in the low-frequency regime and approximately a quadratic power law in the high-frequency regime, while the inverse is true for $\mathbf{e}_y$ aligned rolls.

3. For larger domains (up to $L_x = L_y = 4$) we find that the flow structure consists of the superposition of a set of discrete wavemodes (which for these cases we have named spots/stripes and stripes/spots). Each class of structure will result in either a positive or negative effective viscosity regardless of the frequency but the effective viscosity follows the same frequency dependence as in the smaller domains.

4. In small domains $(L_x = L_y = 2,\ L_z = 1)$ with $R = 100$ we find that S_E follows the trend of $\mathbf{e}_y$ aligned rolls. That is, S_E demonstrates frequency independence at high-frequency regime and approximately a quadratic power law in the low-frequency regime.

5. In our asymptotic analysis in Ch. 4 inclusion of the thermal contribution (which we introduce in our extension of Ogilvie & Lesur 2012) is essential to obtain negative effective viscosities in our model. Interestingly, this addition only manifests as a modification to the pressure term up to the order we consider.

6. In the larger domain sizes with turbulent (chaotic) flow patters, presented in Ch. 6 we found that in the low and intermediate frequency regimes that the effective viscosity was shear amplitude, a_0, independent while in the high-frequency regime we observed signs of dependence on the magnitude of a_0.

7. In Ch. 6 we demonstrated that, for a number of decades in frequency, the frequency spectrum of the volume average kinetic energy follows a -0.5 power law. This occurs in the sub-inertial range $(\omega < \omega_c)$ which is a regime that has received very little attention from the convection community.

It would be interesting to explore further the contributions of different wavemode contributions to the effective viscosity as this may shed light on the physical mechanism behind the negative viscosity.

8.2 Astrophysical consequences

We consider here some of the applications of these results to various astrophysical systems. This is by no means an exhaustive list but will cover what we consider to be the most important.

8.2.1 Hot Jupiters

One implication of our results is that the inferred orbital decay of the shortest-period hot Jupiters[4] with observed transit timing variations (e.g. Maciejewski et al. 2016; Patra et al. 2017; Maciejewski et al. 2018; Bouma et al. 2019) is unlikely to result from the interaction between tides and convection. Instead, these observations are probably explained by the tidal excitation and dissipation of internal gravity waves in radiative regions (Goodman & Dickson, 1998; Ogilvie & Lin, 2007; Barker & Ogilvie, 2010; Barker, 2011; Weinberg et al., 2012; Essick & Weinberg, 2016; Chernov et al., 2017; Barker, 2020). This mechanism is able to provide the required level of dissipation to explain the decaying orbit of WASP-12 b[5] (e.g. Barker 2011; Chernov et al. 2017; Weinberg et al. 2017; Bailey & Goodman 2019), if we assume that these waves are fully dissipated. However, uncertainties remain regarding the structure of the star (whether or not it has a radiative core), and whether these waves should in fact be fully damped. In general, our results imply that convective damping of equilibrium tides is unlikely to be an important mechanism for planetary migration around main-sequence stars. Instead, dynamical tides such as inertial waves in young rapidly-rotating stars (Mathis, 2015; Bolmont & Mathis, 2016; Barker, 2020), and internal gravity waves, are likely to be much more important.

Aside 8.1: Ultra Short-Period planets (USP's)

USP's are the terrestrial equivalent to HJ's in that they are small rocky planets in sub 1 day orbits around their host star.

Recently, the survival over the main sequence lifetimes of Sun-like stars of USP's on circular orbits has been considered. Observations suggest that USP's do not undergo significant inspiral over the lifetime of the star (Hamer & Schlaufman, 2020). One explanation for this is that these planets are deep into the high-frequency regime and hence dissipation of the equilibrium tide would be weak (and hence extremely long inspiral timescales).

8.2.2 Giant planet satellites

Another implication of our results is that the strong tidal dissipation required to explain the outward migration of the satellites of Jupiter and Saturn (Lainey et al., 2009, 2012, 2017) is unlikely to be produced by the convective damping of large-scale tidal flows. This supports prior theoretical arguments by Goldreich & Nicholson (1977). However, these planets rotate sufficiently rapidly that convection is likely to be strongly rotationally constrained, motivating further simulations like those in this paper, but in the presence of rapid rotation (e.g. Barker

---

[4] For a non-exhaustive list of the most favourable HJ's for migration detection see Barker (2020); Patra et al. (2020).

[5] The transit time variation of WASP-4 b has been attributed to the star's acceleration towards Earth Bouma et al. (2020). It is possible this star is too small for dissipation due to wave breaking of internal gravity waves.

et al. 2014, by building upon the phenomenology of e.g. Mathis et al. 2016). Dynamical tides such as inertial waves (Ogilvie & Lin, 2004) or internal gravity waves may be essential here. In particular, the presence of a stably-stratified layer caused by gradients in heavy elements may be important (André et al., 2017; André et al., 2019; Pontin et al., 2020), as may the mechanism of resonance locking (Fuller et al., 2016)

8.2.3 White dwarf giant planets

Recently, observations have discovered a giant planet on a short-period orbit around a white dwarf (Vanderburg et al. 2020; Lagos et al. 2020; Muñoz & Petrovich 2020). Convective damping of equilibrium tides is believed to cause planetary destruction around evolved stars (e.g. Mustill & Villaver 2012). Our findings suggest that the effective viscosity from the equilibrium tides interacting with convection is strongest in the low-frequency regime and this is usually the most relevant regime for evolved stars (such as red giants). As such our results may have important consequences to constrain the state of the system before the evolved giant star transitioned into a white dwarf and the subsequent migration[6] of the planet.

8.2.4 Stellar binaries containing an evolved star

When low to intermediate mass stars $(0.3 \text{ to } 10M_\odot)$ evolve off of the main sequence[7] they expand into evolved giants with deep convective envelopes. Tidal dissipation of inertial waves is not thought to contribute in these stars as, due to expansion and conservation of angular momentum, they are slow rotators where inertial waves may not be efficiently excited (or at all). Due to being slow rotators, evolved stars find themselves in the low-frequency regime of the tidal dissipation of the equilibrium tide, and hence where this mechanism has its greatest strength.

The work of Verbunt & Phinney (1995) explored the circularization of binaries containing a white dwarf. In their work they used the description of the incompressible equilibrium tide of Zahn (1989) as described[8] in § 1.2.1. Further, for lack of a better model at the time, they took $\alpha = 1/3$, as per Zahn (1966, 1977); Zahn (1989) (which we remind the reader has no real physical basis). Their work found good agreement with observations despite both of these shortcomings. As pointed out by Barker (2020), the incorrect use of the incompressible equilibrium tide results in an order one over prediction while the $\alpha = 1/3$ assumption makes an order one under prediction, hence neither having an adverse affect on the results in this case. Hence the Verbunt & Phinney (1995) conclusion may be approximately correct after both of these corrections have been accounted for.

8.2.5 Young stellar binaries

Much of the previous work in considering tidal evolution of young stellar systems has assumed that dissipation of the equilibrium tide is the dominant mechanism (Zahn & Bouchet, 1989;

---

[6] Some work has already considered the migration of planets around white dwarfs, e.g. Veras et al. (2019); Veras & Fuller (2019, 2020)

[7] We are considering the evolved stars on the Red Giant Branch, Asymptotic Giant Branch, Horizontal Branch, etc.

[8] Note that the incompressible equilibrium tide is only applicable in the radiative regions of stars and hence their application to the convective regions is incorrect.

Zahn, 2008; Nine et al., 2020). However, such young stars are typically rapid rotators and hence, not only are these systems likely to be in the high-frequency regime where the equilibrium tide is weak, but they will also be susceptible to the efficient excitation of inertial waves (and hence dissipation of the dynamical tide). The question of which of these sources of dissipation is dominant has been explored by Barker (2020) where it was shown that the dissipation of inertial waves (providing they are excited) dominates, see also Mathis (2015).

8.2.6 Anti-dissipation

It is important to note that we obtained statistically significant negative effective viscosities, particularly at high frequencies, indicating the possibility of tidal anti-dissipation. In principle, this could drive the opposite tidal evolution to that which is commonly expected e.g. excitation rather than damping of planetary eccentricities. Despite our results indicating negative values are likely pushed to non-physically high frequencies in physical systems, it is nevertheless an important consideration for more realistic models (such as inclusion of rotation, fully compressible, magnetic fields, etc.), which may allow for negative effective viscosities. The recent work[9] of Fuller (2020) has indicated that in close stellar binaries anti-dissipation (what they refer to as inverse tides) is also possible if one of the stars is undergoing self-excited pulsations. Similar to how what we have explored in this work, where convection could theoretically transfer energy into the tidal flow, these pulsations can pump energy into the tidal flow.

8.3 Where do we go from here?

Much further work is required to explore the interaction between tidal flows and convection, to study: more turbulent regimes of convection, the incorporation of rotation, modelling significant density variation (e.g. by simulating convection using the anelastic approximation), and the extension of this problem to idealised (and, ultimately, more realistic) global models of stars or planets.

Despite much progress having being made in recent years on this problem there is still much work to do to understand the physics of the interaction between tidal flows and convection. In this work we performed Boussinesq simulations, which effectively limits them to small domains relative to a pressure scale height, but convection in stars can occur over many scale heights so that compressible effects could be important. We propose that simulations to investigate anelastic convection, which would build upon Penev et al. (2009b) by exploring a much wider range of parameters, and in particular tidal frequencies, would be of great interest. These simulations would be able to make a more quantitative comparison with mixing-length theory. In addition, since all stars and planets rotate, it is important to study the effects of convection in this problem. It is known that sufficiently rapid rotation acts to constrain convection (Stevenson, 1979; Barker et al., 2014; Currie et al., 2020), which probably affects the effective viscosity (Mathis et al., 2016). The consequences of the inclusion of rotation, and its effects on the frequency spectrum of kinetic energy, have not yet been explored numerically.

---

[9] The work in Fuller (2020) was conducted after the work presented here.

Appendix A

Effective viscosity with frequency spectra for $R \in \{50, 200, 1000\}$

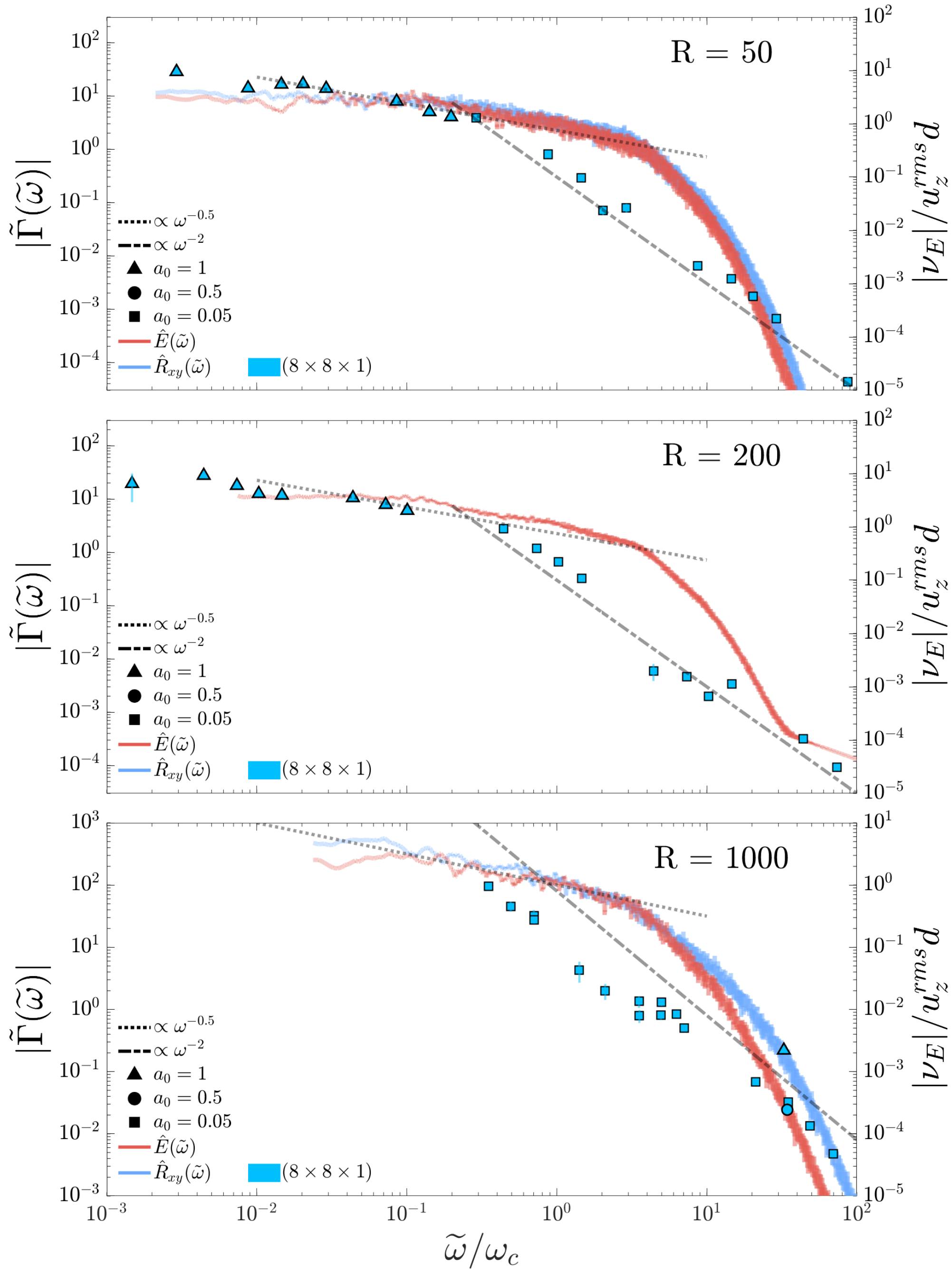

Figure A.1: See Fig. 6.8 for a detailed description (and the associated text § 6.2.3)

Common symbols

a	Semi-major axis. 9, 119
$\mathcal{A}$	Tidal amplitude. 11
α^{mlt}	Mixing-length parameter. 27, 118
a_0	Tidal displacement amplitude. 38
α	Scaled effective viscosity. Scaled by the convective frequency. 49, 89, 110
β	Quadratic fit parameter for small domains. 89
$\boldsymbol{d}$	The vector pointing from the centre of the primary to the point mass secondary. 9, 10
d	layer depth of the Cartesian domain. 33, 40
δ	Dirac delta function. 36
D_ν	Viscous dissipation of the equilibrium tide. 124
$\hat{E}$	Kinetic energy. Specifically this symbol is used for the wavenumber (spatial) spectrum of kinetic energy. 77, 94, 96
$\tilde{E}$	Temporal Fourier transform of the volume averaged kinetic energy. This gives the frequency spectrum of the kinetic energy. 83, 107
F_{lum}	Stellar luminosity flux. 118, 119
$f_\aleph$	Viscosity reduction factor. 119, 121
G	The gravitational constant. 10
Γ	Reynolds stress or kinetic energy. 96
γ	Quadratic fit parameter for large domains. 110, 112
H_p	Pressure scale height. 23, 27
H	Heaviside step function. 36
H_w	Hann window function. 96
k_l^m	Tidal Love number. 13, 14
k_2^2	Tidal Love number for the quadrupole moment. 14
$\mathbf{k}$	The vector of wavemodes. 20
k_x	Wavemode in x. 20, 94
k_y	Wavemode in y. 20, 94
k_z	Wavemode in z. 20
$k_\perp^2$	Sum of the square of horizontal wavenumbers. 41, 77

k^2	The sum of squared wavenumbers, $k^2 = k_x^2 + k_y^2 + k_z^2$. 41, 72
$k_\perp$	The horizontal wavenumber. 94
l^{mlt}	The mixing length. 23, 27, 118
L_x	Length of the Cartesian domain's x axis. 33
L_y	Length of the Cartesian domain's y axis. 33
L_{rad}	Radiative luminosity. 119
M_1	Mass of the primary. 9
M_2	Mass of the secondary. 9
$M_\star$	Stellar internal mass. 118
M_p	Planet mass. 119
M_{env}	Mass of the stellar convective envelope. 120
N^2	Buoyancy (Brunt–Väisälä) frequency. 18, 21, 39
ν_e	Effective viscosity from mixing-length theory. 26, 56
ν_E	Effective viscosity (also see eddy viscosity). 26, 27, 28, 47, 48, 50, 63, 65, 70, 118
N_x	The discrete resolution in the $\mathbf{e}_x$ direction. 44
ν_{mol}	molecular viscosity. 47, 90
n_x	The wavenumber for the wavemode k_x. 54, 76, 94
n_y	The wavenumber for the wavemode k_y. 54, 76, 94
$\hat{\nu}_E$	Fourier transform of the effective viscosity as a function of the wavemodes (k_x, k_y). 82
ν_{FIT}	Model for the effective viscosity frequency dependence. 124
Ω_{s}	Spin frequency of the primary. 10
Ω_{o}	Orbital frequency of the primary. 10
ω	Tidal forcing frequency. 14, 33, 38, 56
ω_c	Convective frequency. 26, 41, 118
$\tilde{\omega}$	The angular frequency associated with the frequency spectra. 83, 107
Φ	Newtonian (gravitational) potential. 9
Ψ	Tidal potential. 10, 15
p	Pressure. 15
Pr	Prandtl number. 41, 42
P_{orb}	Orbital period. 119
P_{dyn}	Dynamical timescale. 120
Q	Tidal quality factor. 14
Q'	Modified tidal quality factor. 14, 25

$Q'_\star$	Stellar modified tidal quality factor. 121, 123

R_1	Radius of the primary. 11
ρ	Density. 15
Ra	Rayleigh number. 41, 42
R	Scaled Rayleigh number (scaled by the critical Rayleigh number for the onset of convection). 41
Ra_c	The critical Rayleigh number for the onset of convection. 41, 54
R_{xy}	Reynolds stress. 46
$\hat{R}_{xy}$	Fourier transform of the Reynolds stress as a function of the wavemodes (k_x, k_y) and time t. 82
$\tilde{R}_{xy}$	Temporal Fourier transform of the volume averaged Reynolds stress. This gives the frequency spectrum of the Reynolds stress. 83

S	Background (tidal) flow amplitude, which is a function of frequency. 38
S_E	Effective elasticity. 49, 50, 51, 70

θ	Temperature perturbation. 39, 40
T	Linear background temperature. 39, 40
τ_c	Convective turnover time. 118
τ_a	Inspiral timescale. 120, 126

$\mathbf{u}_0$	Background tidal flow. 38, 39
$\mathbf{u}^*$	The total velocity. 39
$\mathbf{u}$	Flow field neglecting some background. 39
u_z^{rms}	The root mean square of the vertical component of velocity. 41
u^{mlt}	The mixing-length velocity. 118

$\boldsymbol{\xi}$	Tidal displacement vector. 17, 18, 125

Y_l^m	Spherical harmonic of degree l and order m. 11

ζ	Tidal displacement potential. 35

Common terms

AU	An astronomical unit. Defined as the mean distance between the Sun and Earth.. 4
buoyancy (Brunt–Väisälä) frequency	Buoyancy (Brunt–Väisälä) frequency, see also N^2. 21
background flow	We describe the tidal shear flow as an imposed background flow within the domain. 38
constant time lag model	A model for the dissipation of tidal energy by assuming a constant time lag. 25
constant Q model	A model for tidal dissipation in which the tidal quality factor Q is constant. 26
eddy viscosity	Also see *effective viscosity*. 23, 49
effective viscosity	Viscosity due to fluid motion (not to be confused with molecular viscosity). Also see ν_E. 23
frequency spectrum	The temporal Fourier transform of some quantity. 83, 96
HJ	Hot Jupiter. 4
integral scale	The largest spatial scale of energy injection into a system. 26
line of centres	An imaginary line between the centres of the primary and secondary. 11, 25
Love number	The measure of a bodies central concentration, see also k_l^m. 13
mixing-length theory (MLT)	The mixing-length theory of Prandtl. 23
non-wavelike equilibrium tide	The equilibrium tide valid within convective regions (also see § 1.2.1). 19
primary	The more massive object in a binary system. 9
resonant eddies	Eddies with timescales similar to the tidal period. 28
Reynolds stress	Determines the energy transfer rate between the tidal (shear) flow and the convection. 46

secondary	The second most massive object in a binary system. 9
turbulent viscosity	Also see *effective viscosity*. 23
temperature perturbation	The perturbed temperature about a linear background. 39
tidal anti-dissipation	Conventional tidal theory considers the energy of the tidal flow being dissipated. Tidal anti-dissipation is a process by which energy is injected into the tidal flow by some mechanism. 80
weak friction approximation	The approximation that the angle between the tidally excited deformation and the line of centres is small. 25
wavenumber spectrum	The spatial spectrum of some quantity. 77, 94

Bibliography

Albrecht S., et al., 2012, *"Obliquities of Hot Jupiter host stars: Evidence for tidal interactions and primordial misalignments"*, The Astrophysical Journal, 757, 18

Alexander M. E., 1973, *"The weak friction approximation and tidal evolution in close binary systems"*, Astrophysics and Space Science, 23, 459

André Q., Mathis S., Barker A. J., 2019, *"Layered semi-convection and tides in giant planet interiors: II. Tidal dissipation"*, Astronomy & Astrophysics, 626, A82

André Q., Barker A. J., Mathis S., 2017, *"Layered semi-convection and tides in giant planet interiors. I. Propagation of internal waves"*, Astronomy & Astrophysics, 605, A117

Arnett D., 1996, *"Supernovae and nucleosynthesis"*. Princeton University Press

Ashkenazi S., Steinberg V., 1999, *"Spectra and statistics of velocity and temperature fluctuations in turbulent convection"*, Physical Review Letters, 83, 4760

Bailey A., Goodman J., 2019, *"Understanding WASP-12b"*, Monthly Notices of the Royal Astronomical Society, 482, 1872

Barker A. J., 2011, *"Three-dimensional simulations of internal wave breaking and the fate of planets around solar-type stars"*, Monthly Notices of the Royal Astronomical Society, 414, 1365

Barker A. J., 2016a, *"Non-linear tides in a homogeneous rotating planet or star: global simulations of the elliptical instability"*, Monthly Notices of the Royal Astronomical Society, 459, 939

Barker A. J., 2016b, *"On turbulence driven by axial precession and tidal evolution of the spin–orbit angle of close-in giant planets"*, Monthly Notices of the Royal Astronomical Society, 460, 2339

Barker A. J., 2020, *"Tidal dissipation in evolving low-mass and solar-type stars with predictions for planetary orbital decay"*, Monthly Notices of the Royal Astronomical Society, 498, 2270

Barker A. J., Lithwick Y., 2013, *"Non-linear evolution of the tidal elliptical instability in gaseous planets and stars"*, Monthly Notices of the Royal Astronomical Society, 435, 3614

Barker A. J., Ogilvie G. I., 2009, *"On the tidal evolution of Hot Jupiters on inclined orbits"*, Monthly Notices of the Royal Astronomical Society, 395, 2268

Barker A. J., Ogilvie G. I., 2010, *"On internal wave breaking and tidal dissipation near the centre of a solar-type star"*, Monthly Notices of the Royal Astronomical Society, 404, 1849

Barker A. J., Dempsey A. M., Lithwick Y., 2014, *"Theory and simulations of rotating convection"*, The Astrophysical Journal, 791, 13

Barker A. J., Braviner H. J., Ogilvie G. I., 2016, *"Non-linear tides in a homogeneous rotating planet or star: global modes and elliptical instability"*, Monthly Notices of the Royal Astronomical Society, 459, 924

Batygin K., Bodenheimer P., Laughlin G., 2009, *"Determination of the interior structure of transiting planets in multiple-planet systems"*, The Astrophysical Journal, 704, L49

Beck P., Mathis S., Kallinger T., García R., Benbakoura M., 2019, *"Observations of tides and circularization in red-giant binaries from Kepler photometry"*, EAS Publications Series, 82, 119

Birkby J. L., et al., 2014, *"WTS-2 b: a hot Jupiter orbiting near its tidal destruction radius around a K dwarf"*, Monthly Notices of the Royal Astronomical Society, 440, 1470

von Boetticher A., et al., 2019, *"The EBLM Project: V. Physical properties of ten fully convective, very-low-mass stars"*, Astronomy & Astrophysics, 625, A150

Böhm-Vitense E., 1958, *"Über die wasserstoffkonvektionszone in sternen verschiedener effektivtemperaturen und leuchtkräfte. Mit 5 Textabbildungen"*, Zeitschrift fur Astrophysik, 46, 108

Bolgiano R., 1959, *"Turbulent spectra in a stably stratified atmosphere"*, Journal of Geophysical Research, 64, 2226

Bolmont E., Mathis S., 2016, *"Effect of the rotation and tidal dissipation history of stars on the evolution of close-in planets"*, Celestial Mechanics and Dynamical Astronomy, 126, 275

Bouma L. G., et al., 2019, *"WASP-4b arrived early for the TESS mission"*, The Astronomical Journal, 157, 217

Bouma L. G., Winn J. N., Howard A. W., Howell S. B., Isaacson H., Knutson H., Matson R. A., 2020, *"WASP-4 is accelerating toward the Earth"*, The Astrophysical Journal, 893, L29

Boyd J. P., 2001, *"Chebyshev and Fourier spectral methods"*. Courier Corporation

Braviner H. J., 2015, *"Stellar and planetary tides at small orbital radii"*, PhD thesis, University of Cambridge

Cartwright D. E., 2000, *"Tides: a scientific history"*. Cambridge University Press

Cartwright D., 2001, *"On the origins of knowledge of the sea tides from Antiquity to the thirteenth century"*, Earth Sciences History, 20, 105

Cattaneo F., Emonet T., Weiss N., 2003, *"On the interaction between convection and magnetic fields"*, The Astrophysical Journal, 588, 1183

Chandrasekhar S., 1961, *"Hydrodynamic and hydromagnetic stability"*. Courier Corporation

Chernov S. V., Ivanov P. B., Papaloizou J. C. B., 2017, *"Dynamical tides in exoplanetary systems containing hot Jupiters: confronting theory and observations"*, Monthly Notices of the Royal Astronomical Society, 470, 2054

Christensen-Dalsgaard J., et al., 1996, *"The current state of Solar modeling"*, Science, 272, 1286

Clanton C., Gaudi B. S., 2014, *"Synthesizing exoplanet demographics from radial velocity and microlensing surveys. II. The frequency of planets orbiting M dwarfs"*, The Astrophysical Journal, 791, 91

Cooley J. W., Tukey J. W., 1965, *"An algorithm for the machine calculation of complex Fourier series"*, Mathematics of Computation, 19, 297

Correia A. C. M., Laskar J., 2001, *"The four final rotation states of Venus"*, Nature, 411, 767

Correia A. C. M., Levrard B., Laskar J., 2008, *"On the equilibrium rotation of Earth-like extra-solar planets"*, Astronomy & Astrophysics, 488, L63

C̀uk M., Hamilton D. P., Lock S. J., Stewart S. T., 2016, *"Tidal evolution of the Moon from a high-obliquity, high-angular-momentum Earth"*, Nature, 539, 402

Currie L. K., Barker A. J., Lithwick Y., Browning M. K., 2020, *"Convection with misaligned gravity and rotation: simulations and rotating mixing length theory"*, Monthly Notices of the Royal Astronomical Society, 493, 5233

Damiani C., Mathis S., 2018, *"Influence of stellar structure, evolution, and rotation on the tidal damping of exoplanetary spin-orbit angles"*, Astronomy & Astrophysics, 618, A90

Darwin G. H., 1879a, *"VIII. The determination of the secular effects of tidal friction by a graphical method"*, Philosophical Transactions of the Royal Society, 29, 14

Darwin G. H., 1879b, *"XIII. On the precession of a viscous spheroid, and on the remote history of the Earth"*, Philosophical Transactions of the Royal Society, 170

Darwin G. H., 1879c, *"I. On the bodily tides of viscous and semi-elastic spheroids, and on the ocean tides upon a yielding nucleus"*, Philosophical Transactions of the Royal Society, 170, 35

Darwin G. H., 1879d, *"XX. On the secular changes in the elements of the orbit of a satellite revolving about a tidally distorted planet"*, Philosophical Transactions of the Royal Society, 171, 179

Davidson P. A., 2015, *"Turbulence: An introduction for scientists and engineers"*, second edn. Oxford University Press, Oxford, United Kingdom ; New York, NY, United States of America

Dawson R. I., Johnson J. A., 2018, *"Origins of Hot Jupiters"*, Annual Review of Astronomy and Astrophysics, 56, 175

Dehant V., 1991, *"Review of the Earth tidal models and contribution of Earth tides in geodynamics"*, Journal of Geophysical Research: Solid Earth, 96, 20235

Dmitruk P., Matthaeus W. H., 2007, *"Low-frequency 1/f fluctuations in hydrodynamic and magnetohydrodynamic turbulence"*, Physical Review E, 76

Duchêne G., Kraus A., 2013, *"Stellar multiplicity"*, Annual Review of Astronomy and Astrophysics, 51, 269

Duguid C. D., Barker A. J., Jones C. A., 2020a, *"Tidal flows with convection: frequency-dependence of the effective viscosity and evidence for anti-dissipation"*, Monthly Notices of the Royal Astronomical Society, 491, 923

Duguid C. D., Barker A. J., Jones C. A., 2020b, *"Convective turbulent viscosity acting on equilibrium tidal flows: new frequency scaling of the effective viscosity"*, Monthly Notices of the Royal Astronomical Society, 497, 3400

Eggleton P. P., Kiseleva L. G., Hut P., 1998, *"The equilibrium tide model for tidal friction"*, The Astrophysical Journal, 499, 853

Essick R., Weinberg N. N., 2016, *"Orbital decay of Hot Jupiters due to nonlinear tidal dissipation within Solar-type hosts"*, The Astrophysical Journal, 816, 18

Fairén A. G., 2017, in Deeg H. J., Belmonte J. A., eds, , Handbook of Exoplanets. Springer International Publishing, Cham, pp 1–25, doi:10.1007/978-3-319-30648-3˙43-1, `http://link.springer.com/10.1007/978-3-319-30648-3_43-1`

Fakhouri O., 1995, *"Exoplanet Orbit Database | Exoplanet Data Explorer"*, `http://exoplanets.org/`

Favier B., Barker A. J., Baruteau C., Ogilvie G. I., 2014, *"Non-linear evolution of tidally forced inertial waves in rotating fluid bodies"*, Monthly Notices of the Royal Astronomical Society, 439, 845

Feynman R. P., 1970, *"The Feynman lectures on physics, Vol. I"*. Addison Wesley Longman

Fuller J., 2020, *"Inverse tides in pulsating binary stars"*, arXiv:2011.06613 [astro-ph]

Fuller J., Luan J., Quataert E., 2016, *"Resonance locking as the source of rapid tidal migration in the Jupiter and Saturn moon systems"*, Monthly Notices of the Royal Astronomical Society, 458, 3867

Gaudi B. S., Seager S., Mallen-Ornelas G., 2005, *"On the period distribution of close-in extrasolar giant planets"*, The Astrophysical Journal, 623, 472

Goldman I., 2008, *"The effective tidal viscosity in close solar-type binaries"*, Astronomische Nachrichten, 329, 762

Goldreich P., 1963, *"On the eccentricity of satellite orbits in the solar system"*, Monthly Notices of the Royal Astronomical Society, 126, 257

Goldreich P., Nicholson P. D., 1977, *"Turbulent viscosity and Jupiter's tidal Q"*, Icarus, 30, 301

Goldreich P., Nicholson P. D., 1989, *"Tidal friction in early-type stars"*, The Astrophysical Journal, 342, 1079

Goluskin D., 2016, *"Internally heated convection and Rayleigh-Bénard convection"*. SpringerBriefs in Applied Sciences and Technology, Springer International Publishing, Cham, doi:10.1007/978-3-319-23941-5, `http://link.springer.com/10.1007/978-3-319-23941-5`

Goodman J., Dickson E. S., 1998, *"Dynamical tide in Solar-type binaries"*, The Astrophysical Journal, 507, 938

Goodman J., Lackner C., 2009, *"Dynamical tides in rotating planets and stars"*, The Astrophysical Journal, 696, 2054

Goodman J., Oh S. P., 1997, *"Fast tides in slow stars: The efficiency of eddy viscosity"*, The Astrophysical Journal, 486, 403

Guo Z., Shporer A., Hambleton K., Isaacson H., 2020, *"Tidally excited oscillations in heartbeat binary stars: Pulsation phases and mode identification"*, The Astrophysical Journal, 888, 95

Hambleton K., et al., 2018, *"KIC 8164262: a heartbeat star showing tidally induced pulsations with resonant locking"*, Monthly Notices of the Royal Astronomical Society, 473, 5165

Hamer J. H., Schlaufman K. C., 2019, *"Hot Jupiters are destroyed by tides while their host stars are on the main sequence"*, The Astronomical Journal, 158, 190

Hamer J. H., Schlaufman K. C., 2020, *"Ultra-short-period planets are stable against tidal inspiral"*, The Astronomical Journal, 160, 138

Hanasoge S., Gizon L., Sreenivasan K. R., 2016, *"Seismic sounding of convection in the Sun"*, Annual Review of Fluid Mechanics, 48, 191

Hansen B. M. S., 2012, *"Calibration of equilibrium tide theory for extrasolar planet systems. II"*, The Astrophysical Journal, 757, 6

Hartnett J. G., Luiten A. N., 2011, *"Colloquium : Comparison of astrophysical and terrestrial frequency standards"*, Reviews of Modern Physics, 83, 1

Heideman M., Johnson D., Burrus C., 1985, *"Gauss and the history of the fast Fourier transform"*, Archive for history of exact sciences, 34, 265

Hubbard W., 1974, *"Tides in the giant planets"*, Icarus, 23, 42

Hubbard W. B., 1984, *"Planetary interiors"*. Van Nostrand Reinhold International

Hut P., 1980, *"Stability of tidal equilibrium"*, Astronomy & Astrophysics, 92, 167

Hut P., 1981, *"Tidal evolution in close binary systems."*, Astronomy & Astrophysics, 99, 126

Ivanov P. B., Papaloizou J. C. B., 2004, *"On equilibrium tides in fully convective planets and stars"*, Monthly Notices of the Royal Astronomical Society, 353, 1161

Ivanov P. B., Papaloizou J. C. B., 2010, *"Inertial waves in rotating bodies: a WKBJ formalism for inertial modes and a comparison with numerical results: Inertial waves in rotating bodies"*, Monthly Notices of the Royal Astronomical Society, 407, 1609

Jones C., 2007, in Schubert G., ed., , Treatise on geophysics. Elsevier, Amsterdam, pp 131 – 185, doi:https://doi.org/10.1016/B978-044452748-6.00130-9, `http://www.sciencedirect.com/science/article/pii/B9780444527486001309`

King E. M., Stellmach S., Buffett B., 2013, *"Scaling behaviour in Rayleigh-Bénard convection with and without rotation"*, Journal of Fluid Mechanics, 717, 449

Kippenhahn R., Weigert A., Weiss A., 2012, *"Stellar structure and evolution"*, second edition edn. Astronomy and astrophysics library, Springer, Berlin ; New York

Kolmogorov A. N., 1941, *"The local structure of turbulence in incompressible viscous fluid for very large Reynolds numbers"*, Dokl. Akad. Nauk SSSR, 30, 9

Kumar A., Verma M. K., 2018, *"Applicability of Taylor's hypothesis in thermally driven turbulence"*, Royal Society Open Science, 5, 172152

Kumar A., Chatterjee A. G., Verma M. K., 2014, *"Energy spectrum of buoyancy-driven turbulence"*, Physical Review E, 90

Lagos F., Schreiber M. R., Zorotovic M., Gänsicke B. T., Ronco M. P., Hamers A. S., 2020, *"WD 1856 b: a close giant planet around a white dwarf that could have survived a common-envelope phase"*, Monthly Notices of the Royal Astronomical Society, 501, 7

Lai D., 2012, *"Tidal dissipation in planet-hosting stars: damping of spin-orbit misalignment and survival of hot Jupiters: Tidal dissipation in planet-hosting stars"*, Monthly Notices of the Royal Astronomical Society, 423, 486

Lainey V., Arlot J.-E., Karatekin z., Van Hoolst T., 2009, *"Strong tidal dissipation in Io and Jupiter from astrometric observations"*, Nature, 459, 957

Lainey V., et al., 2012, *"Strong tidal dissipation in Saturn and constraints on Enceladus' thermal state from astrometry"*, The Astrophysical Journal, 752, 14

Lainey V., et al., 2017, *"New constraints on Saturn's interior from Cassini astrometric data"*, Icarus, 281, 286

Lainey V., et al., 2020, *"Resonance locking in giant planets indicated by the rapid orbital expansion of Titan"*, Nature Astronomy, 4, 1053

Lamb H., 1994, *"Hydrodynamics"*. Cambridge University Press

Landau L. D., Lifshitz E. M., 1987, *"Fluid Mechanics (Second Edition)"*. Course of theoretical physics, Butterworth-Heinemann

Lesur G., Longaretti P.-Y., 2005, *"On the relevance of subcritical hydrodynamic turbulence to accretion disk transport"*, Astronomy & Astrophysics, 444, 25

Lesur G., Ogilvie G. I., 2010, *"On the angular momentum transport due to vertical convection in accretion discs"*, Monthly Notices of the Royal Astronomical Society: Letters, 404, L64

Lin Y., Ogilvie G., 2017, *"Tidal interactions in spin-orbit misaligned systems"*, Monthly Notices of the Royal Astronomical Society, 468, 1387

Liot O., et al., 2016, *"Simultaneous temperature and velocity Lagrangian measurements in turbulent thermal convection"*, Journal of Fluid Mechanics, 794, 655

Love A. E. H., 1892, *"A Treatise on the mathematical theory of elasticity"*. Cambridge University Press, `https://hal.archives-ouvertes.fr/hal-01307751/document`

Love A. E. H., 1909, *"The yielding of the earth to disturbing forces"*, Proceedings of the Royal Society of London. Series A: Mathematical and Physical Sciences, 82, 16

Maciejewski G., et al., 2016, *"Departure from the constant-period ephemeris for the transiting exoplanet WASP-12"*, Astronomy & Astrophysics, 588, L6

Maciejewski G., et al., 2018, *"Planet-star interactions with precise transit timing. I. The refined orbital decay rate for WASP-12 b and initial constraints for HAT-P-23 b, KELT-1 b, KELT-16 b, WASP-33 b and WASP-103 b"*, Acta Astronomica, 68, 371

Mathis S., 2015, *"Variation of tidal dissipation in the convective envelope of low-mass stars along their evolution"*, Astronomy & Astrophysics, 580, L3

Mathis S., Remus F., 2013, in Rozelot J.-P., Neiner C. E. ., eds, , Vol. 857, In: The Environments of the Sun and the Stars. Ed by J.-P. Rozelot and C. Neiner. Lecture Notes in Physics, 2013, Volume 857/2013, pp. 111-147, DOI: 10.1007/978-3-642-30648-8_4. Springer, pp 111–147, doi:10.1007/978-3-642-30648-8˙4

Mathis S., Auclair-Desrotour P., Guenel M., Gallet F., Le Poncin-Lafitte C., 2016, *"The impact of rotation on turbulent tidal friction in stellar and planetary convective regions"*, Astronomy & Astrophysics, 592, A33

Mayor M., Queloz D., 1995, *"A Jupiter-mass companion to a solar-type star"*, Nature, 378, 355

Mayor, M. et al., 2003, *"Setting New Standards with HARPS"*, The Messenger, 114, 20

Mazeh T., 2008, *"Observational evidence for tidal interaction in close binary systems"*, EAS Publications Series, 29, 1

McCormac J., et al., 2020, *"NGTS-10b: the shortest period hot Jupiter yet discovered"*, Monthly Notices of the Royal Astronomical Society, 493, 126

McIntyre M. E., 1994, in Nesme-Ribes E., ed., , The Solar Engine and Its Influence on Terrestrial Atmosphere and Climate. Springer Berlin Heidelberg, Berlin, Heidelberg, pp 293–320, doi:10.1007/978-3-642-79257-1˙18, `http://link.springer.com/10.1007/978-3-642-79257-1_18`

Meibom S., Mathieu R. D., 2005, *"A robust measure of tidal circularization in Coeval binary populations: The Solar-type spectroscopic binary population in the open cluster M35"*, The Astrophysical Journal, 620, 970

Meibom S., Mathieu R. D., Stassun K. G., 2006, *"An observational study of tidal synchronization in Solar-type binary stars in the open clusters M35 and M34"*, The Astrophysical Journal, 653, 621

Mignard F., 1980, *"The evolution of the Lunar orbit revisited - part two"*, Moon and Planets, 23, 185

Munk W., Wunsch C., 1998, *"Abyssal recipes II: energetics of tidal and wind mixing"*, Deep Sea Research Part I: Oceanographic Research Papers, 45, 1977

Muñoz D. J., Petrovich C., 2020, *"Kozai migration naturally explains the white dwarf planet WD1856 b"*, The Astrophysical Journal, 904, L3

Murray C. D., Dermott S. F., 2000, *"Solar system dynamics"*. Cambridge University Press, Cambridge, doi:10.1017/CBO9781139174817

Mustill A. J., Villaver E., 2012, *"Foretellings of Ragnarök: World-engulfing asymptotic giants and the inheritance of white dwarfs."*, The Astrophysical Journal, 761, 121

Ni D., 2018, *"Empirical models of Jupiter's interior from Juno data: Moment of inertia and tidal Love number k_2"*, Astronomy & Astrophysics, 613, A32

Nine A. C., Milliman K. E., Mathieu R. D., Geller A. M., Leiner E. M., Platais I., Tofflemire B. M., 2020, *"WIYN open cluster study. LXXVII. Radial-velocity measurements and spectroscopic binary orbits in the open cluster NGC 7789"*, arXiv e-prints, p. arXiv:2003.09732

Obukhov A., 1959, *"Effect of Archimedean forces on the structure of the temperature field in a turbulent flow"*, Dokl. Akad. Nauk SSSR, 125, 1246

Ogilvie G. I., 2009, *"Tidal dissipation in rotating fluid bodies: a simplified model"*, Monthly Notices of the Royal Astronomical Society, 396, 794

Ogilvie G. I., 2013, *"Tides in rotating barotropic fluid bodies: the contribution of inertial waves and the role of internal structure"*, Monthly Notices of the Royal Astronomical Society, 429, 613

Ogilvie G. I., 2014, *"Tidal dissipation in stars and giant planets"*, Annual Review of Astronomy and Astrophysics, 52, 171

Ogilvie G. I., Lesur G., 2012, *"On the interaction between tides and convection: Tides and convection"*, Monthly Notices of the Royal Astronomical Society, 422, 1975

Ogilvie G. I., Lin D. N. C., 2004, *"Tidal dissipation in rotating giant planets"*, The Astrophysical Journal, 610, 477

Ogilvie G. I., Lin D. N. C., 2007, *"Tidal dissipation in rotating Solar-type stars"*, The Astrophysical Journal, 661, 1180

Oppenheim A. V., Schafer R. W., 2010, *"Discrete-time signal processing"*, 3rd ed edn. Pearson, Upper Saddle River

Orszag S. A., 1971, *"On the elimination of aliasing in finite-difference schemes by filtering high-wavenumber components."*, Journal of the Atmospheric sciences, 28, 1074

Papaloizou J. C. B., Ivanov P. B., 2010, *"Dynamic tides in rotating objects: a numerical investigation of inertial waves in fully convective or barotropic stars and planets"*, Monthly Notices of the Royal Astronomical Society, 407, 1631

Patra K. C., Winn J. N., Holman M. J., Yu L., Deming D., Dai F., 2017, *"The apparently decaying orbit of WASP-12b"*, The Astronomical Journal, 154, 4

Patra K. C., et al., 2020, *"The continuing search for evidence of tidal orbital decay of Hot Jupiters"*, The Astronomical Journal, 159, 150

Paxton B., Bildsten L., Dotter A., Herwig F., Lesaffre P., Timmes F., 2011, *"Modules for Experiments in Stellar Astrophysics (MESA)"*, Astrophysical Journal, Supplement, 192, 3

Paxton B., et al., 2013, *"Modules for Experiments in Stellar Astrophysics (MESA): Planets, oscillations, rotation, and massive stars"*, Astrophysical Journal, Supplement, 208, 4

Paxton B., et al., 2015, *"Modules for Experiments in Stellar Astrophysics (MESA): Binaries, pulsations, and explosions"*, Astrophysical Journal, Supplement, 220, 15

Paxton B., et al., 2018, *"Modules for Experiments in Stellar Astrophysics (MESA): Convective boundaries, element diffusion, and massive star explosions"*, Astrophysical Journal, Supplement, 234, 34

Paxton B., et al., 2019, *"Modules for Experiments in Stellar Astrophysics (MESA): Pulsating variable stars, rotation, convective boundaries, and energy conservation"*, Astrophysical Journal, Supplement, 243, 10

Penev K., Sasselov D., Robinson F., Demarque P., 2007, *"On dissipation inside turbulent convection zones from three-dimensional simulations of solar convection"*, The Astrophysical Journal, 655, 1166

Penev K., Sasselov D., Robinson F., Demarque P., 2009a, *"Dissipation efficiency in turbulent convective zones in low-mass stars"*, The Astrophysical Journal, 704, 930

Penev K., Barranco J., Sasselov D., 2009b, *"Direct calculation of the turbulent dissipation efficiency in anelastic convection"*, The Astrophysical Journal, 705, 285

Pereira M., Gissinger C., Fauve S., 2019, *"1/f noise and long-term memory of coherent structures in a turbulent shear flow"*, Physical Review E, 99, 023106

Perryman M., 2018, *"The exoplanet handbook, 2nd edition"*. Cambridge University Press

Petrucci R., Jofré E., Gómez Maqueo Chew Y., Hinse T. C., Mašek M., Tan T.-G., Gómez M., 2019, *"Discarding orbital decay in WASP-19b after one decade of transit observations"*, Monthly Notices of the Royal Astronomical Society, 491, 1243

Pontin C. M., Barker A. J., Hollerbach R., André Q., Mathis S., 2020, *"Wave propagation in semiconvective regions of giant planets"*, Monthly Notices of the Royal Astronomical Society, 493, 5788

Prandtl L., 1925, *"7. Bericht über Untersuchungen zur ausgebildeten Turbulenz"*, ZAMM - Journal of Applied Mathematics and Mechanics / Zeitschrift für Angewandte Mathematik und Mechanik, 5, 136

Price-Whelan A. M., Goodman J., 2018, *"Binary companions of evolved stars in APOGEE DR14: Orbital circularization"*, The Astrophysical Journal, 867, 5

Ragozzine D., Wolf A. S., 2009, *"Probing the interiors of very hot Jupiters using transit light curves"*, The Astrophysical Journal, 698, 1778

Rasio F. A., Tout C. A., Lubow S. H., Livio M., 1996, *"Tidal decay of close planetary orbits"*, The Astrophysical Journal, 470, 1187

Remus F., Mathis S., Zahn J. P., 2012, *"The equilibrium tide in stars and giant planets. I. The coplanar case"*, Astronomy & Astrophysics, 544, A132

Rieutord M., Valdettaro L., 2010, *"Viscous dissipation by tidally forced inertial modes in a rotating spherical shell"*, Journal of Fluid Mechanics, 643, 363

Sahlmann J., Lazorenko P. F., Ségransan D., Martín E. L., Queloz D., Mayor M., Udry S., 2013, *"Astrometric orbit of a low-mass companion to an ultracool dwarf"*, Astronomy & Astrophysics, 556, A133

Sano M., Wu X. Z., Libchaber A., 1989, *"Turbulence in helium-gas free convection"*, Physical Review A, 40, 6421

Shang X.-D., Xia K.-Q., 2001, *"Scaling of the velocity power spectra in turbulent thermal convection"*, Physical Review E, 64, 065301

Souchay J., Mathis S., Tokieda T., eds, 2013, *"Tides in Astronomy and Astrophysics"*. Lecture notes in physics Vol. 861, Springer Berlin Heidelberg, Berlin, Heidelberg, `http://link.springer.com/10.1007/978-3-642-32961-6`

Spiegel E. A., 1971, *"Convection in stars: I. basic Boussinesq bonvection"*, Annual Review of Astronomy and Astrophysics, 9, 323

Spiegel E. A., Veronis G., 1960, *"On the Boussinesq approximation for a compressible fluid."*, Astrophysical Journal, 131, 442

Stevenson D. J., 1979, *"Turbulent thermal convection in the presence of rotation and a magnetic field: A heuristic theory"*, Geophysical & Astrophysical Fluid Dynamics, 12, 139

Stevenson D., 2015, in , Treatise on Geophysics. Elsevier, pp 1–9, doi:10.1016/B978-0-444-53802-4.00151-2, `https://linkinghub.elsevier.com/retrieve/pii/B9780444538024001512`

Sun M., Arras P., Weinberg N. N., Troup N. W., Majewski S. R., 2018, *"Orbital decay in binaries containing post-main-sequence stars"*, Monthly Notices of the Royal Astronomical Society, 481, 4077

Terquem C., Papaloizou J. C. B., Nelson R. P., Lin D. N. C., 1998, *"On the tidal interaction of a Solar-type star with an orbiting companion: Excitation of g-mode oscillation and orbital evolution"*, The Astrophysical Journal, 502, 788

Trefethen L. N., 2000, *"Spectral methods in MATLAB"*. SIAM

Triaud A. H. M. J., et al., 2017, *"The EBLM Project. IV. Spectroscopic orbits of over 100 eclipsing M dwarfs masquerading as transiting hot Jupiters"*, Astronomy & Astrophysics, 608, A129

Turner J. D., Ridden-Harper A., Jayawardhana R., 2020, *"Decaying orbit of the hot Jupiter WASP-12b: Confirmation with TESS observations"*, arXiv:2012.02211 [astro-ph]

Van Eylen V., Winn J. N., Albrecht S., 2016, *"Orbital circularization of hot and cool Kepler eclipsing binaries"*, The Astrophysical Journal, 824, 15

Vanderburg A., et al., 2020, *"A giant planet candidate transiting a white dwarf"*, Nature, 585, 363

Veras D., Fuller J., 2019, *"Tidal circularization of gaseous planets orbiting white dwarfs"*, Monthly Notices of the Royal Astronomical Society, 489, 2941

Veras D., Fuller J., 2020, *"The dynamical history of the evaporating or disrupted ice giant planet around white dwarf WD J0914+1914"*, Monthly Notices of the Royal Astronomical Society, 492, 6059

Veras D., et al., 2019, *"Orbital relaxation and excitation of planets tidally interacting with white dwarfs"*, Monthly Notices of the Royal Astronomical Society, 486, 3831

Verbunt F., Phinney E. S., 1995, *"Tidal circularization and the eccentricity of binaries containing giant stars."*, Astronomy & Astrophysics, 296, 709

Verma M. K., 2018, *"Physics of buoyant flows: From instabilities to turbulence"*. WORLD SCIENTIFIC, doi:10.1142/10928, `https://www.worldscientific.com/worldscibooks/10.1142/10928`

Vick M., Lai D., 2020, *"Tidal evolution of eccentric binaries driven by convective turbulent viscosity"*, Monthly Notices of the Royal Astronomical Society, 496, 3767

Vidal J., Barker A. J., 2020a, *"Efficiency of tidal dissipation in slowly rotating fully convective stars or planets"*, Monthly Notices of the Royal Astronomical Society, 497, 4472

Vidal J., Barker A. J., 2020b, *"Turbulent viscosity acting on the equilibrium tidal flow in convective stars"*, The Astrophysical Journal, 888, L31

Vidal J., Duguid C. D., Barker A. J., 2020, *"Anomalous 1/f frequency spectrum of thermal convection"*, Physical Review Fluids (submitted)

Wang J., Fischer D. A., Horch E. P., Huang X., 2015, *"On the occurrence rate of Hot Jupiters in different stellar environments"*, The Astrophysical Journal, 799, 229

Weinberg N. N., Arras P., Quataert E., Burkart J., 2012, *"Nonlinear tides in close binary systems"*, The Astrophysical Journal, 751, 136

Weinberg N. N., Sun M., Arras P., Essick R., 2017, *"Tidal dissipation in WASP-12"*, The Astrophysical Journal, 849, L11

Welsh W. F., et al., 2011, *"KOI-54: The Kepler discovery of tidally excited pulsations and brightenings in a highly eccentric binary"*, Astrophysical Journal, Supplement, 197, 4

Wilkins A. N., Delrez L., Barker A. J., Deming D., Hamilton D., Gillon M., Jehin E., 2017, *"Searching for rapid orbital decay of WASP-18b"*, The Astrophysical Journal, 836, L24

Williams G. E., 2000, *"Geological constraints on the Precambrian history of Earth's rotation and the Moon's orbit"*, Reviews of Geophysics, 38, 37

Wolszczan A., Frail D. A., 1992, *"A planetary system around the millisecond pulsar PSR1257+12"*, Nature, 355, 145

Wu Y., 2005a, *"Origin of tidal dissipation in Jupiter. II. the value of Q"*, The Astrophysical Journal, 635, 23

Wu Y., 2005b, *"Origin of tidal dissipation in Jupiter. I. properties of inertial modes"*, The Astrophysical Journal, 635, 674

Wu Y., 2005c, *"Origin of tidal dissipation in Jupiter. II. The value of Q"*, The Astrophysical Journal, 635, 688

Wu X.-Z., Kadanoff L., Libchaber A., Sano M., 1990, *"Frequency power spectrum of temperature fluctuations in free convection"*, Physical Review Letters, 64, 2140

Yee S. W., et al., 2019, *"The orbit of WASP-12b is decaying"*, The Astrophysical Journal, 888, L5

Zahn J. P., 1966, *"Les marées dans une étoile double serrée"*, Annales d'Astrophysique, 29, 313

Zahn J., 1975, *"The dynamical tide in close binaries"*, Astronomy & Astrophysics, 41, 329

Zahn J., 1977, *"Tidal friction in close binary stars"*, Astronomy & Astrophysics, 57, 383

Zahn J. P., 1989, *"Tidal evolution of close binary stars. I - Revisiting the theory of the equilibrium tide"*, Astronomy & Astrophysics, 220, 112

Zahn J. P., 2008, in Goupil M. J., Zahn J. P., eds, EAS Publications Series Vol. 29, EAS Publications Series. pp 67–90 (`arXiv:0807.4870`), doi:10.1051/eas:0829002

Zahn J. P., Bouchet L., 1989, *"Tidal evolution of close binary stars. II. Orbital circularization oflate-type binaries."*, Astronomy & Astrophysics, 223, 112

Zimmerman M. K., Thompson S. E., Mullally F., Fuller J., Shporer A., Hambleton K., 2017, *"The pseudosynchronization of binary stars undergoing strong tidal interactions"*, The Astrophysical Journal, 846, 147